

INFORMATION TO USERS

This manuscript has been reproduced from the microfilm master. UMI films the text directly from the original or copy submitted. Thus, some thesis and dissertation copies are in typewriter face, while others may be from any type of computer printer.

The quality of this reproduction is dependent upon the quality of the copy submitted. Broken or indistinct print, colored or poor quality illustrations and photographs, print bleedthrough, substandard margins, and improper alignment can adversely affect reproduction.

In the unlikely event that the author did not send UMI a complete manuscript and there are missing pages, these will be noted. Also, if unauthorized copyright material had to be removed, a note will indicate the deletion.

Oversize materials (e.g., maps, drawings, charts) are reproduced by sectioning the original, beginning at the upper left-hand corner and continuing from left to right in equal sections with small overlaps. Each original is also photographed in one exposure and is included in reduced form at the back of the book.

Photographs included in the original manuscript have been reproduced xerographically in this copy. Higher quality 6" x 9" black and white photographic prints are available for any photographs or illustrations appearing in this copy for an additional charge. Contact UMI directly to order.

UMI

A Bell & Howell Information Company
300 North Zeeb Road, Ann Arbor MI 48106-1346 USA
313/761-4700 800/521-0600

University of Alberta

**Critical Currents and Intrinsic Properties of
 $Y_1Ba_2Cu_3O_{7-\delta}$ Thin Films**

By

HASSANE DARHMAOUI



A thesis submitted to the Faculty of Graduate Studies and Research
in partial fulfillment of the requirements for the degree of
Doctor of Philosophy
in
Solid State Physics

Department of Physics

Edmonton, Alberta

Fall 1997



National Library
of Canada

Acquisitions and
Bibliographic Services

395 Wellington Street
Ottawa ON K1A 0N4
Canada

Bibliothèque nationale
du Canada

Acquisitions et
services bibliographiques

395, rue Wellington
Ottawa ON K1A 0N4
Canada

Your file *Votre référence*

Our file *Notre référence*

The author has granted a non-exclusive licence allowing the National Library of Canada to reproduce, loan, distribute or sell copies of this thesis in microform, paper or electronic formats.

The author retains ownership of the copyright in this thesis. Neither the thesis nor substantial extracts from it may be printed or otherwise reproduced without the author's permission.

L'auteur a accordé une licence non exclusive permettant à la Bibliothèque nationale du Canada de reproduire, prêter, distribuer ou vendre des copies de cette thèse sous la forme de microfiche/film, de reproduction sur papier ou sur format électronique.

L'auteur conserve la propriété du droit d'auteur qui protège cette thèse. Ni la thèse ni des extraits substantiels de celle-ci ne doivent être imprimés ou autrement reproduits sans son autorisation.

0-612-22972-6

UNIVERSITY OF ALBERTA
LIBRARY RELEASE FORM

NAME OF AUTHOR: Hassane Darhmaoui
TITLE OF THESIS: Critical Currents and Intrinsic Properties of $Y_1Ba_2Cu_3O_{7-\delta}$ Thin Films
DEGREE: Doctor of Philosophy
YEAR THE DEGREE GRANTED: 1997

Permission is hereby granted to the University of Alberta library to reproduce single copies of this thesis and to lend or sell such copies for private, scholarly or scientific research purposes only.

The author reserves all other publication and other rights in association with the copyright in the thesis, and except as hereinbefore provided, neither the thesis nor any substantial portion thereof may be printed or otherwise reproduced in any material form whatever without the author's prior written permission.



Hassane Darhmaoui

983 Bloc 45

Hay Hassani

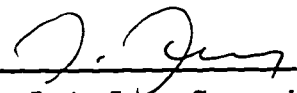
Marrakech, Morocco

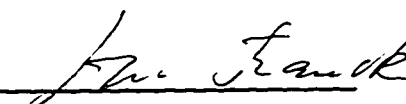
Date: Aug 22/1997

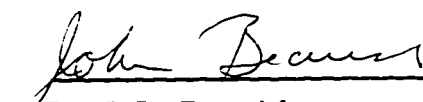
UNIVERSITY OF ALBERTA

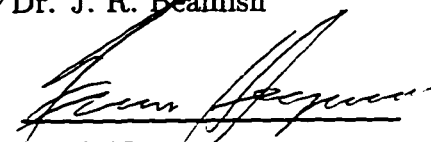
FACULTY OF GRADUATE STUDIES AND RESEARCH

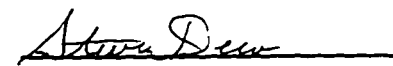
The undersigned certify that they have read, and recommend to the Faculty of Graduate Studies and Research for acceptance, a thesis entitled "Critical Currents and Intrinsic Properties of $Y_1Ba_2Cu_3O_{7-\delta}$ Thin Films" submitted by Hassane Darhmaoui in partial fulfillment of the requirements for the degree of Doctor of Philosophy in Solid State Physics.



Dr. J. A. Jung, Supervisor


Dr. J. P. Franck


Dr. J. R. Beamish


Dr. F. Hegmann


Dr. S. Dew


Dr. M. B. Mapple

Date: Aug. 21, 1997

to
My Mother,
My Wife,
Abd Errahman and Hibat Errahman.

Abstract

We investigated the physical processes which govern the supercurrent limiting mechanism in $Y_1Ba_2Cu_3O_{7-\delta}$ (YBCO) thin films. The following problems have been studied: (1) temperature dependence of the critical current $I_c(T)$, (2) dissipation of the current and the effective activation energy barrier $U_{\text{eff}}(J)$ for vortex motion, and (3) magnetic flux penetration and current distribution in disk-shaped YBCO thin films. The experiments were carried out with an unconventional technique which uses ring- and disk-shaped samples and a scanning Hall probe to measure the profiles of a magnetic field due to a persistent current circulating in a ring or due to magnetic vortices penetrating a disk.

The studies of $I_c(T)$ revealed the crossover between an Ambegaokar-Baratoff-like (AB) temperature dependence of the critical current at low temperatures to a Ginzburg-Landau-like (GL) $(T_c - T)^{3/2}$ dependence at higher temperatures. The crossover was observed for both depairing and depinning critical currents in c-axis oriented YBCO thin films (and in granular YBCO). The experimental data imply the presence of superconducting nanometer-size domains (of an effective diameter of about 30-40 Å) coupled by Josephson tunnel junctions in the a-b planes of YBCO, in agreement with the Clem's model for $I_c(T)$ in strongly coupled granular superconductors [Phys. Rev. B **35**,6637 (1987)] and electron microscopy studies of Etheridge [Phil. Mag. A **73**, 643 (1996)]. The size of these domains decreases with a decreasing oxygen content and with an increasing applied magnetic field.

Regarding the dissipation of the current, we found the correlation between the temperature dependence of the critical current $I_c(T)$ and the dependence of $U_{\text{eff}}(J)$ on the current density in YBCO thin films. When $I_c(T)$ is dominated by a GL-like temperature dependence [$I_c(T) \propto (T_c - T)^{3/2}$], the empirical formula for the energy barrier is $U_{\text{eff}}(J) = a J_c(T) \exp(-\frac{3\pi}{2} J/J_{c0})$. In an AB regime of

$I_c(T)$, $U_{\text{eff}}(J) = J_c(T)[a_1 \exp(-\frac{3\pi}{2}J/J_{c0}) + a_2 \exp(-\frac{9\pi}{2}J/J_{c0})]$. These relationships were found to describe an intrinsic property of all thin films studied, independent of the growth conditions, substrates, film thickness, T_c , and the magnitude of the critical current density. According to our interpretation, the factors $\frac{3\pi}{2}J/J_{c0}$ and $\frac{9\pi}{2}J/J_{c0}$ in the exponents of $U_{\text{eff}}(J)$ represent a tilted washboard potential $U_j(\phi)/E_j = -\cos\phi - (J/J_{c0})\phi$ for an overdamped (resistively shunted) Josephson tunnel junction, locked at phases of $3\pi/2$ and $9\pi/2$. These phases correspond to the maximum resistive dissipation in a junction. The experimental data imply that the superconductor behaves like a single overdamped Josephson junction (or an extremely coherent array of resistively shunted Josephson junctions). The dissipation of the persistent current occurs due to the collective motion of vortices through the Josephson nanostructures in YBCO.

Magnetic flux penetration and current distribution in YBCO disk-shaped thin films was investigated at low magnetic fields. We studied the conditions characteristic of complete and partial flux penetration regimes. Magnetic flux penetration and current distribution in disk-shaped YBCO thin films are well described by the critical state model of Mikheenko and Kuzovlev [Physica C 204, 229 (1993)] and Zhu et al [Physica C 212, 216 (1993)].

Acknowledgements

I would like to express great appreciation to my advisor Dr. Jan Jung. It is a pleasure to have an advisor with such deep insight in his field and great ambition. I'm indebted to him for much of the things I learned in the field of superconductivity. I thank him for his continuous support and friendly supervision.

I would like to thank the members of my committee Prof. J. P. Frank, Prof. J. R. Beamish, Dr. F. Hegmann, Dr. S. Dew and Prof. M. B. Maple for their comments on my research.

The completion of this thesis required the assistance of several people. I would like to thank Mr. T. Walford for his valuable technical support in building the measurement system and also upgrading the sputtering system, Mr. D. Mullin for his help in the thin film laboratory, Mr. B. Burris for his assistance in interfacing and computer programming, Ms. L. Chandler for her administrative help and the staff in the Alberta Microelectronics Center for their help in photolithography.

I am also pleased to acknowledge useful discussions with Prof. S. B. Woods, Dr. M. A. K. Mohammed and Dr. I. Isaac.

I am also grateful to Dr. J. S. Preston of McMaster University; Dr. A. A. Fife of CTF systems; Dr. J. Z. Sun of IBM T. J. Watson Research Centre; Dr. J. Talvacchio of Westinghouse STC and Dr. M. W. McElfresh of Purdue University for supplying us with YBCO thin films.

I am grateful to all my teachers and friends in Edmonton who have directly and indirectly contributed to this thesis.

Contents

1	Introduction	1
1.1	Temperature dependence of the critical current	6
1.1.1	Theoretical Models	6
1.1.2	Temperature dependence of the intragrain and intergrain critical current in YBCO	9
1.2	Dissipation of the persistent current and the magnetic vortex dynamics	11
1.2.1	Theoretical Models	11
1.2.2	Dissipation of the persistent current and flux pinning in YBCO thin films	15
1.3	Distribution of the currents and the critical state	18
1.3.1	Theory of the critical state in a superconducting disk	18
1.3.2	Current distribution and magnetic flux penetration in YBCO thin films	20
2	Experimental Procedures	24
2.1	Introduction	24
2.2	Measurement Technique	25
2.2.1	Experimental set up	25
2.2.2	Sample preparation	28

2.2.3	Critical current measurement procedure	33
2.2.4	Magnetic flux relaxation measurement procedure	36
2.2.5	Magnetic flux penetration measurement procedure	42
3	Temperature Dependence of the Critical Current	47
3.1	Experimental Results	47
3.1.1	Temperature dependence of J_c in YBCO thin films	47
3.1.2	Magnetic field dependence of $J_c(T)$ in YBCO thin films	49
3.1.3	Magnetic field dependence of $J_c(T)$ in granular YBCO	50
3.1.4	Magnetic field dependence of $J_c(T)$ in YBCO/Ag granular composite	50
3.2	Discussion	56
3.2.1	Crossover effects in the temperature dependence of J_c in YBCO	56
3.2.2	Origin of the $AB \rightarrow GL$ crossover in the temperature dependence of J_c in YBCO	62
3.2.3	Comparison between the intergrain and the intragrain $J_c(T)$ in YBCO	67
3.2.4	Microgranularity in YBCO	68
4	Dissipation of the persistent current and flux pinning in YBCO thin films	70
4.1	Experimental Results	70

4.1.1	Effect of relaxation on the distribution of the persistent current in ring-shaped YBCO thin films	70
4.1.2	Relaxation measurements and calculation of $U_{\text{eff}}(J)$ for YBCO thin films	75
4.1.3	Relationship between U_{eff} and $J_c(T)$	80
4.2	Discussion	87
4.2.1	Origin of the universal exponential dependence of $U_{\text{eff}}(J)$	95
4.2.2	Pinning mechanism and vortex dynamics in YBCO thin films	98
5	Distribution of currents and the critical state in YBCO thin films	104
5.1	Experimental Results	104
5.1.1	Magnetic-flux penetration into disk-shaped and ring-shaped YBCO thin films	104
5.1.2	Crossover between partial and complete flux penetration regimes	121
5.1.3	Magnetic relaxation in the partial and complete flux penetra- tion regimes	121
5.2	Discussion:	134
5.2.1	Calculation of the current density profiles in a disk- and ring- shaped YBCO thin films	134
5.2.2	Temperature dependence of the magnetic flux penetration in YBCO thin films	150
5.2.3	Characterization of the complete and partial penetration regimes using magnetic relaxation measurements	151

6 Summary and Conclusions	153
Bibliography	160
Appendix A	169
Appendix B	176

List of Tables

- 4.1 Superconducting transition temperature T_c at zero resistance, film thickness, critical current density J_c at 10K and 77K, deposition method and substrates used, are listed for all YBCO thin films that were investigated in the course of this work. Note that J_c^a denotes an “apparent” critical current density which is defined as the ratio of the critical current I_c to the cross-sectional area A of the sample. The actual J_c may be higher if the current flow occurs through a reduced cross-sectional area A 72
- 5.1 The calculated normalized radius a/R (where $a = R/\cosh(H_a/H_d)$) of the vortex free region and the normalized inner radius b/R (where $b = R/\cosh(H_a/2H_d)$) of the annular region where J_c is constant for the remnant regime. The computations were performed for different temperatures at a maximum available applied field of 750G and minimum applied field at which a saturation of the trapped field is observed. 145

List of Figures

1.1.1	Ambegaokar-Baratoff-like type temperature dependence of the critical current and Ginzburg-Landau-like dependence.	10
2.2.1	The measurement system.	26
2.2.2	Schematic of the ring's geometry used in the measurements of the magnetic field profiles above the ring. Scanning direction denotes the direction of motion of a Hall probe across the ring.	27
2.2.3	Thin film sputtering system.	29
2.2.4	X-ray diffraction pattern obtained for a YBCO film grown on (a) SrTiO ₃ and (b) LaAlO ₃ . Both films have a c-axis orientation typical of YBCO films that were used in this study.	32
2.2.5	The profiles of the axial component of the magnetic self-field generated by the persistent (self-supporting) currents in the zero-field-cooled YBCO thin film ring at 10 K. The persistent currents of various magnitudes were induced by applying and subsequently removing an external magnetic field. Critical persistent current is reached when the current's self-field saturates. The field was measured with a scanning axial Hall probe at a distance of 2.5 mm above the surface of thin film. Distances ± 4.25 mm and ± 2.5 mm mark the ring's outer and inner edges, respectively.	34

2.2.6	Dependence of the persistent current's self-field measured at the ring's center on an applied magnetic field at 10 and 20 K. Saturation value of the self-field is proportional to the magnitude of the critical current at a given temperature.	35
2.2.7	The profiles of the axial component $B_z(r)$ of the persistent current's self-field at the critical value, measured at temperatures of 30 K (open circles), 50 K (open triangles) and 70 K (full circles) in a zero-field cooled ring of YBCO film #1 at a distance of 2.5 mm above it. The profiles are normalized to the value of the field at the center of the ring. Note that the shape of the profile is independent of temperature. Distances $r = \pm 2.5mm$ and $r = \pm 4.25mm$ mark the ring's inner and outer edges.	40
2.2.8	The profiles of the axial field H_z (a) and the radial field H_r (b) above a pancake-shaped disk coil. The measurements were taken at distances of: 1.4, 3, 4, 5, 6, 7, 8, 9, 10, 11 and 12mm above the disk coil. Solid lines represent the theoretical calculation of the profiles generated by a constant current $I = 1.0 A$	45
2.2.9	The profiles of the axial field H_z (a) and the radial field H_r (b) above a pancake-shaped ring coil. The measurements were taken at distances of: 1.25, 2.25, 3.25, 4.24, 5.25, 6.25, 7.25, 8.25, 9.25, 10.25 and 11.25mm above the ring coil. Solid lines represent the theoretical calculation of the profiles generated by a constant current $I = 0.25 A$	46

- 3.1.1 Temperature dependence of the critical current in *c*-axis oriented YBCO thin films with T_c over a range of 52 – 90K. The critical current is normalized to its value at 10K. The results show a transition from an Ambegaokar-Baratoff-like (AB) temperature dependence to a Ginzburg-Landau-like (GL) one upon reduction of T_c . The $AB \rightarrow GL$ crossover is seen in the film of $T_c \simeq 90K$ at a temperature of about 80–82K. T_c is a temperature at which the level of critical persistent current is less than about 5mA (which corresponds to a noise level of a Hall probe). The critical current level at 10K was within a range of 2 – 45A for various samples. 48
- 3.1.2 Temperature dependence of the depairing critical current measured in *c*-axis oriented YBCO thin film in magnetic fields up to 700G. For the ZFC case the thin film has $T_c \simeq 90K$ and is characterized by an Ambegaokar-Baratoff-like $I_c(T)$ below 80 – 82K and by a Ginzburg-Landau-like $I_c(T)$ above this temperature. A magnetic field of 700G removes the low temperature plateau of $I_c(T)$ and reduces the $AB \rightarrow GL$ crossover temperature. 51
- 3.1.3 Temperature dependence of the depairing critical current measured in *c*-axis oriented YBCO thin film in magnetic fields up to 700G. For the ZFC case, this thin film has $T_c \simeq 83K$ and is characterized by a Ginzburg-Landau-like $(T - T_c)^{3/2}$ temperature dependence of $I_c(T)$. A magnetic field of 700G does not have any effect on the shape of $I_c(T)$ 52

3.1.4	Temperature dependence of the intergrain critical current measured in a granular YBCO in magnetic fields up to 100G for depairing critical currents. A gradual transition from an Ambegaokar-Baratoff -like to a Ginzburg-Landau-like behaviour can be seen.	53
3.1.5	Temperature dependence of the intergrain critical current measured in a granular YBCO in magnetic fields up to 100G for depinning critical currents. A gradual transition from an Ambegaokar-Baratoff -like to a Ginzburg-Landau-like behaviour can be seen.	54
3.1.6	Temperature dependence of the intergrain critical current in a granular YBCO/Ag (2 wt %) composite. In the ZFC case, I_c reveals an Ambegaokar-Baratoff-like behaviour below 80K, and a DeGennes type behaviour above 80K with $I_c \propto (T - T_c)^2$ shown in the inset. An applied magnetic field causes almost complete transformation of $I_c(T)$ into a Ginzburg-Landau-like one.	55
3.2.1	Comparison of the experimental data for I_c in a c-axis oriented YBCO thin film # A1 of $T_c = 90K$ (solid symbols) with the calculated ones from the Ambegaokar-Baratoff theory for Josephson tunnel junctions [14], represented by the curve A-B, and from the Clem's model [5] of an Ambegaokar-Baratoff to a Ginzburg-Landau crossover effects in granular weakly-coupled ($\epsilon_0 = 0.1$) and strongly-coupled ($\epsilon_0 = 100$) superconductors. The best fit to the experimental data was obtained for the case of $I_c(T)$ in strongly-coupled granular superconductors (Clem, $\epsilon_0 = 100$) with a temperature of the crossover from an Ambegaokar-Baratoff behaviour at low temperatures to a Ginzburg-Landau behaviour at high temperatures at 80 – 82K.	57

3.2.2 Temperature dependence of the critical current in c-axis oriented YBCO thin films plotted for the results shown in Figure (3.1.1) as $[I_c(T)/I_c(10K)]^{2/3}$ versus temperature. This allowed us to identify the Ginzburg-Landau portions of $I_c(T)$ (solid lines). All the experimental results are enclosed by two curves: by the Ambegaokar-Baratoff (A-B) $I_c(T)$ or by the Clem's ($AB \rightarrow GL$ with $\epsilon_0 = 100$) form of $I_c(T)$ on the high T_c side, and by the Ginzburg-Landau $(T - T_c)^{3/2}$ form of $I_c(T)$ on the low T_c side. A gradual expansion of the Ginzburg-Landau $(T - T_c)^{3/2}$ tail to low temperatures can be seen upon reduction of T_c 58

3.2.3 Dependence of $[I_c(T)/I_c(10K)]^{2/3}$ on temperature plotted for the experimental results obtained for YBCO thin film #A1 in a magnetic field of 275G and 700G (Figure (3.1.2)). The magnetic field-induced expansion of the Ginzburg-Landau portion of $I_c(T)$ present in the zero-field-cooled film can be seen. For the ZFC case, $I_c(T)$ is reproduced by the Clem's model with $\epsilon_0 = 100$. Note that discrepancy between the experimental data and the Ginzburg-Landau solid lines very close to T_c is caused by the experimental difficulty in measuring the self-fields of very small persistent currents in the presence of much larger external magnetic fields. 59

- 3.2.4 Dependence of $[I_c(T)/I_c(10K)]^{2/3}$ on temperature plotted for the experimental results obtained for YBCO thin film #A7 in a magnetic field of 275G and 700G [Figure (3.1.3)]. Magnetic field does not affect the Ginzburg-Landau temperature dependence of $I_c(T)$ measured in the zero-field-cooled thin film. Note that discrepancy between the experimental data and the Ginzburg-Landau solid lines very close to T_c is caused by the experimental difficulty in measuring the self-fields of very small persistent currents in the presence of much larger external magnetic fields. 60
- 3.2.5 $[I_c(T)/I_c(10K)]^{2/3}$ versus temperature plotted for the case of depairing $I_c(T)$ measured in a granular YBCO #1 [Figure (3.1.4)]. A transition from an Ambegaokar-Baratoff form of $I_c(T)$ (dotted and dashed lines) to a Ginzburg-Landau one (solid lines) is observed upon application of an increasing external magnetic field. Note that deviation of the experimental points from the solid lines very close to T_c is a result of experimental difficulties of measuring small persistent current's self-fields in the presence of much larger external magnetic fields. 63
- 3.2.6 $[I_c(T)/I_c(10K)]^{2/3}$ versus temperature plotted for the case of depinning $I_c(T)$ measured in a granular YBCO #2 [(Figure (3.1.5)]. A transition from an Ambegaokar-Baratoff form of $I_c(T)$ (dotted and dashed lines) to a Ginzburg-Landau one (solid lines) is observed upon application of an increasing external magnetic field. Note that deviation of the experimental points from the solid lines very close to T_c is a result of experimental difficulties of measuring small persistent current's self-fields in the presence of much larger external magnetic fields. 64

- 4.1.1 The profiles of the axial and radial trapped fields $B_z(r)$ and $B_r(r)$ measured across the ring of YBCO film #1 at a distance of $3mm$ above it, after waiting 30 s (open circles) and $10,000\text{ s}$ (full circles). The profiles represent the axial and radial components of the persistent current's self-field. Distances $r = \pm 2.5mm$ and $r = \pm 4.25mm$ mark the inner and the outer edges of the ring. The sample was zero-field-cooled down to $30K$, before an external field of $700G$ was applied and subsequently reduced to zero in order to generate the persistent current at the critical level. The solid lines represent the computer simulations (see text) of the axial and radial profiles using the Biot-Savart law and the current distribution shown in Figure 4.1.3. 71
- 4.1.2 The profiles of the axial and radial trapped field taken from Figure 4.1.1, which are normalized using the maximum values of the axial and the radial trapped fields. Note that the shape of both profiles does not change during persistent current's decay, suggesting that the normalized decay rate remains constant across the ring. 73
- 4.1.3 The distribution of the persistent current density $J(r)$ in the zero-field-cooled ring at $30K$ after waiting 30 s (solid line) and $10,000\text{ s}$ (dotted line). This distribution was used to perform computer calculations of the profiles of the axial and radial components of the self-field of the persistent current in Figure 4.1.1 74

4.1.4 The profiles of the axial component of the self-field of the persistent currents circulating in a ring of YBCO film #1. Persistent currents, of various levels up to the critical value, were induced in the ring at 20 K after external fields between 250 and 540 G were applied to the zero-field-cooled sample. Distances $\pm 2.5\text{mm}$ and $\pm 4.25\text{mm}$ mark the ring's inner and outer edges. The profiles were measured at a distance of 2.5mm above the ring. 76

4.1.5 The dependence of the persistent currents, of various magnitudes up to the critical value, on the logarithm of the waiting time. The decays were measured at a temperature of 20 K in a ring of YBCO film #1. The calculation of the energy barrier was based on the time decay of the persistent current from the highest value over a time interval of 2,000 - 30,000s. Note that the decay curves of the persistent currents close to the critical value merge after waiting approximately 1,000 to 2,000s. 77

4.1.6 The dependence of the persistent currents, of various magnitudes up to the critical value, on the logarithm of the waiting time. The decays were measured at a temperature of 50 K in a ring of YBCO film #1. The calculation of the energy barrier was based on the time decay of the persistent current from the highest value over a time interval of 2,000 - 30,000s. Note that the decay curves of the persistent currents close to the critical value merge after waiting approximately 1,000 to 2,000s. 78

4.1.7 The dependence of the energy barrier on the magnitude of the persistent current for six YBCO ring-shaped films (from #1 up to #6) calculated from the relaxation data [Figures (4.1.5 and (4.1.6)] using the Maley's procedure. The "Maley's" segments were calculated every 5 K for temperatures between 10 and 85 K. 79

4.1.8 The comparison of the temperature dependence of the critical current $I_c(T)$ (see Figures on the left) with the dependence of the energy barrier on the current $U_{\text{eff}}(I)$ (Figures on the right), measured in YBCO ring-shaped films #1, #2, and #3. Note that the similarities of the shape of $I_c(T)$ to that of $U_{\text{eff}}(I)$ imply that the energy barrier is a function of $I_c(T)$ 82

4.1.9 The comparison of the temperature dependence of the critical current $I_c(T)$ (see Figures on the left) with the dependence of the energy barrier on the current $U_{\text{eff}}(I)$ (Figures on the right), measured in YBCO ring-shaped films #4, #5, and #6. These films have different temperature dependence of I_c from that observed in YBCO films #1, #2, and #3 [Figure (4.1.8)], which is characterized by the larger low temperature reduction of $I_c/I_c(10K)$. Note that the similarities of the shape of $I_c(T)$ to that of $U_{\text{eff}}(I)$ imply that the calculated energy barrier is a function of $I_c(T)$. . 83

4.1.10	The comparison of the temperature dependence of the critical current $I_c(T)$ (see Figures on the left) with the dependence of the energy barrier on the current $U_{\text{eff}}(I)$ (Figures on the right), measured in YBCO ring-shaped films #7, #8, and #9. These films are characterized by lower T_c than that for YBCO films from #1 to # 6 [Figures (4.1.8) and (4.1.9)]. Note that the similarities of the shape of $I_c(T)$ to that of $U_{\text{eff}}(I)$ imply that the calculated energy barrier is a function of $I_c(T)$	84
4.1.11	The dependence of the magnitude of the persistent current I on time, measured in a ring of YBCO film #6 every $5K$ over a temperature range of $10 - 85K$. The inset shows the same results plotted for the magnitudes of the current $I(t)$ at various times t normalized to the value of $I(t)$ at $10K$. All the data lie on the same curve, indicating that the temperature dependence of the critical current is preserved during the decay of the current. . . .	85
4.1.12	The dependence of $U_{\text{eff}}/I_c(T)$ on the current I presented for six YBCO thin films. The inset present the data plotted using an extended scale.	86
4.2.1	The dependence of $U_{\text{eff}}/I_c(T)$ on the current I presented for four YBCO thin films. $U_{\text{eff}}/I_c(T)$ and the current are plotted using logarithmic scales in order to determine the values of the exponent μ in the power law dependence of $U_{\text{eff}}(J)$ proposed by the collective flux pinning model.	88

4.2.2 The dependence of the critical current on the normalized temperature (plotted as $[I_c(T)/I_c(10K)]^{\frac{2}{3}}$ versus T/T_c in Figures on the left) compared with the dependence of the energy barrier on the current (plotted as $\log[U_{\text{eff}}/I_c(T)]$ versus $[I/I_c(0K)]$ in Figures on the right) for YBCO ring-shaped films #1, #2 and #3. In Figures (a), (b) and (c) the open circles mark the experimental data for $I_c(T)$. The solid lines represent theoretical fits to the experimental data: they are the superposition of the GL-like dependence (dashed lines) at low temperature and the AB-like dependence [Clem's model (solid triangles) with the coupling constant $\varepsilon_0 = 0.1$ for (a) and (c), and $\varepsilon_0 = 100$ for (b)]. In Figures (d), (e) and (f) the solid straight lines indicate that the dependence of $[U_{\text{eff}}/I_c(T)]$ on $[I/I_c(0K)]$ is exponential. Note that their slopes are sample independent. 89

4.2.4 The dependence of the critical current on the normalized temperature (plotted as $[I/I_c(10K)]^{\frac{2}{3}}$ versus T/T_c in Figures on the left) compared with the dependence of the energy barrier on the current (plotted as $\log[U_{\text{eff}}/I_c(T)]$ versus $[I(T)/I_c(0K)]$ in Figures on the right) for YBCO ring-shaped films #7, #8 and #9. In Figures (a), (b) and (c) the open circles mark the experimental data for $I_c(T)$. The solid lines represent theoretical fits to the experimental data: they are the superposition of the GL-like dependence (dashed lines) and the AB-like dependence [Clem's model (solid triangles) with the coupling constant $\varepsilon_0 = 100$ for (a), (b) and (c)]. In Figures (d), (e) and (f) the solid lines indicate that the dependence of $[U_{\text{eff}}/I_c(T)]$ on $[I/I_c(0K)]$ is exponential. Note that their slopes are sample independent and identical to those presented in Figures (4.2.2) and (4.2.3) for YBCO from #1 to #6. 91

4.2.5 The dependence of the critical current I_c on the normalized temperature T/T_c , according to various theoretical models which were utilized in the fits to the experimental data shown in Figures (4.2.2), (4.2.3) and (4.2.4) (a), (b) and (c). Figures (a) and (b) show a GL-like $(T_c - T)^{\frac{3}{2}}$ dependence of $I_c(T)$, AB dependence of $I_c(T)$, and Clem's calculations of the crossover from AB to GL in $I_c(T)$ with coupling constants $\varepsilon_0 = 0.1$ and 100. Figure (c) presents a superposition of the GL-like $I_c(T)$ with that of the Ambegaokar-Baratoff and Clem. Figures (d), (e) and (f) contain the results of (a), (b) and (c), plotted as $[I_c(T)]^{\frac{2}{3}}$ versus T/T_c . . . 92

- 4.2.6 The dependence of the energy barrier $U_{\text{eff}}/I_c(T)$ on the normalized current $I/I_c(0K)$ plotted for YBCO ring-shaped films #4, 5, 6 and 8. These films are characterized by the pronounced AB-like behavior of $I_c(T)$ close to T_c [Figures (4.2.2), (4.2.3) and (4.2.4)], and the deviation of $U_{\text{eff}}/I_c(T)$ from the straight solid line at small currents. The segments on the dashed lines represent the data obtained by subtracting $U_{\text{eff}}/I_c(T)$ at low currents from the solid lines. In these cases $U_{\text{eff}}/I_c(T)$ is a double exponential function of $I/I_c(0K)$ 94
- 4.2.7 The magnitudes of the argument in the exponents of $[U_{\text{eff}}/I_c(T)]$ for each YBCO thin film sample, which are represented: (a) by the slope of the straight solid lines in Figures (4.2.2), (4.2.3) and (4.2.4) (e), (f) and (g) for GL-like regime of $I_c(T)$; and (b) by the slope of the straight dashed lines in Figure (4.2.6) for an AB-like regime of $I_c(T)$ 96
- 4.2.8 The schematic of the nanoscale cells (a few nanometers in size) in the a-b planes of YBCO as described by Etheridge[43] on the basis of the high resolution electron microscopy. According to our studies, the walls between the cells form Josephson tunnel junctions with the spatial variation of the coupling energy in the a-b planes $\Delta E_j^{a,b}(x,y)$ and between the planes $\Delta E_j^c(x,y)$. Crystallographic directions of the cell walls are along the x,y axes. The a,b-axes are positioned at an angle of about 45° relative to the x,y axes. 100

- 5.1.1 The profiles of the axial (a) and radial (b) magnetic fields shielded by a zero-field-cooled disk #2 at various applied fields and 30 K . The shielding field reaches maximum at applied field of about 300G. The profiles were measured by scanning axial and radial Hall probes at a distance of 3mm above the sample. Distances 0mm and 7.5mm mark the center and the edge of the disk, respectively. 106
- 5.1.2 The profiles of the axial (a) and radial (b) magnetic fields shielded by a zero-field-cooled ring #1 at various applied fields and 30 K . The shielding field reaches maximum at applied field of about 250 G. The profiles were measured by scanning axial and radial Hall probes at a distance of 3 mm above the sample. Distances $\pm 4.25mm$ and $\pm 2.50mm$ mark the outer and inner ring's edges, respectively. 107
- 5.1.3 The profiles of the axial (a) and radial (b) magnetic fields trapped at 30 K by a zero-field-cooled disk #2 after applying and subsequently removing external fields up to 750 G. The profiles were measured by scanning axial and radial Hall probes at a distance of 3mm above the sample. Distances 0mm and 7.5mm mark the center and the edge of the disk, respectively. 108
- 5.1.4 The profiles of the axial (a) and radial (b) magnetic fields trapped at 30 K by a zero-field-cooled ring #1 after applying and subsequently removing external fields up to 750 G. The profiles were measured by scanning axial and radial Hall probes at a distance of 3mm above the sample. Distances $\pm 4.25mm$ and $\pm 2.50mm$ mark the outer and inner ring's edges, respectively. 109

5.1.5	Axial and radial components of the shielding and trapped fields in zero-field-cooled disk #2 measured as a function of the applied field at various temperatures. The axial components (a) and (c) were taken at the center of the disk while the radial components (b) and (d), correspond to a maximum radial field. The applied field was perpendicular to the sample surface. The shielding and trapped fields were measured by scanning axial and radial Hall probes at a distance of $3mm$ above the sample.	110
5.1.6	Axial and radial components of the shielding and trapped fields in zero-field-cooled ring #1 measured as a function of the applied field at various temperatures. The axial components (a) and (c) were taken at the center of the ring while the radial components (b) and (d), correspond to a maximum radial field. The applied field was perpendicular to the sample surface. The shielding and trapped fields were measured by scanning axial and radial Hall probes at a distance of $3mm$ above the sample.	111
5.1.7	The vectors of the shielding field measured at $30K$ as a function of position along the diameter of disk #2 (and a distance of $3mm$ above its surface) for different applied fields. The magnitude of each vector is proportional to the magnitude of the total field at the same position. Distances $-7.5mm$ and $7.5mm$ mark the disk's edges.	113

- 5.1.8 The vectors of the trapped field measured at $30K$ as a function of position along the diameter of disk #2 (and a distance of $3mm$ above its surface) for different applied fields. The magnitude of each vector is proportional to the magnitude of the total field at the same position. Distances $-7.5mm$ and $7.5mm$ mark the disk's edges. 114
- 5.1.9 The vectors of the shielding field measured at $30K$ as a function of position along the diameter of ring #1 (and a distance of $3mm$ above its surface) for different applied fields. The magnitude of each vector is proportional to the magnitude of the total field at the same position. Distances $\pm 4.25mm$ and $\pm 2.50mm$ mark the outer and inner ring's edges, respectively. 115
- 5.1.10 The vectors of the trapped field measured at $30K$ as a function of position along the diameter of ring #1 (and a distance of $3mm$ above its surface) for different applied fields. The magnitude of each vector is proportional to the magnitude of the total field at the same position. Distances $\pm 4.25mm$ and $\pm 2.50mm$ mark the outer and inner ring's edges, respectively. 116
- 5.1.11 The vectors of the shielding field measured at distances between 3 and $12mm$ (every $1mm$) above the surface of disk #2 at $30K$ and at applied magnetic fields of 35, 50, 100, 200, 375 and $700G$. The magnitude of each vector is proportional to the magnitude of the total field at the same position normalized to the maximum magnitude of the shielding field in each Figure. Distances $-7.5mm$ and $7.5mm$ mark the disk's edges. 117

5.1.12 The vectors of the trapped field measured at distances between 3 and 12mm (every 1mm) above the surface of disk #2 at 30K and at applied magnetic fields of 35, 50, 100, 200, 375 and 700G. The magnitude of each vector is proportional to the magnitude of the total field at the same position normalized to the maximum magnitude of the trapped field in each Figure. Distances $-7.5mm$ and $7.5mm$ mark the disk's edges. $\times 2$, $\times 10$ and $\times 20$ mark the magnification of the vectors. 118

5.1.13 The vectors of the shielding field measured at distances between 3 and 12mm (every 1mm) above the surface of ring #1 at 30K and at applied magnetic fields of 35, 50, 100, 200, 375 and 700G. The magnitude of each vector is proportional to the magnitude of the total field at the same position normalized to the maximum magnitude of the shielding field in each Figure. Distances $\pm 4.25mm$ and $\pm 2.50mm$ mark the outer and inner ring's edges, respectively. 119

5.1.14 The vectors of the trapped field measured at distances between 3 and 12mm (every 1mm) above the surface of ring #1 at 30K and at applied magnetic fields of 35, 50, 100, 200, 375 and 700G. The magnitude of each vector is proportional to the magnitude of the total field at the same position normalized to the maximum magnitude of the trapped field in each Figure. Distances $\pm 4.25mm$ and $\pm 2.50mm$ mark the outer and inner ring's edges, respectively. $\times 10$, $\times 20$ and $\times 100$ mark the magnification of the vectors. 120

- 5.1.15 The profiles of the axial component of the magnetic field shielded by a zero-field-cooled disk #1 which were measured at a distance of 3mm above the disk's surface at various temperatures between 60 and 90 K in the presence of an external field of 200 G. Distances $+7.5\text{ mm}$ and -7.5 mm mark the disk's edges. 122
- 5.1.16 The profiles of the axial component of the magnetic field trapped in a zero-field cooled disk #1 which were measured at a distance of 3mm above the disk's surface at various temperatures between 60 and 90K after an external field of 200 G was removed. A complete flux-penetration-state is reached, above 77K. Distances $+7.5\text{ mm}$ and -7.5 mm mark the disk's edges. 123
- 5.1.17 Open symbols mark temperature dependence of the axial component of the magnetic field shielded in the center of a zero-field-cooled disk #1 in the presence of external fields of 40 G (a), 80 G (b) and 200 G (c). Solid symbols mark temperature dependence of axial component of the the magnetic field trapped in the center of the disk after the applied field was reduced to zero. The maximum trapped field indicates the crossover between a partial and complete flux-penetration-regimes. Note that this maximum coincides with the inflection point on the shielding field versus temperature curve. (d) Temperature dependence of the field trapped in disk #1, plotted for various applied fields between 40 G and 200 G. The complete-flux-penetration regime is common for all trapped fields at temperatures higher than that corresponding to the maximum trapped field. Discrepancies observed for various applied fields are caused by the time decay of the trapped field. . 124

5.1.18 (a) Temperature dependence of the maximum axial magnetic field which can be trapped in the center of a zero-field-cooled disk #1. (b) Dependence of the maximum axial trapped field on the minimum magnitude of the external magnetic field required for a complete flux penetration.	125
5.1.19 Temperature dependence of the maximum axial field trapped in a zero-field-cooled disk #1 (solid symbols) and that of the axial component of the magnetic field generated by the critical persistent current circulating in a zero-field-cooled ring #1 (open symbols) which was etched out from disk #1. A magnetic field of 750 G was used to saturate the trapped magnetic field and the persistent current.	127
5.1.20 Upper figure: The distributions of the axial component of the trapped magnetic field measured across disk #1 at a distance of 3mm above the disk's surface at 79 K. This represents the case of a complete flux penetration after a field of 200G was applied to the zero-field-cooled sample and subsequently removed . Lower figure: The corresponding distributions of the normalized decay rate $S = (1/B_0)(dB/d\ln t)$ for the motion of the trapped flux. . .	129
5.1.21 The distributions of the axial component of the trapped field (upper figure) and the normalized decay rate S (lower figure) measured across disk #1 at a distance of 3mm above the disk's surface at 67K. This represents the case of an incomplete flux penetration after a field of 200 G was applied to the zero-field-cooled sample and subsequently removed.	130

5.1.22	Temperature dependence of the axial component of the trapped field (upper figure) and the normalized decay rate S (lower figure) measured in the center of disk #1 at a distance of $3mm$ above the surface when a field of $200 G$ was applied to the zero-field-cooled sample and subsequently removed.	131
5.1.23	Temperature dependence of the axial component of the trapped field and the normalized decay rate S measured in the center of ring #1 at a distance of $3mm$ above the ring's surface when a field of $200 G$ was applied to the zero-field-cooled sample.	132
5.1.24	The distributions of the axial component of the trapped field in ring #1 at various temperatures between 50 and $8K$, after an external field of $200 G$ was applied to the zero-field-cooled sample. Distances $\pm 4.25mm$ and $\pm 2.50mm$ mark the outer and inner ring's edges, respectively.	133
5.2.1	The profiles of the axial (a) and radial (b) magnetic fields shielded by a zero-field cooled disk #2 in various applied fields and at $30K$. Open symbols represent the experimental data measured at a distance of $3mm$ above the sample, and the solid lines are the theoretical fits based on the current distributions shown in Figure (5.2.2).	135

- 5.2.2 Normalized current density profiles across disk #2 for the shielding at 30K, calculated using Equation (1.17) for applied fields (H_a) of (1) 12.5 , (2) 25, (3) 50, (4) 75, (5) 100, (6) 125, (7) 150, (8) 350, (9) 650 and (10) 750G . The radius a of the vortex free region was calculated from the formula $a = R/\cosh(H_a/H_d)$ and it marks a distance at which the current I reaches I_c . The critical current density J_c was taken to be $8.7 \times 10^6 A/cm^2$ 136
- 5.2.3 The profiles of the axial (a) and radial (b) magnetic fields trapped in zero-field-cooled disk #2 in various applied fields and at 30K. Open symbols represent the experimental data measured at a distance of 3mm above the sample, and the solid lines are the theoretical fits based on the current distributions shown in Figure (5.2.4). 138
- 5.2.4 Normalized current density profiles across disk #2 at 30K calculated using Equation (1.19) for an applied field $H_a = 150, 250, 350, 450, 550$ and 750G. The radius a of the vortex free shielded region was calculated from the formula $a = R/\cosh(H_a/H_d)$ and it marks a distance at which the current I (for each H_a) achieves the lowest negative value. The inner radius b of the annular ring at which the current I reaches I_c is given by $b = R/\cosh(H_a/2H_d)$. The critical current density was taken to be $9.9 \times 10^6 A/cm^2$. . . 139

5.2.5	The profiles of the axial (a) and radial (b) magnetic fields trapped in a zero-field-cooled disk #2 in various applied fields and at 40K. Open symbols represent the experimental data measured at a distance of 3mm above the sample, and the solid lines are the theoretical fits based on the current distributions shown in Figure (5.2.6).	141
5.2.6	Normalized current density profiles across disk #2 at 40K calculated using Equation (1.19) for an applied field $H_a = 56, 96, 130, 190, 250, 310, 400$ and 750G. The radius a of the vortex free shielded region was calculated from the formula $a = R/\cosh(H_a/H_d)$ and it marks a distance at which the current I (for each H_a) achieves the lowest negative value. The inner radius b of the annular ring at which the current I reaches I_c is given by $b = R/\cosh(H_a/2H_d)$. The critical current density was taken to be $7.8 \times 10^6 A/cm^2$	142
5.2.7	The profiles of the axial (a) and radial (b) magnetic fields trapped in a zero-field-cooled disk #2 in various applied fields and at 50K. Open symbols represent the experimental data measured at a distance of 3mm above the sample, and the solid lines are the theoretical fits based on the current distributions shown in Figure (5.2.8).	143

- 5.2.8 Normalized current density profiles across disk #2 at 50K calculated using Equation (1.19) for an applied field $H_a = 30, 70, 90, 130, 160, 230, 300$ and 700G. The radius a of the vortex free shielded region was calculated from the formula $a = R/\cosh(H_a/H_d)$ and it marks a distance at which the current I (for each H_a) achieves the lowest negative value. The inner radius b of the annular ring at which the current I reaches I_c is given by $b = R/\cosh(H_a/2H_d)$. The critical current density was taken to be $6.11 \times 10^6 A/cm^2$ 144
- 5.2.9 The profiles of the axial (a) and radial (b) magnetic shielding fields in a zero-field-cooled disk #2 at 700G, and 50K, which were measured as a function of an increasing distance above the sample from 3 up to 12mm. Open symbols represent the experimental data and the solid lines are the theoretical fits which use the Bean current distribution with $J_c = 5.2 \times 10^6 A/cm^2$ over the entire disk.146
- 5.2.10 The profiles of the axial (a) and radial (b) magnetic trapped fields in a zero-field-cooled disk #2 at 700G, and 50K, which were measured as a function of an increasing distance above the sample from 3 up to 12mm. Open symbols represent the experimental data and the solid lines are the theoretical fits which use the Bean current distribution with $J_c = 6.11 \times 10^6 A/cm^2$ over the entire disk. 147

5.2.11	The profiles of the axial (a) and radial (b) magnetic shielding fields in a zero-field-cooled ring #1 at 700G, and 30K, which were measured as a function of an increasing distance above the sample from 3 up to 12mm. Open symbols represent the experimental data and the solid lines are the theoretical fits which use the Bean current distribution with $J_c = 6.3 \times 10^6 \text{ A/cm}^2$ over the entire width of the ring.	148
5.2.12	The profiles of the axial (a) and radial (b) magnetic trapped fields in a zero-field-cooled ring #1 at 700G, and 30K, which were measured as a function of an increasing distance above the sample from 3 up to 12mm. Open symbols represent the experimental data and the solid lines are the theoretical fits which use the Bean current distribution with $J_c = 8.55 \times 10^6 \text{ A/cm}^2$ over the entire width of the ring.	149
1.0.1	The vectors of the shielding field measured at distances between 3 and 12mm (every 1mm) above the surface of disk #2 at 50K and at applied magnetic fields of 35, 50, 100, 200, 375 and 700G. The magnitude of each vector is proportional to the magnitude of the total field at the same position normalized to the maximum magnitude of the shielding field in each Figure. Distances -7.5mm and 7.5mm mark the disk's edges.	170

- 1.0.2 The vectors of the trapped field measured at distances between 3 and 12mm (every 1mm) above the surface of disk #2 at 50K and at applied magnetic fields of 35, 50, 100, 200, 375 and 700G. The magnitude of each vector is proportional to the magnitude of the total field at the same position normalized to the maximum magnitude of the trapped field in each Figure. Distances $-7.5mm$ and $7.5mm$ mark the disk's edges. $\times 5$ marks the magnification of the vectors. 171
- 1.0.3 The vectors of the shielding field measured at distances between 3 and 12mm (every 1mm) above the surface of disk #2 at 70K and at applied magnetic fields of 35, 50, 100, 200, 375 and 700G. The magnitude of each vector is proportional to the magnitude of the total field at the same position normalized to the maximum magnitude of the shielding field in each Figure. Distances $-7.5mm$ and $7.5mm$ mark the disk's edges. 172
- 1.0.4 The vectors of the trapped field measured at distances between 3 and 12mm (every 1mm) above the surface of disk #2 at 70K and at applied magnetic fields of 35, 50, 100, 200, 375 and 700G. The magnitude of each vector is proportional to the magnitude of the total field at the same position normalized to the maximum magnitude of the trapped field in each Figure. Distances $-7.5mm$ and $7.5mm$ mark the disk's edges. $\times 2$, $\times 10$, and $\times 20$ mark the magnification of the vectors. 173

- 1.0.5 The profiles of the axial (a) and radial (b) magnetic shielding fields in a zero-field-cooled disk #2 at 700G, and 70K, which were measured as a function of an increasing distance above the sample from 3 up to 12mm. Open symbols represent the experimental data and the solid lines are the theoretical fits which use the Bean current distribution with $J_c = 1.75 \times 10^6 \text{ A/cm}^2$ over the entire disk. 174
- 1.0.6 The profiles of the axial (a) and radial (b) magnetic trapped fields in a zero-field-cooled disk #2 at 700G, and 70K, which were measured as a function of an increasing distance above the sample from 3 up to 12mm. Open symbols represent the experimental data and the solid lines are the theoretical fits which use the Bean current distribution with $J_c = 2.5 \times 10^6 \text{ A/cm}^2$ over the entire disk.175
- 2.0.1 The vectors of the shielding field measured at distances between 3 and 12mm (every 1mm) above the surface of ring #1 at 50K and at applied magnetic fields of 35, 50, 100, 200, 375 and 700G. The magnitude of each vector is proportional to the magnitude of the total field at the same position normalized to the maximum magnitude of the shielding field in each Figure. Distances $\pm 4.25\text{mm}$ and $\pm 2.50\text{mm}$ mark the outer and inner ring's edges, respectively. 177

- 2.0.2 The vectors of the trapped field measured at distances between 3 and 12mm (every 1mm) above the surface of ring #1 at 50K and at applied magnetic fields of 35, 50, 100, 200, 375 and 700G. The magnitude of each vector is proportional to the magnitude of the total field at the same position normalized to the maximum magnitude of the trapped field in each Figure. Distances $\pm 4.25mm$ and $\pm 2.50mm$ mark the outer and inner ring's edges, respectively. $\times 2$, $\times 20$ and $\times 100$ mark the magnification of the vectors. . . . 178
- 2.0.3 The vectors of the shielding field measured at distances between 3 and 12mm (every 1mm) above the surface of ring #1 at 70K and at applied magnetic fields of 35, 50, 100, 200, 375 and 700G. The magnitude of each vector is proportional to the magnitude of the total field at the same position normalized to the maximum magnitude of the shielding field in each Figure. Distances $\pm 4.25mm$ and $\pm 2.50mm$ mark the outer and inner ring's edges, respectively. 179
- 2.0.4 The vectors of the trapped field measured at distances between 3 and 12mm (every 1mm) above the surface of ring #1 at 70K and at applied magnetic fields of 35, 50, 100, 200, 375 and 700G. The magnitude of each vector is proportional to the magnitude of the total field at the same position normalized to the maximum magnitude of the trapped field in each Figure. Distances $\pm 4.25mm$ and $\pm 2.50mm$ mark the outer and inner ring's edges, respectively. 180

- 2.0.5 The profiles of the axial (a) and radial (b) magnetic shielding fields in a zero-field-cooled ring #1 at 700G, and 50K, which were measured as a function of an increasing distance above the sample from 3 up to 12mm. Open symbols represent the experimental data and the solid lines are the theoretical fits which use the Bean current distribution with $J_c = 3.61 \times 10^6 \text{ A/cm}^2$ over the entire width of the ring. 181
- 2.0.6 The profiles of the axial (a) and radial (b) magnetic trapped fields in a zero-field-cooled ring #1 at 700G, and 50K, which were measured as a function of an increasing distance above the sample from 3 up to 12mm. Open symbols represent the experimental data and the solid lines are the theoretical fits which use the Bean current distribution with $J_c = 5.73 \times 10^6 \text{ A/cm}^2$ over the entire width of the ring. 182
- 2.0.7 The profiles of the axial (a) and radial (b) magnetic shielding fields in a zero-field-cooled ring #1 at 700G, and 70K, which were measured as a function of an increasing distance above the sample from 3 up to 12mm. Open symbols represent the experimental data and the solid lines are the theoretical fits which use the Bean current distribution with $J_c = 1.12 \times 10^6 \text{ A/cm}^2$ over the entire width of the ring. 183

2.0.8 The profiles of the axial (a) and radial (b) magnetic trapped fields in a zero-field-cooled ring #1 at 700G, and 70K, which were measured as a function of an increasing distance above the sample from 3 up to 12mm. Open symbols represent the experimental data and the solid lines are the theoretical fits which use the Bean current distribution with $J_c = 2.82 \times 10^6 A/cm^2$ over the entire width of the ring. 184

Chapter 1

Introduction

High current density flowing at a tolerable low dissipation is one of the requirements for high temperature superconductors (HTSC) to be technologically useful. Immediate applications would be a large scale power technology such as superconducting magnets, energy storage power systems, current leads, etc. Unfortunately, bulk HTSC exhibits low current carrying capacity (eg. in $Y_1Ba_2Cu_3O_{7-\delta}$ (YBCO) $J_c \simeq 10 - 10^2 A/cm^2$ at $77K$) and dissipation, which limit the expected technological applications. The reason for very low values of J_c in bulk HTSC is the sample's granularity which can be visualized as a collection of small grains (of a few micrometers in size) coupled by intergrain weak links (tunnel junctions). Low values of the critical current are due to the small magnitude of the critical current flowing through the intergrain regions. Structural imperfections, impurity phases and non-stoichiometry stimulate the formation of weak links. Special techniques, such as growth from a melt [1], have been developed to overcome the weak link problem. The method allows one to produce grain-aligned materials. The resulting grain boundaries are low-angle ones in contrast to high-angle ones that are present in standard ceramic samples. As a consequence, the coupling between the grains in a grain-aligned material increases, which leads to the higher value of the intergrain J_c of the order of $10^3 - 10^4 A/cm^2$ at $77 K$ in YBCO. However, this value is still smaller than that of YBCO epitaxial thin films which is approximately $10^5 - 10^6 A/cm^2$ at $77 K$, which suggests that thin films behave like strongly coupled superconductors. Therefore, the studies of the critical current and its dissipation using epitaxial, single phase, c-axis oriented YBCO could

help one to understand the physical origin of high critical current density and its relationship to intrinsic properties of thin films. This is important from the point of view of fundamental theories and future technological applications.

It is known that in conventional superconductors, J_c is limited by depairing and magnetic flux depinning processes [2, 3]. In the former case, the magnitude of the critical current (depairing critical current) is determined by pair-breaking and subsequent suppression of the order parameter of the superconductor. In the latter case, the magnitude of the critical current (depinning critical current) is determined by the magnetic flux movement and the pinning forces. If the flux lines move in response to the Lorentz force exerted by the current, a voltage is induced in the superconductor, according to Maxwell's equations. The superconductor can support the current if the flux lines are held in place by the pinning forces (and also by the interactions with the rest of the flux line lattice).

The first question is: could one distinguish between both types of the critical current in HTSC? In order to identify depinning critical current, this would require the measurement of the dissipation of the current from the critical level. The second question is about the origin of the temperature dependence of the critical current density $J_c(T)$ in high temperature superconductors. The results of the measurements of $J_c(T)$ in HTSC thin films, single crystals and granular materials revealed that J_c has a similar temperature dependence to that of a Superconductor-Normal Metal-Superconductor (SNS) or a Superconductor-Insulator-Superconductor (SIS) junction [4]. For conventional granular superconductors, Clem *et al* [5] have shown that $J_c(T)$ has an Ambegaokar-Baratoff dependence at low temperatures (characteristic of Josephson tunnel junctions) which exhibits a crossover to a Ginzburg-Landau $(1 - T/T_c)^{\frac{3}{2}}$ dependence near T_c . In this model the superconductor consists of an array of weakly coupled grains with a lattice parameter a_0 . The crossover occurs at the temperature for which the Josephson coupling energy of a junction between

the grains is approximately equal to the superconducting condensation energy of a grain. This generates the third question, whether this model is appropriate to describe the behavior of $J_c(T)$ in HTSC. So far it has been successful in explaining electromagnetic properties of granular HTSC samples [6]. The validity of the Clem's model could be extended to YBCO epitaxial thin films and single crystals due to the growing experimental evidence of the intragrain microgranularity. For example, the recent measurements of the dynamic resistance of YBCO single crystals [7] suggest the presence of intra- and inter-unit-cell Josephson junctions implying the presence of the Josephson junction array in the grains. The presence of intragrain granularity in single crystals of YBCO has been suggested first by Daeumling *et al* [8] and Osofsky *et al* [9]. Electromigration experiments in YBCO thin films by Moeckly *et al* [10] indicated that regions of strong oxygen disorder could result in a network of superconducting filaments within the bulk film. Superconductivity across a grain boundary is believed to arise from an overlap of these filaments [10, 11].

For the depinning critical currents in HTSC it is important to study the nature of the dissipation of the critical current. The related questions are about the type of the weak pinning centers that are responsible for the decay of the current and their relationship to the intragrain microgranularity.

In the present work we investigated mainly the dependence of the critical current on the intrinsic properties of YBCO thin films deposited, using different methods, on LaAlO_3 and SrTiO_3 substrates. The films were characterized by high J_c of the order of $10^6 - 10^7 \text{ A/cm}^2$ at 10 K , and T_c over a range of $81-91 \text{ K}$. Granular YBCO samples were used in some cases in order to compare the temperature dependence of the intergrain critical current with that measured in YBCO thin films.

Our main objectives were to perform the following experiments:

- (1) The measurements of the temperature dependence of J_c in YBCO thin films and

granular bulk samples in order to identify the physical processes which limit the critical current;

- (2) The measurement of the decay of the transport current as a function of temperature in order to identify which type of structural defect is responsible for weak pinning of magnetic vortices and consequently for the dissipation of the current;
- (3) The measurements of the spatial distribution of the magnetic fields above the superconducting sample in the complete and partial flux penetration states, in order to analyze the changes in the distribution of the critical currents in the sample at different temperatures.

These three experiments allowed us to test available theories of $J_c(T)$, vortex pinning and the critical state in YBCO thin films. We anticipated that they could provide answers regarding:

- (a) The physical mechanisms responsible for the behavior of the critical current and its dissipation, whether they are intrinsic in nature, or they are determined by the growth condition of YBCO thin films, and by their superconducting parameters such as the magnitude of J_c and T_c .
- (b) The correlation between the temperature dependence of the critical current and the dissipation process.

The experiments were performed using an unconventional technique which uses a superconducting ring in a persistent mode and a scanning Hall probe in order to measure the profiles of the axial components of the magnetic field generated by the persistent current circulating in the ring. This technique offers more advantages if compared to standard four-probe (I-V) and ac-magnetic-induction methods. It allows one to record both the magnitude of the critical current as a function of temperature,

and the relaxation of the current from the critical level. Using rings in the persistent mode eliminated an unwanted contribution of normal currents to the measured value of the critical current. Using a scanning Hall probe eliminated the need for electrical contacts and consequently any heating effects. A Hall probe also permitted us to test the critical state in YBCO thin films, by the measurement of both the axial and radial components of the magnetic field above the sample, which were followed by a computer simulation of the current distribution.

In the following three sections, we address in detail the problems presented above. These are: (1) Temperature dependence of the critical current; (2) Dissipation of the persistent current and associated vortex dynamics and; (3) Distribution of the currents and the critical state in YBCO thin films.

1.1 Temperature dependence of the critical current

1.1.1 Theoretical Models

In this section, we present a brief description of the theoretical models, which have been applied to explain the behavior of both the intragrain and intergrain $J_c(T)$ in high temperature superconductors.

Proximity Effect (DeGennes model) :

DeGennes [12] considered the Superconductor-Normal-Superconductor (SNS) junctions. Proximity effect results when a normal metal is deposited onto a superconductor. If the electrical contact is of a sufficiently good quality, the normal metal will alter the order parameter ψ close to the interface. Superconductivity can be induced in the normal metal within a sheath of thickness ξ_N , called the normal metal coherence length. For the junction between two superconductors, if the insulating material is replaced by a normal metallic layer (SNS junction), Cooper pairs can diffuse into the normal layer between the two superconductors [12]. The critical value of the current through the junction (due to the diffusion process) is given by

$$I_c \propto (T - T_c)^2 \exp(-2d_N/\xi_N(T)) \quad (1.1)$$

where $2d_N$ is the barrier width. Near T_c , the current through the junction has a quadratic dependence on temperature

$$I_c(T) \propto (T_c - T)^2 \quad (1.2)$$

Ambegaokar-Baratoff model:

Josephson [13] has shown that the supercurrent which flows between two superconductors separated by a tunnel barrier (SIS junction) is related to the phase difference $\gamma = \varphi_1 - \varphi_2$ between the order parameters in the two superconductors according to

$$I = I_c \sin \gamma \quad (1.3)$$

where the critical current I_c is the maximum Josephson current which can flow across the junction.

By applying the BCS theory, Ambegaokar-Baratoff [14] worked out an exact result for the temperature dependence of I_c for the Josephson tunnel junction. For a symmetrical SIS junction , $I_c(T)$ is expected to have the following temperature dependence:

$$I_c = \frac{\pi \Delta(T)}{2eR_n} \tanh \frac{\Delta(T)}{2k_B T} \quad (1.4)$$

where R_n is the normal state resistance and Δ is the energy gap. Close to T_c , I_c varies linearly with temperature ($I_c(T) \propto (T_c - T)$).

Clem's model:

Clem [5] assumed the Josephson-coupled grain model [15] in which the grains are arranged in a cubic array with lattice parameter a_0 and coupled by identical Josephson tunnel junctions. The critical current due to the tunneling between the grains is given by the Ambegaokar Baratoff (AB) expression (Eq. 1.4) and the critical current density is

$$J_c(T) = I_c/A \quad (1.5)$$

where $A = a_0^2$ (for three dimensional array) or $A = a_0 d$ (for two dimensional array) is the cross-sectional area of the grain with d being the average thickness of

the grains. The AB model does not account for the ability of the supercurrent to suppress the gap parameter and predicts that $J_c(T)$ varies linearly with temperature close to T_c . Clem modified the AB model by using a Ginzburg-Landau-like free-energy functional approach to account for the current-induced gap suppression. Clem introduced a dimensionless parameter $\varepsilon = E_J/2E_g$, where $E_J = (\hbar/2e)I_0$ is the Josephson coupling energy with I_0 being the Ambegaokar-Baratoff critical current near T_c and $E_g = (H_{c_g}^2/8\pi)V_g$ is the intragranular condensation energy, with V_g being the average volume of the grain. ε also can be expressed as $\varepsilon = (2\xi_J^2/a_0^2)$, where $\xi_J(T)$ is the Ginzburg-Landau temperature-dependent coherence length. When $\varepsilon \ll 1$ (weak coupling limit), the intergranular currents are too small to suppress the order parameter, and the critical current density is given by Eq. (1.4). In this limit, the effect of granularity is pronounced, and the Josephson weak links dominate the critical current. When $\varepsilon \gg 1$ (strong coupling limit), current induced suppression of the order parameter becomes important, and close to T_c the critical current is given by the Ginzburg-Landau theory in the form

$$J_c(T) \propto (1 - T/T_c)^{\frac{3}{2}} \quad (1.6)$$

Tinkham's Model (flux creep model):

Tinkham [16] considered the case when the critical current in a superconductor is limited by flux creep. $J_c(B, t)$ where $t = T/T_c$, is given by

$$J_c(B, t) = J_c(B, 0)[1 - \alpha(B)t - \beta t^2] \quad (1.7)$$

for $t \ll 1$, with B being the magnetic flux density. The coefficient β is related to the temperature dependence of the free-energy difference between pinned and unpinned flux quantum, expanded in the form $U(B, t) \simeq U(B, 0)(1 - \beta t^2)$. The coefficient $\alpha(B)$ is given by $\alpha(B) = (kT_c/U(B, 0)) \ln(aB\Omega/E_{min})$ where a is the average hopping

distance of the flux quantum, Ω is the attempt frequency for escape of the flux quantum, and E_{min} is the electric field criterion that defines J_c .

1.1.2 Temperature dependence of the intragrain and intergrain critical current in YBCO

The measurements of temperature dependence of the critical current $I_c(T)$ in thin films, single crystals and granular bulk samples have been carried out in order to distinguish between different models of supercurrent limiting mechanisms. Most measurements of $I_c(T)$ over a temperature range of 4-90 K were done on YBCO thin films and on thin film YBCO/YBCO junctions. The reasons for that were the experimental difficulties (like heating effects) in measuring high critical currents at low temperatures on bulk samples, exhibited by standard I-V four probe and ac-magnetic induction methods. The Tinkham model [16] and the Ginzburg-Landau theory [17] were employed in order to explain $I_c(T)$ of the intragrain critical current. The intergrain $I_c(T)$ was interpreted using theories developed by Ambegaokar-Baratoff [14], DeGennes [12] and Likharev [18]. Regarding the intragrain critical current, the experimental data for YBCO thin films revealed three different dependencies of I_c on temperature, which are characterized by a “convex” upward curvatures [19, 20] (characteristic of an Ambegaokar-Baratoff type temperature dependence), a quasi-linear behavior [19, 20, 21, 22, 23], and “concave” downward curvature (a Ginzburg-Landau-like dependence) [19, 20, 23, 24, 25, 26, 27] [1.1.1]. The data of Mannhart *et al* [19] showed the transition from a quasi-linear temperature dependence of I_c at zero-magnetic field to a concave temperature dependence upon application of high fields of 0.5-1.0 T. The crossover from a quasi-linear to a concave temperature dependence was also seen by Jones *et al* [21] upon reduction of the oxygen content. In most cases, Tinkham’s model [16] for a flux-creep-limited $I_c(B,T)$ has been applied in order to

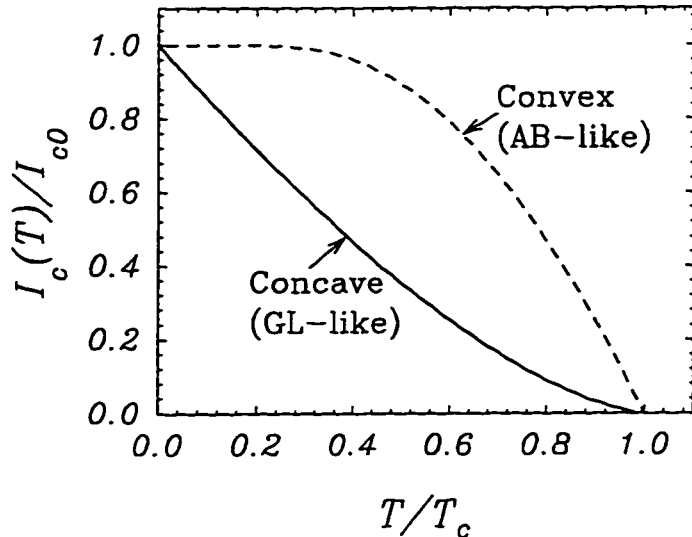


Figure 1.1.1: Ambegaokar-Baratoff-like type temperature dependence of the critical current and Ginzburg-Landau-like dependence.

explain a convex and a quasi-linear-like temperature dependence of I_c . A concave behavior of $I_c(T)$ was in general interpreted as due to the presence of an intragrain SNS weak-link structure. Regarding the intergrain critical current, the available experimental data showed a convex temperature dependence of I_c across a grain boundary of thin film bicrystals of YBCO and a concave one across YBCO/YBCO thin film junctions containing $Y_1Ba_2(Cu_{1-x}Co_x)O_{7-\delta}$ normal layer [28]. In the former case, it has been suggested that the results are consistent with Likharev's model [18] which predicts $I_c(T)$ for dirty SNS junctions, however, the possibility that $I_c(T)$ can be described by Ambegaokar-Baratoff's theory [14, 12] for SIS junctions has not been ruled out. In the latter case, it has been claimed that the conventional proximity effect of DeGennes [12], modified by pair-breaking scattering, predicts the observed $I_c(T)$. The available data for $I_c(T)$ in YBCO single crystals are those of Gough et al [29, 30] who measured the transport $I_c(T)$ over a temperature range of 4-70 K on YBCO single crystal rings using ac hysteresis loops and those of Thompson *et al* [30, 31] (in a field of 1T parallel to the c-axis) and Abulafia *et al* [31], who measured the magnetization over a temperature range of 3-77 K. The results show a concave

(downward) curvature of $I_c(T)$.

The experimental fact that both the intragrain and intergrain critical currents exhibit similar dependencies on temperature, and variety of theories applied to interpret the same behavior of $I_c(T)$ imply lack of consensus about the supercurrent limiting mechanism in YBCO for both intragrain and intergrain transport currents.

In view of the above, we decided to investigate the temperature dependence of the critical current in c-axis-oriented thin films of YBCO characterized by various superconducting transition temperatures, and in granular samples of YBCO as a function of the applied magnetic field. The results revealed the crossover from an Ambegaokar-Baratoff-like to a Ginzburg-Landau-like temperature dependence of I_c for both intragrain and intergrain current. The experimental data were interpreted using Clem's theory [5] of the crossover effects from an Ambegaokar-Baratoff to a Ginzburg-Landau behavior of $I_c(T)$ in conventional granular superconductors. The crossover was observed for both depairing and depinning critical currents in c-axis-oriented YBCO thin films and in granular YBCO samples. The experimental data implied the presence of nanometer-size superconducting domains coupled by Josephson tunnel junctions in the a-b planes of YBCO thin films.

1.2 Dissipation of the persistent current and the magnetic vortex dynamics

1.2.1 Theoretical Models

It is known that the magnitude of the depinning critical current depends on the vortex motion and the associated energy barrier U_{eff} . The Lorentz force exerted by the current of density J , overcomes the pinning forces which hold the magnetic flux

lines in place, and consequently stimulates the movement of the flux. Since the drift velocity of the flux lines depends on the pinning energy barrier U_{eff} , it is essential to know what is the dependence of U_{eff} on the current density J . So far many theoretical models of $U_{\text{eff}}(J)$ has been proposed. In the section below we describe the models, which have been frequently used in order to explain the magnetic relaxation in high temperature superconductors.

Anderson-Kim Model:

The standard analysis of magnetic relaxation, due to the thermally activated motion of flux lines out of the potential wells aided by the Lorentz force, was initially developed by Anderson and Kim [32]. At current densities J close to the critical value J_c , the dependence of the energy barrier $U_{\text{eff}}(J)$ on the current for the flux bundle motion is assumed to be linear

$$U_{\text{eff}}(J) = U_0 - JBVa = U_0(1 - \frac{J}{J_c}) \quad (1.8)$$

where J is the current density, B is the magnetic induction, V is the flux bundle volume, a is the hopping distance and U_0 is the apparent pinning potential at zero current density . The model gives a logarithmic dependence of the current density J on time due to flux creep, according to the equation

$$J(t) \approx J(0)[1 - \frac{k_B T}{U_0} \ln(1 + \frac{t}{t_0})] \quad (1.9)$$

where t_0 is the characteristic time and k_B is the Boltzmann constant. The apparent pinning potential is then given by

$$U_0 = -k_B T J(0) / (\frac{dJ}{d \ln t}) = \frac{k_B T}{S} \quad (1.10)$$

where $S = -(1/J(0))(d \ln J / d \ln t)$ is the normalized relaxation rate .

Logarithmic $U_{\text{eff}}(J)$ model :

Zeldov *et al.* [33] suggested a phenomenological form of the energy barrier in order to account for the $J - E$ data close to the irreversibility line in YBCO thin films according to the equation

$$U_{\text{eff}}(J) = U_0 \ln (J_c/J) \quad (1.11)$$

In this model the decay of the current density due to the motion of vortices is given by

$$J(t) = J_c \left(\frac{\tau_i + t}{\tau} \right)^{-\frac{k_B T}{U_0}} \quad (1.12)$$

where τ is the characteristic time related to the attempt hop frequency and τ_i is the time at which the “steady state” relaxation starts [34].

Vinokur *et al* [35] stated that this model is the exact result for the case when the vortex motion is controlled by intrinsic pinning in a layered superconductor (with the magnetic field parallel to the layers) and it is also a good approximation of the activation barrier in the single-vortex-creep regime.

Vortex glass and collective pinning models:

The Anderson-Kim approximation (Eq.1.8) is only valid when $U_0 \gg k_B T$. This is generally true in conventional superconductors but not in high temperature superconductors where the ratio $U_0/k_B T$ is much smaller. This results in rapid relaxation of the supercurrent. The relationship between U_{eff} and J is usually non-linear, contrary to Eq. (1.8). The vortex glass [36] and collective pinning models [37] were suggested to explain this non-linearity. Both models take into account the interaction between flux lines during their collective motion. They present similar pictures for vortex motion and share the same inverse power-law expression for $U_{\text{eff}}(J)$ which can be

generally expressed as [36, 37]

$$U_{\text{eff}} = U_0 \left(\frac{J_c}{J} \right)^\mu \quad (1.13)$$

with $\mu \leq 1$ for the vortex model. In the collective-pinning model, μ is determined by the pinning regime (single vortex, small bundles or large bundles) and the dimensionality of the system [37]. In a three dimensional system:

$$\mu = \frac{1}{7} \text{ for single vortex hopping (large currents } J \sim J_c)$$

$$\mu = \frac{3}{2} \text{ for small vortex bundles hopping (intermediate currents } J < J_c)$$

$$\mu = \frac{7}{9} \text{ for large bundle hopping (small currents } J \ll J_c)$$

In a two dimensional system:

$$\mu = \frac{8}{9} \text{ for small vortex bundles (large currents } J \lesssim J_c)$$

$$\mu = \frac{1}{2} \text{ for large vortex bundles (small currents } J \ll J_c)$$

In order to satisfy $U_{\text{eff}} = 0$ at $J = J_c$, Eq. (1.13) should be modified to

$$U_{\text{eff}} = U_0 \left[\left(\frac{J_c}{J} \right)^\mu - 1 \right] \quad (1.14)$$

which does not change the physical picture. The collective pinning theory yields the current dissipation according to

$$J(t) \approx J_0 \left(1 + \frac{\mu k_B T}{U_0} \ln \left(1 + \frac{t}{t_0} \right) \right)^{-\frac{1}{\mu}} \quad (1.15)$$

with the normalized relaxation rate S given by

$$S = T / \left[\frac{U_0}{k_B} + \mu T \ln \left(\frac{t}{t_0} \right) \right] \quad (1.16)$$

Both the logarithmic and the power-law activation barriers U_{eff} diverge in the limit of $J = 0$.

1.2.2 Dissipation of the persistent current and flux pinning in YBCO thin films

It has been argued that the fast relaxation of the persistent current from its critical value in high temperature superconductors can be attributed to the thermally activated motion of vortices between weak pinning centers [37]. According to the collective pinning theory, the weak short-range disorder is responsible for the pinning [38]. Two types of pinning were considered: δT_c pinning, which is associated with the disorder in the transition temperature T_c , and δl pinning, which arises from the spatial variations in the charge carrier mean free path l near lattice defects. The critical current and the pinning energy have been studied by Griessen *et al* [39] in $Y_1Ba_2Cu_3O_{7-\delta}$ (YBCO) thin films over a wide range of temperatures (10 – 80K) using a torque magnetometer and a magnetic field sweeping technique. The authors suggested that for $B < 2$ Tesla and $T < 80K$, the temperature dependence of the critical current and that of the pinning energy could be understood in the framework of the δl -pinning of single vortices pinned by randomly distributed weak pinning centers. Moreover, they argued that the independence of the δl -pinning mechanism on the thin film growth conditions and substrates suggests that the source of the δl -pinning is related to randomly distributed oxygen vacancies, as pointed out earlier by Tinkham [16]. Subsequent work by the same group [40] on oxygen-deficient YBCO thin films, supported the model of a single vortex pinning by spatial fluctuations in the charge carrier mean free path. On the other hand, it has been found (taking into account an increase in anisotropy with a decreasing oxygen content) that the pinning energy and the critical current density systematically decrease with an increasing oxygen deficiency leading to the conclusion that the oxygen vacancies are not the main source of pinning in YBCO films. Berghuis *et al* [41] performed the current-voltage measurements in order to probe the activation barriers for flux creep

in thin films of YBCO at 77K and fields up to 8T. They argued that in the low-field regime flux creep may be dominated by extended strong pinning centers such as densely distributed twin boundaries or screw dislocation cores. When the vortex density exceeds the density of the strong pinning centers, weakly pinned vortices start to affect the flux-creep characteristics e.g., by shearing along strong pinning centers. Hylton and Beasley [42] proposed a model of pinning in the CuO_2 planes of YBCO thin films with very large critical current densities. Their analysis of typical pinning energies and critical current densities indicated that the pinning is due to a very large density of point defects, beyond the density of the extended defects seen in typical transmission electron micrographs. The model predicted a spacing between defects between 38 and 53 Å which is much smaller than the typical 500 Å or higher spacing between the extended defects. The authors pointed out that if the values of 38-53 Å were the spacing between the extended defects, then the pinning energy should be about 1.3 eV which is significantly higher than the experimental values. They suggested that the pinning must be due to a large density of local defects, caused for example by small regions of reduced-order parameter in the strongly conducting CuO_2 plane pairs. Recent high resolution electron microscopy investigations at 300 K by Etheridge at Cambridge University [43] of $Y_1Ba_2Cu_3O_{7-\delta}$ ($\delta < 0.1$) revealed the presence of the electron diffraction patterns due to cells of size approximately 10-20 Å in the a-b planes, in addition to those due to twin boundaries with spacing about 500 Å. The cells form an irregular network with walls aligned about 45° to the $\langle 100 \rangle$ and $\langle 010 \rangle$ axes (a-b axes), and arise from a local perturbation of the charge density distribution. This is an apparently universal feature, present in YBCO samples prepared in different ways and imaged in different microscopes. It was suggested that YBCO ($\delta < 0.1$) “buckles” into a network of slightly misaligned cells in a struggle to relieve internal stresses. The coarse order of the cells across each crystal implies the influence of long-range strain fields. The two dimensional networks of cells are

correlated along the c axis. Our earlier studies [44] of the temperature dependence of the critical current in YBCO thin films also implied the presence of Josephson nanostructures formed by superconducting microdomains (of an effective size about 30-40 Å) coupled by Josephson tunnel junctions in the a - b planes of YBCO.

One of the important questions that is related to the presence of the a - b plane Josephson nanostructures is how this kind of structure could influence magnetic flux pinning and consequently the dissipation of the transport current. In this study, we investigated this problem in c -axis oriented YBCO thin films over a wide temperature range. We chose films of various thickness and T_c that were grown on different substrates using various deposition methods. These thin films have allowed us to study whether the dissipation is intrinsic in nature or whether it is affected by extended defects such as twin boundaries or dislocations. We have used ring-shaped thin films in order to generate a circulating persistent supercurrent at the critical level. The persistent current's self-field was measured by a scanning Hall probe which was also applied to record the time-decay of the self-field over a time range up to 30000s, at temperatures over a range of 10-90 K. This procedure is equivalent to a standard procedure of measuring relaxation of remnant magnetization in a SQUID magnetometer. We have measured the relaxation of the persistent current from the critical level and calculated the dependence of the effective barrier $U_{\text{eff}}(J)$ for vortex motion on the current density using Maley's method [45]. $U_{\text{eff}}(J)$ was then compared with the temperature dependence of the critical current $J_c(T)$. An empirical formula for $U_{\text{eff}}(J)$ was found to depend on a particular regime of $J_c(T)$, which is represented by either an Ambegaokar-Baratoff-like or a Ginzburg-Landau-like behavior. $U_{\text{eff}}(J)$ is independent of thin film growth conditions, substrate, film thickness and T_c , suggesting that an intrinsic property of YBCO is responsible for the dissipation of the persistent current. Discussion of these results is provided within the framework of the resistively-shunted Josephson junction (RSJ) model, in which the a - b planes are

described as a collection of superconducting domains, each comparable in size to the coherence length and coupled together by resistively-shunted Josephson junctions.

1.3 Distribution of the currents and the critical state

1.3.1 Theory of the critical state in a superconducting disk

In the Bean critical state model [46] it is assumed that there exists a relationship $J_c(B)$ such that the critical current is solely determined by \mathbf{B} at any point in the superconductor. The specimen is capable of sustaining virtually lossless currents up to $J_c(B)$, but not beyond. In a quasi-steady state the vortices penetrate only to a certain distance in such a way that the magnitude of the local current density J is reduced to the level of the critical density J_c [47]. In general, J_c depends upon the local flux density B , but in the Bean model J_c is assumed constant.

Mikheenko and Kuzovlev [27] and Zhu *et al* [48] applied the critical-state theory to thin film disk-shaped type II superconductors in the perpendicular external magnetic field and presented analytical solutions of the field and the current patterns in the disk under the following assumptions :

- (a) the film thickness d is approximately less than 2λ , where λ is the London penetration depth. Circulating currents are treated as having uniform density throughout the thickness of the superconductor.
- (b) the external magnetic field H_a is assumed weak enough so that the critical current in the film is independent of the local density of trapped vortices.

In a superconducting thin film disk, shielding currents are generated when an

external field H_a is applied. Mikheenko and Kuzovlev assumed that $|J| = J_c$ is constant within the vortex-penetrated region which has the form of a ring of inner radius $a(H_a)$ and outer radius R . The inner region $\rho \leq a$ is in the Meissner state (i.e. vortex-free region). The current distribution is determined as a linear combination of both distributions in the following form:

$$J_\phi(\rho) = \begin{cases} -(2J_c/\pi) \arctan \left[\frac{\rho}{R} \left(\frac{R^2 - a^2}{a^2 - \rho^2} \right)^{\frac{1}{2}} \right] & \text{for } \rho \leq a \\ -J_c & \text{for } a \leq \rho < R \end{cases} \quad (1.17)$$

where a represents the minimum distance from the disk center to the region where the vortices penetrate

$$a = \frac{R}{\cosh(H_a/H_d)} \quad (1.18)$$

here $H_d = (2\pi/c)J_c d$ is a characteristic field for disk geometry.

If the external field is monotonically decreased from H_a to a field H ($|H| \leq H_a$), the vortices near the outer radius R experience a Lorentz force that drives them out of the sample as the field is initially decreasing [49]. The resulting current-density profile is given by Zhu *et al* [48]

$$J_\phi(\rho) = \begin{cases} -(2J_c/\pi) \arctan \left[\frac{\rho}{R} \left(\frac{R^2 - a^2}{a^2 - \rho^2} \right)^{\frac{1}{2}} \right] + (4J_c/\pi) \arctan \left[\frac{\rho}{R} \left(\frac{R^2 - b^2}{b^2 - \rho^2} \right)^{\frac{1}{2}} \right] & \text{for } \rho \leq a \\ -J_c + (4J_c/\pi) \arctan \left[\frac{\rho}{R} \left(\frac{R^2 - b^2}{b^2 - \rho^2} \right)^{\frac{1}{2}} \right] & \text{for } a \leq \rho \leq b \\ +J_c & \text{for } b \leq \rho \leq R \end{cases} \quad (1.19)$$

Note that $J_\phi(\rho) = J_c$ within an annulus of inner and outer radii b and R , where

$$b = \frac{R}{\cosh[(H - H_a)/2H_d]} \quad (1.20)$$

When the external field is reduced to $H = 0$, we obtain the trapped field case and $b = R/\cosh(H_a/2H_d)$

1.3.2 Current distribution and magnetic flux penetration in YBCO thin films

Studies of the magnetic flux penetration into superconducting thin films have been recognized as those which provide important information on critical currents, on distribution of shielding currents and weak links, on demagnetization effects, and on complete and partial flux penetration states. Results obtained on thin films of circular geometry, such as a disk or ring, (which ensures homogeneous penetration of flux) seem to be particularly useful due to the need for verification of the conventional critical state model. Penetration of magnetic flux into disk-shaped thin films of YBCO has been studied with the magneto-optical Faraday rotation method [50, 51]. Calculation of the distribution of both the axial and radial components of the magnetic field across a thin circular film has been performed by Theuss *et al* [52] for film thickness smaller than the London penetration depth. Good agreement was obtained between the calculated distribution of the axial component of the field and the experimental data [51]. However, the authors admitted that the magneto-optical measurements do not provide an evidence of a complete flux penetration (which is, on the other hand, given by the saturation of dc magnetization in an increasing applied magnetic field) due to the insensitivity of a central fringe area, of width about 20% of the disk's radius, to the penetrating magnetic field. The available experimental data are insufficient to explain deviation of the magnetic flux distribution from that predicted by the conventional critical state model. This applies both to the distribution of the radial component of the magnetic induction B_r , for which there are recorded no experimental data, and to the distribution of the axial components B_z , with missing temperature and magnetic field dependence of the complete flux-penetration-states. This information is crucial for the analysis of the critical state model (and its applicability to thin film superconductors) which has been proposed by Theuss *et al* [52],

Däumling and Larbalestier [60], Conner and Malozemoff [54], and Brandt [55]. The leading conclusion of this analysis is that in the case of thin film circular samples, the critical state model requires modification by taking into account the dominating influence of the gradient of the field component $\partial B_r/\partial z$ on the critical current density $J_c = (1/\mu_0) (\partial B_r/\partial z - \partial B_z/\partial r)$ where $\partial B_r/\partial z$ is much larger than $\partial B_z/\partial r$. Therefore, the critical state in the disk occurs rather through the thickness d , and not the radius r . Theuss *et al* [52] showed that in the absence of the experimental data for the radial component $B_r(r)$, one could calculate it using experimental results for $B_z(r)$. Their computation consists of the following steps:

- (a) Fitting of the current distribution $I(r)$ to the Biot-Savart-law, so it could reproduce the experimental distribution of $B_z(r)$;
- (b) Calculation of the radial component $B_r(r)$ from the Biot-Savart-law using the current distribution $I(r)$;
- (c) Estimation of $\partial B_r/\partial z$ by taking $\partial B_r/\partial z \approx 2B_r(d/2)/d$ [where $B_r(d/2)$ is the field on the surface] under the assumption that $B_r(z)$ vary smoothly through the film thickness d .

This procedure was used to compare the $\partial B_z/\partial r \approx B_z(R)/R$ term (where R is the radius of the thin film disk) with that for $\partial B_r/\partial z \approx 2B_r(d/2)/d$ in the formula for the current density. Comparison of the experimental $B_z(r)$ with the calculated $B_r(r)$ shows that at low magnetic inductions $B_r(d/2)$ on the disk's surface and $B_z(R)$ on the disk's surface and at the disk's edge are of the same order of magnitude. This implies that $\partial B_r/\partial z$ is greater than $\partial B_z/\partial r$ approximately by a factor of R/d .

Mikheenko and Kuzovlev [27] derived an exact analytical expression for the shielding current and the corresponding field distribution in thin film disk-shaped type II superconductors in perpendicular external magnetic fields (see previous section).

Zhu *et al* [48] further developed the theory of Mikheenko and Kuzovlev for the case when the external applied field is reduced from H_a to H ($|H| \leq H_a$). In both cases [27, 48] the critical state model was assumed and the critical current density was taken as independent of the external field. This latter assumption was based on the experiments by Theuss *et al* [52] with YBCO thin films, who found a weak magnetic field dependence of J_c at fields up to 1 kG. Clem *et al* [49] extended the results of Mikheenko and Kuzovlev [27] and Zhu *et al* [48] in order to calculate the critical-state current-density, the flux-density profiles and the ac susceptibility components for a thin film superconducting disk under a varying (periodic) external magnetic field. Brandt *et al* [56, 57] and Darwin *et al* [58] analyzed the critical state in thin superconducting strips and slabs and revealed that the critical state behavior is similar in many respects to that of thin-film disks. Frankel [59], Däumling and Larbalestier [60] and Conner and Malozemoff [54] used numerical methods to obtain field and current patterns in disk-shaped superconducting films, assuming either magnetic field-independent or field-dependent critical currents according to Kim model [61]. In the latter case, the calculations with an iteration procedure were used to reproduce the axial component $B_z(r)$ of the local magnetic field. Xing *et al* [62] used an inversion scheme to derive the local currents in a thin film superconductor using the magnitude of B_z measured close to the surface. Wijngaarden *et al* [63] extended an inversion scheme method in order to include samples of arbitrary thickness.

In all previous studies described above only the measured axial component of the magnetic field was used either to extract the current distribution or to verify an assumed current density. The radial field was subsequently calculated from the obtained current distribution. The reason for this was the absence of the experimental measurements of the radial component B_r . In the present work, we extended the studies of the critical state by measuring both radial and axial fields above thin films (disk and ring). This allowed us to find the distribution of the field lines above the

sample and to calculate the distribution of the currents responsible for the observed fields in incomplete (partial) and complete flux penetration regimes. Note that in this thesis, we use the following terminology: incomplete (partial) and complete flux penetration regimes instead of partial and full critical states.

We also performed additional investigations of $B(r)$ by performing the following experiments:

- (a) Measurements of the temperature and magnetic field dependence of incomplete-complete flux penetration states;
- (b) Measurements of the time dependence of the $B_z(r)$ profiles for incomplete and complete flux penetration states, and
- (c) Measurements of the magnitude of the applied magnetic field required for a complete flux penetration.

Transverse and axial scanning Hall-probes have been used in this study. The Hall probe-scanning system provides better accuracy regarding the measurement of a magnitude of the magnetic field than the corresponding magneto-optical Faraday effect method. It is also free of the unwanted change in sensitivity, shown by a magneto-optical method [52], during the measurement of the field distribution between the edge and the center of the disk-shaped sample. The Hall-probes allowed us to measure, with high accuracy, the time-dependent changes in $B(r)$ at any point along the disk's diameter.

The obtained experimental results were compared with the predictions of the existing critical state models [52, 60, 54, 55, 27, 48].

Chapter 2

Experimental Procedures

2.1 Introduction

Standard measurements techniques usually applied to study critical currents and their relaxation in high temperature superconductors are dc and ac magnetization measurements and a I-V transport measurement. In magnetization measurements, one determines J_c as a density of the current circulating within a grain. The critical state model (Bean's model [46]) is used to relate magnetization to J_c . According to this model when an external magnetic field H (equal to a field at which a complete flux penetration occurs) is applied to a superconductor of a dimension D , the superconductor responds to this new situation by setting up the surface currents of $J_c = H/D$. Therefore, the application of the magnetization method depends strongly on the validity of the critical state model. The I-V transport measurements of the critical current in high temperature superconductors depend on the magnitude of the contact resistance which lead to Joule heating if the critical currents are high. Since J_c decreases with an increasing temperature, local heating results in an underestimation of J_c . The method is also insensitive to a resistive dissipation of supercurrent since it uses a constant current generator as a source of the current. On the other hand, it does not make a clear distinction between very low resistance and superconductivity. A minimum resistance that can be measured is about $10^{-7} - 10^{-5}\Omega$, which is related to the sensitivity of instruments; a voltage criterion of $0.1 - 10\mu V$. The magnitude of the critical current is set by this voltage criterion. Different criteria result in different

values of J_c .

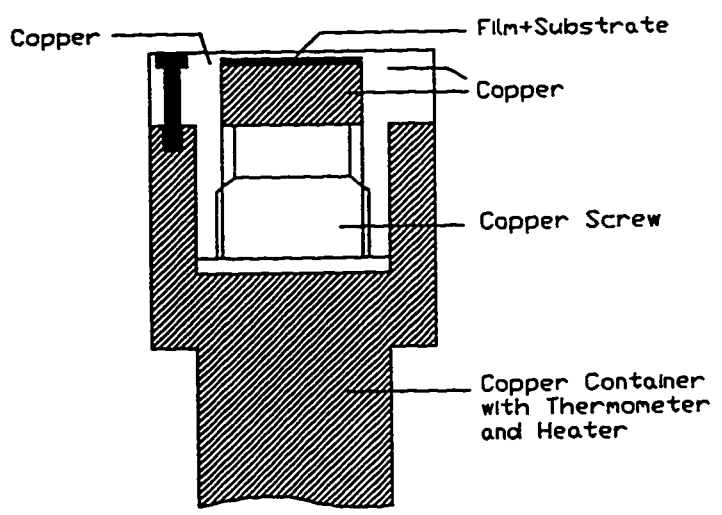
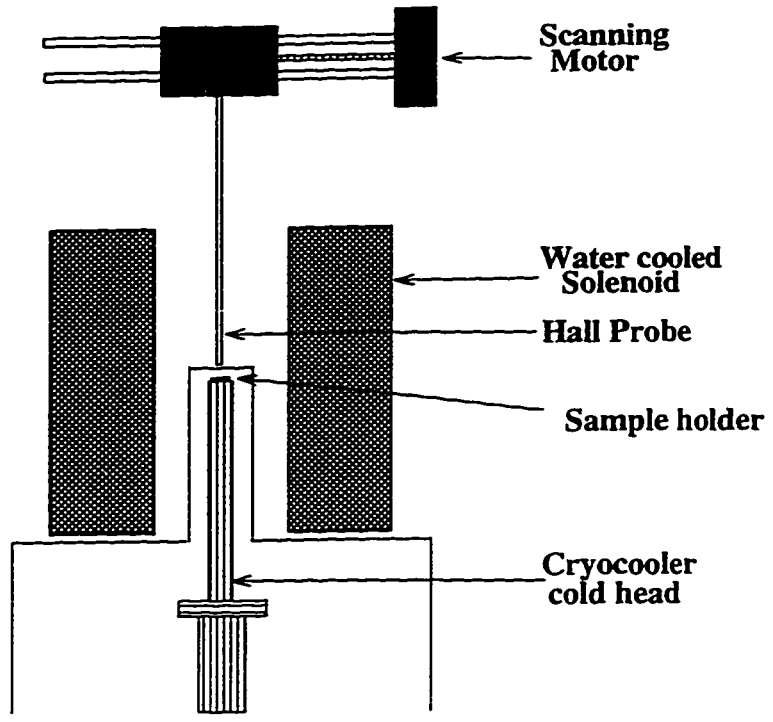
In the view of the above, an alternative technique has been developed. It uses self-supporting (persistent) supercurrent circulating in a ring-shaped samples, and a scanning Hall probe to measure the profiles of the persistent current's self field above the sample. It allowed us to determine the magnitude of the critical current flowing in a superconducting ring as a function of temperature and magnetic field and the corresponding relaxation of the current from the critical current level.

In the following section we describe in detail the Hall probe measurement system.

2.2 Measurement Technique

2.2.1 Experimental set up

The scanning Hall probe measurement system shown in Figure (2.2.1) consists of a cryogenic refrigerator (CTI22) which cools the sample to a minimum stable temperature of $10K$. Thin film samples are mounted inside a copper sample holder positioned 2.5 inches above the cryocooler head (a $10K$ stage). An aluminum cylinder is attached to a $77K$ stage of the cold head to provide a thermal shield for the sample holder. A Hall probe is connected to a gaussmeter and a computer controlled system which allow the measurements of the magnetic field profiles across the ring or disk diameter over a scanning distance of $25mm$ and a constant minimum vertical distance of $2.5mm$ above the ring [Figure (2.2.2)]. The sensitive area of the Hall probe is $0.4mm^2$ and its sensitivity is $\pm 2mG$. Variation of the vertical distance with temperature at low temperatures (over a range of $10 - 120K$) was tested using a copper wire wound ring-shaped coil instead of the sample. This coil was able to produce magnetic field



Sample Holder Scale 1:1.5

Figure 2.2.1: The measurement system.

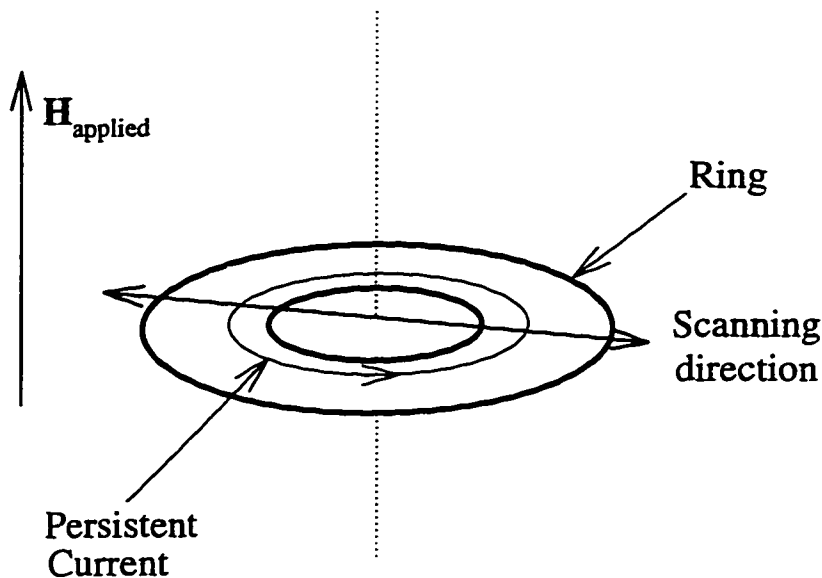


Figure 2.2.2: Schematic of the ring's geometry used in the measurements of the magnetic field profiles above the ring. Scanning direction denotes the direction of motion of a Hall probe across the ring.

profiles similar to those generated by the persistent current in a superconducting ring, with the magnitude at a distance of 2.5mm above the coils center over a range of $0 - 10\text{G}$. It was found that the changes in a magnetic field recorded by a Hall probe are within $0.5 - 1.0\%$ of the reading over the whole applied temperature range. A Hall probe is kept at room temperature and in air in order to avoid any offsets in the reading of the magnetic field. The Hall probe scanning distance is read by a Mutotoyo digital micrometer device with an accuracy of 0.01mm and a micrometer screw is used to set the vertical distance of the probe from the sample. An external magnetic field of up to a maximum of $\simeq 1\text{ kG}$ is generated along the ring or disk axis by a non-superconducting (water cooled) solenoid. The sample temperature is controlled over a range of $10 - 90\text{ K}$ with GaAlAs diode and Pt resistance thermometers, and an inductionless heater.

2.2.2 Sample preparation

YBCO thin films

One of the methods successfully applied to produce HTSC thin films is through sputter deposition. It allows one to deposit stoichiometric films over a large area. In this study, we have applied an rf magnetron sputtering technique to grow YBCO superconducting thin films on (100) oriented LaAlO_3 and SrTiO_3 substrates.

The sputtering deposition system that was used to prepare YBCO thin films consists of a vacuum chamber with a base pressure of 1×10^{-7} *mtorr* produced by a cryopump, an rf magnetron sputter gun and a heater with a nickel plate and a chromel-alumel thermocouple. A temperature controller was used to control the substrate temperature with a stability of $\pm 1^\circ\text{C}$.

It is known that the growth of epitaxial thin films depends on the deposition conditions and the substrates. For a sputtering deposition technique, these conditions include: the substrate temperature, the O_2/Ar gas pressure ratio, the total gas pressure, the substrate-target distance, the on-axis or off-axis configuration and the deposition rate. YBCO thin films were deposited on (100) oriented SrTiO_3 and LaAlO_3 substrates (of dimensions $10 \times 10 \text{ mm}^2$) using the off-axis configuration. The substrates were attached to the heater plate using a silver paste in order to achieve uniform heating. Figure (2.2.3) shows details of this sputtering system. A 2-inch diameter commercial stoichiometric $\text{Y}_1\text{Ba}_2\text{Cu}_3\text{O}_{7-\delta}$ target of 99.999% purity was used during the deposition. The sputtering was performed using 50W rf power at a total pressure of 100 – 120 *mtorr* in 1:1, 1.5:1 and 5:1 oxygen-argon gas mixtures. The substrate temperatures were kept between 650 and 730 $^\circ\text{C}$ for LaAlO_3 and between 700 and 800 $^\circ\text{C}$ for SrTiO_3 substrates. The deposition temperatures correspond to those which are required to achieve less than 20% of a-axis growth (alignment) in the

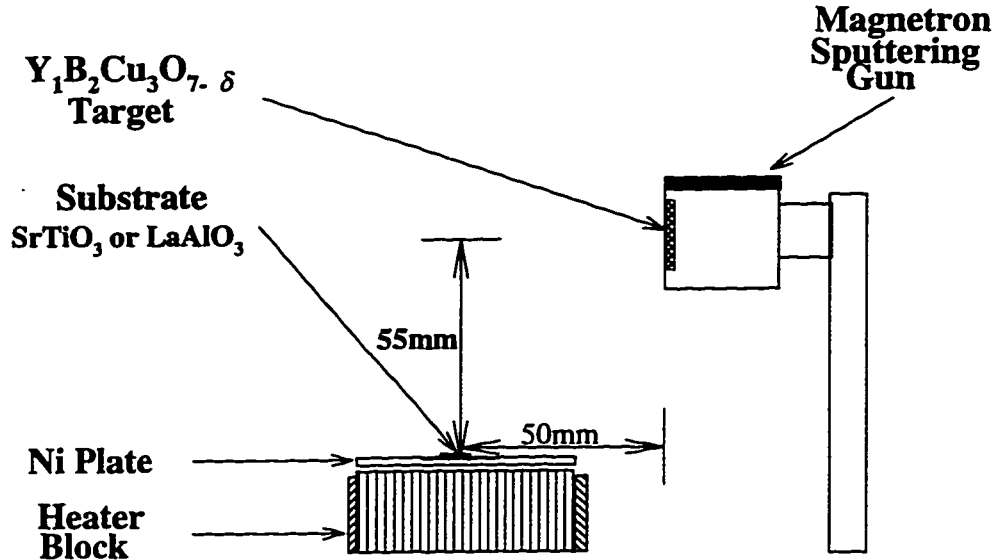


Figure 2.2.3: Thin film sputtering system.

c-axis oriented YBCO films according to studies done by Jeschke et al [64]. After deposition, the chamber was filled with oxygen at a pressure of 760 Torr and the films were subsequently cooled to 500 °C for 15 – 30 minute annealing and then to room temperature.

We also investigated YBCO thin films that were deposited in different laboratories with a dc magnetron sputtering (Westinghouse STC) and a laser ablation technique (IBM T. J. Watson, McMaster University, CTF Systems and Purdue University).

Two YBCO thin films were sputter-deposited on disk-shaped (100) oriented $LaAlO_3$ substrates (disk #1 and #2 of 15mm in diameter) using off-axis dc magnetron sputtering from a stoichiometric YBCO target [65]. The deposition temperature was kept at 650 – 700 °C. The dc magnetron sputtering source was operated with a power between 40 and 80 W in argon-oxygen gas mixture of partial pressure of ~ 200 mtorr

Ar and 20 *mtorr* O_2 . After deposition films were annealed at 400 °C in oxygen at a pressure of 20 *Torr* for 15 – 30 minutes.

Laser ablated thin films were deposited on (100) oriented $LaAlO_3$ and $SrTiO_3$ substrates at 800 °C and 300 *mtorr* oxygen pressure.

The standard photolithography technique patterning was used to pattern YBCO thin films into rings of outer and inner dimensions of 8.5 and 5 mm or 10 and 6 mm, respectively. A diluted phosphoric acid was used to etch ring-shape films.

YBCO granular samples

YBCO granular ceramics and YBCO/Ag (2 wt %) were prepared by the standard solid state reaction method from high purity (99.999%) compounds. A homogeneous powder mixture of Y_2O_3 , CuO and $BaCO_3$ was first pressed into disk shaped pellets under 2.5 – 2.7 *kbar* pressure. The disks were calcined in flowing oxygen or air for 24 hours at temperatures of 925 – 950 °C. The resulting product was pulverized and a new disk shaped pellet was formed under a pressure of about 7 *kbar*. The disks (16 *mm* in diameter and 3.0 – 3.5 *mm* thick) were then sintered in flowing oxygen at 925 – 930 °C for 7 hours and cooled at variable rates down to room temperature (3°C/minute between 925 – 700 °C and 1 °C/minute below 700 °C). For YBCO/Ag(2 wt %) composite, silver powder was added to YBCO before the sintering process. After sintering a 6 *mm* diameter hole was cut in the disk center using a diamond drill sprayed with water. Two parallel constrictions were cut along the ring's diameter, forming bridges of the cross-sectional area of about 3.0 – 3.5 *mm*².

Thin film characterization

Measurements of the resistance vs temperature were performed on thin films deposited with an rf magnetron technique on a narrow strip of LaAlO_3 or SrTiO_3 substrates under the same conditions as the larger ($10 \times 10\text{mm}^2$) substrates that were later used to make thin films rings. Silver contacts were sputtered on the strips and the resistance vs temperature was measured using a four-probe method. The transition temperature T_c (over a range of 83-91K) was found to be within $\pm 0.5\text{K}$ of that at which $J_c = 0$ as determined by the critical current measurement procedure (see below).

Ac susceptibility measurements were performed on two disk-shaped YBCO thin films used for the study of flux penetration and supercurrent distributions [66]. Two ac pickup coils were used to measure the ac susceptibility χ with frequency $f = 3.22\text{kHz}$ and $H_{rms} = 1.8\text{G}$. The measurement of the real part of ac susceptibility $\chi(T)$ gave a transition temperature $T_c = 87\text{K}$, for disk #1 and 86K for disk #2, and the width of the superconducting transition about 1.5K in both cases. The imaginary part of ac susceptibility $\chi'(T)$ revealed a sharp peak at 86K for disk #1 and at 85K for disk #2. A Hall probe method applied in this study was able to detect a magnetic flux trapped in the disks at temperatures up to 89K for disk #1 and 90K for disk #2.

X-ray diffraction measurement was used to verify the c-axis orientation of the films. This is represented by the presence of the (00l) peaks in the x-ray diffraction spectrum. Figure (2.2.4) shows typical x-ray diffraction patterns of two YBCO thin films; one grown in the IBM laboratory on SrTiO_3 substrate using a laser ablation and the other one deposited on LaAlO_3 substrate using the rf magnetron sputtering system described above.

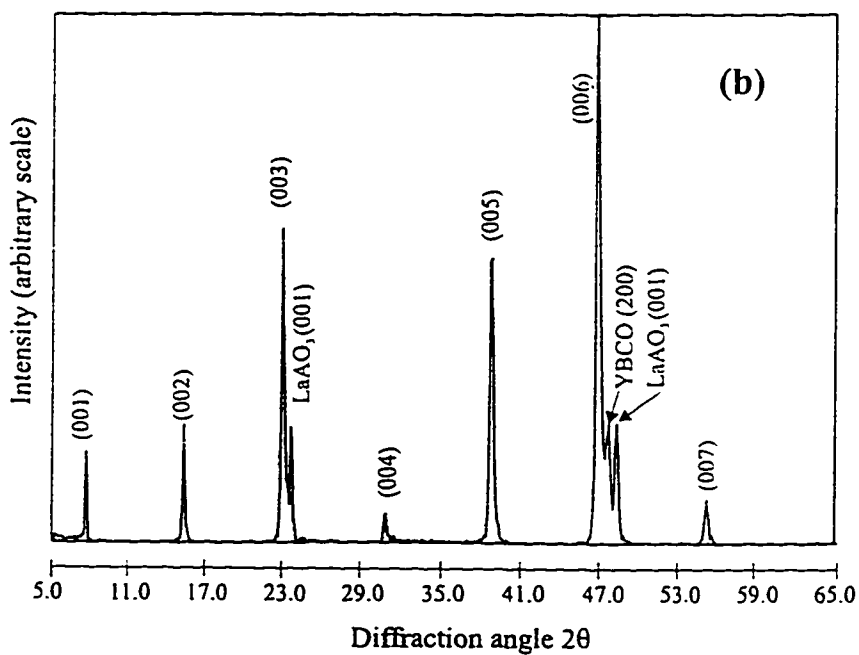
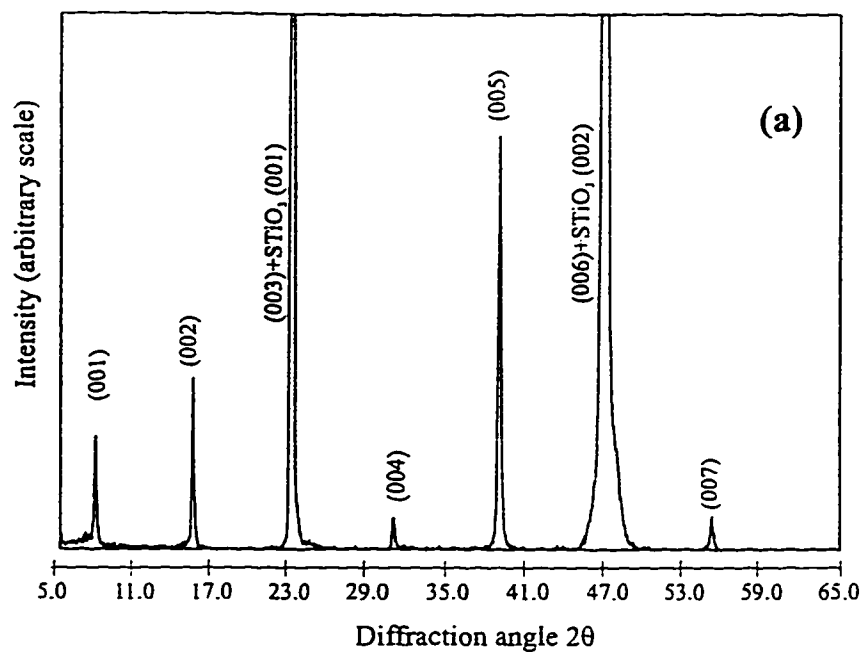


Figure 2.2.4: X-ray diffraction pattern obtained for a YBCO film grown on (a) SrTiO₃ and (b) LaAlO₃. Both films have a c-axis orientation typical of YBCO films that were used in this study.

2.2.3 Critical current measurement procedure

The magnitude of the critical current was inferred from the magnitude of the axial component of the magnetic field generated by a maximum self-supporting supercurrent circulating in a ring-shaped sample. For YBCO thin films persistent current was induced in a ring by applying and subsequently switching off the external magnetic field generated by a solenoid along the axis of the ring (c-axis). An external magnetic field less than $1kG$ was sufficient to saturate the self-field over a temperature range between $10K$ and T_c . The profile of the current's self-magnetic field was recorded with a scanning Hall probe at a constant distance from the sample. Figure (2.2.5) shows the profiles of the axial magnetic field due to persistent currents of various magnitudes, flowing in a zero-field-cooled (ZFC) YBCO thin film. The profiles have very symmetrical bell-like shape. It should be pointed out here that the axial component of the persistent current's self-field has a single maximum in the ring's center, whereas a field due to magnetic vortices trapped in the ring's bulk exhibits a profile with the maximum above the ring's bulk and a minimum in the ring's center. It is therefore possible to distinguish the field produced by the trapped vortices from that due to a circulating persistent current. The experiments were designed to minimize contribution of the trapped vortices to the self-field of the persistent current. Persistent currents were generated in the ring, starting at low applied magnetic field [Figure (2.2.5)]. This allowed us to detect any changes in the symmetric bell shaped profiles of the current's self-field caused by the vortices trapped in the ring's bulk. The experimental data for YBCO thin film rings show that the symmetric profile is preserved for persistent currents of magnitude up to the saturation (critical) value. For YBCO ceramic rings, trapping of the intergrain vortices was minimized by using special geometry, i.e. by cutting two notches (bridges) along the ring's diameter [67]. These bridges allowed the creep of magnetic flux from outside into the ring's central hole at low external magnetic field, minimizing trapping of the intergrain vortices in

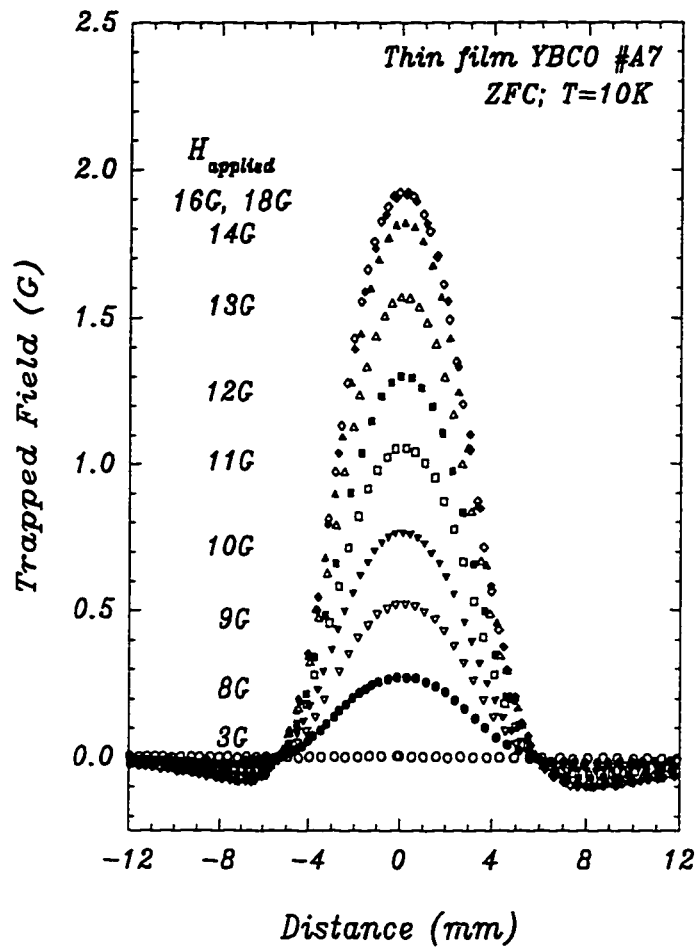


Figure 2.2.5: The profiles of the axial component of the magnetic self-field generated by the persistent (self-supporting) currents in the zero-field-cooled YBCO thin film ring at 10 K. The persistent currents of various magnitudes were induced by applying and subsequently removing an external magnetic field. Critical persistent current is reached when the current's self-field saturates. The field was measured with a scanning axial Hall probe at a distance of 2.5 mm above the surface of thin film. Distances ± 4.25 mm and ± 2.5 mm mark the ring's outer and inner edges, respectively.

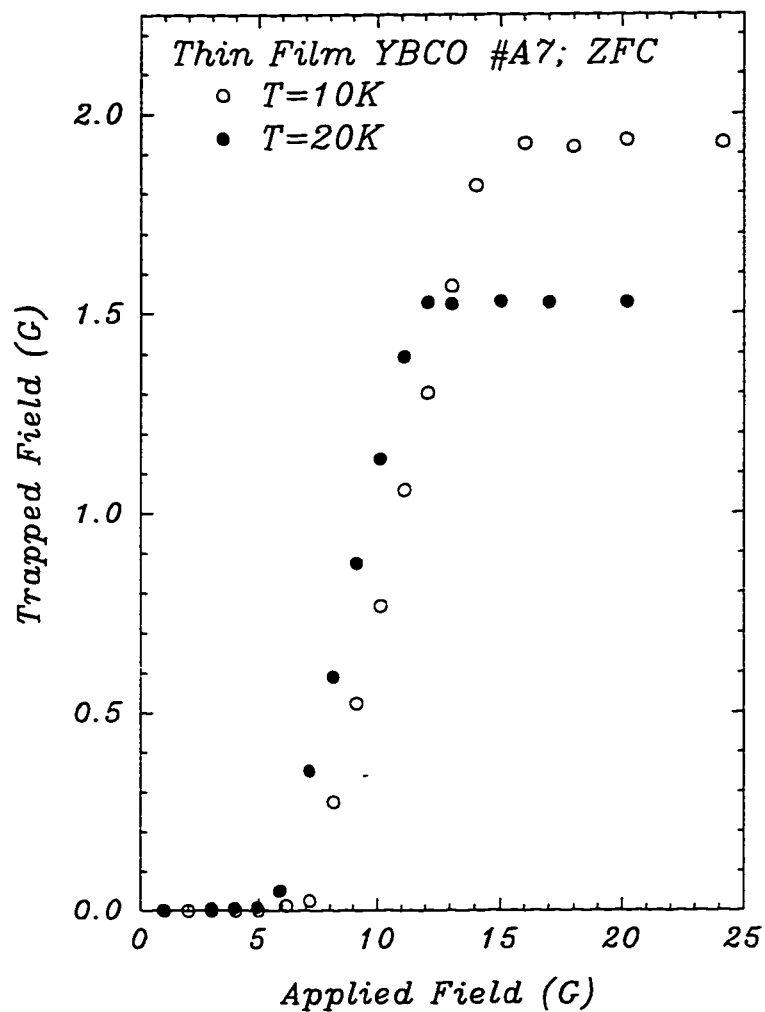


Figure 2.2.6: Dependence of the persistent current's self-field measured at the ring's center on an applied magnetic field at 10 and 20 K. Saturation value of the self-field is proportional to the magnitude of the critical current at a given temperature.

the bulk of the ring.

The magnitude of the critical current was inferred from the maximum magnitude of the current's self field at the ring's center using Biot-Savart equation. Figure (2.2.6) presents the magnitude of the current's self-field measured in the zero-field cooled YBCO thin film as a function of the applied magnetic field. The saturation value of the self-field is proportional to the critical current at a zero magnetic field and at a given temperature.

The measurement of the temperature dependence of the critical current in a magnetic field was performed by using a field-cooling procedure (FC) at a given magnetic field H_0 (applied along the ring's axis) down to a temperature of the measurement. At this temperature the profile of the axial component of the Meissner field (which represents the expulsion of magnetic flux out of the ring in the presence of an external magnetic field H_0) was measured. An additional external field ΔH was then applied and subsequently reduced to zero, in order to induce circulating persistent current at H_0 . Similarly to the zero-field-cooling case, the current's critical value was reached by applying higher ΔH . The critical current at H_0 is proportional to the current's self-field in the ring's center, which equals the difference between the field seen by a Hall probe and the corresponding Meissner field.

2.2.4 Magnetic flux relaxation measurement procedure

We have measured the temperature dependence of the relaxation of the persistent current from the critical level, and the magnitude of the critical current, using a ring geometry and a scanning Hall probe technique (see previous sections). The measurement of the persistent current's self-field enabled us to record the relaxation (time decay) of the persistent current from various levels of the current up to the critical value. The relaxation data were taken over a time range of 1 - 40000s at

temperatures between 10K and T_c . They were used to calculate the dependence of the energy barrier U_{eff} for vortex motion on the current density J in YBCO films. We applied the Maley's method to obtain $U_{\text{eff}}(J)$.

Calculation of $U_{\text{eff}}(J)$ using the Maley's method

The current dependent effective activation energy $U_{\text{eff}}(J)$ can be deduced from the relaxation measurements at different temperatures by employing the procedure of Maley et al [45]. In this method, $U_{\text{eff}}(J)$ is extracted from Beasley-Labusch-Webb equation for thermally activated motion of flux [68]. The relaxation rate of the magnetization M according to this model is

$$\frac{dM}{dt} = \frac{Ba\omega_0}{\pi d} \exp -\frac{U_{\text{eff}}(J)}{k_B T} \quad (2.1)$$

where B , a , ω_0 and d are the magnetic induction, the hopping distance, the characteristic attempt frequency and the thickness of the slab of the superconductor, respectively. The activation energy can be extracted from the above equation in the form

$$U_{\text{eff}}(J) = -k_B T \left(\ln \left| \frac{dM}{dt} \right| - C \right) \quad (2.2)$$

where $C = \ln (Ba\omega_0/\pi d)$ can be treated as a constant at sufficiently low temperatures. According to the critical state model, M is assumed to be proportional to J ($M \propto Jd$). In general, the effective activation energy is a function of J , T and B . At a constant B , $U_{\text{eff}}(J, T)$ can be expressed as a product of two functions

$$U_{\text{eff}}(J, T) = G(T)F(J) \quad (2.3)$$

with $G(T)$ and $F(J)$ being functions of a temperature T and a current density J , respectively. Maley has assumed the $G(T)$ could have the following form [69, 70],

$$G(T) = [1 - (T/T_x)^n]^m \quad (2.4)$$

where T_x is a characteristic temperature (e.g. the irreversibility temperature).

The measurement of the time decay of J from its critical value J_c at a fixed temperature, over an experimentally feasible time range of 1 - 100,000s, allows the change of J by about 20 percent [67]. Maley et al [45] were able to extend the accessible region of J by recording the decay of magnetization from its critical value $M_c \propto J_c$ for various temperatures below T_c . Changing a temperature ensured a continuous change in J_c , and permitted the measurement of $U_{\text{eff}}(J)$ for a wide range of the current. At each temperature, the magnetic relaxation measurements were used to find dM/dt as a function of the current density J . As a result, a curve of $U_{\text{eff}}[J(T)]$ versus $J(T)$ was produced, which consisted of multiple segments, each representing the time decay of magnetization from its critical value, measured at different temperature T . The temperature dependence in $U_{\text{eff}}[J(T)]$ was eliminated by using $G(T) = 1 - (T/T_x)^2$ according to Equation (2.4). Plotting of $U_{\text{eff}}[J(T)]/G(T)$ versus J produced a continuous curve. However, Berghuis et al [41] argued that there is some uncertainty in the Maley's temperature-dependent correction factor $G(T)$, which does not allow one to discriminate between various non-linear scenarios for $U_{\text{eff}}(J)$.

Calculation of $U_{\text{eff}}(J)$ for a ring geometry

When a critical persistent current is induced in a ring, it applies the Lorentz force on the vortices trapped in the bulk of the ring, which pushes flux lines in the radial direction out of the ring. The vortex-line motion generates the electric field $\mathbf{E} = (1/c) (\mathbf{B}' \times \mathbf{v})$. We take \mathbf{B}' in the z-direction (the ring's axis) which represents the local magnetic induction B'_z due to the axial component of the persistent current's self-field, and \mathbf{v} the drift velocity of vortices in the radial direction from the ring's axis. Then \mathbf{E} is in the azimuthal direction (along the axis tangent to the ring's

perimeter) and its magnitude is $E_\theta = (1/c)B_z^l v_r$. Because of the cylindrical symmetry and the independence of the vortex motion on the tangential coordinate θ , one could treat the problem as a one-dimensional one and replace cylindrical coordinates (r, θ, z) with Cartesian ones (x, y, z) . Then for the motion of flux in the x-direction and with the local induction B_z^l , the magnitude of \mathbf{E} is $E_y = (1/c)B_z^l v_x$. Using the Maxwell equation $\nabla \times \mathbf{E} = -(1/c)(\partial \mathbf{B}/\partial t)$, the equation that describes flux motion (and consequently the decay of the persistent current due to the motion of vortices in the ring's bulk) could be written in the following form:

$$\frac{\partial B_z^l}{\partial t} = -c \frac{\partial E_y}{\partial x} = -v_x \frac{\partial B_z^l}{\partial x} \quad (2.5)$$

where the drift velocity is taken constant along the x-direction and equal to

$$v_x = \omega_0 a \exp[-U_{\text{eff}}(J)/k_B T] \quad (2.6)$$

Here ω_0 is the characteristic attempt frequency, a is the hopping distance, and $U_{\text{eff}}(J)$ is the effective energy barrier for the thermally activated hopping. The resulting equation

$$\frac{\partial B_z^l}{\partial t} = -\omega_0 a \frac{\partial B_z^l}{\partial x} \exp[-U_{\text{eff}}(J)/k_B T] \quad (2.7)$$

can be modified further by taking into account the gradient of B_z^l over a distance x , which was measured by a Hall probe at a height z above the ring. The data [see Figure (2.2.7)] show that the gradient of B_z^l is

$$\frac{\partial B_z^l}{\partial x} = -\frac{B_z^l(R_{id}) - B_z^l(R_{od})}{d} \simeq -\frac{B_z^l(R_{id})}{R_{id}} \quad (2.8)$$

where R_{id} and R_{od} are the inner and outer radii of the ring, respectively and d is the width of the ring.

Equation (2.7) written for the local induction B_z^l at $x = R_{id}$ is

$$\frac{\partial B_z^l}{\partial t} \Big|_{x=R_{id}} = -\omega_0 a \frac{\partial B_z^l}{\partial x} \Big|_{x=R_{id}} \exp[-U_{\text{eff}}(J)/k_B T] \quad (2.9)$$

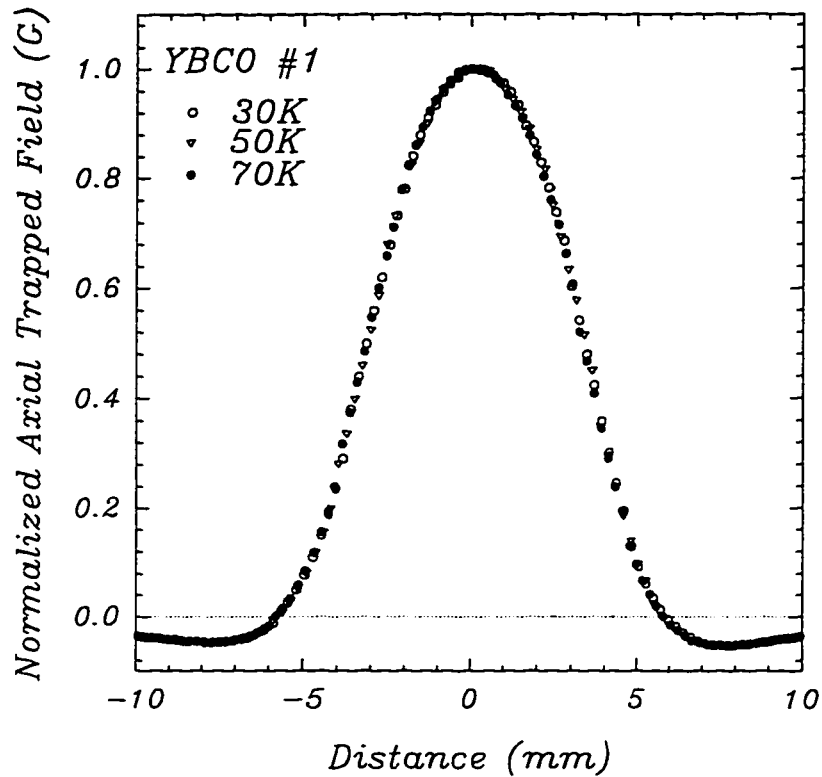


Figure 2.2.7: The profiles of the axial component $B_z(r)$ of the persistent current's self-field at the critical value, measured at temperatures of 30 K (open circles), 50 K (open triangles) and 70 K (full circles) in a zero-field cooled ring of YBCO film #1 at a distance of 2.5 mm above it. The profiles are normalized to the value of the field at the center of the ring. Note that the shape of the profile is independent of temperature. Distances $r = \pm 2.5\text{mm}$ and $r = \pm 4.25\text{mm}$ mark the ring's inner and outer edges.

Using Equation (2.8), one can transform this relation to

$$\frac{\partial B_z^l(R_{id})}{\partial t} = \omega_0 a \frac{B_z^l(R_{id})}{R_{id}} \exp[-U_{\text{eff}}(J)/k_B T] \quad (2.10)$$

Taking into account the relationship between $B_z^l(R_{id})$ and the magnitude of the persistent current I , given by the Biot-Savart law, the decay of the persistent current is described by

$$\frac{dI}{dt} = \frac{\omega_0 a}{R_{id}} I \exp[-U_{\text{eff}}(J)/k_B T] \quad (2.11)$$

or

$$\frac{dJ}{dt} = \frac{\omega_0 a}{R_{id}} J \exp[-U_{\text{eff}}(J)/k_B T] \quad (2.12)$$

The effective energy barrier can be extracted from the above equation, in the following form:

$$U_{\text{eff}}(J) = -k_B T \ln \left[\left(\frac{dJ}{dt} / J \right) \right] + k_B T \left\{ \ln \left(\frac{\omega_0 a}{R_{id}} \right) \right\} = -k_B T \left\{ \ln \left[\left(\frac{dJ}{dt} / J \right) \right] - C \right\} \quad (2.13)$$

where $C = \ln(\omega_0 a / R_{id})$ is a constant which is independent of the magnetic field or the current. The constant $\omega_0 a$ is a prefactor in the Equation (2.6) for v_x and it equals the velocity of a vortex line when the probability of each hopping process in the direction of the Lorentz force is one.

Maley et al. [45] estimated the constant C in Equation (2.2) using $\omega_0 a \simeq 0.25 \text{ m/s}$ from the measurement of magnetic relaxation in a grain-aligned sample of YBCO powder. The upper limit of $\omega_0 a \simeq 10 \text{ m/s}$ for the thermally activated flux motion was estimated by Schnack et al [71]. They took smaller value of $\omega_0 a \simeq 2 \text{ m/s}$ in the calculation of the magnetic moment hysteresis loop by means of a numerical solution of the flux-creep differential equation. For a ring geometry, we used $\omega_0 a \simeq 2 \text{ m/s}$ and $R_{id} = 2.5 \text{ mm}$ to obtain a tentative value of $C = 6.7$.

We applied the Maley's method [45] in order to calculate $U_{\text{eff}}(J)$ over a wide range of J . Our procedure involves the measurements of the relaxation rates of the

persistent current from the critical level as a function of the current density J for temperatures taken every 5 K between 10 K and 85 K. These measurements were used to find dJ/dt vs J , whose value is necessary for the calculation of $U_{\text{eff}}(J)$ from Equation (2.13).

2.2.5 Magnetic flux penetration measurement procedure

Two thin-film YBCO disks #1 and #2, having a diameter of 15mm and a thickness of 5000 \AA and 2000 \AA , respectively were used to study magnetic flux penetration. Later a ring (ring #1) was etched from disk #1 and a similar study was performed on the ring for comparison. Magnetic-flux penetration was inferred from the measurements of a trapped and a shielding magnetic-flux density across a disk (or a ring) for both axial and radial fields as a function of temperature and applied magnetic field. After cooling a disk in zero field down to various temperatures below T_c , an external magnetic field was increased monotonically from zero to a certain value H_a in a direction perpendicular to the disk's plane and parallel to the film's c-axis. This was followed by the measurement of the profile of the shielding field (which is the difference between the applied field and the field measured by the Hall probe). The applied field was then reduced monotonically from H_a to zero and the trapped field was measured. Both radial and axial components of the field (either for shielding or trapping) were recorded at the same distance above the sample surface. The profiles were also measured as a function of the distance above the disk surface from 3mm (minimum) up to 12mm (maximum). This allowed us to obtain the distribution of the magnetic field lines above the sample. An additional information on partial and complete flux penetration regimes was obtained by (a) plotting the magnitude of the trapped field in the disk's center versus temperature for a constant applied magnetic field, and by (b) plotting the decay rates of the trapped field (recorded at various points along

the disk's diameter) versus distance from the disk's center for fixed temperature and applied field.

We performed numerical calculation of the axial (H_z) and radial (H_r) components of the magnetic field above a disk- (or a ring-) shaped sample. The procedure is as follows.

Using cylindrical coordinates, the radial and axial magnetic field components at some point ρ and z , generated by a ring of radius a , centered at the origin and carrying a current $I(a)$, are given by [72]

$$h_r(a, \rho, z) = \frac{I(a)}{2\pi} \frac{z}{\sqrt{r(a+\rho)^2 + z^2}} \left[-K(k) + \frac{a^2 + \rho^2 + z^2}{(a-\rho)^2 + z^2} E(k) \right] \quad (2.14)$$

and

$$h_z(a, \rho, z) = \frac{I(a)}{2\pi} \frac{1}{\sqrt{(\rho+a)^2 + z^2}} \left[K(k) + \frac{a^2 - \rho^2 - z^2}{(a-\rho)^2 + z^2} E(k) \right] \quad (2.15)$$

here $k^2 = 4a\rho / [(a+\rho)^2 + z^2]$, and K and E are complete elliptic integrals of the first and the second kind. The magnetic field at any point generated by the assumed azimuthal current distribution in a disk (or a ring) can be found by integrating these equations over the volume of the disk (or a ring). In order to integrate Equations (2.14) and (2.15), we used a numerical method. The calculation was carried out for a ring of inner radius R_{id} and outer radius R_{od} . The disk is a special case of the ring where $R_{id} = 0$. The computer program divides the sample into $n \times m$ ring segments (n along the radius and m along the thickness). A typical segmentation in our calculations is $0.5\mu m$ in the x-y plane and the thickness of the film in the z-x plane. The magnetic field at any point above the sample is obtained by summing up the fields generated by all the ring segments. The input current $I(a)$ in each segment is calculated from the critical state current distributions in a thin film superconducting disk. Using this procedure we calculated the profiles of H_r and H_z along the diameter of the sample.

We tested the above procedure using the magnetic field profiles generated by a constant current flowing in a pancake-shaped (flat) disk coil (of 16mm in diameter) and a pancake-shaped ring coil (of 8.1mm in outer diameter and 4.9mm in inner diameter). Both coils were made of thin copper wire of a diameter of 0.13mm for the disk-coil and 0.06mm for the ring-coil. The coils have diameters approximately equal to those of YBCO thin film disks and rings studied. Calculation of the radial and axial magnetic profiles generated by a circulating current in the coils was made using the magnitude of the current, the exact numbers of turns of each coil (56 turns for the disk and 26 turns for the ring) and the distance of the probe above the coil. Figures (2.2.8) and (2.2.9) show a good agreement between the experimental results (open symbols) and the theoretical calculations (solid lines) for the disk and the ring coils, respectively.

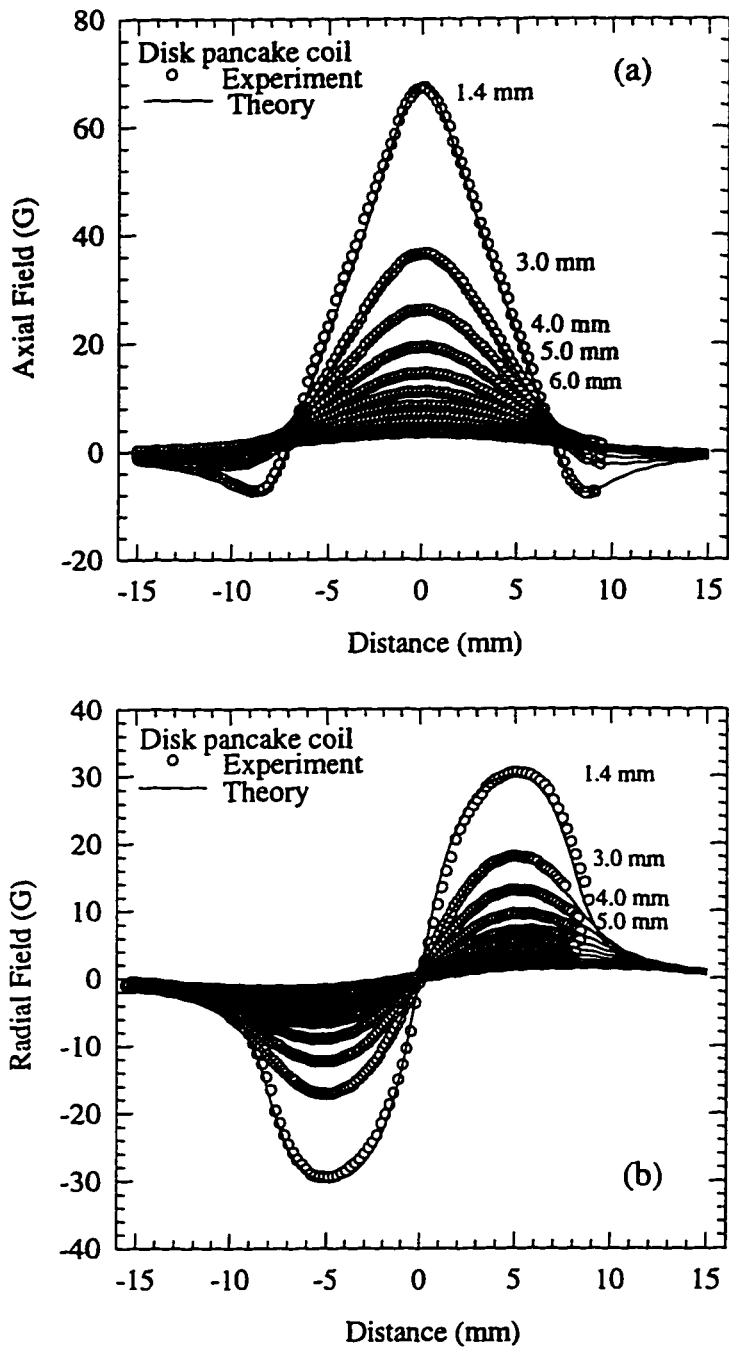


Figure 2.2.8: The profiles of the axial field H_z (a) and the radial field H_r (b) above a pancake-shaped disk coil. The measurements were taken at distances of: 1.4, 3, 4, 5, 6, 7, 8, 9, 10, 11 and 12 mm above the disk coil. Solid lines represent the theoretical calculation of the profiles generated by a constant current $I = 1.0$ A.

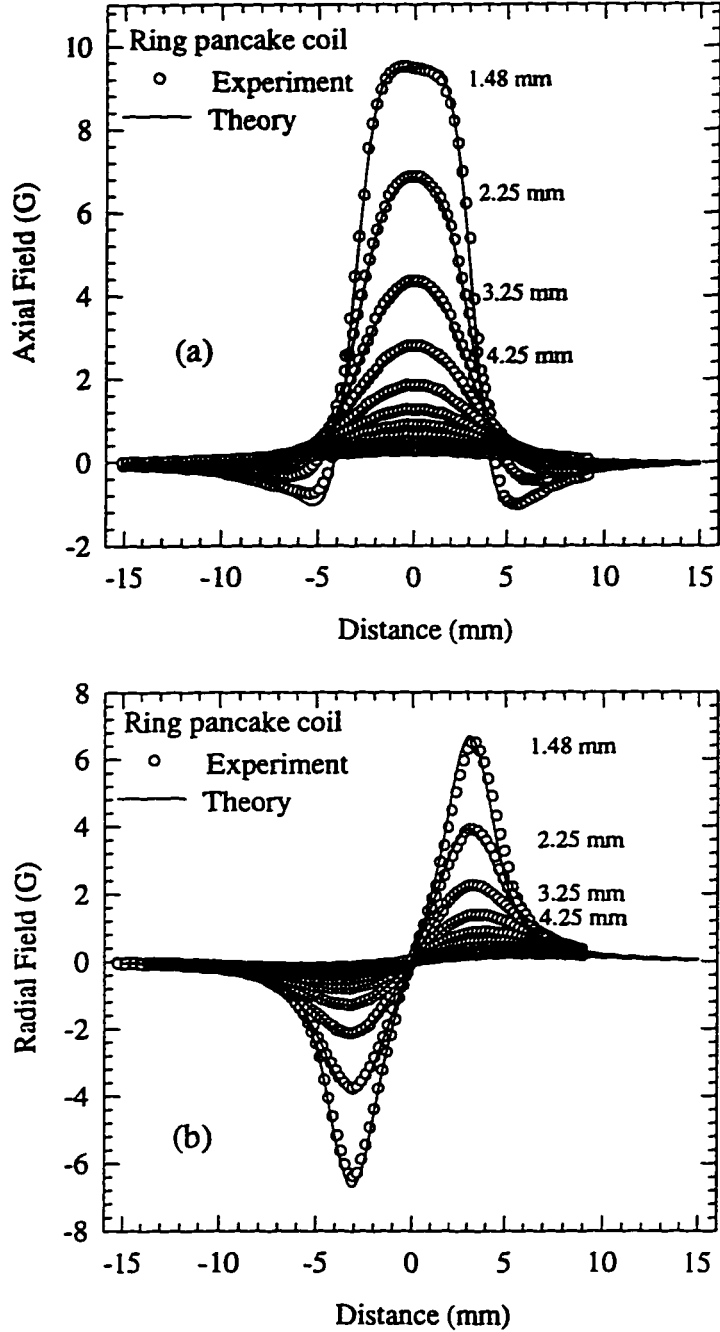


Figure 2.2.9: The profiles of the axial field H_z (a) and the radial field H_r (b) above a pancake-shaped ring coil. The measurements were taken at distances of: 1.25, 2.25, 3.25, 4.24, 5.25, 6.25, 7.25, 8.25, 9.25, 10.25 and 11.25 mm above the ring coil. Solid lines represent the theoretical calculation of the profiles generated by a constant current $I = 0.25$ A.

Chapter 3

Temperature Dependence of the Critical Current

3.1 Experimental Results

We measured the temperature dependence of the critical current (over a 10 – 90K range and in magnetic fields up to 700G) in about twenty c-axis oriented YBCO thin films (manufactured in various laboratories) and in a few granular YBCO samples.

3.1.1 Temperature dependence of J_c in YBCO thin films

The experimental data for selected YBCO thin films, which exhibit the most typical temperature dependence of $I_c(T)$, are presented in Figure (3.1.1). Critical currents in each sample were normalized to their values at 10K. Thin film of the highest T_c of 90 – 91K is characterized by an Ambegaokar-Baratoff-like (AB) convex temperature dependence below approximately 82K (with a plateau between 10 and 20K and a linear regime between 55 and 80K) and a Ginzburg-Landau-like (GL) concave temperature dependence above 80K. In thin films of T_c reduced by only 2 – 4K (i.e. in a 86 – 88K range), the Ambegaokar-Baratoff to Ginzburg-Landau ($AB \rightarrow GL$) crossover temperature shifts down to about 60 – 70K extending the Ginzburg-Landau tail down to low temperatures by about 10 – 20K. In this case the temperature dependence of I_c below the crossover temperature exhibits a quasi-linear behaviour for most samples. The crossover temperature decreases down to about 40K in thin films of $T_c \simeq 84 - 85 K$. A Ginzburg-Landau-like temperature dependence $(T-T_c)^{3/2}$

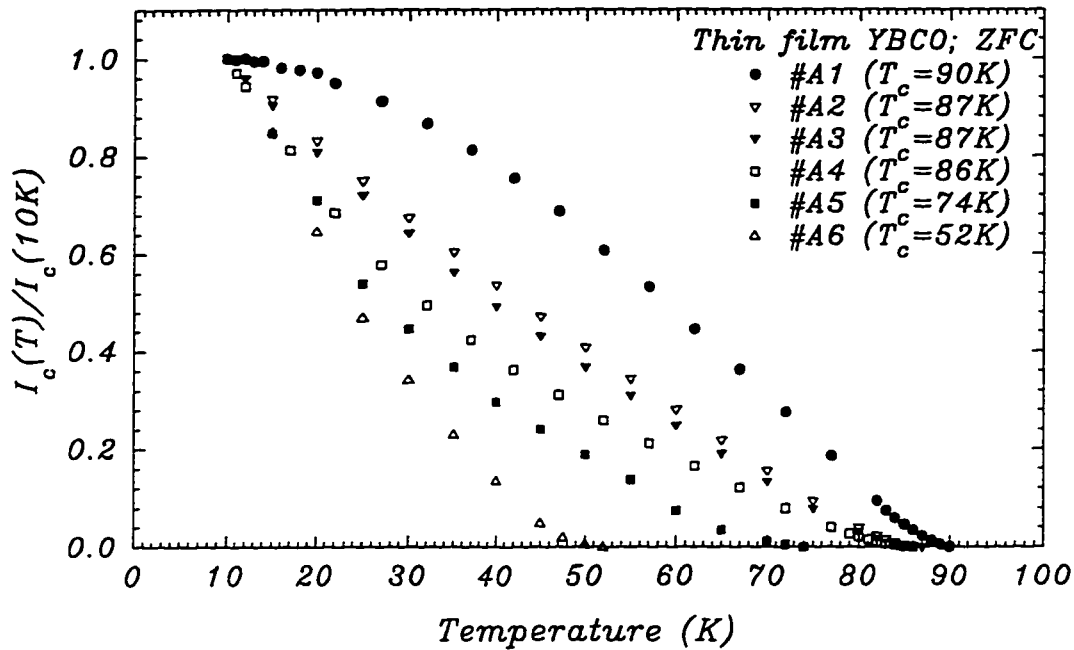


Figure 3.1.1: Temperature dependence of the critical current in c-axis oriented YBCO thin films with T_c over a range of 52 – 90K. The critical current is normalized to its value at 10K. The results show a transition from an Ambegaokar-Baratoff-like (AB) temperature dependence to a Ginzburg-Landau-like (GL) one upon reduction of T_c . The $AB \rightarrow GL$ crossover is seen in the film of $T_c \simeq 90K$ at a temperature of about 80 – 82K. T_c is a temperature at which the level of critical persistent current is less than about 5mA (which corresponds to a noise level of a Hall probe). The critical current level at 10K was within a range of 2 – 45A for various samples.

over a full ($10 - 90K$) temperature range was observed in most thin films of T_c below approximately $84K$. The exponent α in the Ginzburg-Landau expression $(T - T_c)^\alpha$ was determined to be 1.5 ± 0.1 , which was based on the measurements of $I_c(T)$ in all thin films. $AB \rightarrow GL$ crossover effects were found to be independent of the magnitude of the critical current density and depairing or depinning character of the critical current. The magnitude of the “apparent” critical current density at $10K$ (defined as a ratio of the critical current to the ring’s cross-sectional area) in various films was within a range of $5 \times 10^5 - 1 \times 10^7 A/cm^2$ for depinning critical currents. An “apparent” critical current density of $5 - 6 \times 10^5 A/cm^2$ at $10K$, for thin films which do not exhibit any decay of the current from its critical value, is within the lower range of the “apparent” depinning critical current density. This is because depairing critical currents may flow through narrow filaments in the sample.

3.1.2 Magnetic field dependence of $J_c(T)$ in YBCO thin films

We investigated the influence of an external magnetic field up to $700G$ on the temperature dependence of the critical current in two thin films, one with an Ambegaokar-Baratoff-like temperature dependence of I_c and the other with a predominant Ginzburg-Landau-like behaviour. These results are plotted in Figures (3.1.2) and (3.1.3). No decay of the current from its critical value was detected by a Hall probe in both films, suggesting depairing nature of the critical current. A $10 - 20K$ plateau in $I_c(T)$, which is visible in the first film [Figure (3.1.2)], disappears after application of a magnetic field of $700G$. This suggests magnetic field-induced decrease of the $AB \rightarrow GL$ crossover temperature. However, a Ginzburg-Landau-like temperature dependence of I_c , which characterizes the second film, is little affected by this magnetic field [Figure (3.1.3)]. The experiment implies that magnetic field much higher than $750G$ (which was the maximum field available in the experimental set-up) is required in order to

change the temperature dependence of the critical current in c-axis oriented thin film from an Ambegaokar-Baratoff to a Ginzburg-Landau-like one.

3.1.3 Magnetic field dependence of $J_c(T)$ in granular YBCO

We tested the effect of magnetic field on the intergrain critical currents in YBCO granular bulk samples. Previous studies of the intergrain critical currents over a temperature range of 65–90K [73, 19] revealed that small magnetic fields up to 30G cause a suppression of the critical current's magnitude and changes in the Ambegaokar-Baratoff character of $I_c(T)$ curve measured at zero magnetic field. Extension of these studies to a 10 – 90K temperature range allowed us to produce results shown in Figures (3.1.4) and (3.1.5). Two YBCO ceramic rings characterized by depairing and depinning intergrain critical currents were used in the studies. In both of them $I_c(T)$ curves indicate a gradual decrease of the $AB \rightarrow GL$ crossover temperature with an increasing applied magnetic field.

3.1.4 Magnetic field dependence of $J_c(T)$ in YBCO/Ag granular composite

The crossover effects to a Ginzburg-Landau behaviour were investigated in YBCO/Ag (2 wt %) ceramic composite containing intergranular silver. The temperature dependence of the intergrain critical current in this composite under zero-field-cooling conditions [Figure (3.1.6)] manifests an Ambegaokar-Baratoff-like behaviour below 80K and a DeGennes (SNS junction) behaviour above this temperature. The temperature dependence of I_c in the DeGennes regime [12] is $(T - T_c)^\alpha$ with $\alpha = 2.0 \pm 0.1$ (see the inset in Figure (3.1.6)). An external magnetic field of 100G is sufficient to cause almost complete conversion to a Ginzburg-Landau-like regime.

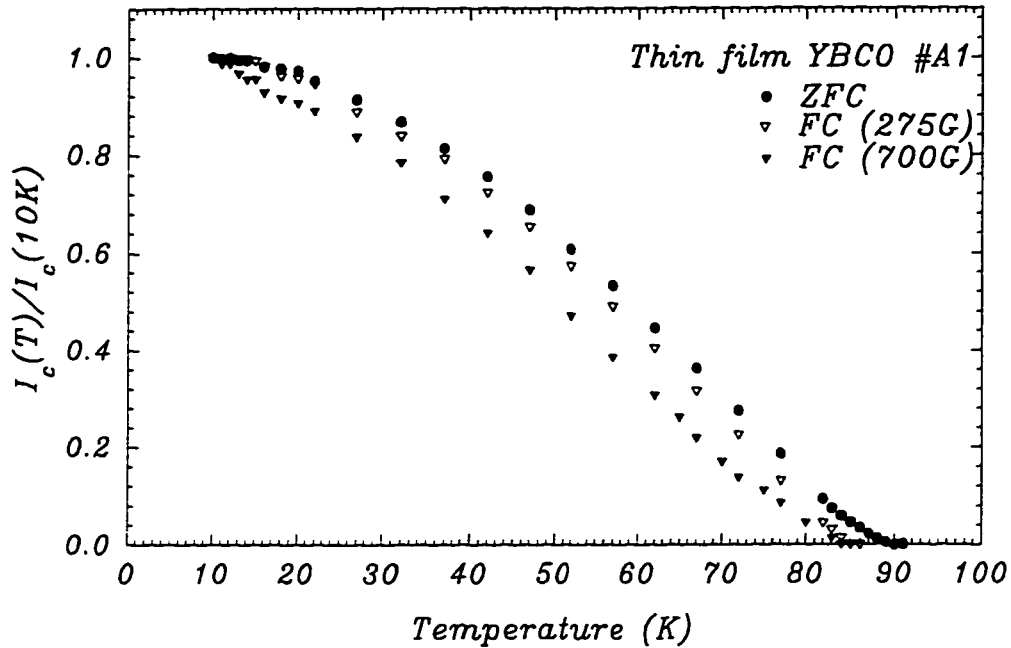


Figure 3.1.2: Temperature dependence of the depairing critical current measured in c-axis oriented YBCO thin film in magnetic fields up to 700G. For the ZFC case the thin film has $T_c \simeq 90K$ and is characterized by an Ambegaokar-Baratoff-like $I_c(T)$ below 80 – 82K and by a Ginzburg-Landau-like $I_c(T)$ above this temperature. A magnetic field of 700G removes the low temperature plateau of $I_c(T)$ and reduces the $AB \rightarrow GL$ crossover temperature.

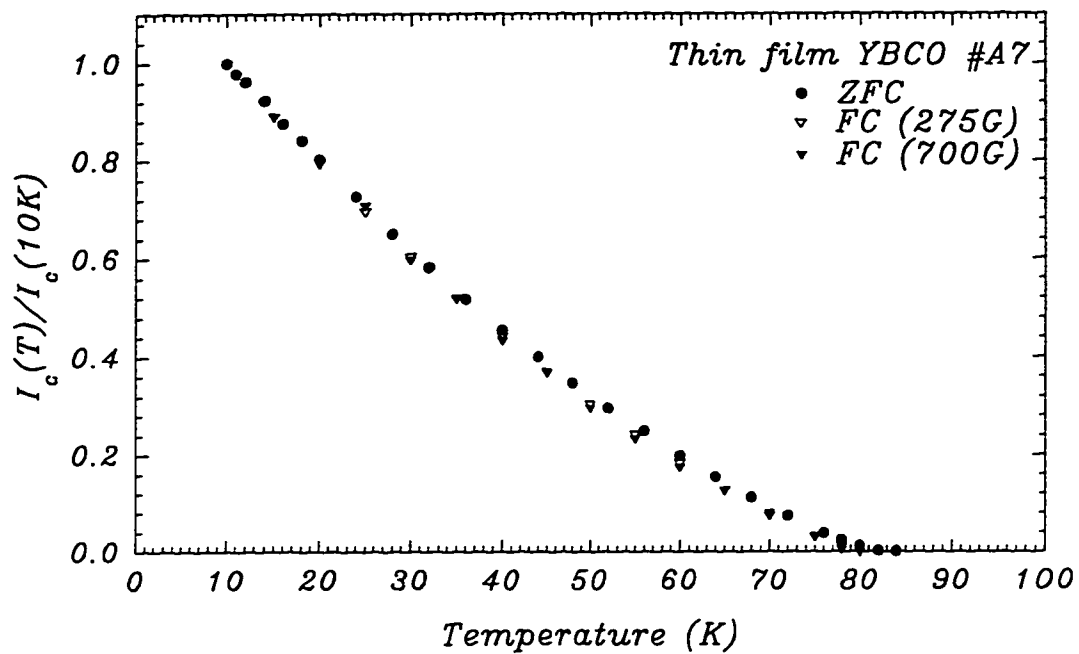


Figure 3.1.3: Temperature dependence of the depairing critical current measured in c-axis oriented YBCO thin film in magnetic fields up to 700G. For the ZFC case, this thin film has $T_c \simeq 83K$ and is characterized by a Ginzburg-Landau-like $(T - T_c)^{3/2}$ temperature dependence of $I_c(T)$. A magnetic field of 700G does not have any effect on the shape of $I_c(T)$.

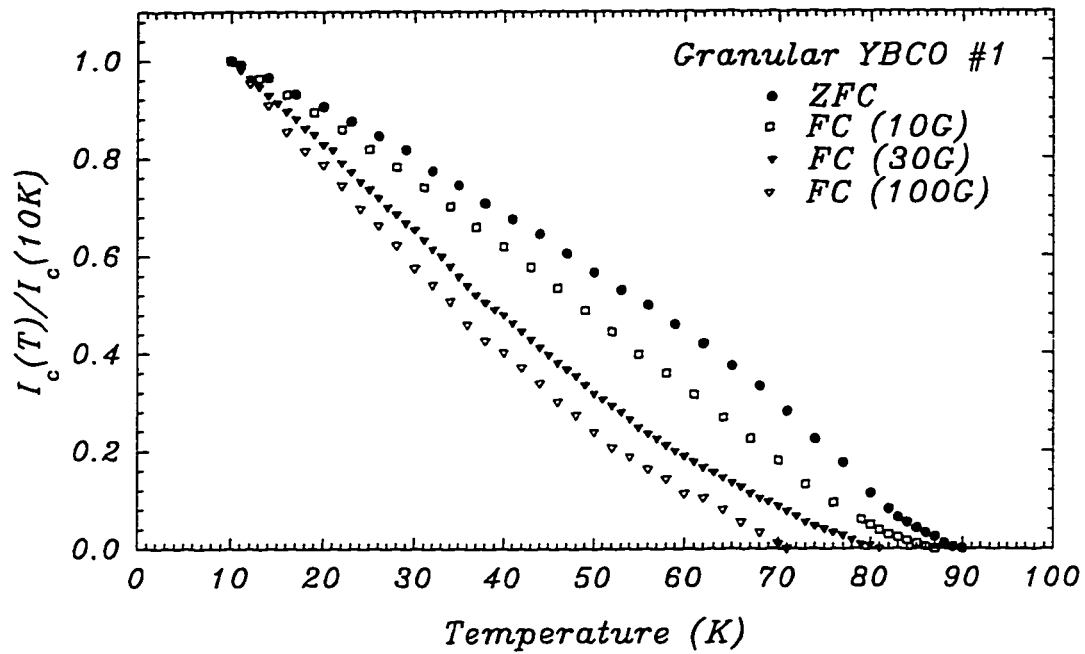


Figure 3.1.4: Temperature dependence of the intergranular critical current measured in a granular YBCO in magnetic fields up to 100G for depairing critical currents. A gradual transition from an Ambegaokar-Baratoff-like to a Ginzburg-Landau-like behaviour can be seen.

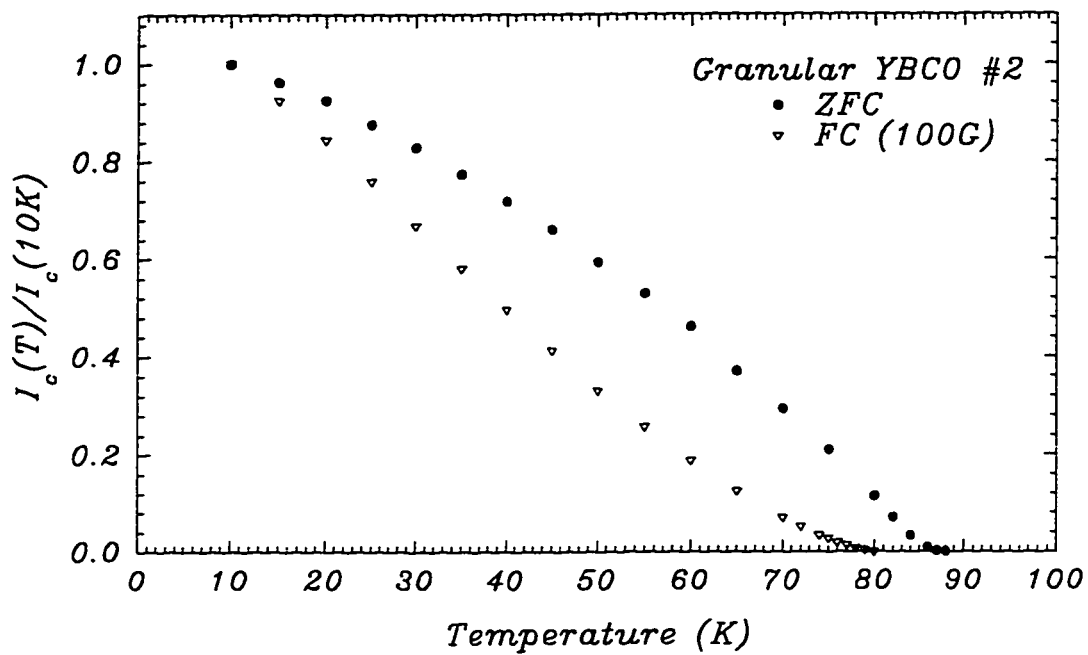


Figure 3.1.5: Temperature dependence of the intergrain critical current measured in a granular YBCO in magnetic fields up to 100G for depinning critical currents. A gradual transition from an Ambegaokar-Baratoff-like to a Ginzburg-Landau-like behaviour can be seen.

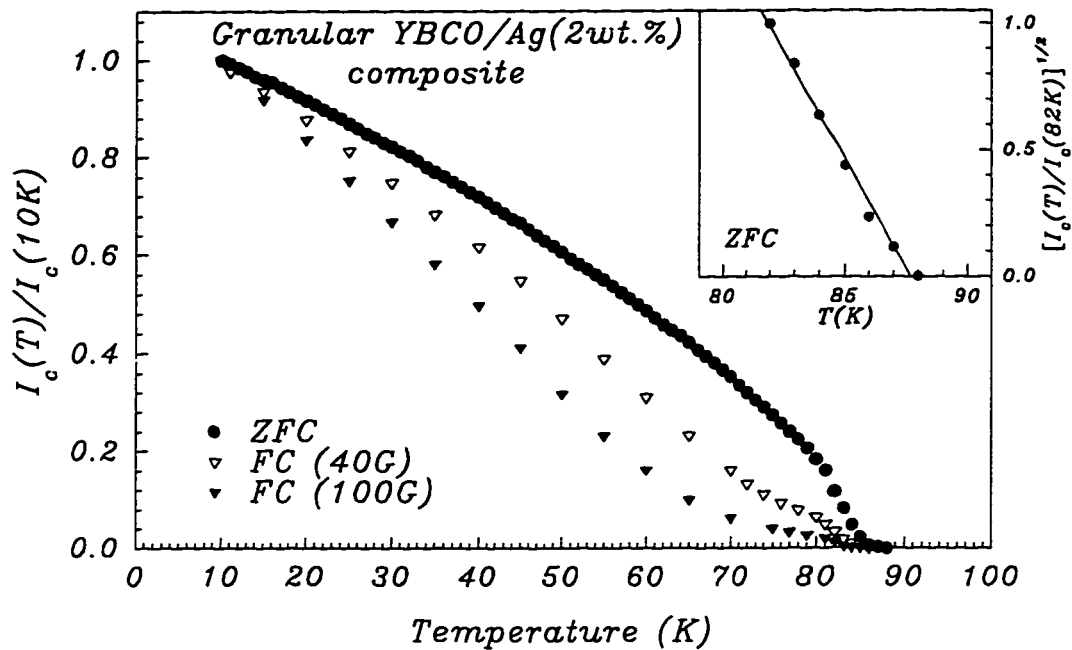


Figure 3.1.6: Temperature dependence of the intergrain critical current in a granular YBCO/Ag (2 wt %) composite. In the ZFC case, I_c reveals an Ambegaokar-Baratoff-like behaviour below 80K, and a DeGennes type behaviour above 80K with $I_c \propto (T - T_c)^2$ shown in the inset. An applied magnetic field causes almost complete transformation of $I_c(T)$ into a Ginzburg-Landau-like one.

3.2 Discussion

3.2.1 Crossover effects in the temperature dependence of J_c in YBCO

The experimental results for pure $Y_1Ba_2Cu_3O_{7-\delta}$ show clearly the presence of both an Ambegaokar-Baratoff-like (AB) and a Ginzburg-Landau-like (GL) temperature dependence of the critical current in c-axis oriented thin films and in randomly oriented granular ceramics if plotted as $I_c(T)^{2/3}$ versus temperature, in order to identify a GL-like $(T_c - T)^{3/2}$ portion of $I_c(T)$ [Figures (3.2.2) - (3.2.6)]. The crossover from an AB to a GL temperature dependence of I_c can be induced by either a reduction in T_c [Figure (3.2.2)] or by an increasing external magnetic field [Figures (3.2.5) and (3.2.6)]. These features are independent of the type of the transport critical current (depairing or depinning) and the magnitude of the critical current density (for the depinning critical current), suggesting that the type of a flux pinning defect does not affect the temperature dependence of the critical current. A recent study by Lin et al [74] revealed that the temperature dependence of J_c in YBCO thin films is not affected by the inclusion of an ordered array of columnar defects of the size of $10 - 20nm$. These pinning centers cause a 70 % enhancement of J_c at $77 K$ in the presence of a magnetic field.

A shift of the $AB \rightarrow GL$ crossover temperature down to lower temperatures with a decreasing T_c [Figures (3.1.1) and (3.2.2)] implies its dependence on oxygen deficiency δ . According to Jorgensen et al [75], $Y_1Ba_2Cu_3O_{7-\delta}$ of $T_c \simeq 80K$ is characterized by oxygen deficiency of $\delta = 0.20 - 0.25$. This means that for $\delta \geq 0.20 - 0.25$, the temperature dependence of I_c is mostly that of a Ginzburg-Landau-like $(T-T_c)^{3/2}$. Additional support of this statement is provided by the data of Jones *et al* [23] who studied the effect of oxygen deficiency on the transport properties of c-axis oriented

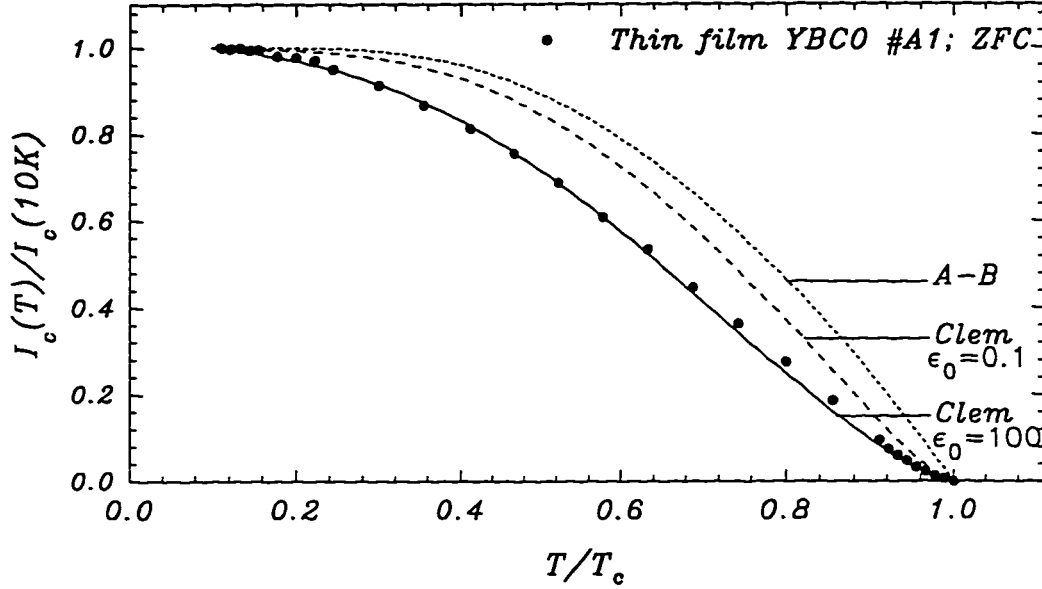


Figure 3.2.1: Comparison of the experimental data for I_c in a c-axis oriented YBCO thin film # A1 of $T_c = 90K$ (solid symbols) with the calculated ones from the Ambegaokar-Baratoff theory for Josephson tunnel junctions [14], represented by the curve A-B, and from the Clem's model [5] of an Ambegaokar-Baratoff to a Ginzburg-Landau crossover effects in granular weakly-coupled ($\epsilon_0 = 0.1$) and strongly-coupled ($\epsilon_0 = 100$) superconductors. The best fit to the experimental data was obtained for the case of $I_c(T)$ in strongly-coupled granular superconductors (Clem, $\epsilon_0 = 100$) with a temperature of the crossover from an Ambegaokar-Baratoff behaviour at low temperatures to a Ginzburg-Landau behaviour at high temperatures at 80 – 82K.

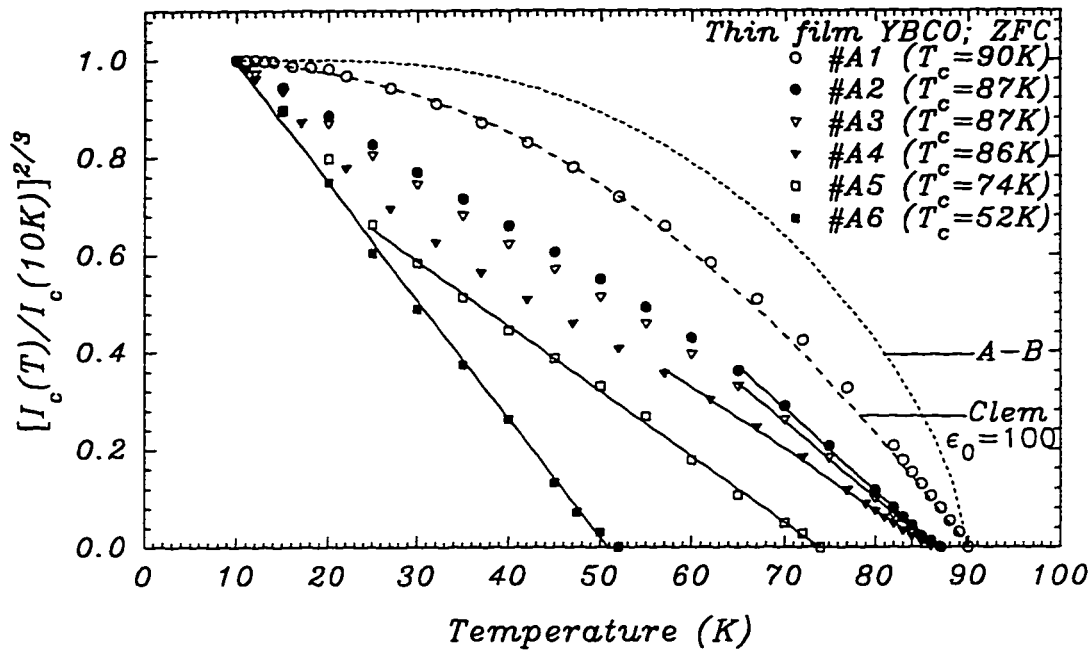


Figure 3.2.2: Temperature dependence of the critical current in c-axis oriented YBCO thin films plotted for the results shown in Figure (3.1.1) as $[I_c(T)/I_c(10K)]^{2/3}$ versus temperature. This allowed us to identify the Ginzburg-Landau portions of $I_c(T)$ (solid lines). All the experimental results are enclosed by two curves: by the Ambegaokar-Baratoff (A-B) $I_c(T)$ or by the Clem's ($AB \rightarrow GL$ with $\epsilon_0 = 100$) form of $I_c(T)$ on the high T_c side, and by the Ginzburg-Landau $(T - T_c)^{3/2}$ form of $I_c(T)$ on the low T_c side. A gradual expansion of the Ginzburg-Landau $(T - T_c)^{3/2}$ tail to low temperatures can be seen upon reduction of T_c .

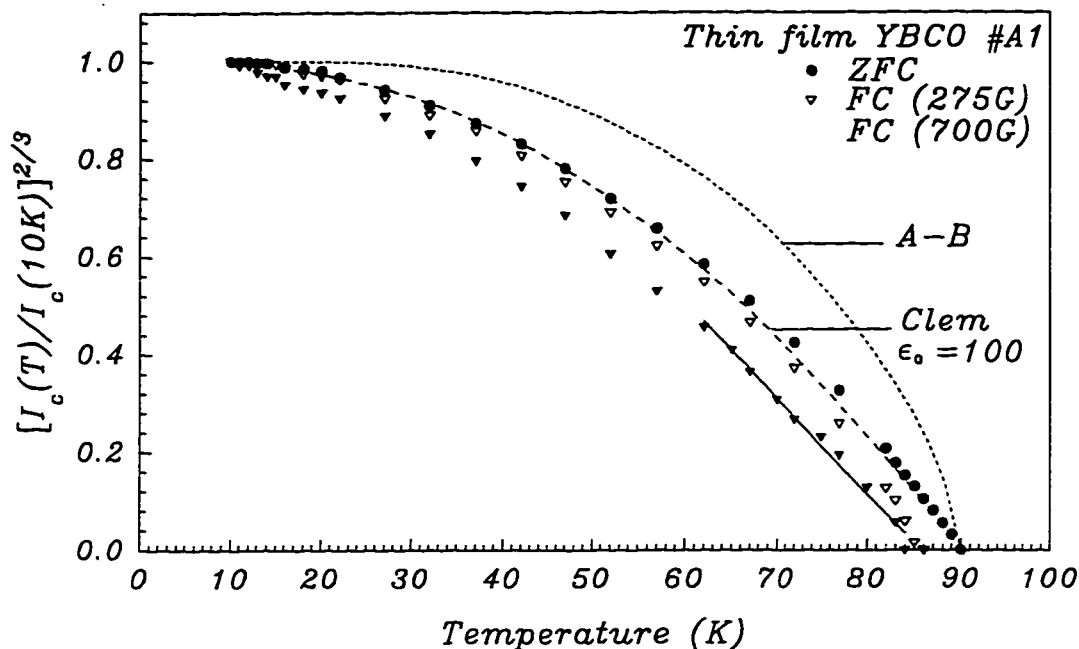


Figure 3.2.3: Dependence of $[I_c(T)/I_c(10K)]^{2/3}$ on temperature plotted for the experimental results obtained for YBCO thin film #A1 in a magnetic field of 275G and 700G (Figure (3.1.2)). The magnetic field-induced expansion of the Ginzburg-Landau portion of $I_c(T)$ present in the zero-field-cooled film can be seen. For the ZFC case, $I_c(T)$ is reproduced by the Clem's model with $\epsilon_0 = 100$. Note that discrepancy between the experimental data and the Ginzburg-Landau solid lines very close to T_c is caused by the experimental difficulty in measuring the self-fields of very small persistent currents in the presence of much larger external magnetic fields.

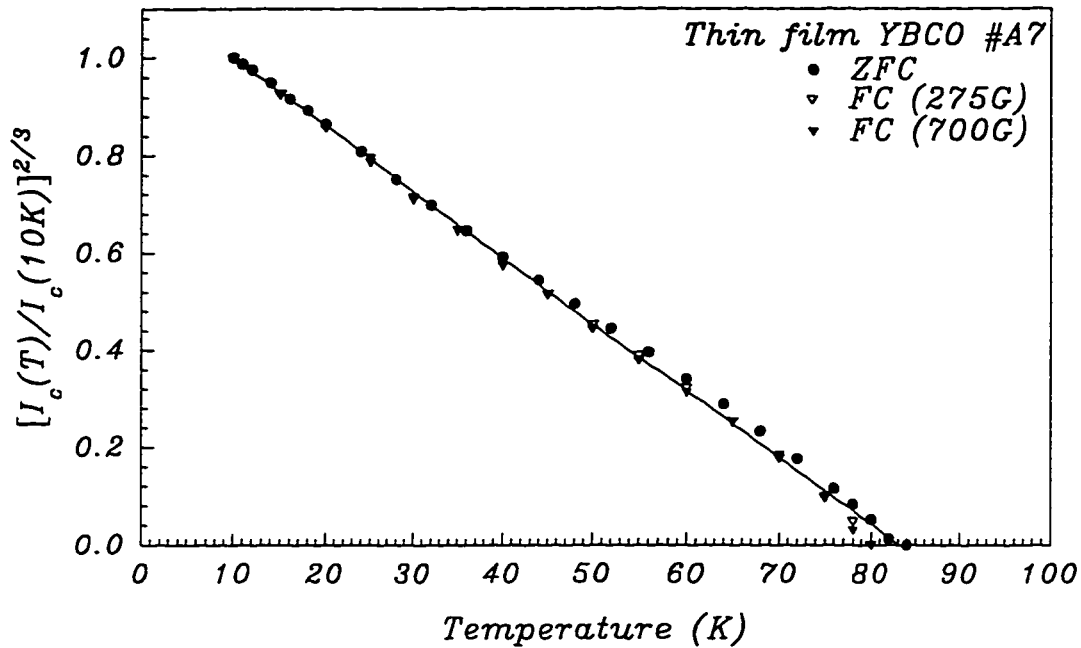


Figure 3.2.4: Dependence of $[I_c(T)/I_c(10K)]^{2/3}$ on temperature plotted for the experimental results obtained for YBCO thin film #A7 in a magnetic field of 275G and 700G [Figure (3.1.3)]. Magnetic field does not affect the Ginzburg-Landau temperature dependence of $I_c(T)$ measured in the zero-field-cooled thin film. Note that discrepancy between the experimental data and the Ginzburg-Landau solid lines very close to T_c is caused by the experimental difficulty in measuring the self-fields of very small persistent currents in the presence of much larger external magnetic fields.

YBCO thin films. The temperature dependence of I_c in their best film (with $\delta = 0.1$) is a quasi-linear at low temperatures and a concave close to T_c [Figure (3a) in Ref. [23]]. This temperature dependence corresponds to an intermediate stage [Figure (3.1.1)] of the transition from an AB to a GL type behaviour of $I_c(T)$. Oxygen was removed from YBCO by sequential isobaric anneals at 550°C under reduced partial pressure of O_2 . A change of δ from 0.1 to 0.2 leads to a Ginzburg-Landau-like temperature dependence of I_c . Our analysis of their data at $\delta = 0.2$ revealed that I_c is proportional to $(T - T_c)^\alpha$ with $\alpha = 1.4 - 1.5$.

Oxygen deficient thin films are characterized by a GL-like dependence, and thin films close to the optimum doping exhibit an AB-like $I_c(T)$. Therefore, the presence of the superposition of both a GL-like and an AB-like behaviour in $I_c(T)$ indicates that YBCO film could be modeled as a stack of two films of low and high oxygen deficiency (see Chapter 4, Figure (4.2.5)).

A decrease in the $AB \rightarrow GL$ crossover temperature can also be stimulated by applying an external magnetic field. However, a magnetic field of 700G , which we used in the experiments on thin films [Figure (3.1.2)], did not produce a complete transformation of $I_c(T)$ from an Ambegaokar-Baratoff to a Ginzburg-Landau behaviour. We have to refer, therefore, to an early work of Mannhart *et al* [19] on c-axis oriented thin films. The measurement of magnetic field dependence of $I_c(T)$ was performed on a thin film for which the zero field $I_c(T)$ exhibits a quasi-linear behaviour at low temperature and a pronounced concave tail close to T_c (Figure (3) in Ref. [19]). A magnetic field of the order of $0.5 - 1.1\text{T}$ transforms their temperature dependence into a Ginzburg-Landau-like $I_c(T)$. Our calculations based on their data revealed that $I_c = (T - T_c)^\alpha$ with $\alpha = 1.5 \pm 0.1$. When temperature dependence of the critical current at zero magnetic field is already that of a Ginzburg-Landau-like type, an external magnetic field does not change it. This can be seen in Figures (3.1.3) and (3.2.4) for magnetic fields up to 700G and in Figure (6) of Ref. [25] for magnetic

fields up to $12T$. In both cases the direction of magnetic field was perpendicular to the surface of c-axis oriented thin films.

A magnetic field as low as $30G$ is able to convert an Ambegaokar-Baratoff temperature dependence of the intergrain (weak-link) critical current to a Ginzburg-Landau-like one. The results of systematic measurements of the $AB \rightarrow GL$ crossover in YBCO granular superconductors, presented in Figures (3.1.4), (3.1.5), (3.2.5) and (3.2.6), are identical to those obtained on c-axis oriented thin films. This implies that the $AB \rightarrow GL$ crossover effects are a characteristic property of $Y_1Ba_2Cu_3O_{7-\delta}$ superconductor.

3.2.2 Origin of the $AB \rightarrow GL$ crossover in the temperature dependence of J_c in YBCO

An essential question that has to be answered here is what is the physical reason for the observed $AB \rightarrow GL$ crossover in the temperature dependence of the critical current. Clem *et al* [5] stated that the Ambegaokar-Baratoff to Ginzburg-Landau crossover effects can be observed in conventional granular superconductors. The crossover from an Ambegaokar-Baratoff to a Ginzburg-Landau form of $I_c(T)$ occurs when the Josephson-coupling energy of an intergrain junction is approximately equal to the superconducting condensation energy of a grain. For YBCO thin film and granular samples a gradual expansion of the Ginzburg-Landau tail $(T - T_c)^{3/2}$ in $I_c(T)$ to low temperatures is observed upon a reduction of T_c or in an increasing applied magnetic field [Figures (3.2.2), (3.2.5) and (3.2.6)]. An Ambegaokar-Baratoff-like dependence of $I_c(T)$ seems to be a characteristic property of YBCO samples of T_c above approximately $88K$ and in the absence of an external magnetic field. The results presented in Figures (3.2.2), (3.2.5) and (3.2.6) imply, therefore, the $AB \rightarrow GL$ crossover

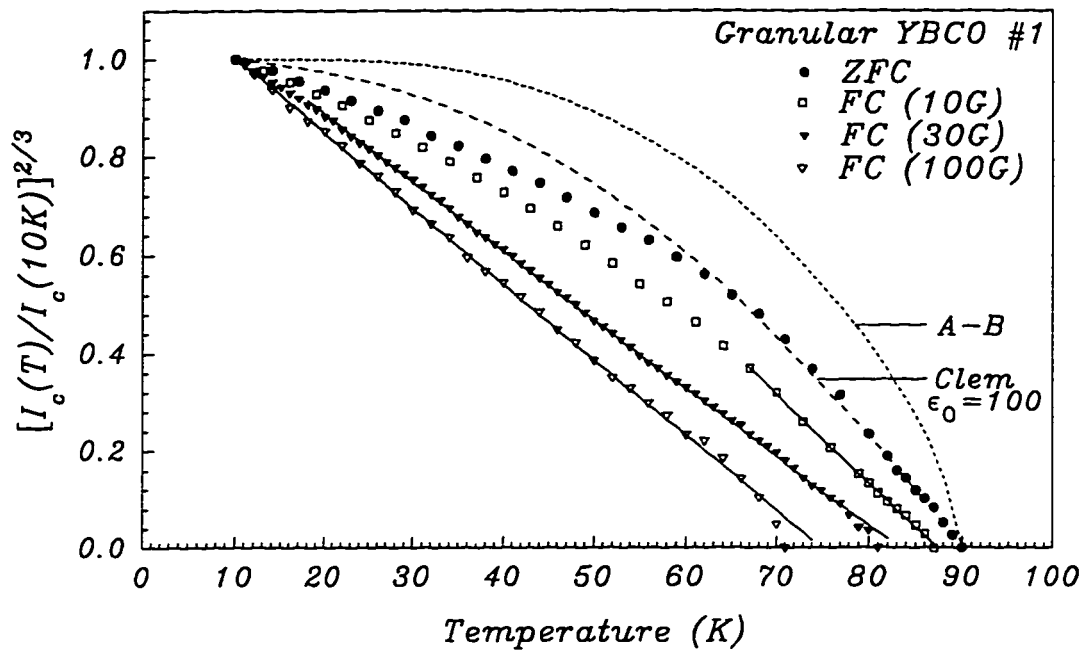


Figure 3.2.5: $[I_c(T)/I_c(10K)]^{2/3}$ versus temperature plotted for the case of depairing $I_c(T)$ measured in a granular YBCO #1 [Figure (3.1.4)]. A transition from an Ambegaokar-Baratoff form of $I_c(T)$ (dotted and dashed lines) to a Ginzburg-Landau one (solid lines) is observed upon application of an increasing external magnetic field. Note that deviation of the experimental points from the solid lines very close to T_c is a result of experimental difficulties of measuring small persistent current's self-fields in the presence of much larger external magnetic fields.

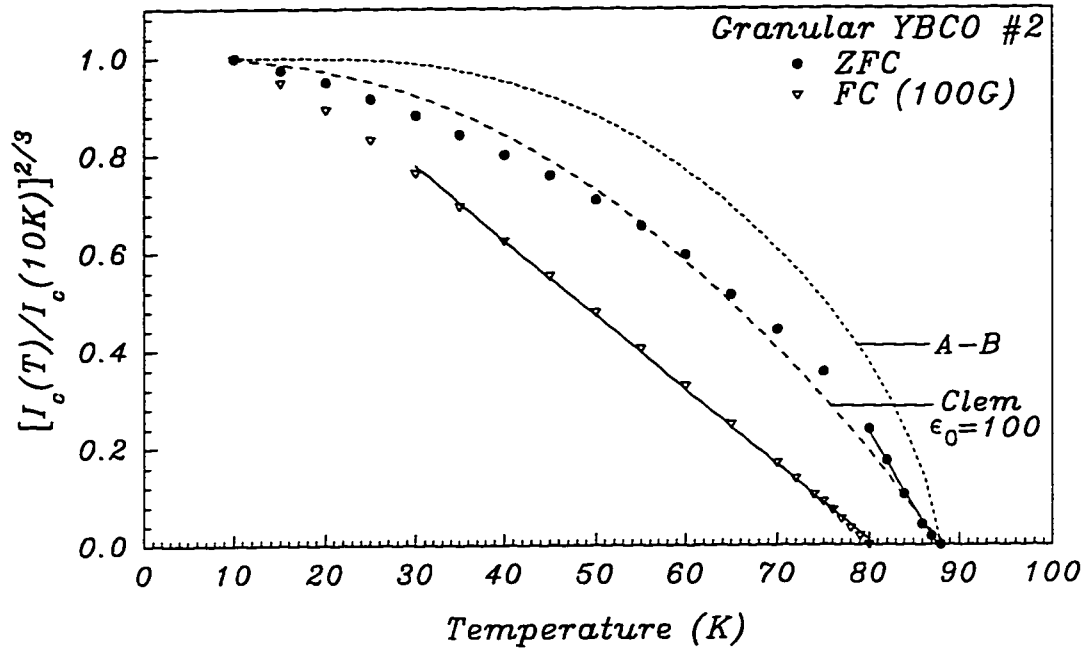


Figure 3.2.6: $[I_c(T)/I_c(10K)]^{2/3}$ versus temperature plotted for the case of depinning $I_c(T)$ measured in a granular YBCO #2 [(Figure (3.1.5))]. A transition from an Ambegaokar-Baratoff form of $I_c(T)$ (dotted and dashed lines) to a Ginzburg-Landau one (solid lines) is observed upon application of an increasing external magnetic field. Note that deviation of the experimental points from the solid lines very close to T_c is a result of experimental difficulties of measuring small persistent current's self-fields in the presence of much larger external magnetic fields.

in $I_c(T)$ of YBCO and a continuous decrease of the crossover temperature if an oxygen deficiency δ or an applied magnetic field are increased. According to Clem *et al* [5] at the $AB \rightarrow GL$ crossover temperature in $I_c(T)$ of granular superconductors, the Ginzburg-Landau coherence length is of the order of the grain size. The observation of the $AB \rightarrow GL$ crossover effects in YBCO in combination with the short coherence length in this compound indicate therefore the presence of granularity (superconducting microdomains coupled by Josephson tunnel junctions) on the level of a few nanometers. In thin films of highest $T_c = 90 - 91K$, the $AB \rightarrow GL$ crossover temperature is around $80 - 82K$. This means that the size of superconducting domains that exist in these films is equal to a coherence length at $80 - 82K$. Temperature dependence of upper critical field H_{c2} in YBCO thin films in magnetic fields (up to 500 Tesla), was recently measured by Goettee *et al* [76]. These results allowed us to make rough estimation of the coherence length ξ_{ab} at various temperatures using the relationship $H_{c2}(T) = \Phi/2\pi\xi^2(T)$. ξ_{ab} varies from about 10 \AA for a temperature range $8 - 30K$ up to about 20 \AA at $80K$ and $30 - 40 \text{ \AA}$ at $83 - 84K$. Therefore, the maximum size of superconducting domains in samples with an optimum doping (of $T_c \simeq 91 K$) and at zero magnetic field should vary between 30 and 40 \AA . Oxygen deficiency and an external magnetic field cause a decrease of the size of these domains and subsequent reduction of the $AB \rightarrow GL$ crossover temperature. In general, at low temperatures $I_c(T)$ is governed by the interdomain Josephson tunnel junctions (an Ambegaokar-Baratoff form). At higher temperatures $I_c(T)$ is affected by the ability of the supercurrent to suppress the gap parameter (a Ginzburg-Landau form) when the coherence length is equal or larger than the size of superconducting domains.

Clem *et al* [5] calculated the dimensionless parameter ε_0 which is proportional to the ratio of the Josephson coupling energy of a junction to the superconducting condensation energy of a grain, both energies being evaluated at zero temperature. For a weakly Josephson-coupled regime, $\varepsilon_0 \ll 1$ and the temperature dependence of

the critical current is that of Ambegaokar-Baratoff. For larger ε_0 , approximately over a range 1 - 100, an Ambegaokar-Baratoff temperature dependence holds only at low temperatures, this behaviour giving way to a Ginzburg-Landau $(T-T_c)^{3/2}$ temperature dependence above the crossover temperature. In the strongly Josephson-coupled regime, ε_0 is very large, current-induced gap suppression is dominant at all temperatures, and the critical current does not obey an Ambegaokar-Baratoff behaviour at any temperature. Instead, the temperature dependence is governed by a Ginzburg-Landau-like behaviour at all temperatures. The coupling parameter ε_0 is given by the following formula:

$$\varepsilon_0 = 2.93 \frac{\hbar k_B}{e^2 \gamma T_c \rho_n a_0^2} \quad (3.1)$$

where γ is the Sommerfeld constant, ρ_n is the normal-state tunneling resistivity of a junction and a_0 is the effective grain diameter.

Reported values of γ for YBCO vary between 16 mJ/molK^2 and 35 mJ/molK^2 ($0.16 - 0.35 \text{ mJ/cm}^3\text{K}^2$) [77, 78], . We take the average $\gamma \simeq 0.26 \text{ mJ/cm}^3\text{K}^2$, and $a_0 = 40 \text{ \AA}$ in YBCO of $T_c = 91\text{K}$. In order to calculate ε_0 , ρ_n of an intrinsic Josephson tunnel junction is needed. Such information was provided by current-voltage characteristics at 72 K of a $1\mu\text{m}$ -wide Dayem microbridge patterned in a YBCO thin film (Ref. [22]). The microbridge was twin-boundary free and had Josephson-like properties. A normal resistivity of the bridge was approximately $0.5 \mu\Omega\text{cm}$. We obtain $\varepsilon_0 = 92$ for YBCO with $T_c = 91\text{K}$. For oxygen deficient YBCO with $\delta = 0.20 - 0.25$, and $T_c \simeq 80 \text{ K}$, the $AB \rightarrow GL$ crossover temperature drops down to $10 - 20 \text{ K}$ implying that $a_0 \simeq \xi \simeq 10 \text{ \AA}$. In this case YBCO is in very strong coupling regime with $\varepsilon_0 \simeq 1650$. The calculations of $J_c(T)$ for various coupling strengths, performed by Clem *et al* [5] indicate the absence of a low temperature plateau in the Ambegaokar-Baratoff's part of $J_c(T)$ for $\varepsilon_0 \geq 1$. This is clearly seen in the temperature dependence of the critical current in the best YBCO samples.

3.2.3 Comparison between the intergrain and the intragrain $J_c(T)$ in YBCO

The same temperature dependence of the critical current in thin film and granular YBCO [Figures (3.1.1) , (3.1.4) and (3.1.5)] implies that intergranular transport in ceramics is limited by microbridges whose internal structure is similar to that of the grain itself, i.e. consisting of superconducting domains separated by Josephson tunnel junctions. If the size of these domains is less than the coherence length, the supercurrent will not “see” the junctions and the temperature dependence of the intergrain critical current changes from an Ambegaokar-Baratoff-like type to a Ginzburg-Landau-like one.

We performed additional verification of this process by introducing different kinds of Josephson junctions into the microbridges. Temperature dependence of the intergrain critical current of a zero-field-cooled YBCO/Ag (2 wt.%) ceramic composite [Figure (3.1.6)] indicates that the intergrain current is controlled by Josephson SIS tunnel junctions [which is expressed by an Ambegaokar-Baratoff form of $I_c(T)$] up to 80K and by Josephson SNS proximity junctions (with $I_c(T) = (T - T_c)^2$) above 80K. This could happen if oxygen depleted superconducting layers (of $T_c \simeq 80K$) cross the microbridges. An increasing applied magnetic field seems to introduce disorder (reduce the size of superconducting domains) in the same manner as an increasing oxygen deficiency does. Figure (3.1.6) shows that an almost complete transformation of the intergrain $I_c(T)$ into a Ginzburg-Landau-like form occurs in a magnetic field of 100G. This suggests that in the case of superconducting domains coupled by SNS proximity junctions, the crossover from a DeGennes-like $(T - T_c)^2$ temperature dependence of $I_c(T)$ to a Ginzburg-Landau-like one may also be observed. A microbridge-type model was proposed very early by Larbalestier *et al* [79] in order to explain the field

independent residual intergrain critical current in granular high temperature superconductors. Halbritter [80] stated that these conclusions may be valid not only for the intergrain weak links but also for the intragrain ones which are formed by twin boundaries. Moeckly *et al* [10] suggested that rf Josephson data and non-ideal I-V characteristics of most tilt boundary weak links favor microbridge limited transport.

3.2.4 Microgranularity in YBCO

As mentioned earlier in Chapter 1, the presence of intragrain granularity in single crystals of YBCO has been suggested by Daeumling *et al* [8] and Osofsky *et al* [9]. The granular behavior was attributed to clusters of oxygen defects, causing a separation of regions of oxygen-rich material by boundaries of oxygen-poor material. Some evidence of ordered superstructures and phase separation in $Y_1Ba_2Cu_3O_{7-\delta}$ on a few nanometer scale has been provided by electron- and neutron-diffraction studies. Phase separation is more evident for oxygen deficient samples with $\delta \leq 0.3$ (Ref. [11, 81, 82, 83]), however, studies of Beyers *et al* [81] have indicated that $90\text{ K} - T_c(\delta)$ plateau may correspond to a two-phase region. Recent scanning tunnelling spectroscopy measurements of YBCO single crystals [84], which show spatially varying energy gap over a few nanometer distances, may also indicate the presence of microdomains in YBCO. The very recent high resolution electron microscopy investigations at 300 K by Etheridge at Cambridge University [43] of $Y_1Ba_2Cu_3O_{7-\delta}$ ($\delta < 0.1$) revealed the presence of the electron diffraction patterns due to the cells of size approximately $10\text{-}20\text{ \AA}$ in the a-b planes, in addition to those due to the twin boundaries with spacing about $500\text{-}1000\text{ \AA}$. The cells form an irregular network with walls aligned about 45° to the $\langle 100 \rangle$ and $\langle 010 \rangle$ axes (a-b axes), and arise from a local perturbation of the charge density distribution. This is an apparently universal feature, present in YBCO samples prepared in different ways and imaged in different microscopes. It

was suggested that YBCO ($\delta < 0.1$) “buckles” into a network of slightly misaligned cells in a struggle to relieve internal stresses.

Interpreting critical current $I_c(T)$ data for YBCO thin film and granular samples requires discussion of the microscopic mechanism by which the microdomain size is being reduced. Both an oxygen depletion or an external magnetic field penetrating through insulating layers can suppress superconductivity through pair-breaking interaction. Oxygen deficiency leads to appearance of Cu^{2+} magnetic moments on CuO_2 planes [85] and CuO chains [86], as shown by nuclear-spin relaxation data. Pair breaking in conventional superconductors caused by magnetic impurities and an external magnetic field has been analyzed by Maki [87] and Skalski *et al* [88]. These external perturbations break the time-reversal symmetry of the electron system and lead to gapless superconductivity. The gapless situation can also be induced by different mechanism; the spatial variation of the order parameter. In the Kresin’s model [89] of gaplessness in high temperature superconductors, YBCO contains two subsystems, i.e. CuO_2 planes and CuO chains. The planes are intrinsically superconducting, whereas the superconducting state in the chains is induced by charge transfer via an intrinsic proximity effect. Magnetic impurities (Cu^{2+} magnetic moments) act like pairbreakers and suppress the induced gap on the chains so that at oxygen content around 6.9 YBCO is already gapless. The gaplessness can be extended without a noticeable shift in T_c . We believe that the oxygen vacancies and the associated Cu^{2+} magnetic moments produce spatial inhomogeneities (domains on the scale of a lattice parameter) already in YBCO of oxygen content of 6.95. These inhomogeneities would be similar to those suggested by J. C. Phillips [90] and N. E. Phillips *et al* [77]. An external magnetic field penetrates the inhomogeneities and reduce the size of superconducting domains through pair breaking interaction.

Chapter 4

Dissipation of the persistent current and flux pinning in YBCO thin films

4.1 Experimental Results

We measured the relaxation of the persistent current from the critical level in nine YBCO thin films of different T_c , J_c and thickness. The films were grown using various deposition methods on LaAlO_3 and SrTiO_3 substrates [Table (4.1)]. The measurements were made on zero-field-cooled ring-shaped films over a temperature range of $10 - 85\text{K}$. The relaxation data were used to calculate the dependence of the energy barrier for vortex motion on the current density, $U_{\text{eff}}(J)$. Comparison of the $U_{\text{eff}}(J)$ data with those for $J_c(T)$ was made. In the section below, we verified that the persistent current distribution in a thin film ring is independent of the relaxation processes.

4.1.1 Effect of relaxation on the distribution of the persistent current in ring-shaped YBCO thin films

Figure 4.1.1 presents the distributions of the axial and radial components of the persistent current's self-field measured 30s and 10,000s after the critical state was established in a zero-field-cooled ring. The self-field (trapped field), normalized to its value at the ring's center [Figure (4.1.2)], reveals that the relaxation processes

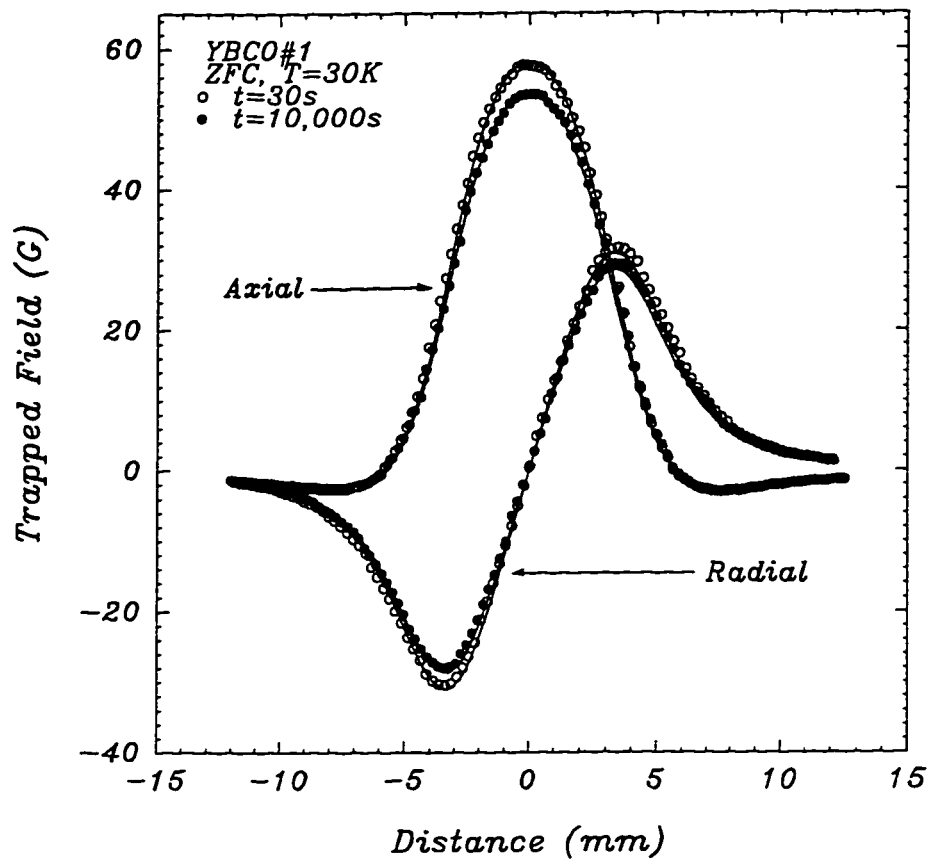


Figure 4.1.1: The profiles of the axial and radial trapped fields $B_z(r)$ and $B_r(r)$ measured across the ring of YBCO film #1 at a distance of $3mm$ above it, after waiting $30s$ (open circles) and $10,000s$ (full circles). The profiles represent the axial and radial components of the persistent current's self-field. Distances $r = \pm 2.5mm$ and $r = \pm 4.25mm$ mark the inner and the outer edges of the ring. The sample was zero-field-cooled down to $30K$, before an external field of $700G$ was applied and subsequently reduced to zero in order to generate the persistent current at the critical level. The solid lines represent the computer simulations (see text) of the axial and radial profiles using the Biot-Savart law and the current distribution shown in Figure 4.1.3.

Table 4.1: Superconducting transition temperature T_c at zero resistance, film thickness, critical current density J_c at 10K and 77K, deposition method and substrates used, are listed for all YBCO thin films that were investigated in the course of this work. Note that J_c^a denotes an “apparent” critical current density which is defined as the ratio of the critical current I_c to the cross-sectional area A of the sample. The actual J_c may be higher if the current flow occurs through a reduced cross-sectional area A.

Film #	T_c (K)	Thickness (nm)	$J_c^a(10K)$ (A/cm^2)	$J_c^a(77K)$ (A/cm^2)	Deposition Method	Substrate
1	90	500	1.1×10^7	1.5×10^6	dc-MAGNETRON	LaAlO ₃
2	90	130	1.8×10^7	1.2×10^6	rf-MAGNETRON	LaAlO ₃
3	90	200	6.4×10^6	7.1×10^5	LASER-ABLATION	LaAlO ₃
4	91	200	1.8×10^7	1.7×10^6	LASER-ABLATION	LaAlO ₃
5	91	200	1.8×10^7	1.7×10^6	LASER-ABLATION	LaAlO ₃
6	90	100	3.3×10^7	2.3×10^6	LASER-ABLATION	SrTiO ₃
7	87	280	6.5×10^6	2.4×10^5	rf-MAGNETRON	SrTiO ₃
8	87	120	2.3×10^7	7.1×10^5	rf-MAGNETRON	LaAlO ₃
9	81	350	7.9×10^6	8.2×10^4	LASER-ABLATION	LaAlO ₃

do not affect the shape of the profiles. This indicates that the normalized relaxation rate is constant across the ring and the fast decay rates are absent at the ring’s outer edges. Solid lines in Figure (4.1.1) represent the computer simulations of the axial field $B_z(r, z)$ and the radial field $B_r(r, z)$, using the computation methods described in Chapter 2 . The ring was divided into 2,000 concentric ring-segments (of cross-sectional area of $0.5 \times 0.5 \mu m^2$) . The axial and radial fields generated by the current in each ring segment were calculated from the Biot-Savart equation [72] . The total axial and radial field above the sample was obtained by summing up the contributions from the individual current loops. Very good fit to the experimental data was achieved with the uniform distribution of the current across the ring’s width [Figure (4.1.3)], indicating that the relaxation processes affect the magnitude of the current density but not its distribution.

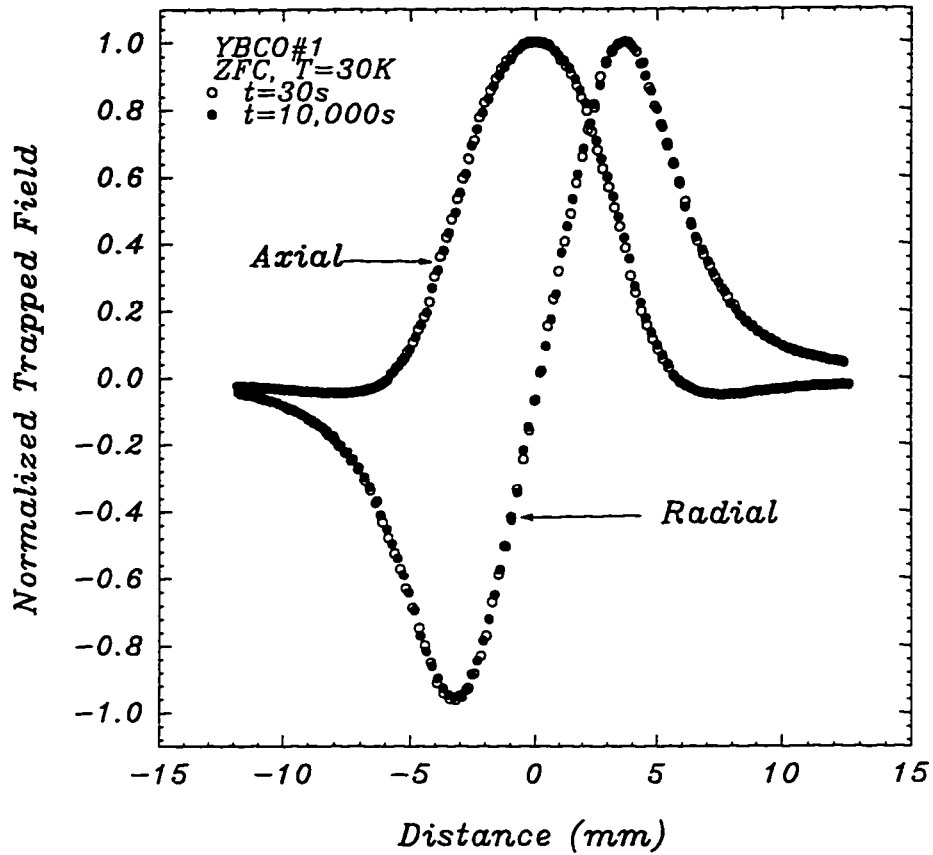


Figure 4.1.2: The profiles of the axial and radial trapped field taken from Figure 4.1.1, which are normalized using the maximum values of the axial and the radial trapped fields. Note that the shape of both profiles does not change during persistent current's decay, suggesting that the normalized decay rate remains constant across the ring.

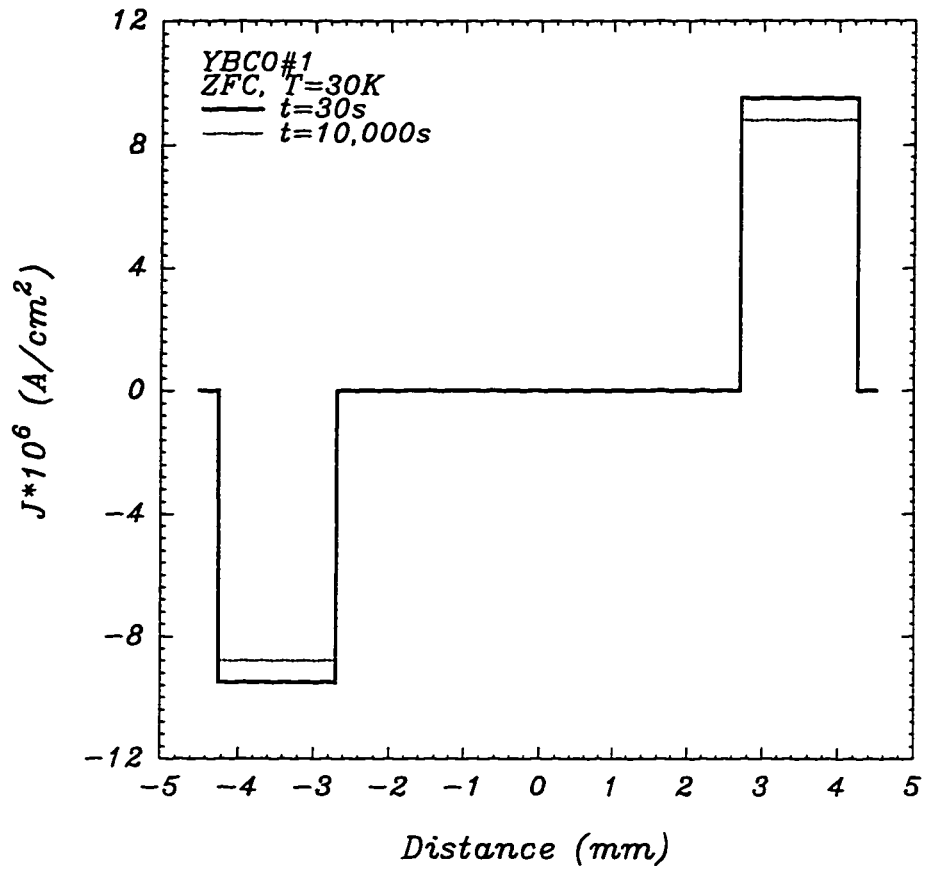


Figure 4.1.3: The distribution of the persistent current density $J(r)$ in the zero-field-cooled ring at 30K after waiting 30 s (solid line) and 10,000 s (dotted line). This distribution was used to perform computer calculations of the profiles of the axial and radial components of the self-field of the persistent current in Figure 4.1.1 .

4.1.2 Relaxation measurements and calculation of $U_{\text{eff}}(J)$ for YBCO thin films

The profiles of the axial component of the self-field of the persistent current circulating in zero-field cooled rings of YBCO thin films, have been measured over a temperature range of 10 - 85 K . Figure (4.1.4) shows typical profiles measured at 20 K for various levels of the persistent current between zero and a critical value . The decays of the persistent current have been recorded over a time range between 1 and 40,000s, and every 5 K over a temperature range 10 - 85 K . Typical plots of the current versus logarithm of time for various currents between zero and I_c at 20 K and 50 K are shown in Figures (4.1.5) and (4.1.6). These plots are similar for all samples and for all temperatures between 10 and 85 K .

For currents close to I_c the initial decays up to approximately 1,000s are not fully logarithmic. After 1,000s the relaxation curves merge and a common “steady-state” logarithmic decay is established. The initial non-logarithmic decay of magnetization in YBCO was reported by Gurevich and Küpfer [92] and interpreted as due to a redistribution of the magnetic flux over the sample volume. Therefore, we have calculated $U_{\text{eff}}(J)$ using the Maley’s method from a “steady-state” logarithmic portion of the relaxation curve for waiting times between 2,000 and 40,000s.

Figure (4.1.7). presents the “Maley’s” segments of U_{eff} as a function of the current calculated from the relaxation data (which were measured every 5 K between 10 K and 85 K) for six different YBCO thin films of $T_c = 90 - 91K$ according to the procedure described in Section 2.2.4.

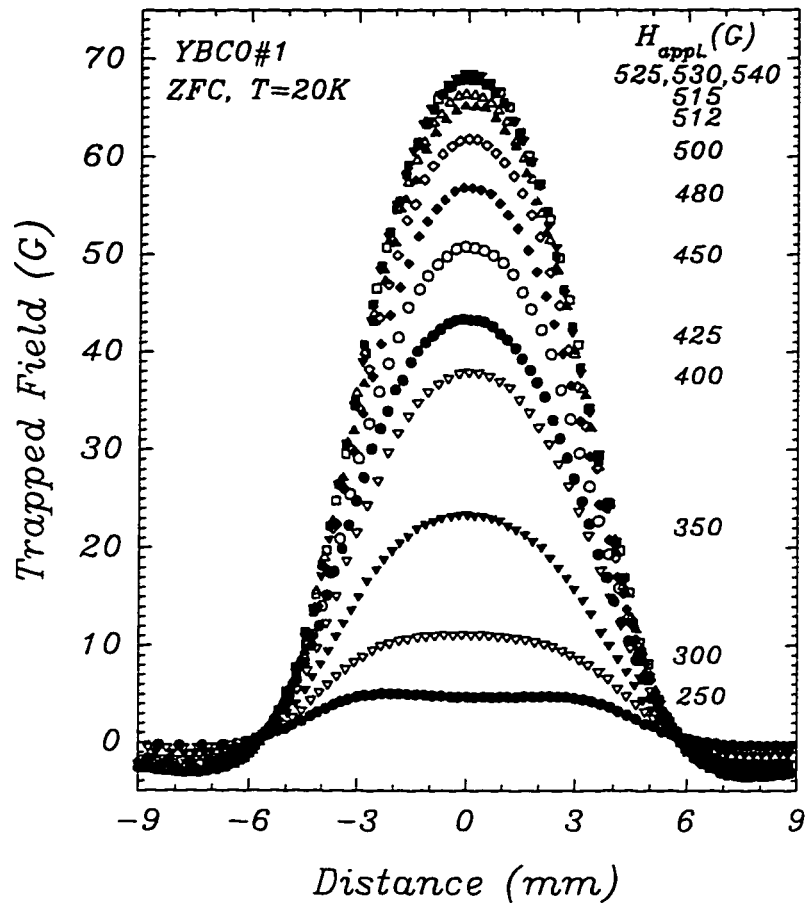


Figure 4.1.4: The profiles of the axial component of the self-field of the persistent currents circulating in a ring of YBCO film #1. Persistent currents, of various levels up to the critical value, were induced in the ring at 20 K after external fields between 250 and 540 G were applied to the zero-field-cooled sample. Distances $\pm 2.5\text{mm}$ and $\pm 4.25\text{mm}$ mark the ring's inner and outer edges. The profiles were measured at a distance of 2.5mm above the ring.

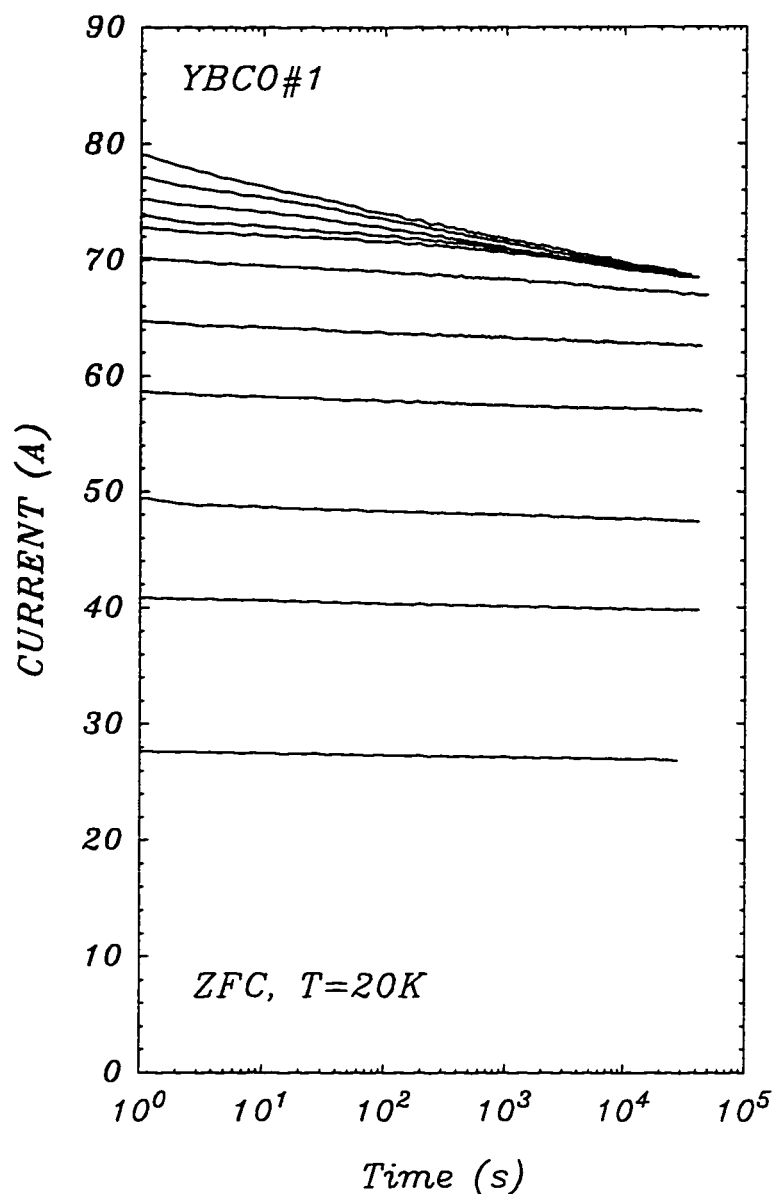


Figure 4.1.5: The dependence of the persistent currents, of various magnitudes up to the critical value, on the logarithm of the waiting time. The decays were measured at a temperature of 20 K in a ring of YBCO film #1. The calculation of the energy barrier was based on the time decay of the persistent current from the highest value over a time interval of 2,000 - 30,000s. Note that the decay curves of the persistent currents close to the critical value merge after waiting approximately 1,000 to 2,000s.

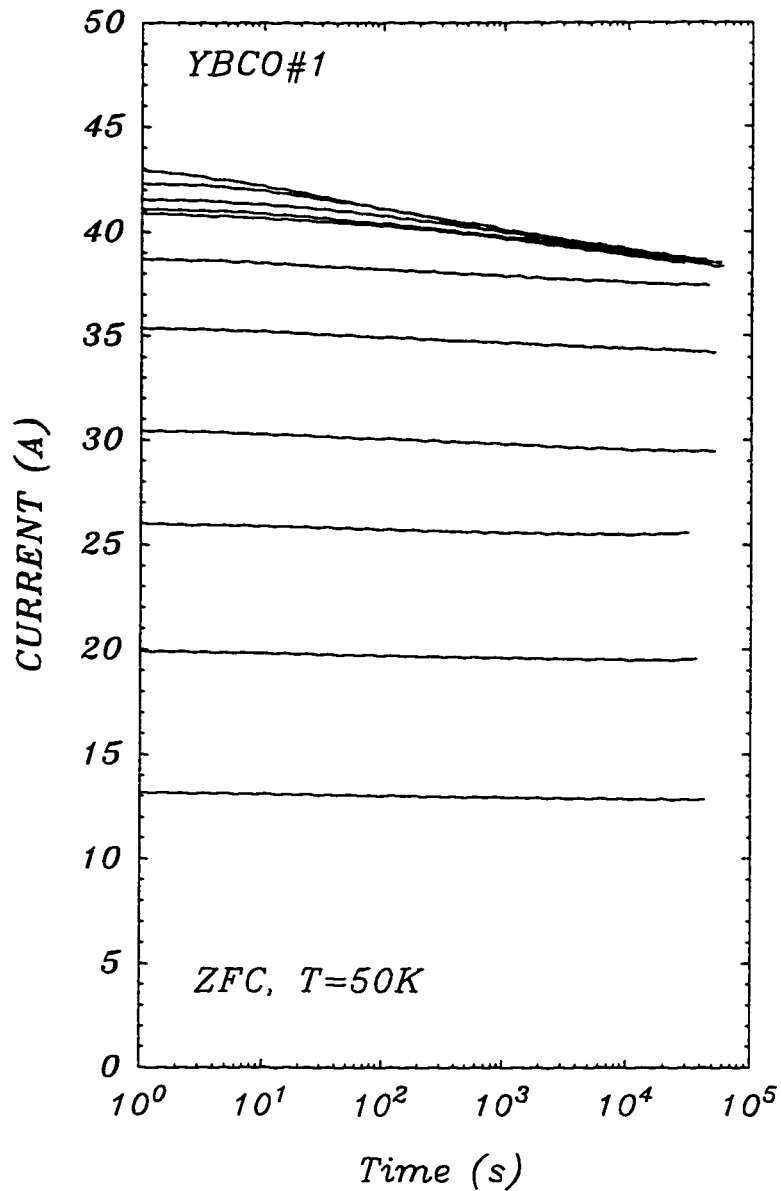


Figure 4.1.6: The dependence of the persistent currents, of various magnitudes up to the critical value, on the logarithm of the waiting time. The decays were measured at a temperature of 50 K in a ring of YBCO film #1. The calculation of the energy barrier was based on the time decay of the persistent current from the highest value over a time interval of 2,000 - 30,000s. Note that the decay curves of the persistent currents close to the critical value merge after waiting approximately 1,000 to 2,000s.

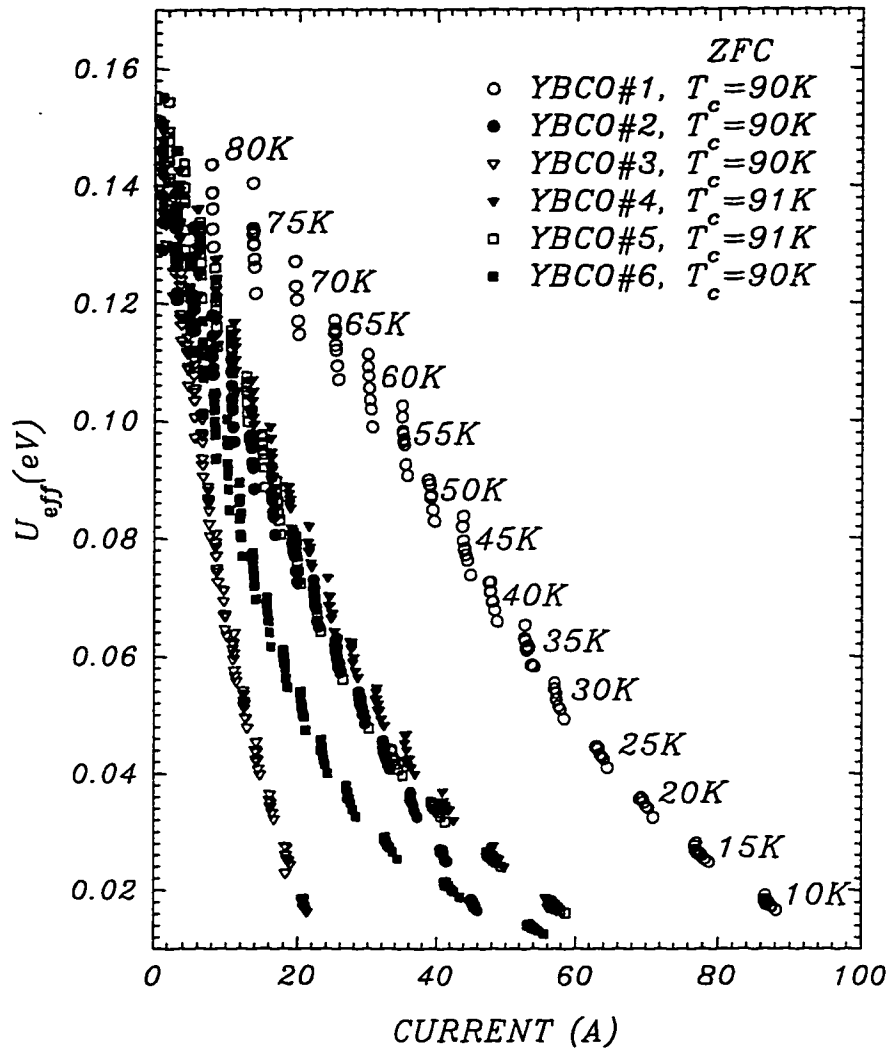


Figure 4.1.7: The dependence of the energy barrier on the magnitude of the persistent current for six YBCO ring-shaped films (from #1 up to #6) calculated from the relaxation data [Figures (4.1.5 and (4.1.6))] using the Maley's procedure. The "Maley's" segments were calculated every 5 K for temperatures between 10 and 85 K.

4.1.3 Relationship between U_{eff} and $J_c(T)$

We have made the comparison of the dependence of U_{eff} on the current with the temperature dependence of the critical current [Figures (4.1.8) - (4.1.10)]. YBCO thin films of $T_c = 90 - 91K$ could be divided into two groups characterized by different $I_c(T)$ curves: the low temperature reduction of I_c normalized to $I_c(10K)$ for YBCO films No.'s 4, 5 and 6 [Figure (4.1.9)] is larger than the corresponding decrease of I_c for YBCO films No.'s 1, 2 and 3 [Figure (4.1.8)]. The temperature dependence of the critical current in YBCO films No.'s 7, 8 and 9 [Figure (4.1.10)], which have a lower T_c equal to $87K$ and $81K$, are essentially similar to those for YBCO with $T_c = 90 - 91K$. The dependence of U_{eff} on the current, seen in Figures (4.1.8), (4.1.9) and (4.1.10), resembles that of the critical current on temperature. One could conclude that $U_{\text{eff}}(J)$ contains the temperature dependence of J_c , which is, in fact, a consequence of the Maley's method adopted in our studies. We assume that $U_{\text{eff}}(J)$ could be, therefore, written in the following form:

$$U_{\text{eff}}(J) = J_c(T).F(J) \quad (4.1)$$

where $F(J)$ is a certain function of the current density. Equation 4.1 is a simplified version of a very general relation for

$$U_{\text{eff}}(J, H, T) = G(T)[J_c(H, T)/J_c(H, 0)]^P f(q, H) \quad (4.2)$$

where $q = J/J_c(H, T)$ and H is the external magnetic field. This relation has been proposed by Schnack *et al* [93] who introduced a general inversion scheme in order to obtain $U_{\text{eff}}(J, H, T)$ from magnetization measurements.

The temperature dependence of J_c is not affected by the decay of the current from the critical level [Figure (4.1.11)]. This means that Equation 4.1 is valid over the whole experimental range of the relaxation times. In order to identify $F(J)$ we plotted $U_{\text{eff}}/I_c(T)$ versus current in Figure (4.1.12) for six YBCO films of $T_c = 90 - 91K$. The

data imply that $F(J)$ could be represented by an exponential or a double-exponential function.

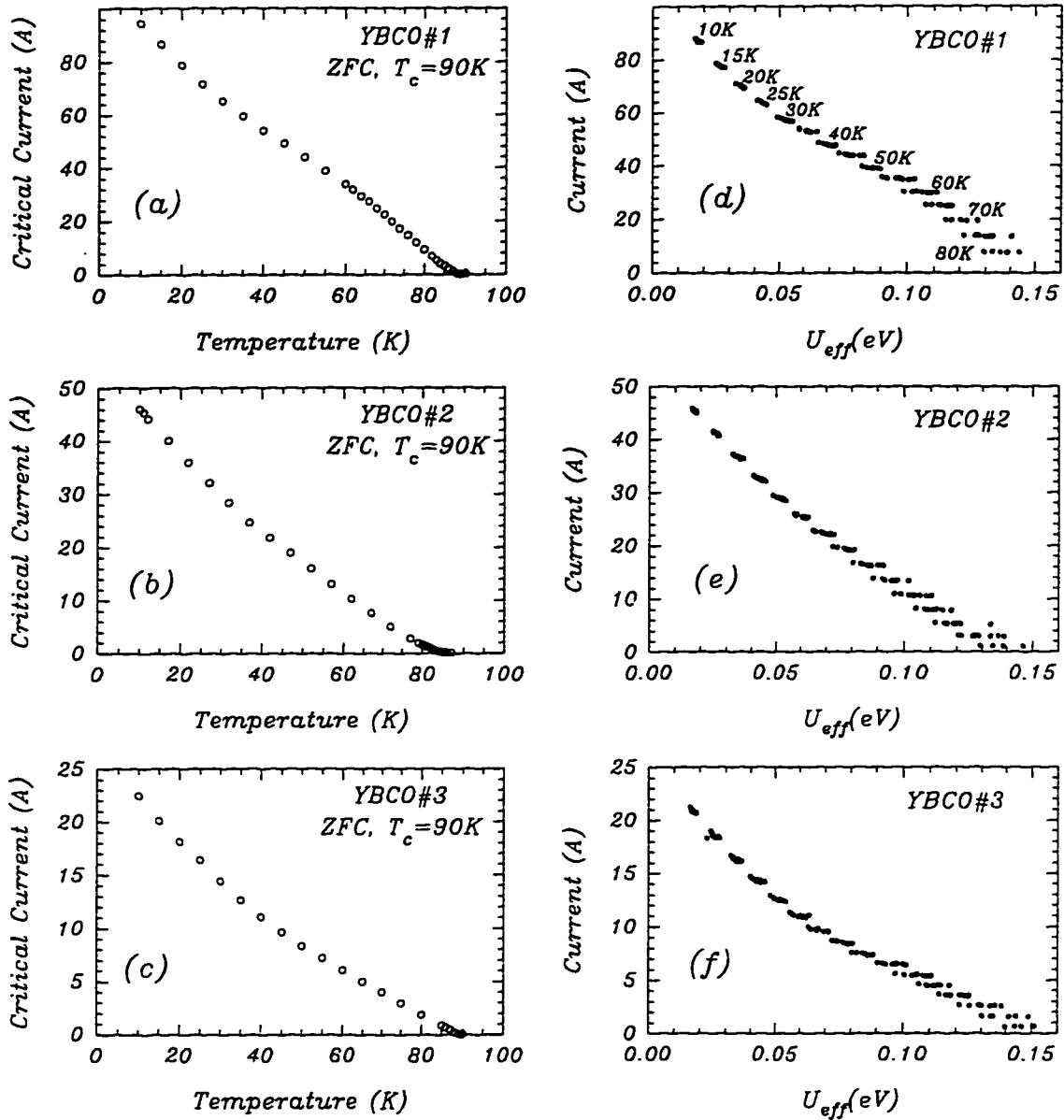


Figure 4.1.8: The comparison of the temperature dependence of the critical current $I_c(T)$ (see Figures on the left) with the dependence of the energy barrier on the current $U_{eff}(I)$ (Figures on the right), measured in YBCO ring-shaped films #1, #2, and #3. Note that the similarities of the shape of $I_c(T)$ to that of $U_{eff}(I)$ imply that the energy barrier is a function of $I_c(T)$.

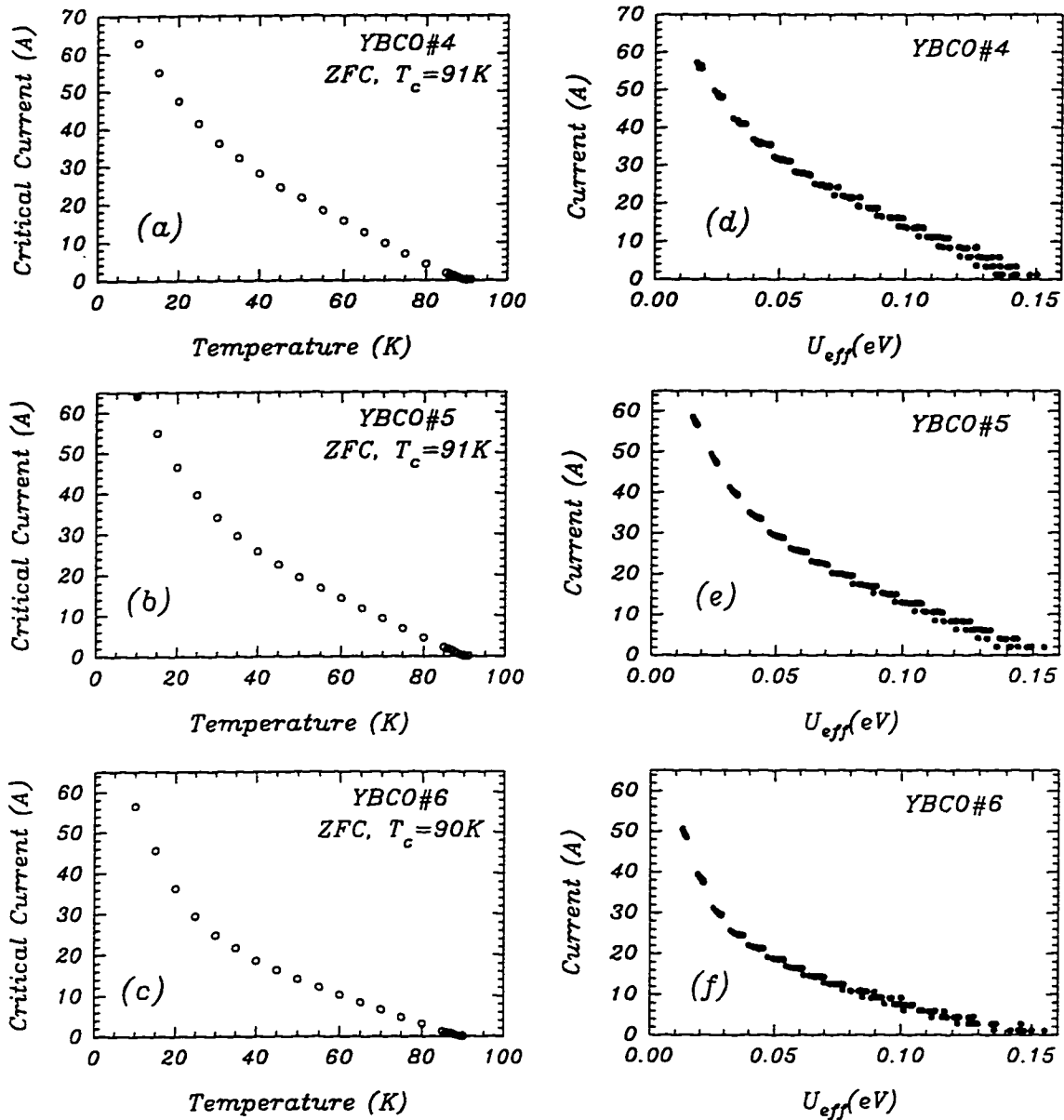


Figure 4.1.9: The comparison of the temperature dependence of the critical current $I_c(T)$ (see Figures on the left) with the dependence of the energy barrier on the current $U_{eff}(I)$ (Figures on the right), measured in YBCO ring-shaped films #4, #5, and #6. These films have different temperature dependence of I_c from that observed in YBCO films #1, #2, and #3 [Figure (4.1.8)], which is characterized by the larger low temperature reduction of $I_c/I_c(10K)$. Note that the similarities of the shape of $I_c(T)$ to that of $U_{eff}(I)$ imply that the calculated energy barrier is a function of $I_c(T)$.

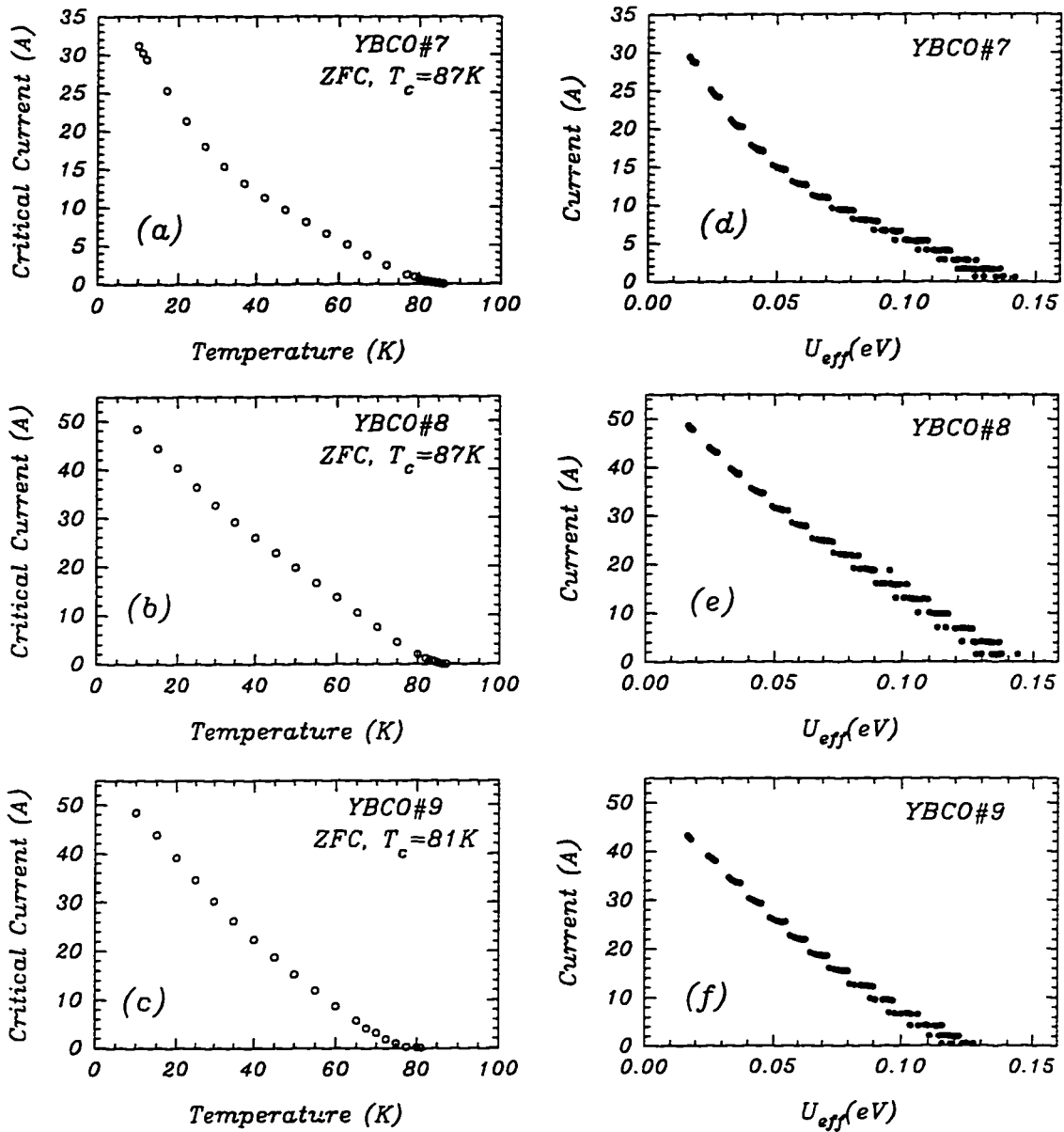


Figure 4.1.10: The comparison of the temperature dependence of the critical current $I_c(T)$ (see Figures on the left) with the dependence of the energy barrier on the current $U_{eff}(I)$ (Figures on the right), measured in YBCO ring-shaped films #7, #8, and #9. These films are characterized by lower T_c than that for YBCO films from #1 to #6 [Figures (4.1.8) and (4.1.9)]. Note that the similarities of the shape of $I_c(T)$ to that of $U_{eff}(I)$ imply that the calculated energy barrier is a function of $I_c(T)$.

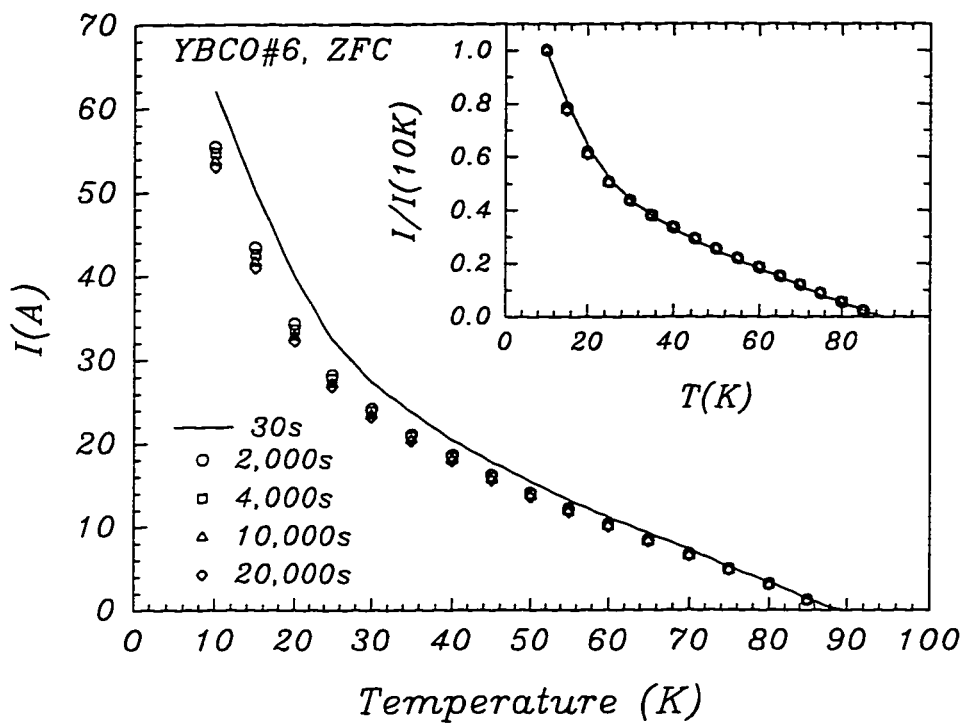


Figure 4.1.11: The dependence of the magnitude of the persistent current I on time, measured in a ring of YBCO film #6 every 5K over a temperature range of 10–85K. The inset shows the same results plotted for the magnitudes of the current $I(t)$ at various times t normalized to the value of $I(t)$ at 10K. All the data lie on the same curve, indicating that the temperature dependence of the critical current is preserved during the decay of the current.

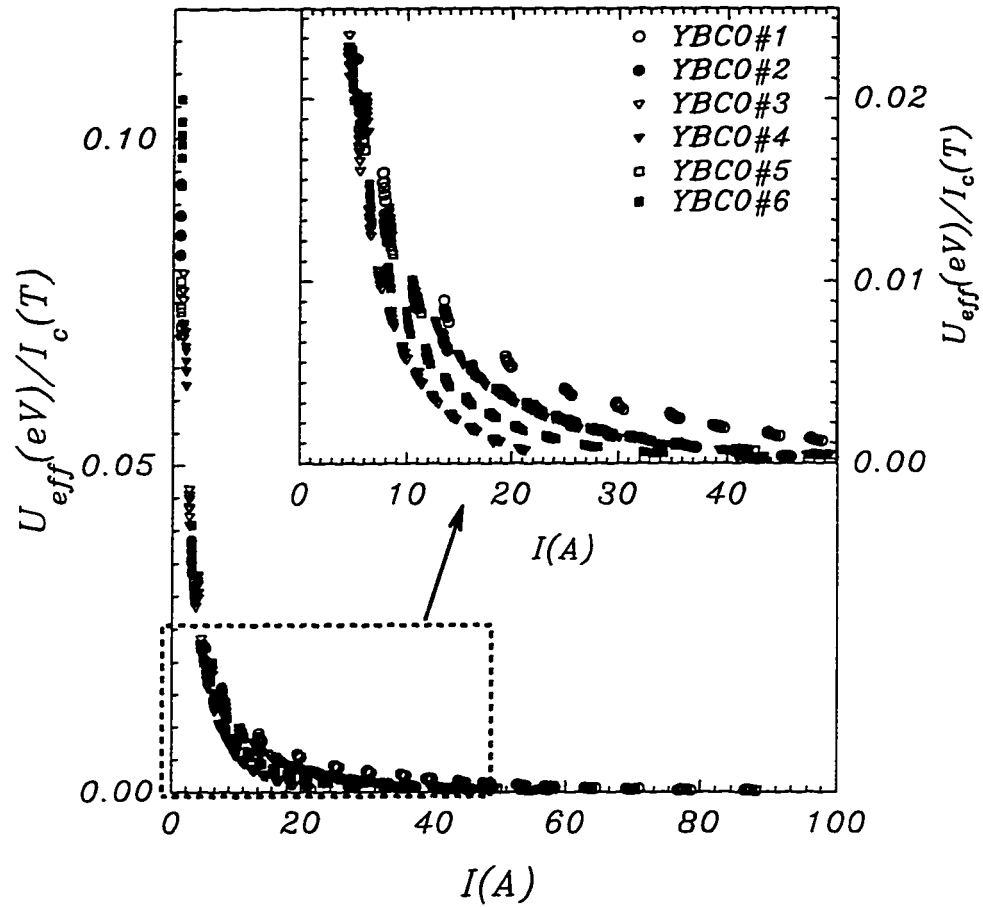


Figure 4.1.12: The dependence of $U_{\text{eff}}/I_c(T)$ on the current I presented for six YBCO thin films. The inset present the data plotted using an extended scale.

4.2 Discussion

We compared the experimental results of $U_{\text{eff}}(J)$ with the predictions of the vortex glass and collective pinning models, which were discussed briefly in Chapter 1. If the $U_{\text{eff}}(J)$ is expressed by a power-law dependence $U_{\text{eff}} = U_0(J_c/J)^\mu$ then the experimental data give $\mu \geq 1$ for very small currents and $\mu \geq 2.5$ for large currents [Figure (4.2.1)]. This is however inconsistent with the values of μ predicted by a collective flux pinning model for both two-dimensional and three-dimensional systems (Section 1.2.1). The analysis of the experimental data revealed that $U_{\text{eff}}(J)$ can be described by an exponential or a double exponential function of J [Figure (4.1.12)], if the temperature dependence of J_c is separated from the current-dependent part of U_{eff} (Eq. 4.1). The question is, what is the origin of the exponential form of $U_{\text{eff}}(J)$ and how it is related to the temperature dependence of the critical current density $J_c(T)$? In an attempt to answer this question, we produced two graphs for each YBCO thin film [Figures (4.2.2), (4.2.3) and (4.2.4)]. The first one shows $[I_c(T)/I_c(10K)]^{\frac{2}{3}}$ versus T/T_c and the other one the logarithm of $U_{\text{eff}}/I_c(T)$ versus $I/I_c(0K)$. Regarding the first graph, by plotting $I_c(T)^{\frac{2}{3}}$ versus temperature, we were able to separate a GL-like dependence of $I_c(T)$ from an AB-like behaviour. Theoretical fits to the experimental data were performed taking a superposition of two dependencies of the critical current on temperature: a GL-like $(T - T_c)^{\frac{2}{3}}$ dependence and an AB-like dependence [Figure (4.2.5)]. An AB-like dependence was calculated from Clem's model of an Ambegaokar-Baratoff to a Ginzburg-Landau crossover in $J_c(T)$ of granular superconductors [5] using the coupling constant ε_0 as a fitting parameter. The experimental results and the theoretical fits for $I_c(T)$ in YBCO films of $T_c = 87 - 91K$ [Figures (4.2.2) -(4.2.4)] suggest that high critical current density YBCO films behave like a stack of two c-axis oriented films each having different $I_c(T)$. From Chapter 3 and earlier studies of the crossover in the temperature dependence of the critical current

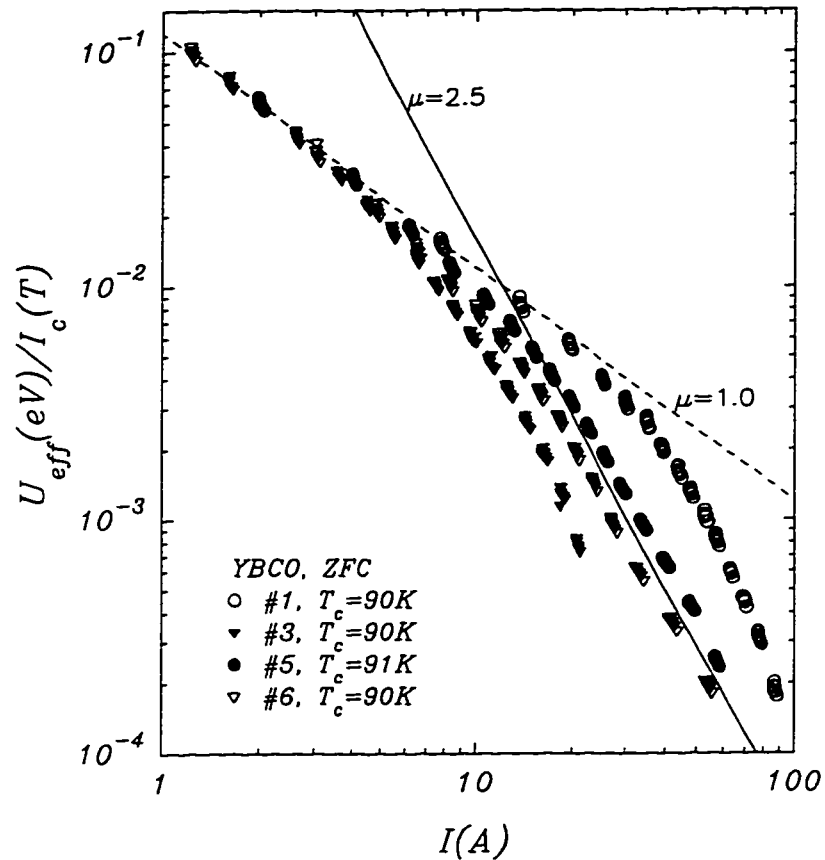


Figure 4.2.1: The dependence of $U_{\text{eff}}/I_c(T)$ on the current I presented for four YBCO thin films. $U_{\text{eff}}/I_c(T)$ and the current are plotted using logarithmic scales in order to determine the values of the exponent μ in the power law dependence of $U_{\text{eff}}(J)$ proposed by the collective flux pinning model.

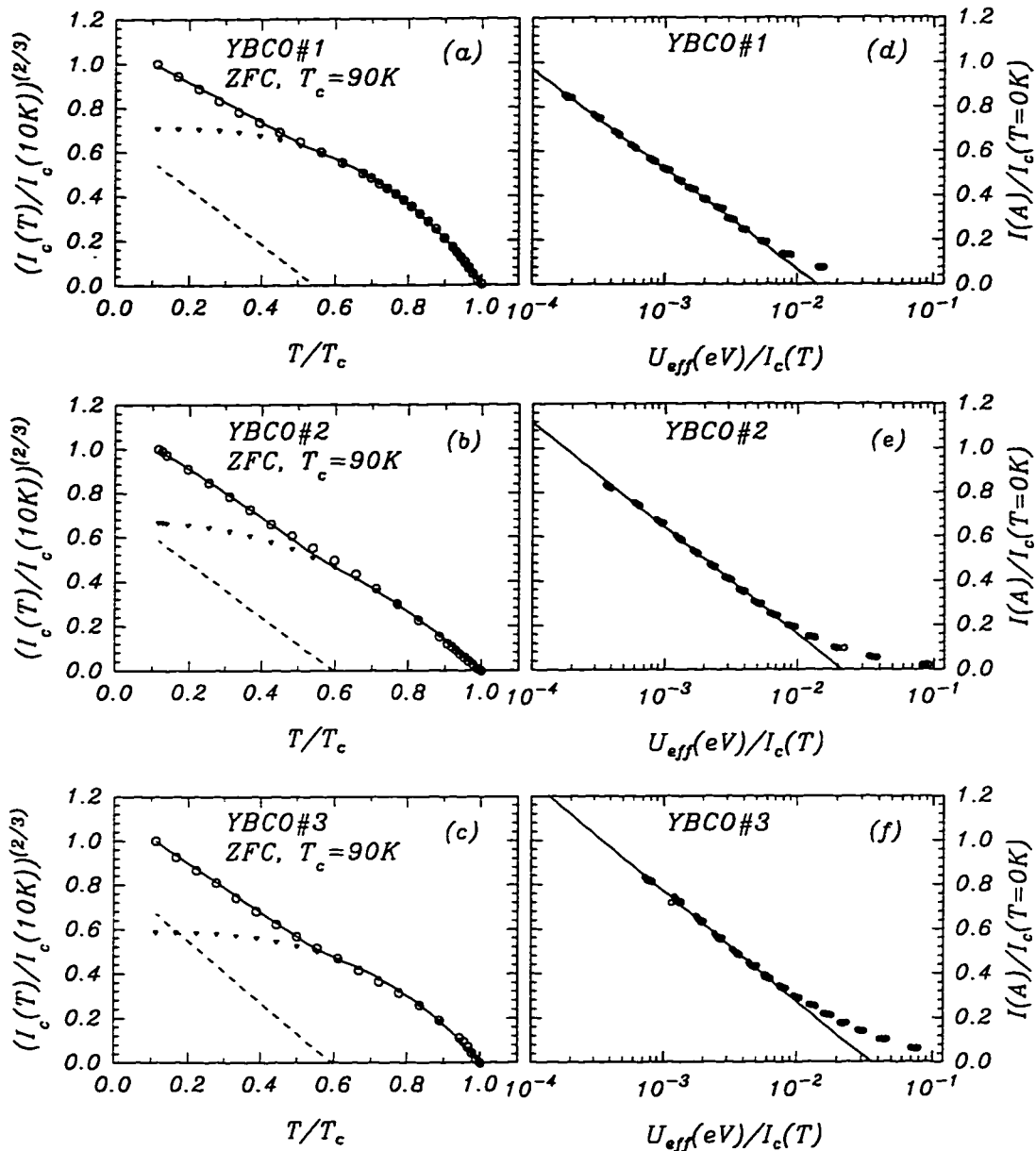


Figure 4.2.2: The dependence of the critical current on the normalized temperature (plotted as $[I_c(T)/I_c(10K)]^{2/3}$ versus T/T_c in Figures on the left) compared with the dependence of the energy barrier on the current (plotted as $\log[U_{eff}/I_c(T)]$ versus $[I/I_c(0K)]$ in Figures on the right) for YBCO ring-shaped films #1, #2 and #3. In Figures (a), (b) and (c) the open circles mark the experimental data for $I_c(T)$. The solid lines represent theoretical fits to the experimental data: they are the superposition of the GL-like dependence (dashed lines) at low temperature and the AB-like dependence [Clem's model (solid triangles) with the coupling constant $\epsilon_0 = 0.1$ for (a) and (c), and $\epsilon_0 = 100$ for (b)]. In Figures (d), (e) and (f) the solid straight lines indicate that the dependence of $[U_{eff}/I_c(T)]$ on $[I/I_c(0K)]$ is exponential. Note that their slopes are sample independent.

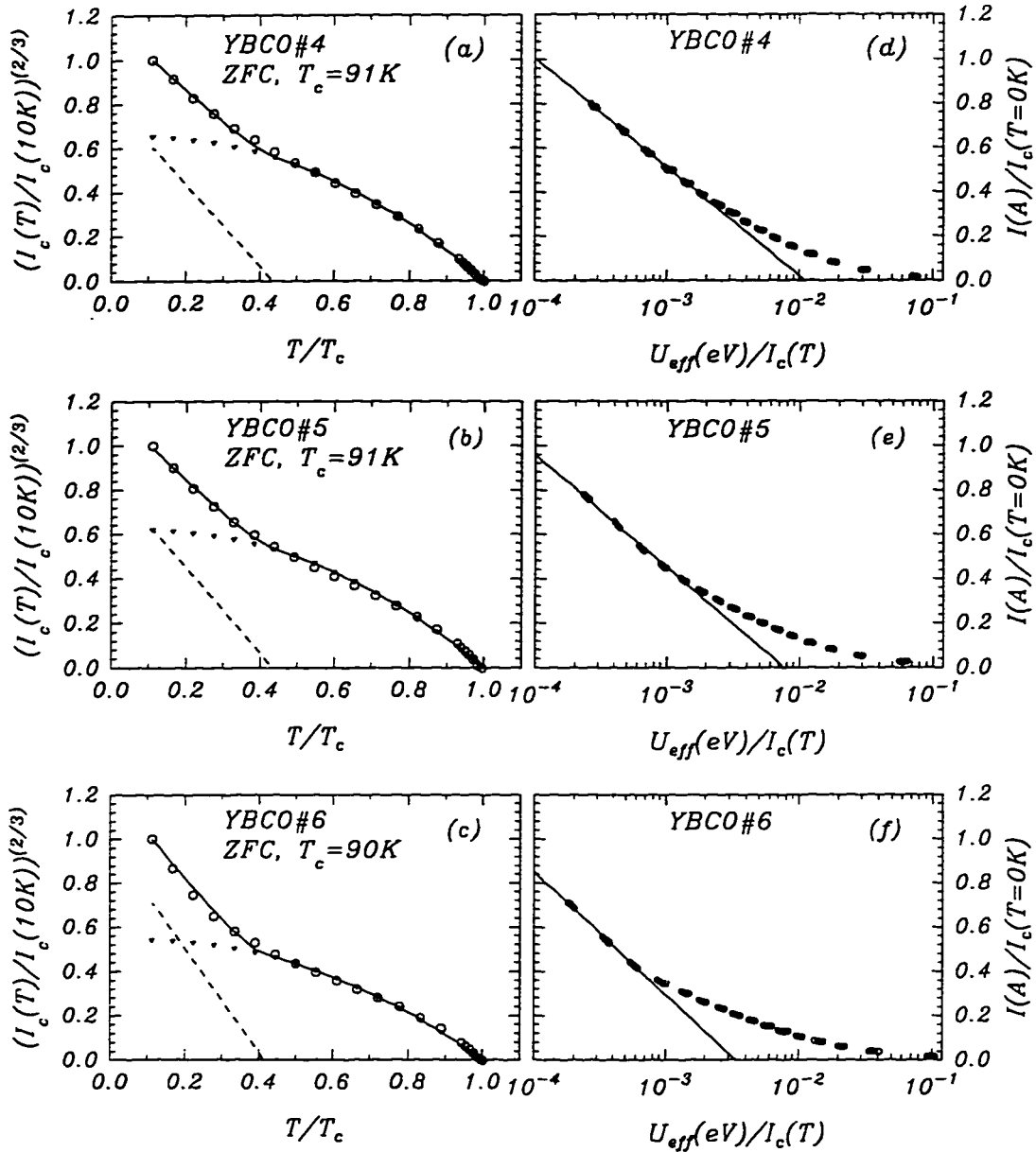


Figure 4.2.3: The dependence of the critical current on the normalized temperature (plotted as $[I_c(T)/I_c(10K)]^{2/3}$ versus T/T_c in Figures on the left) compared with the dependence of the energy barrier on the current (plotted as $\log[U_{eff}/I_c(T)]$ versus $[I/I_c(0K)]$ in Figures on the right) for YBCO ring-shaped films #4, #5 and #6. In Figures (a), (b) and (c) the open circles mark the experimental data for $I_c(T)$. The solid lines represent theoretical fits to the experimental data: they are the superposition of the GL-like dependence (dashed lines) at low temperature and the AB-like dependence [Clem's model (solid triangles) with the coupling constant $\epsilon_0 = 100$ for (a), (b) and (c)]. Note that the GL-like part of $I_c(T)$ is limited to a narrower temperature range in comparison to that for YBCO #1, #2 and #3 [Figure (4.2.2)]. In Figures (d), (e) and (f) the solid straight lines indicate that the dependence of $[U_{eff}/I_c(T)]$ on $[I/I_c(0K)]$ is exponential. Note that their slopes are sample independent, and the same as for YBCO #1, #2 and #3 [Figure (4.2.2)].

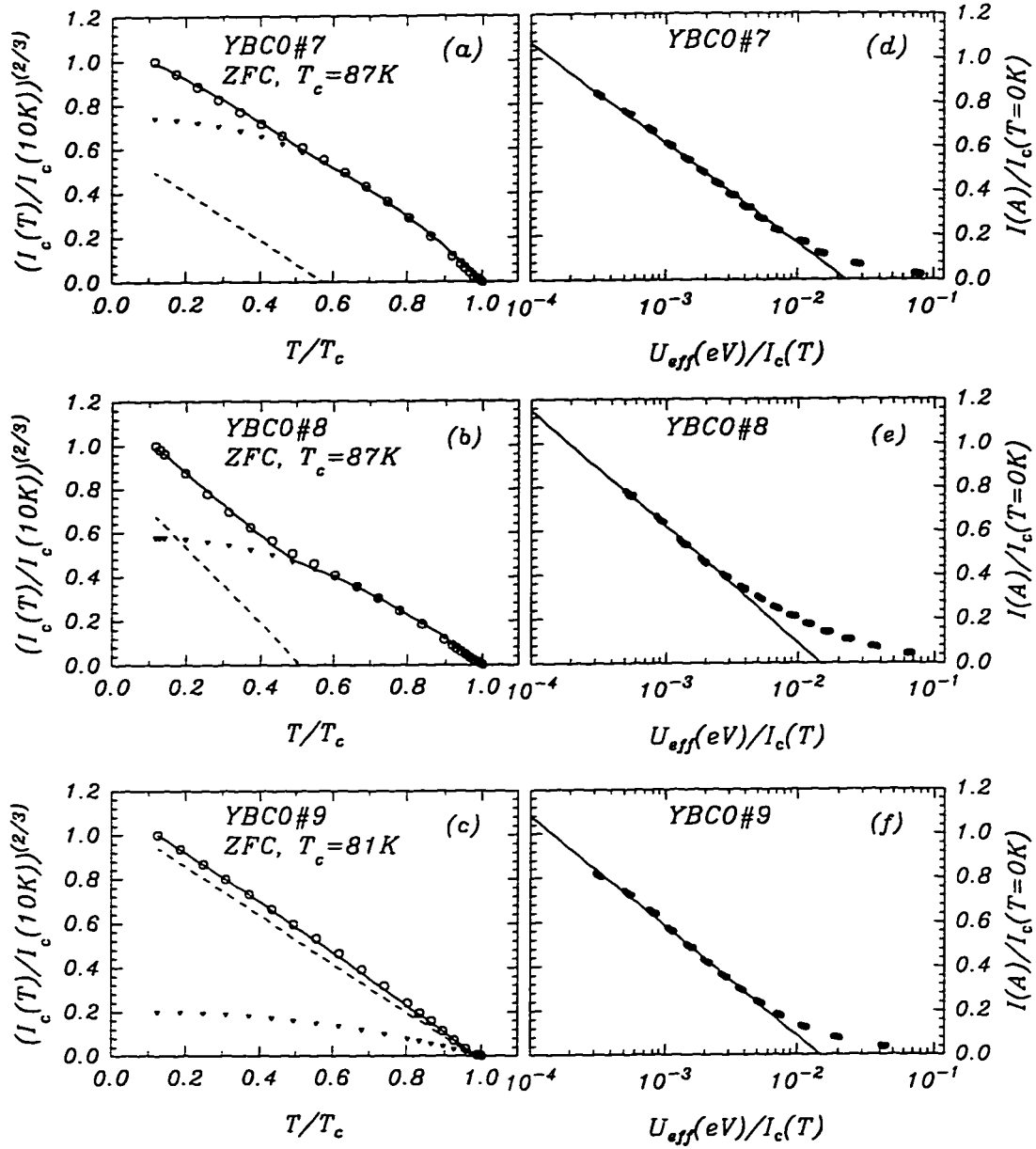


Figure 4.2.4: The dependence of the critical current on the normalized temperature (plotted as $[I/I_c(10K)]^{2/3}$ versus T/T_c in Figures on the left) compared with the dependence of the energy barrier on the current (plotted as $\log[U_{eff}/I_c(T)]$ versus $[I(T)/I_c(0K)]$ in Figures on the right) for YBCO ring-shaped films #7, #8 and #9. In Figures (a), (b) and (c) the open circles mark the experimental data for $I_c(T)$. The solid lines represent theoretical fits to the experimental data: they are the superposition of the GL-like dependence (dashed lines) and the AB-like dependence [Clem's model (solid triangles) with the coupling constant $\epsilon_0 = 100$ for (a), (b) and (c)]. In Figures (d), (e) and (f) the solid lines indicate that the dependence of $[U_{eff}/I_c(T)]$ on $[I/I_c(0K)]$ is exponential. Note that their slopes are sample independent and identical to those presented in Figures (4.2.2) and (4.2.3) for YBCO from #1 to #6.

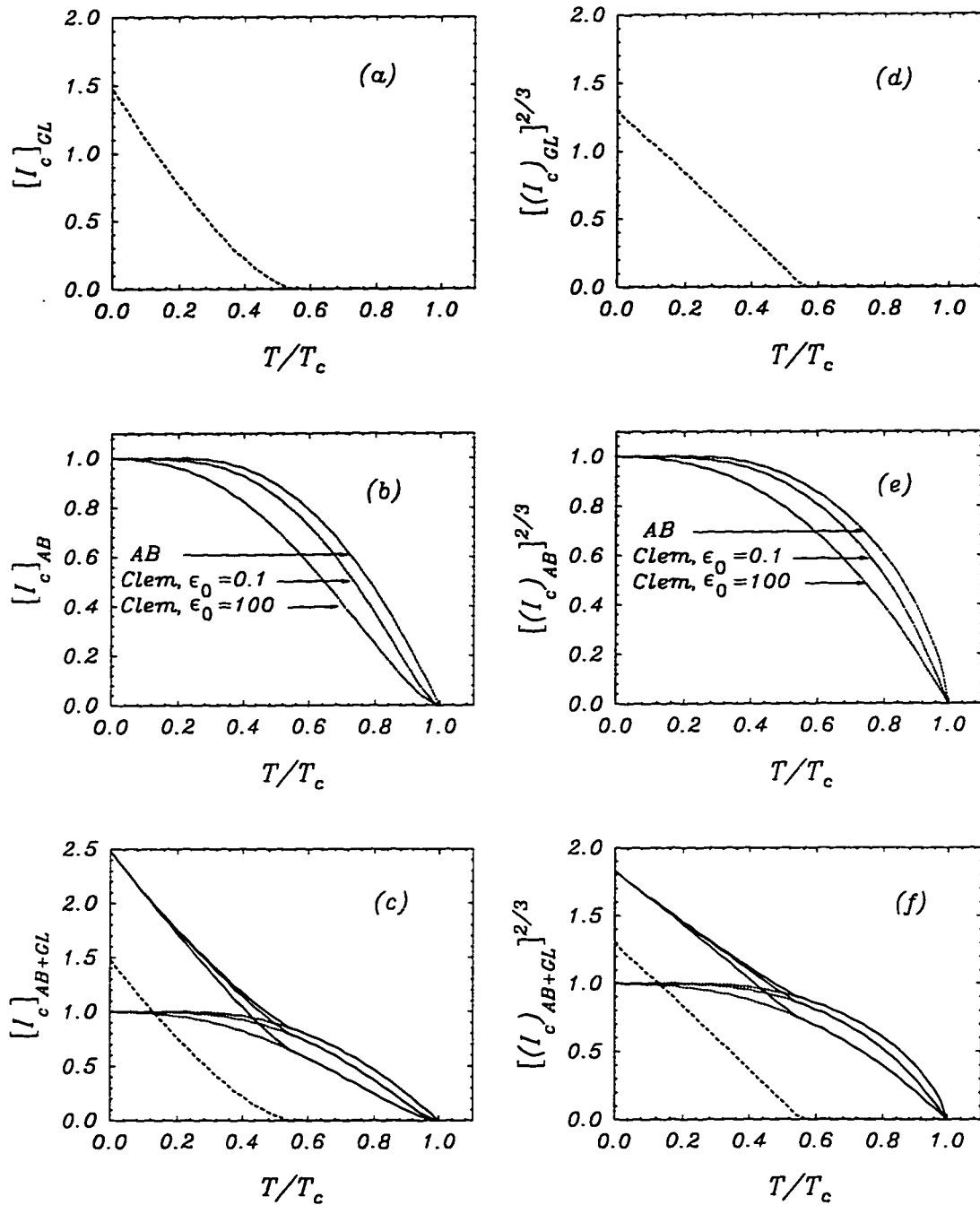


Figure 4.2.5: The dependence of the critical current I_c on the normalized temperature T/T_c , according to various theoretical models which were utilized in the fits to the experimental data shown in Figures (4.2.2), (4.2.3) and (4.2.4) (a), (b) and (c). Figures (a) and (b) show a GL-like $(T_c - T)^{3/2}$ dependence of $I_c(T)$, AB dependence of $I_c(T)$, and Clem's calculations of the crossover from AB to GL in $I_c(T)$ with coupling constants $\epsilon_0 = 0.1$ and 100. Figure (c) presents a superposition of the GL-like $I_c(T)$ with that of the Ambegaokar-Baratoff and Clem. Figures (d), (e) and (f) contain the results of (a), (b) and (c), plotted as $[I_c(T)]^{2/3}$ versus T/T_c .

in YBCO ([44] and Figure (3a) in [23]), oxygen deficient thin films are characterized by a GL-like $(T_c - T)^{\frac{3}{2}}$ dependence, and thin films close to the optimum doping exhibit an AB-like $I_c(T)$. Therefore, the superposition of a GL-like and an AB-like indicates that each YBCO film may be modeled as a stack of two films of low and high oxygen deficiency. At low temperatures, the AB-like part of $I_c(T)$ changes very little, and $I_c(T)$ is dominated by the GL-like dependence. Calculation of $U_{\text{eff}}(J)$ according to the Maley's procedure, requires a continuous change in the critical current as a function of temperature. This means that at low temperatures, the calculated $U_{\text{eff}}(J)$ should characterize flux pinning barrier of a superconductor which exhibits a GL-like $I_c(T)$. At high temperatures close to T_c , on the other hand, $U_{\text{eff}}(J)$ should describe pinning of a superconductor with an AB-like $I_c(T)$.

The comparison of the experimental data for $U_{\text{eff}}/I_c(T)$ versus $I/I_c(0K)$ with those for the temperature dependence of the critical current shown in Figures (4.2.2)-(4.2.4), implies that in a GL-like regime of the critical current, $U_{\text{eff}}/I_c(T)$ is described by an exponential function. For an AB-like regime of $I_c(T)$, $U_{\text{eff}}/I_c(T)$ is represented by a double exponential function. Note that the straight solid lines drawn through the experimental data for $U_{\text{eff}}/I_c(T)$ vs $I/I_c(0K)$ in Figures (4.2.2)-(4.2.4) (d-f) have similar slopes for all samples. This suggests that for thin film superconductors with a GL-like temperature dependence of the critical current, $U_{\text{eff}}/I_c(T)$ has a universal exponential form with a fixed factor in the exponent. Deviation of the data points from the solid lines for small currents (high temperatures), seen especially clearly for YBCO # 3-6 and 8, is related to another exponential function with a fixed argument [see Figure (4.2.6)]. Therefore, for thin film superconductors with an AB-like temperature dependence of the critical current, $U_{\text{eff}}/I_c(T)$ is described by a universal double exponential function.

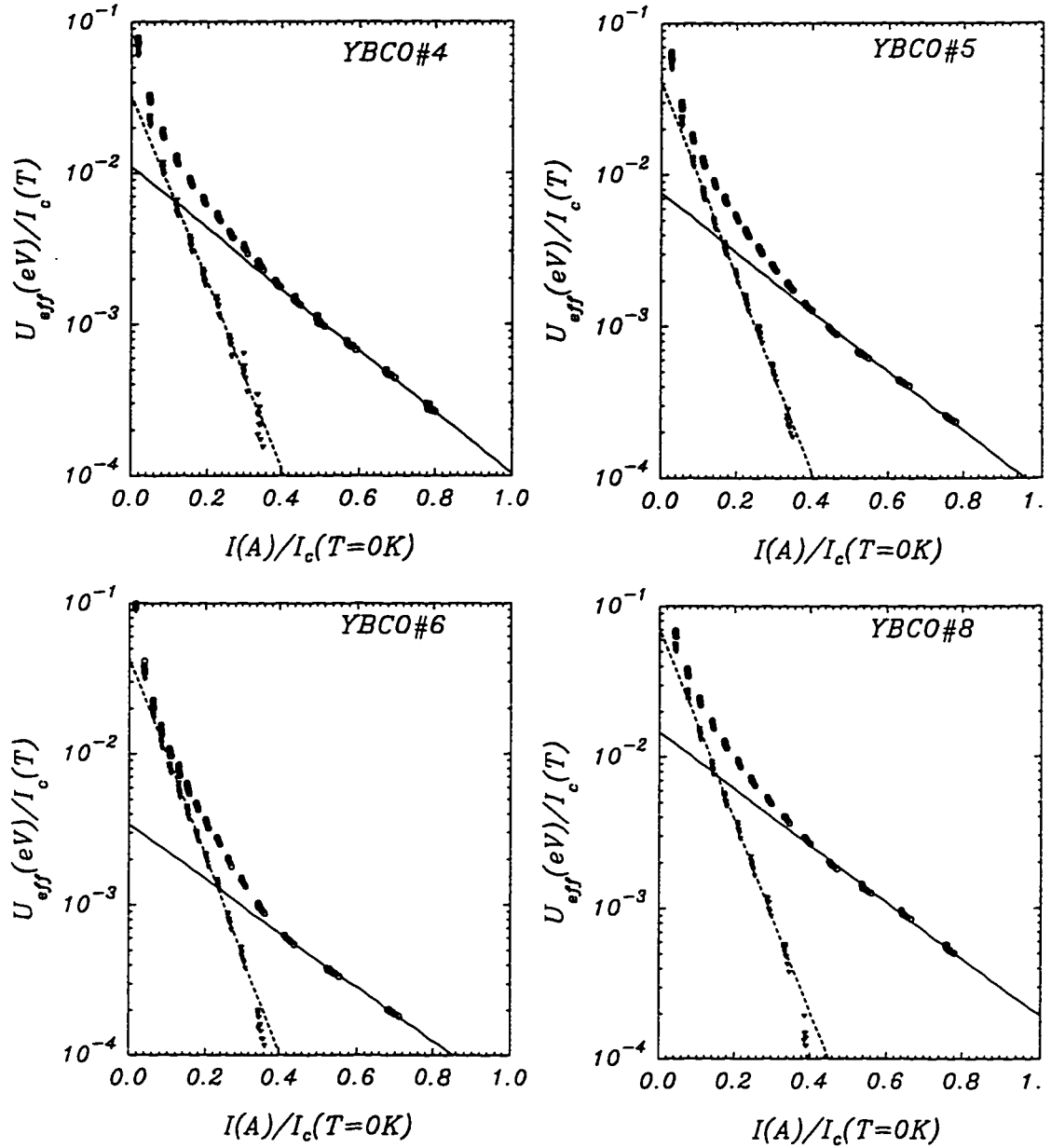


Figure 4.2.6: The dependence of the energy barrier $U_{\text{eff}}/I_c(T)$ on the normalized current $I/I_c(0K)$ plotted for YBCO ring-shaped films #4, 5, 6 and 8. These films are characterized by the pronounced AB-like behavior of $I_c(T)$ close to T_c [Figures (4.2.2), (4.2.3) and (4.2.4)], and the deviation of $U_{\text{eff}}/I_c(T)$ from the straight solid line at small currents. The segments on the dashed lines represent the data obtained by subtracting $U_{\text{eff}}/I_c(T)$ at low currents from the solid lines. In these cases $U_{\text{eff}}/I_c(T)$ is a double exponential function of $I/I_c(0K)$.

4.2.1 Origin of the universal exponential dependence of $U_{\text{eff}}(J)$

In Figure (4.2.7), we have plotted the magnitudes of the argument of the exponents for each sample, which are represented by the slope $-\{d\ln[U_{\text{eff}}/I_c(T)]/d[I/I_c(0K)]\}$. For a GL-like regime, which determines changes in $I_c(T)$ at low temperatures, this slope is $\frac{3\pi}{2}$. For an AB-like behaviour, which dominates $I_c(T)$ at high temperatures close to T_c , $U_{\text{eff}}/I_c(T)$ is a sum of two exponents with slopes of $\frac{3\pi}{2}$ and $\frac{9\pi}{2}$. The slopes for both GL and AB-like regimes do not depend on the choice of the magnitude of the constant C in Equation (2.13). However, for a constant C around 5-10, one obtains the best alignment of the Maley's segments. The experimental results provided us with the empirical formulas for $U_{\text{eff}}(J)$. In a GL-like regime of $I_c(T)$

$$U_{\text{eff}}(J) = aJ_c(T)\exp\left(-\frac{3\pi}{2}\frac{J}{J_{c0}}\right) \quad (4.3)$$

where a is a constant and J_{c0} is the critical current density at $T = 0K$. In an AB-like regime of $I_c(T)$

$$U_{\text{eff}}(J) = J_c(T)\left[a_1\exp\left(-\frac{3\pi}{2}\frac{J}{J_{c0}}\right) + a_2\exp\left(-\frac{9\pi}{2}\frac{J}{J_{c0}}\right)\right] \quad (4.4)$$

where a_1 and a_2 are constants. Note that in Equations (4.3) and (4.4), J and J_{c0} represent the density of the total persistent current flowing in the sample. The magnitude of the second exponent in Equation (4.4) with an argument $-\frac{9\pi}{2}\frac{J}{J_{c0}}$ can be treated as negligible in GL-like case [Equation (4.3)]. Recalling the experimental observations of nanometer-size domains coupled by Josephson tunnel junctions in the a-b planes of YBCO [43, 44], we identify the factors $-\frac{3\pi}{2}\frac{J}{J_{c0}}$ and $-\frac{9\pi}{2}\frac{J}{J_{c0}}$ with tilted washboard potentials for overdamped (resistively-shunted) Josephson junction, which are locked at phases of $\frac{3\pi}{2}$ and $\frac{9\pi}{2}$.

According to Tinkham[2], and Kulik and Yanson [94], within the RSJ (resistively shunted junction) model, the time dependence of the gauge-invariant phase difference ϕ in the presence of an externally supplied bias current, can be derived

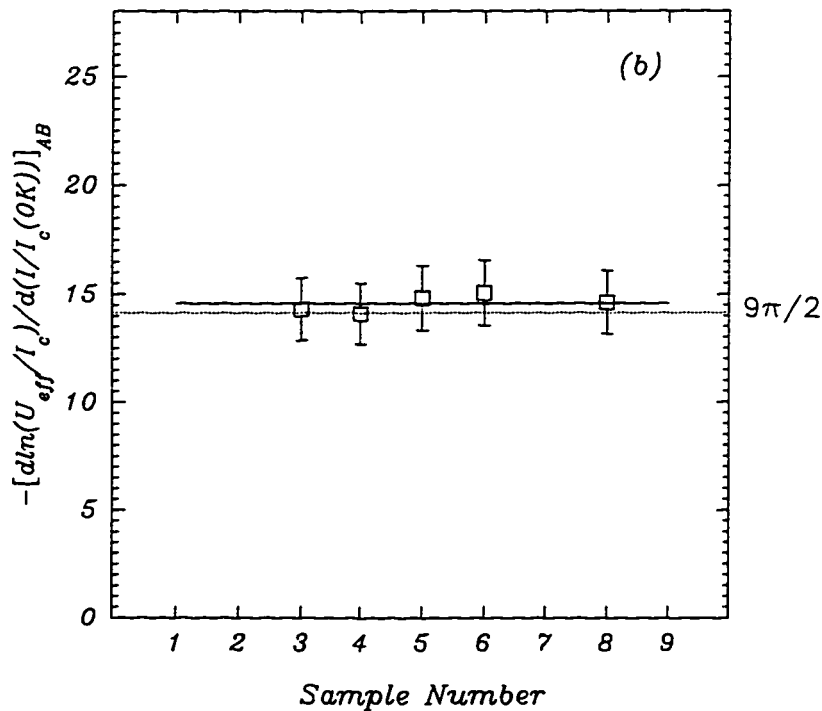
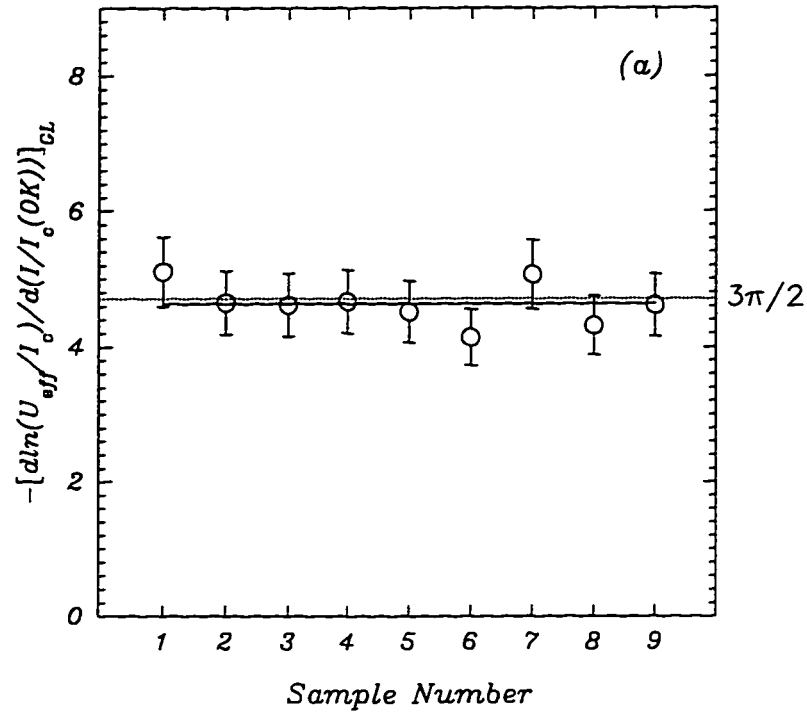


Figure 4.2.7: The magnitudes of the argument in the exponents of $[U_{\text{eff}}/I_c(T)]$ for each YBCO thin film sample, which are represented: (a) by the slope of the straight solid lines in Figures (4.2.2), (4.2.3) and (4.2.4) (e), (f) and (g) for GL-like regime of $I_c(T)$; and (b) by the slope of the straight dashed lines in Figure (4.2.6) for an AB-like regime of $I_c(T)$.

by equating the bias current I to the total junction current from the two parallel channels, as follows:

$$I = I_{c0} \sin\phi + V/R \quad (4.5)$$

where V is a voltage difference which is maintained across the junction, R is the damping resistance, and I_{c0} is the maximum Josephson current. Eliminating V in Equation 4.5, one obtains a first-order differential equation.

$$\left(\frac{\hbar}{2eRI_{c0}}\right) \frac{d\phi}{dt} + \sin\phi = \frac{I}{I_{c0}} \quad (4.6)$$

where $\frac{\hbar}{2e} \frac{d\phi}{dt} = V$. Equation 4.6 can be written as:

$$\frac{d\phi}{dt} = \frac{2eRI_{c0}}{\hbar} \left(\frac{I}{I_{c0}} - \sin\phi\right) \quad (4.7)$$

When I only slightly exceeds I_{c0} , $\frac{d\phi}{dt}$ is always positive but varies periodically with $\sin\phi$. The maximum value of the instantaneous voltage is obtained when the phase passes through $\frac{3\pi}{2} \text{ mod}[2\pi]$ ($\sin\phi = -1$). This case corresponds to a maximum resistive dissipation in a Josephson junction.

Introducing the effective potential of the junction U_j as a function of ϕ

$$U_j(\phi) = -E_j \cos\phi - \left(\frac{\hbar I}{2e}\right)\phi \quad (4.8)$$

where $E_j = \left(\frac{\hbar I_{c0}}{2e}\right)$ is the Josephson coupling energy, the voltage pulses correspond to the value of U_j locked at a phase of $\frac{3\pi}{2}$:

$$U_j\left(\frac{3\pi}{2}\right) = -\frac{3\pi}{2} \left(\frac{I}{I_{c0}}\right) E_j = -\frac{3\pi}{2} \left(\frac{J}{J_{c0}}\right) E_j \quad (4.9)$$

The exponents in Equations 4.3 and 4.4 contain factors of $-\left(\frac{3\pi}{2}\right)\left(\frac{J}{J_{c0}}\right)$ and $-\left(\frac{9\pi}{2}\right)\left(\frac{J}{J_{c0}}\right)$ which represent tilted "washboard" potential $U_j(\phi)/E_j$ locked at phases of $\frac{3\pi}{2}$ and $\frac{9\pi}{2}$. This suggests that the effective energy barrier for vortex motion in YBCO thin films depends on the properties of intrinsic Josephson junctions. From the point of view of the vortex motion, YBCO film behaves like a single Josephson junction or a very coherent array of Josephson junctions.

Note that the current density J in Equations 4.3 and 4.4 represents the magnitude of the persistent current circulating in the ring. The profile of the persistent current's self-field in the ring can be simulated by that of the vortex field trapped in a disk of the diameter equal to the outer diameter of the ring. Therefore, the current density J can be also treated as that due to the total vortex current.

The empirical formulas for the energy barrier given by Equations 4.3 and 4.4, should be modified in order to include the condition $U_{\text{eff}}(J_c) = 0$. We could write $U_{\text{eff}}(J)$ in the form $U_{\text{eff}}(J) = J_c(T)F(J)$, like in Equation 4.1, where $F(J) = a \exp(-\frac{3\pi}{2}J/J_{c0})$ for a GL-like regime of $I_c(T)$, and $F(J) = a_1 \exp(-\frac{3\pi}{2}J/J_{c0}) + a_2 \exp(-\frac{9\pi}{2}J/J_{c0})$ for an AB-like behaviour of $I_c(T)$. The new version of the energy barrier should be represented by

$$U_{\text{eff}} = J_c(T)[F(J) - F(J_c)] \quad (4.10)$$

for both cases.

4.2.2 Pinning mechanism and vortex dynamics in YBCO thin films

We interpret the dissipation of the persistent current as due to the vortex motion through the Josephson nanostructures in YBCO discussed in Chapter 3 [43, 44]. In this model the a-b planes consist of cells of a few nanometers in size [Figure (4.2.8)], which are coupled by resistively shunted Josephson tunnel junctions. We assume that the pinning arises from a variation of the order parameter within the cell structure. The change of the order parameter from cell to cell leads to the spatial variation of the Josephson coupling energy between the cells in the a-b plane and between the cells on adjacent planes in the c-direction. According to Clem *et al* [5] for a square array of Josephson junctions with lattice parameter a_0 , the vortex structure is determined

by the array's geometry and the vortex core size is set by a_0 .

We postulate that the dependence of U_{eff} on the current density J (Equations 4.3 and 4.4) reflects in-phase oscillations of the Josephson array due to the collective motion of all the vortices trapped in the ring. The vortex motion occurs in the radial direction from the inner to the outer edge of the ring under the influence of the Lorentz force exerted by the circulating persistent current. The vortices travel along long Josephson junctions of the array from cell to cell. During this motion they experience a modulation of the Josephson coupling energy on a scale of a few nanometers. A possible scenario for the dissipation of energy in the array involves vortex currents which sweep the array and act as bias currents for Josephson junctions between the array's cells. Because of the modulation of the Josephson coupling energy in the array, if the sum of the vortex current and the persistent current exceeds the Josephson critical current for junctions of the weakest coupling, the phase-dependent voltage appears in the array. Maximum resistive dissipation is expected for the case of a spatial phase-coherence.

Calculation of the power spectrum of the voltage in an $Nb/AlO_x/Nb$ square array of Josephson junctions for different levels of the bias current has been performed recently by Lachenmann *et al* [95]. For large bias currents above the array's critical current, junctions in the array oscillate coherently and the power spectrum $S(\nu)$ consists of sharp peaks at equal multiples of frequency $\nu = eV R_s i_c / \pi \hbar$ (where R_s is the shunt-resistance and i_c is the critical current of each junction in the array).

These results imply that the phase coherence at $3\pi/2$ and $9\pi/2$ observed in our experiments could represent the first and the third harmonics of coherent oscillations of the Josephson junction array.

According to our interpretation, dissipation of the persistent current could be caused by the motion of Josephson vortices in the array. Due to a curvature of

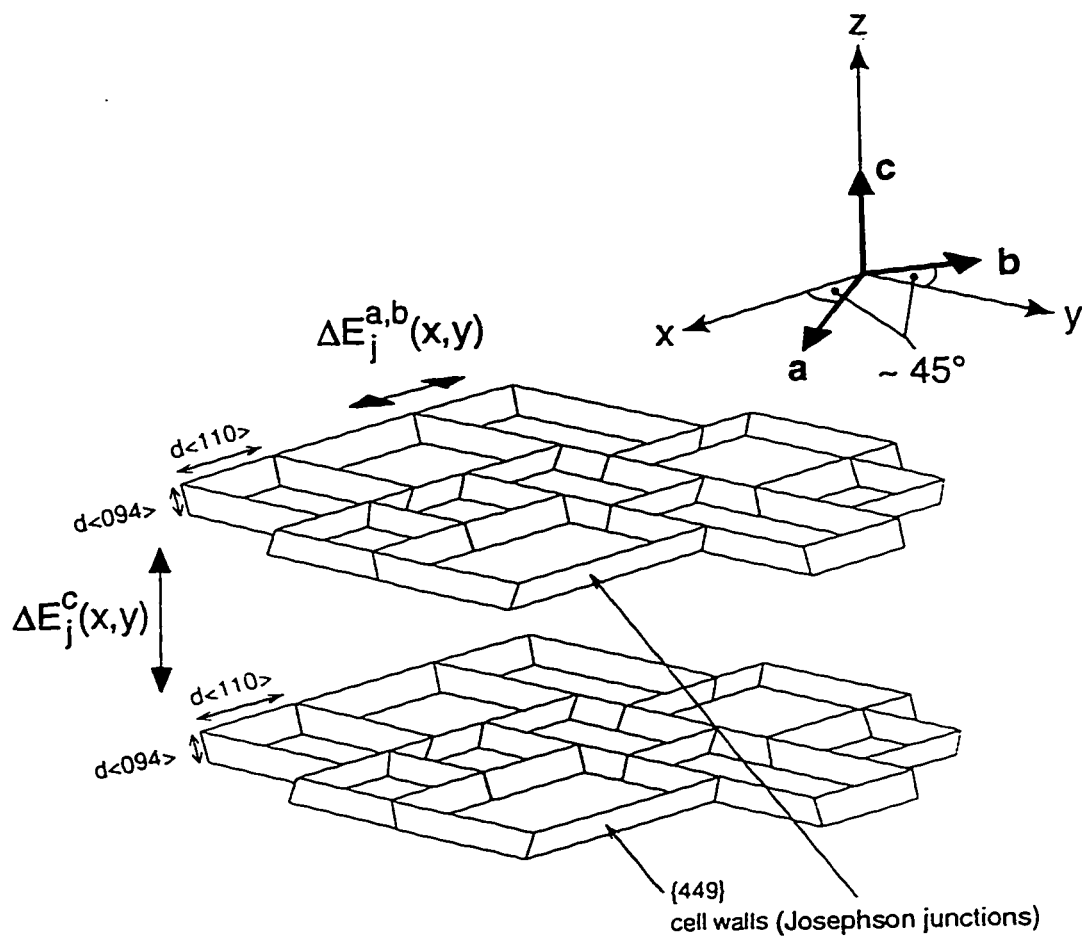


Figure 4.2.8: The schematic of the nanoscale cells (a few nanometers in size) in the a-b planes of YBCO as described by Etheridge[43] on the basis of the high resolution electron microscopy. According to our studies, the walls between the cells form Josephson tunnel junctions with the spatial variation of the coupling energy in the a-b planes $\Delta E_j^{a,b}(x,y)$ and between the planes $\Delta E_j^c(x,y)$. Crystallographic directions of the cell walls are along the x,y axes. The a,b-axes are positioned at an angle of about 45° relative to the x,y axes.

magnetic flux lines trapped in the c-axis oriented ring, the vortex lines form an angle with the direction perpendicular to a-b planes (c-axis direction). In a layered superconductor, these vortices are viewed as chains of two-dimensional pancake vortices connected by interplane Josephson-type vortices [96]. A pancake vortex can be viewed as a finite segment of height equal to the interlayer spacing, of an Abrikosov vortex directed along the c-axis.

The data obtained from our relaxation measurements show that there is a relationship between the temperature dependence of the critical current $I_c(T)$ and the relaxation of the persistent current. We assume that when the temperature dependence of I_c is a GL-like, the supercurrent does not “see” the Josephson nanostructures in the a-b planes. Therefore, the vortex segments perpendicular to the planes are Abrikosov-like. The interplane segments which join the Abrikosov ones are the Josephson strings which experience the spatial modulation of the Josephson coupling energy between the planes. Persistent current circulating in the ring exerts the Lorentz force on the Abrikosov segments but not on the Josephson strings. The Josephson strings move between the planes due to the drag force applied to them by the Abrikosov segments. In this case the energy barrier for vortex motion $U_{\text{eff}}(J)$, (expressed by Equation 4.3) should be determined solely by the spatial variation of the Josephson coupling energy between the planes. When the temperature dependence of I_c is an AB-like, the supercurrent flows through the Josephson nanostructures in the a-b planes. Therefore, the in-plane pancake vortices change their character from an Abrikosov- to a Josephson-like. The flux lines experience the modulation of the Josephson coupling energy both in the a-b planes and between the planes. In this case, the first exponent with a phase of $3\pi/2$ in the expression for $U_{\text{eff}}(J)$ (Equation 4.4) is determined by the spatial variation of the Josephson coupling energy between the planes, similarly to a GL-like case described above. The second exponent with a phase of $9\pi/2$ is attributed to the modulation of the Josephson coupling within the

array in the a-b planes.

Additional experimental evidence which relates the exponent with a phase of $3\pi/2$ to the motion of the interplane Josephson vortices in the a-b planes in a superconductor with a GL-like $I_c(T)$, has been provided by the measurements on YBCO thin film #9 with $T_c = 81K$ [Figure (4.2.4) (c) and (f)]. The temperature dependence of the critical current in this sample is dominated by a GL-like regime [Figure (4.2.4) (c)] over a wide temperature range of 10 – 60K. The reduction of an AB-like contribution to $I_c(T)$ at low temperatures by a factor of 3-4 in comparison to that in other samples, does not change the magnitude of the phase in Equation (4.3).

Recent measurements of the microwave surface impedance in the a-b planes of ultra-pure YBCO single crystals [97] performed by Zhai et al [98] imply that the crystal responds like a single Josephson junction (or a coherent array of Josephson junctions) to an ac-drive-current in the a-b plane. Their data were analyzed using a resistively-shunted Josephson junction model. The authors concluded that the extraordinary coherence of the data suggests an intrinsic effect, however, they expressed doubts that defects like twin boundaries in YBCO crystals could respond in such a coherent manner.

We have ruled out that the structure of the twin boundaries in YBCO thin films is responsible for the observed vortex motion and consequently for the dissipation of the persistent current. This is the result of the independence of the experimental data for the energy barrier $U_{\text{eff}}(J)$ and the critical current $I_c(T)$, on the growth conditions of YBCO thin films, substrates, film thickness and the magnitude of the critical current density J_c . The structure of the twin boundaries is known to be sensitive to oxygen content [99, 100]. Since $U_{\text{eff}}(J)$ is also independent of T_c [see Figure 4.2.4 (d), (e) and (f)], this is an additional evidence that the energy barrier for vortex motion is not affected by the presence of extended defects in the films. Similar conclusions

about the role of extended defects in the pinning mechanism in YBCO have been also drawn by Griessen *et al* [39] in his work on pinning in YBCO thin films.

According to earlier results (e.g. Ref. [44]) and the Halbritter's model [101], the major channel of the supercurrent conduction across the grain boundaries is established through the intergrain strong links. These strong links are the microbridges whose structure is the same as the grain i.e., consists of Josephson nanostructures. The twin boundary layer thickness was found to be between 10 and 20 Å in optimally doped YBCO [99]. This is of the order of the cell size in the Josephson array in the a-b planes of YBCO. This means that the temperature dependence of the critical current in this case is governed by the Josephson tunnel junctions in the array and weakly pinned vortices are able to shear along these which are strongly pinned by the grain boundaries such as twin boundaries or high angle boundaries.

Very good fit of the experimental results for $U_{\text{eff}}(J)$ in TlBCCO (2223) single crystal to a double exponential function has been produced by Mexner *et al* [102]. The authors applied the Maley's method to calculate $U_{\text{eff}}(J)$ from the relaxation data taken at magnetic fields up to 12 T and over a temperature range of 4 – 77K. The analysis of the data was, however, based on the collective flux creep model of Feigelman *et al* [37] with the power-law dependence of the energy barrier on J.

Chapter 5

Distribution of currents and the critical state in YBCO thin films

5.1 Experimental Results

We performed the measurements of magnetic flux penetration into disk- and ring-shaped YBCO thin films as a function of applied field and temperature. The experimental procedure included the measurement of the axial and radial components of magnetic field profiles (for both shielding and trapped fields) above the sample and the magnetic relaxation effects for both complete and partial flux penetration states. We investigated two disk-shaped films with a diameter of $15mm$ and with a thickness of $500nm$ (disk #1) and $200nm$ (disk #2), and one ring-shaped film (ring #1) with outer and inner diameters of $8.5mm$ and $5mm$ respectively, and thickness of $500nm$. Ring #1 was etched from disk #1.

5.1.1 Magnetic-flux penetration into disk-shaped and ring-shaped YBCO thin films

We performed a series of measurements in order to observe the process of flux penetration into zero-field-cooled disk- and ring-shaped samples. The measurement of the profiles of the radial and axial components of the magnetic shielding field was carried out in the presence of an applied field H_a perpendicular to the surface of the

film. The profiles were measured at different temperatures (30, 40, 50 and 70 K) for different values of H_a up to 750G. Figures (5.1.1) and (5.1.3) show the results at $T = 30K$ for disk #2 and ring #1, respectively. The profiles of the radial and axial components of the trapped magnetic field were measured when the applied field H_a was removed. Figures (5.1.3) and (5.1.4) show the trapped field measurements at $T = 30K$ for disk #2 and ring #1, respectively. The radial shielding field profiles for the disk [Figure (5.1.1)] show that less applied magnetic field is shielded from a larger section at the center of the disk than at higher applied field. The corresponding trapped field profiles [Figure (5.1.3)] show that the trapped field propagates into the sample from the edges to the center of the disk with an increasing applied field. This behaviour does not change at higher temperatures of 50 and 70K (see Appendix A for disk #2 and Appendix B for ring #1)

The axial and radial components of the trapped and the shielding field depend on the applied field [Figure (5.1.5) for disk #2 and Figure (5.1.6) for ring #1]. The applied field required to reach the saturation of the trapped field, decreases with an increasing temperature. At higher applied field, the trapped fields for the disk and the ring are independent of the applied field, however the shielding fields reach a maximum at a certain applied field which decreases with an increasing temperature, and with an increasing applied field. For the disk and the ring, the dependence of the maximum trapped (or shielding) field, for both axial and radial directions, on the applied field is similar. This similarity indicates that the dependence of the total trapped (shielding) field ($H_t = \sqrt{H_z^2 + H_r^2}$) on the applied field could be identical to that of its axial and radial components.

In order to verify how the magnetic field lines penetrate thin film samples, we plotted the vectors of the shielding and trapped fields as a function of position along the disk (ring) diameter, which were measured at a distance of 3 mm above the sample and for different applied fields. The length of the vector at a certain position

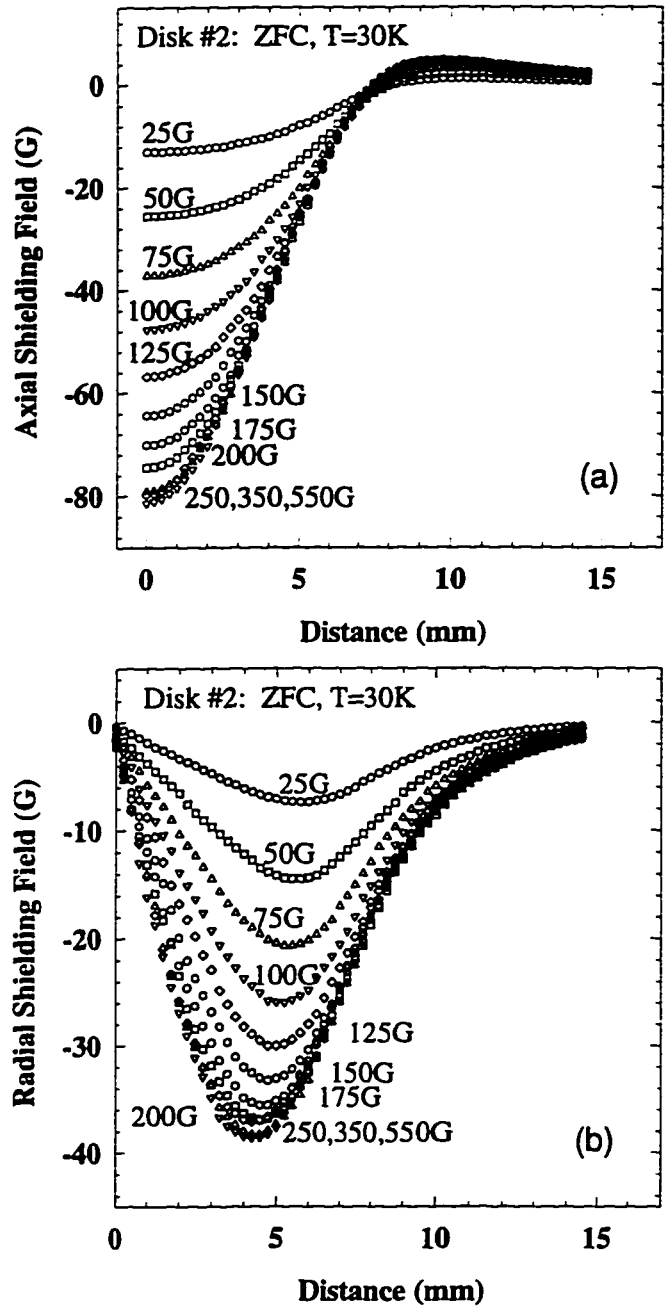


Figure 5.1.1: The profiles of the axial (a) and radial (b) magnetic fields shielded by a zero-field-cooled disk #2 at various applied fields and 30 K . The shielding field reaches maximum at applied field of about 300G. The profiles were measured by scanning axial and radial Hall probes at a distance of 3mm above the sample. Distances 0mm and 7.5mm mark the center and the edge of the disk, respectively.

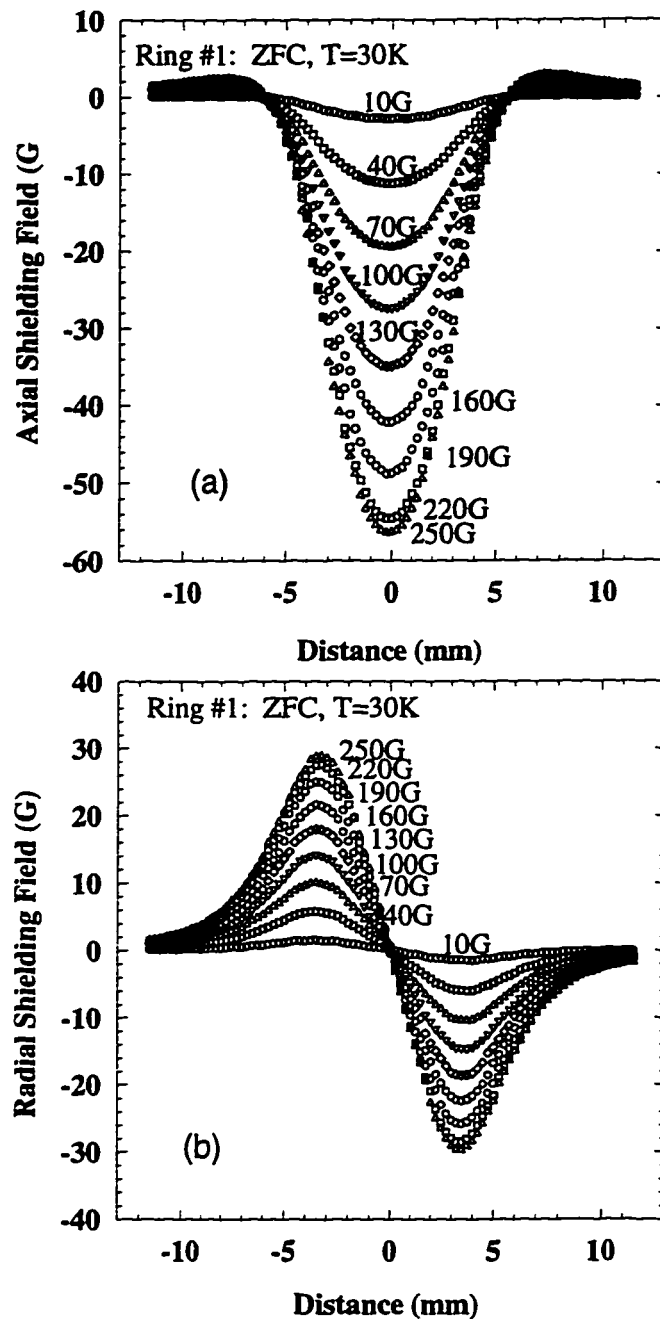


Figure 5.1.2: The profiles of the axial (a) and radial (b) magnetic fields shielded by a zero-field-cooled ring #1 at various applied fields and 30 K . The shielding field reaches maximum at applied field of about 250 G. The profiles were measured by scanning axial and radial Hall probes at a distance of 3 mm above the sample. Distances $\pm 4.25\text{mm}$ and $\pm 2.50\text{mm}$ mark the outer and inner ring's edges, respectively.

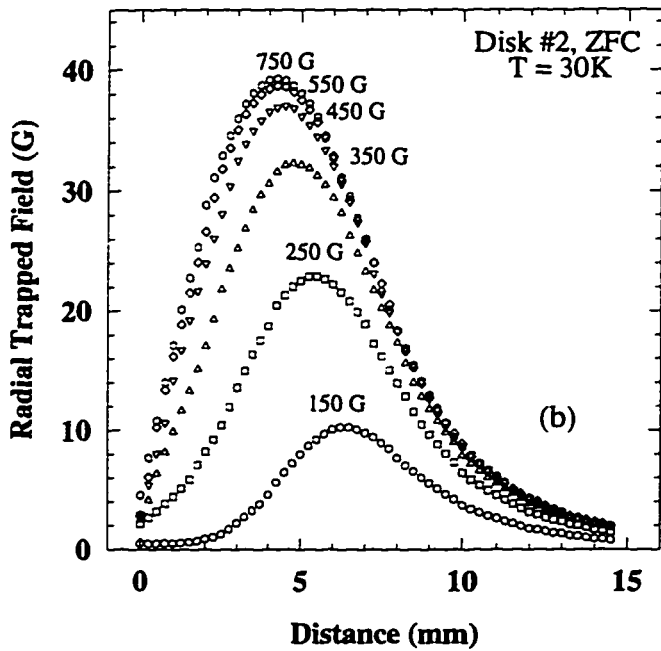
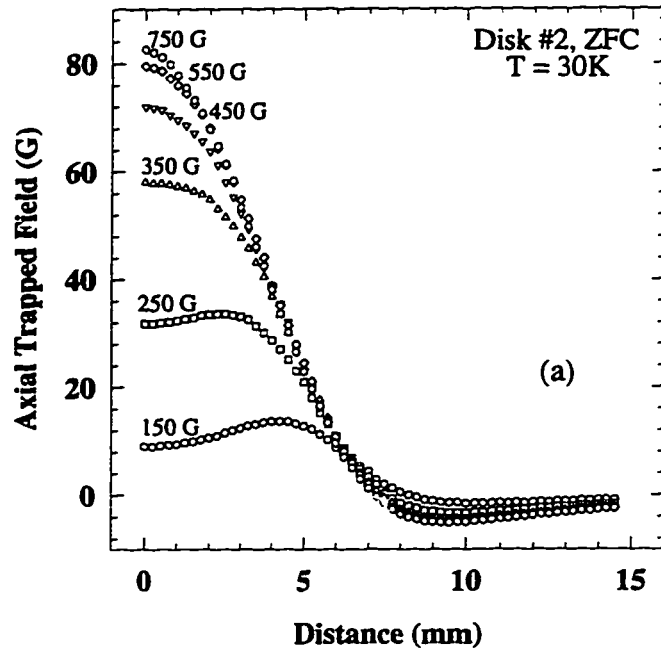


Figure 5.1.3: The profiles of the axial (a) and radial (b) magnetic fields trapped at 30 K by a zero-field-cooled disk #2 after applying and subsequently removing external fields up to 750 G. The profiles were measured by scanning axial and radial Hall probes at a distance of 3mm above the sample. Distances 0mm and 7.5mm mark the center and the edge of the disk, respectively.

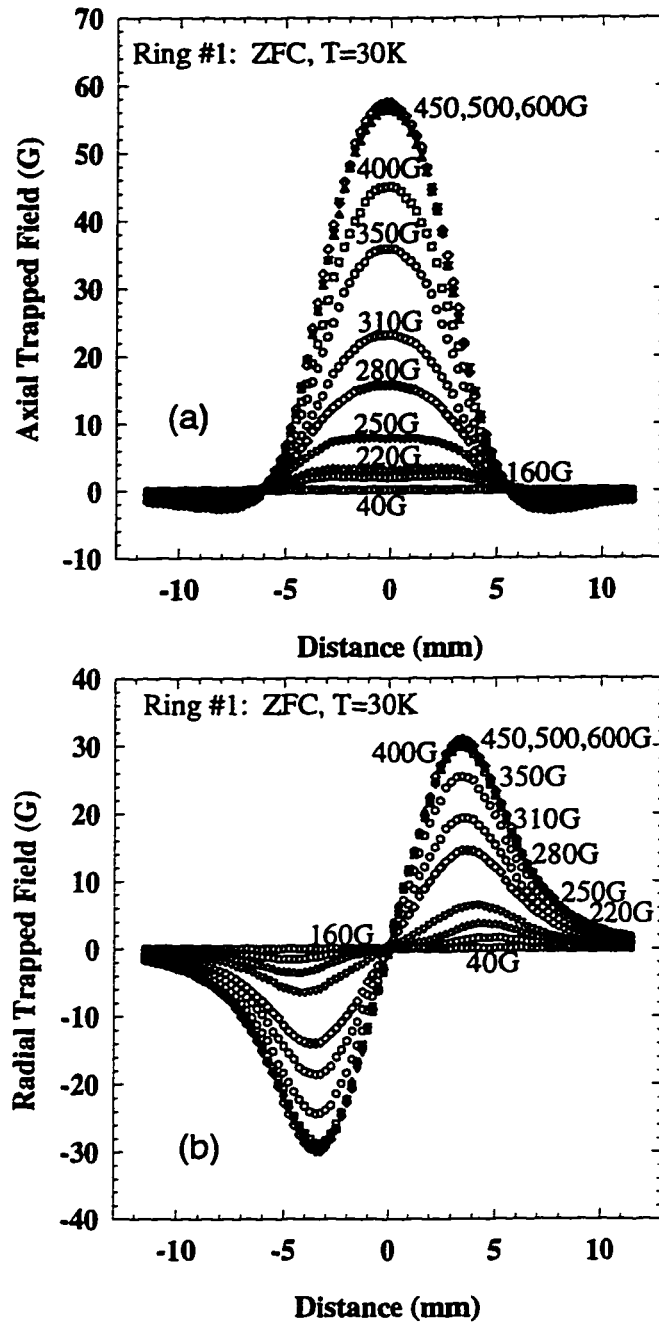


Figure 5.1.4: The profiles of the axial (a) and radial (b) magnetic fields trapped at 30 K by a zero-field-cooled ring #1 after applying and subsequently removing external fields up to 750 G. The profiles were measured by scanning axial and radial Hall probes at a distance of 3mm above the sample. Distances $\pm 4.25\text{mm}$ and $\pm 2.50\text{mm}$ mark the outer and inner ring's edges, respectively.

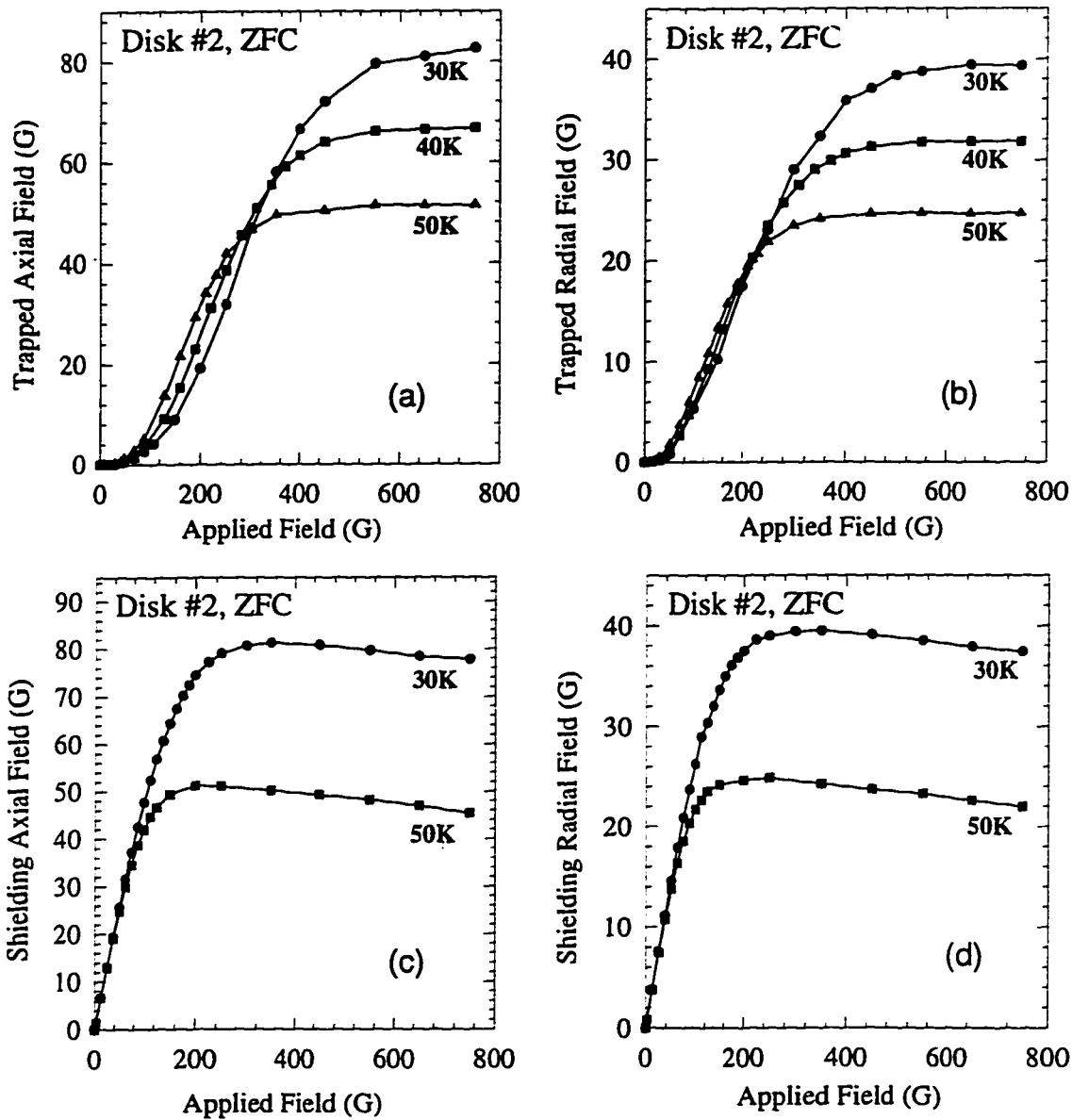


Figure 5.1.5: Axial and radial components of the shielding and trapped fields in zero-field-cooled disk #2 measured as a function of the applied field at various temperatures. The axial components (a) and (c) were taken at the center of the disk while the radial components (b) and (d), correspond to a maximum radial field. The applied field was perpendicular to the sample surface. The shielding and trapped fields were measured by scanning axial and radial Hall probes at a distance of 3mm above the sample.

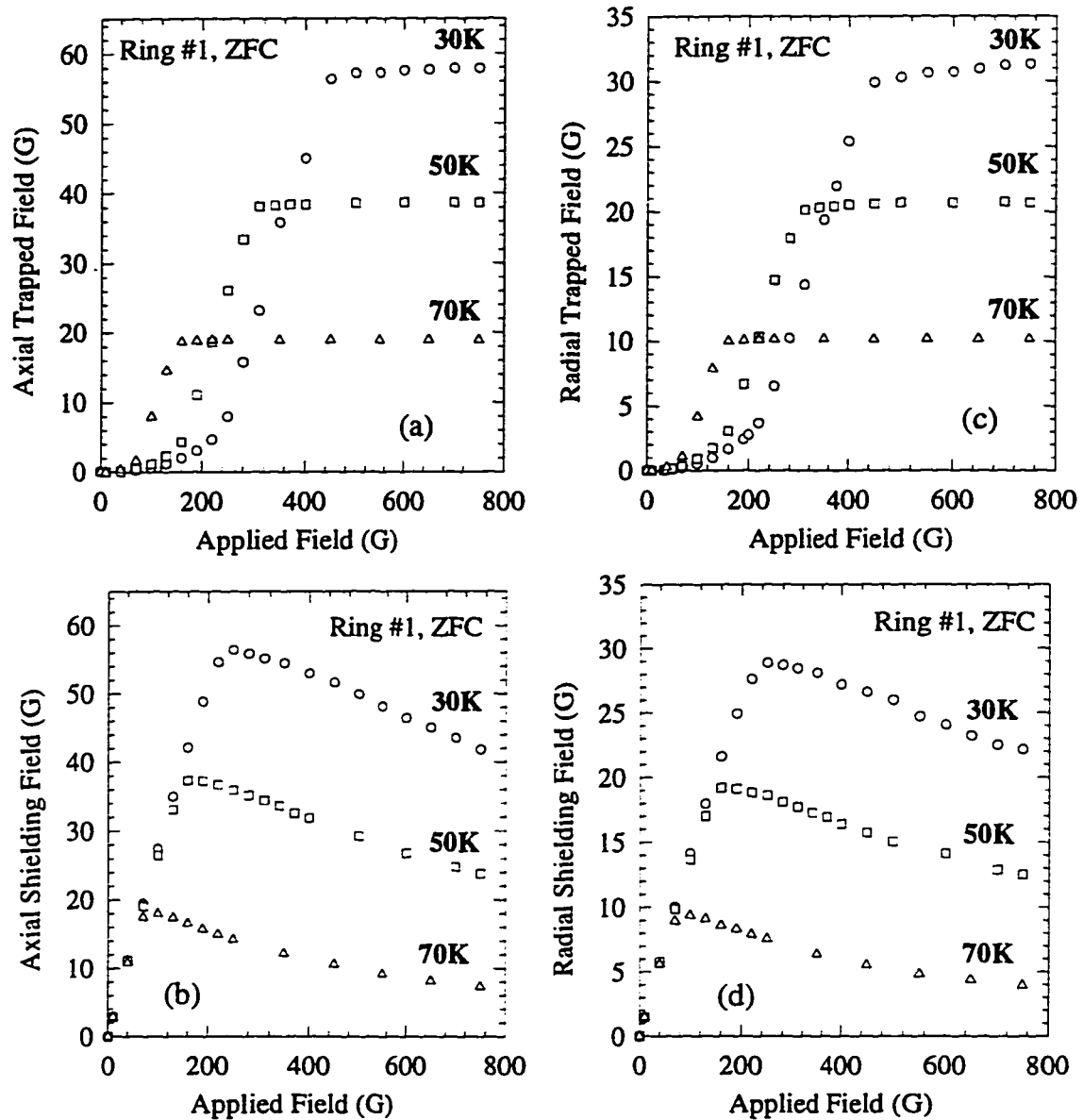


Figure 5.1.6: Axial and radial components of the shielding and trapped fields in zero-field-cooled ring #1 measured as a function of the applied field at various temperatures. The axial components (a) and (c) were taken at the center of the ring while the radial components (b) and (d), correspond to a maximum radial field. The applied field was perpendicular to the sample surface. The shielding and trapped fields were measured by scanning axial and radial Hall probes at a distance of 3mm above the sample.

determines the magnitude of the shielding (trapped) field at that point [Figures (5.1.7) and (5.1.7) for disk #2 and Figures (5.1.9) and (5.1.10) for ring #1 at a temperature of 30K; See Appendices A and B for results at temperatures of 50K and 70K]. The shielding field vectors show that the disk (and the ring) is uniformly shielded at very low fields within a circular area of diameter D_s , approximately equal to the diameter of the disk (or the outer diameter of the ring). D_s decreases with an increasing applied field. For higher applied fields the shielding fields are stronger at the center of the sample indicating that the field lines penetrate the sample from its edges, as expected. The magnetic flux penetration is also shown by the trapped field vectors for both the disk and the ring. The measurements of the shielding and trapped field for disk #2 and ring #1 have been extended to include the distance above the sample surface from 3mm up to 12mm. Since the field vectors are tangent to the field lines, this allowed us to demonstrate an approximate mapping of the magnetic shielding (trapped) field lines at distances higher than 3mm above the sample surface. The results are shown for a temperature of 30K for disk #2 in Figures (5.1.11) and (5.1.12), and for ring #1 in Figures (5.1.13) and (5.1.14). (See Appendices A and B for results at temperatures of 50K and 70K).

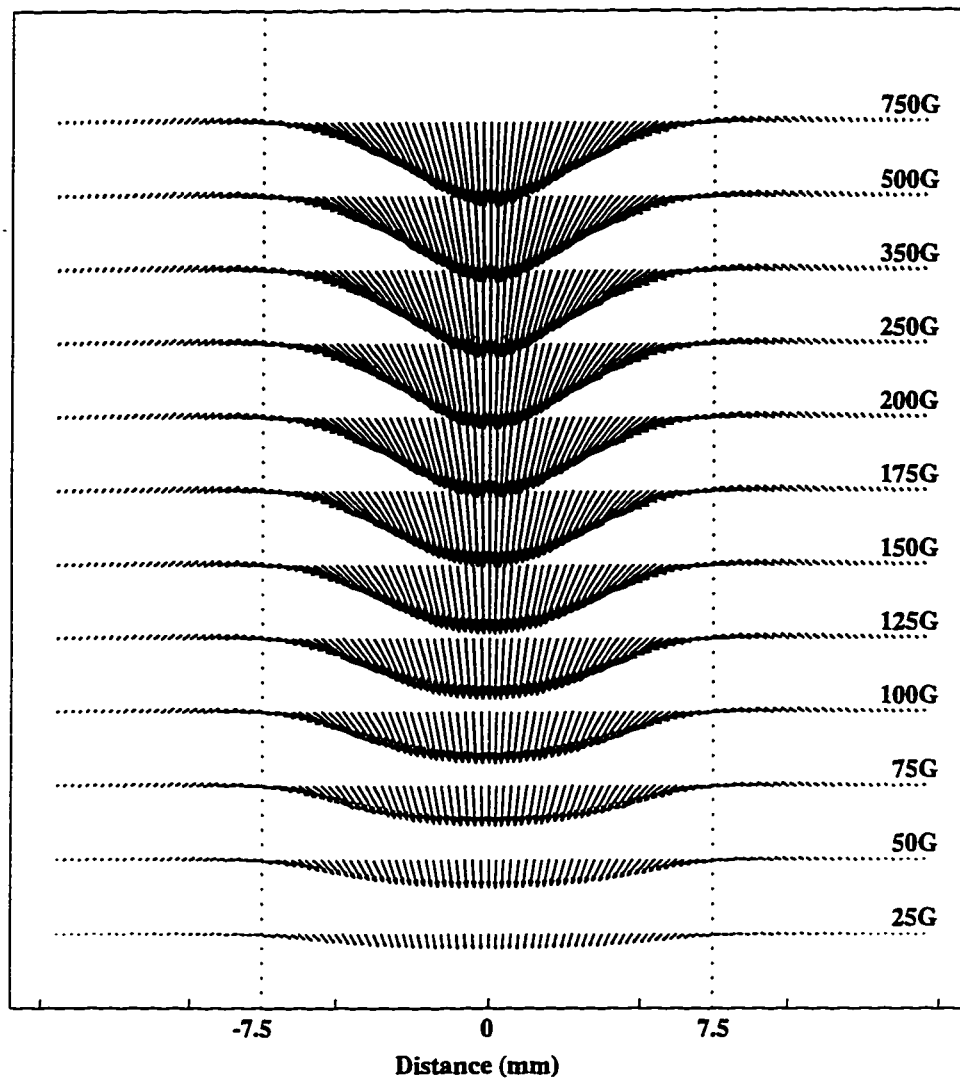


Figure 5.1.7: The vectors of the shielding field measured at $30K$ as a function of position along the diameter of disk #2 (and a distance of $3mm$ above its surface) for different applied fields. The magnitude of each vector is proportional to the magnitude of the total field at the same position. Distances $-7.5mm$ and $7.5mm$ mark the disk's edges.

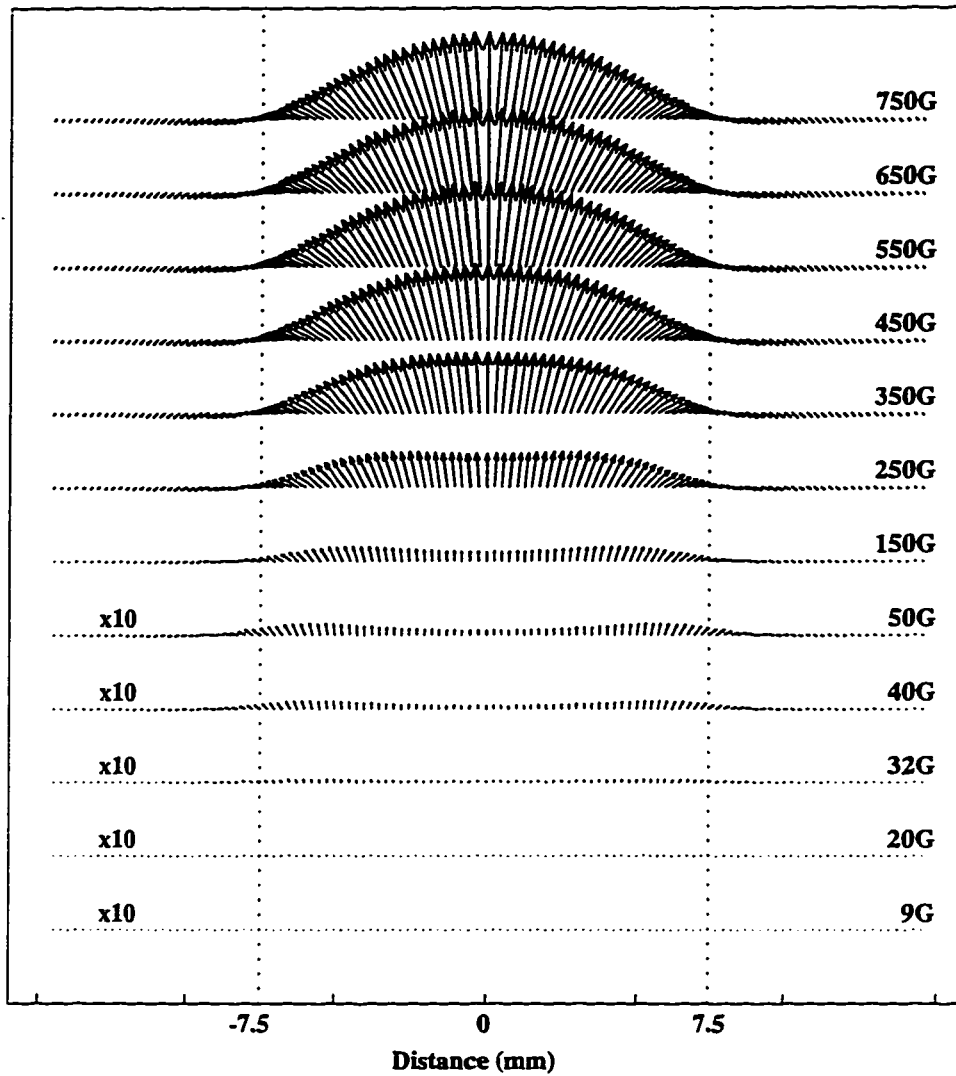


Figure 5.1.8: The vectors of the trapped field measured at $30K$ as a function of position along the diameter of disk #2 (and a distance of $3mm$ above its surface) for different applied fields. The magnitude of each vector is proportional to the magnitude of the total field at the same position. Distances $-7.5mm$ and $7.5mm$ mark the disk's edges.

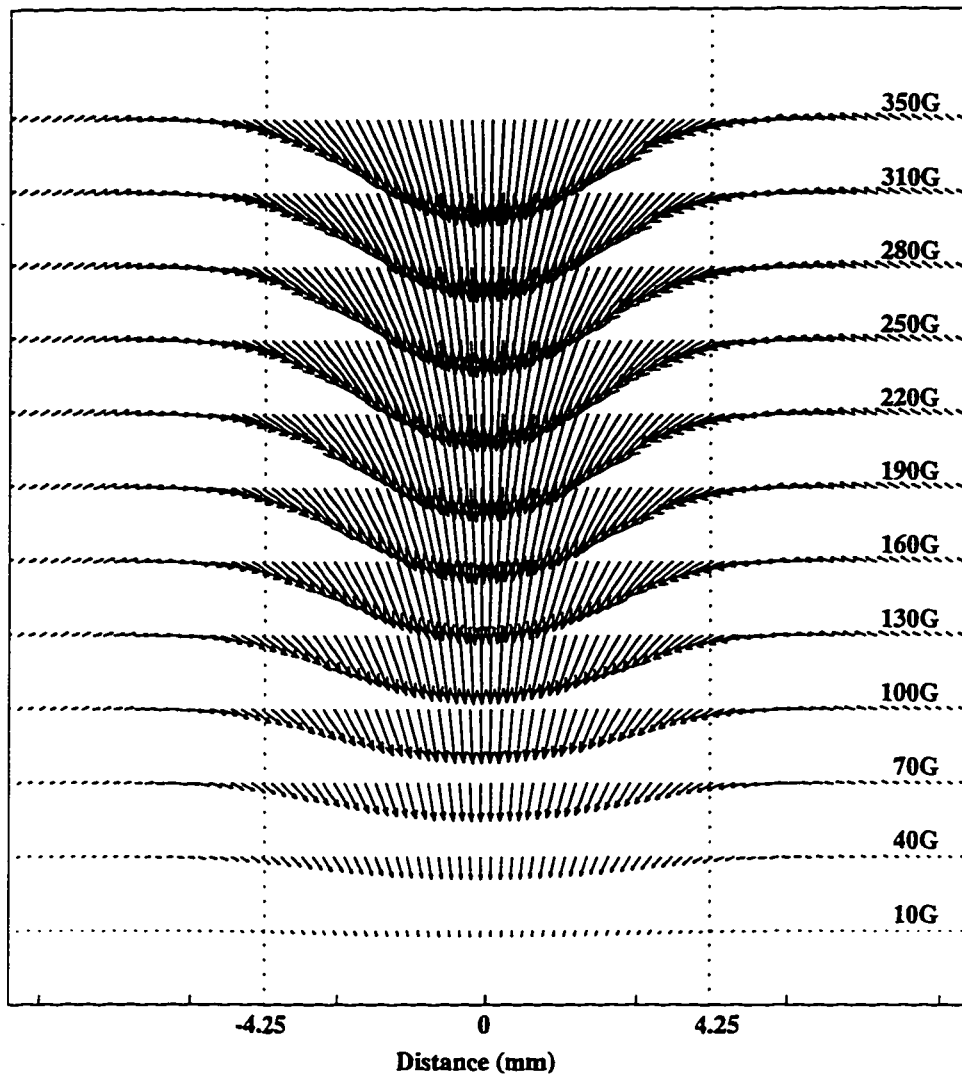


Figure 5.1.9: The vectors of the shielding field measured at $30K$ as a function of position along the diameter of ring #1 (and a distance of $3mm$ above its surface) for different applied fields. The magnitude of each vector is proportional to the magnitude of the total field at the same position. Distances $\pm 4.25mm$ and $\pm 2.50mm$ mark the outer and inner ring's edges, respectively.

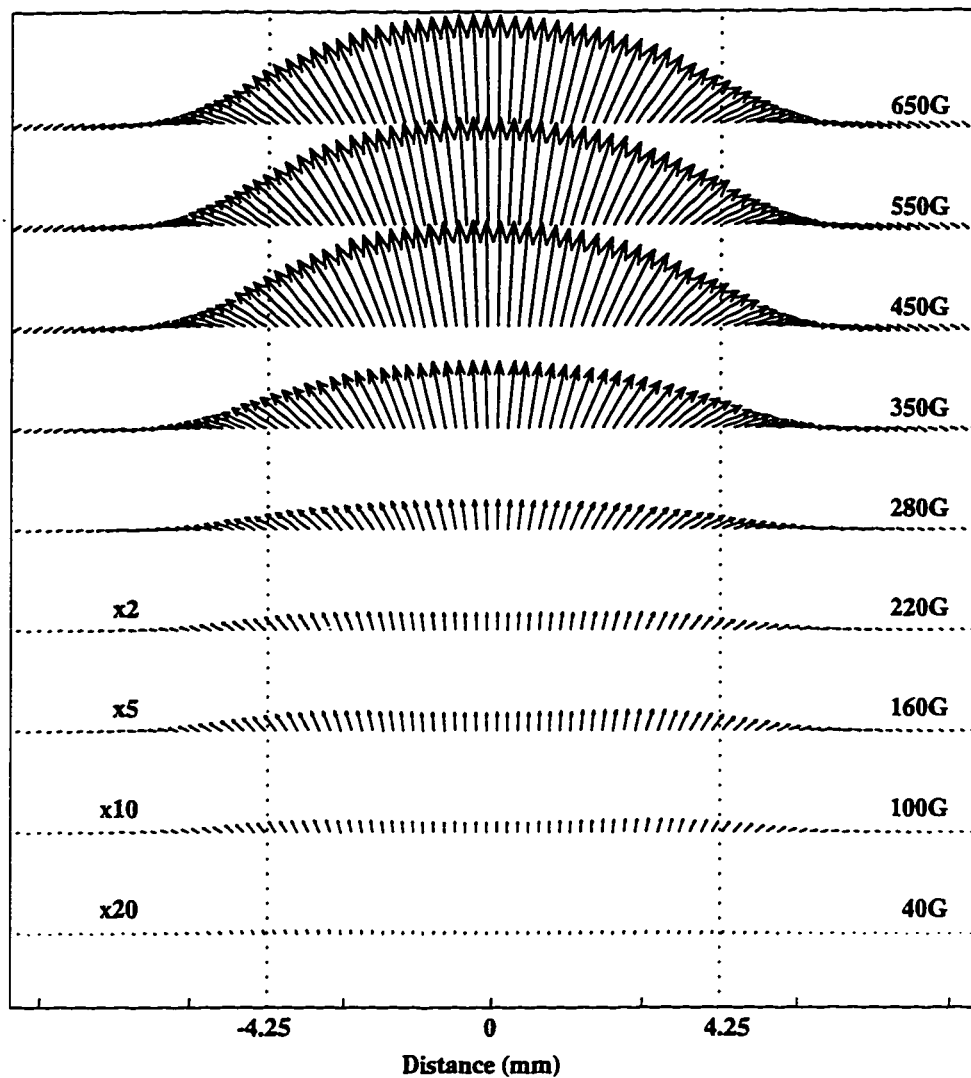


Figure 5.1.10: The vectors of the trapped field measured at $30K$ as a function of position along the diameter of ring #1 (and a distance of $3mm$ above its surface) for different applied fields. The magnitude of each vector is proportional to the magnitude of the total field at the same position. Distances $\pm 4.25mm$ and $\pm 2.50mm$ mark the outer and inner ring's edges, respectively.

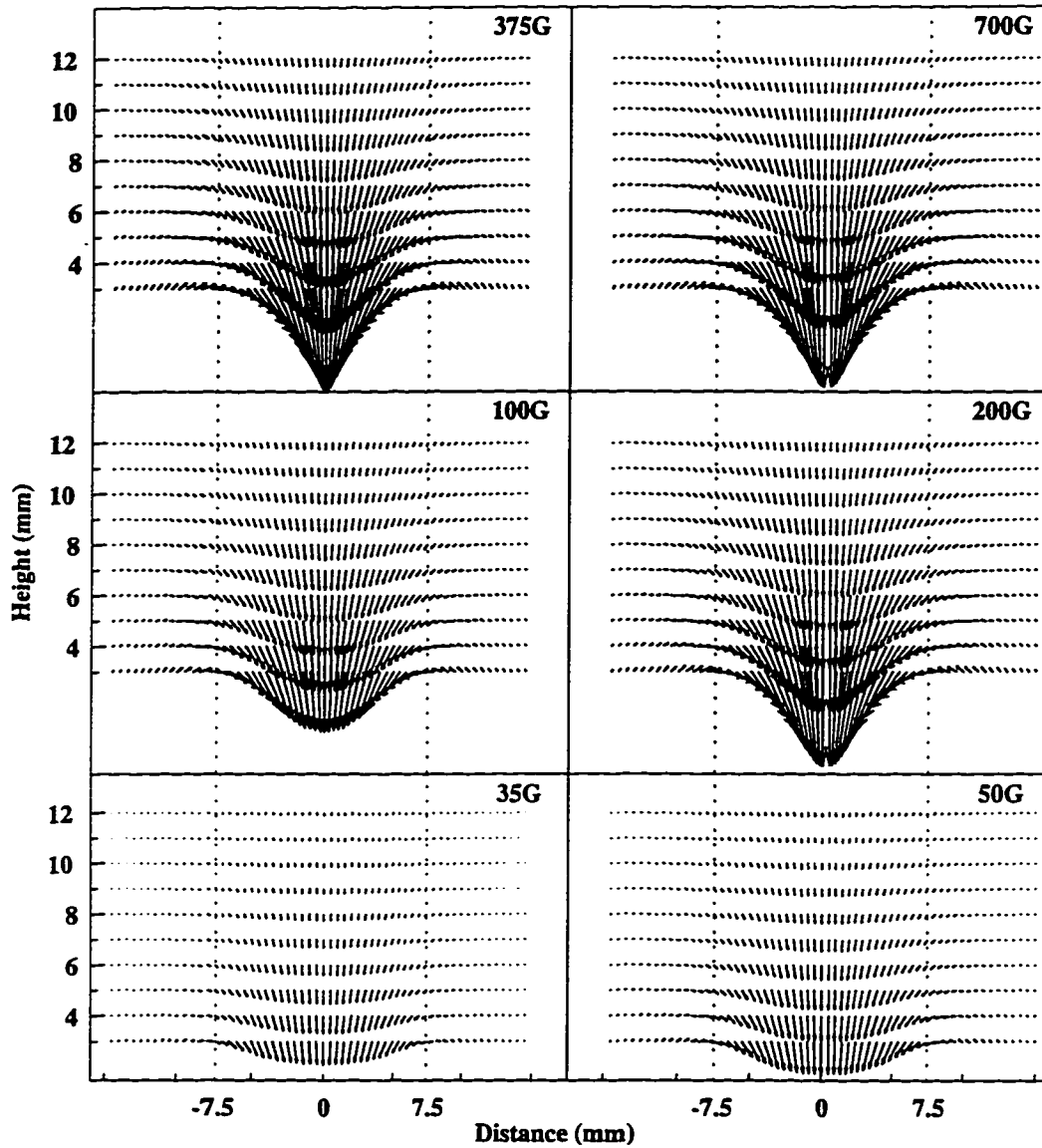


Figure 5.1.11: The vectors of the shielding field measured at distances between 3 and 12mm (every 1mm) above the surface of disk #2 at 30K and at applied magnetic fields of 35, 50, 100, 200, 375 and 700G. The magnitude of each vector is proportional to the magnitude of the total field at the same position normalized to the maximum magnitude of the shielding field in each Figure. Distances -7.5mm and 7.5mm mark the disk's edges.

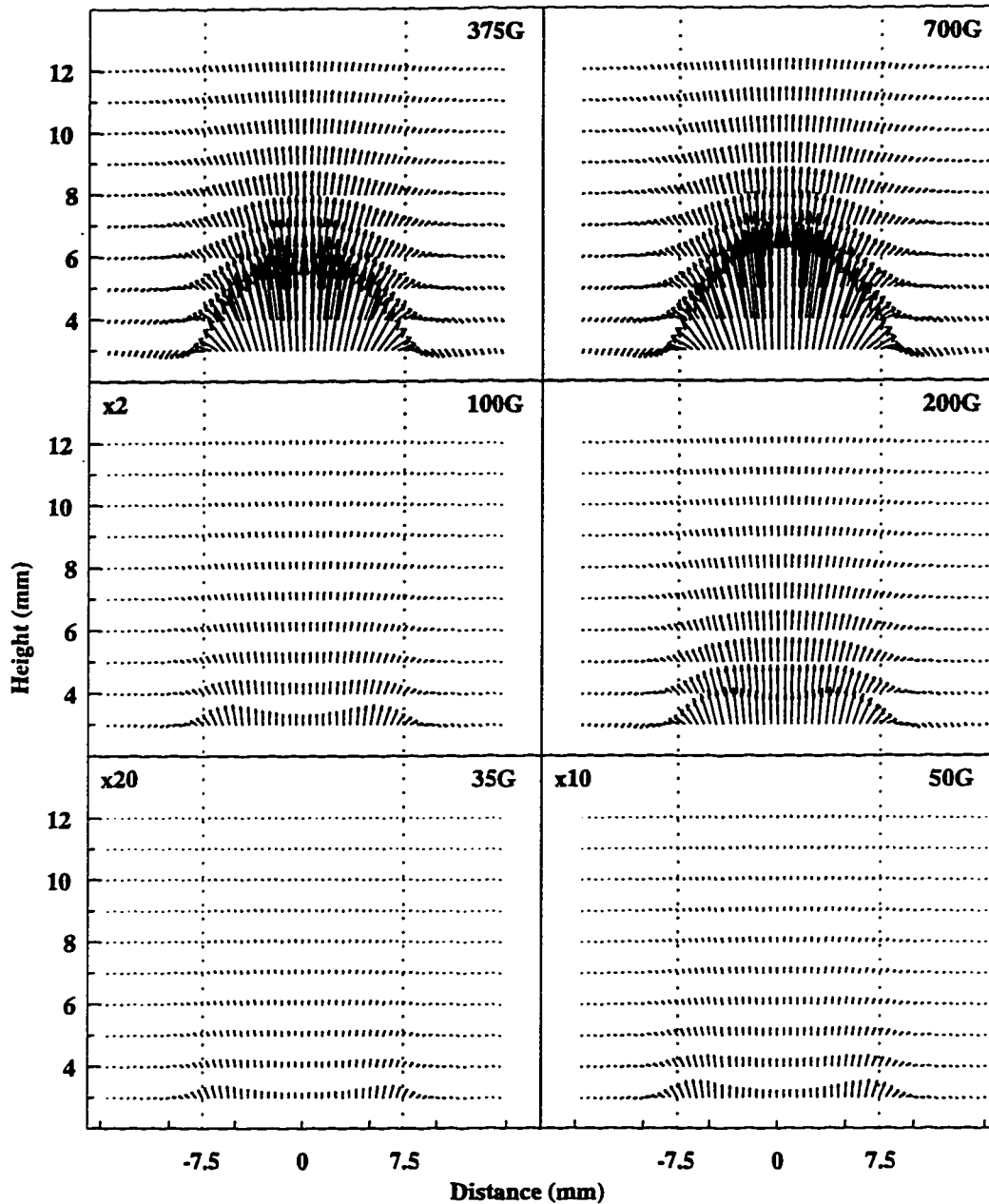


Figure 5.1.12: The vectors of the trapped field measured at distances between 3 and 12mm (every 1mm) above the surface of disk #2 at 30K and at applied magnetic fields of 35, 50, 100, 200, 375 and 700G. The magnitude of each vector is proportional to the magnitude of the total field at the same position normalized to the maximum magnitude of the trapped field in each Figure. Distances -7.5mm and 7.5mm mark the disk's edges. $\times 2$, $\times 10$ and $\times 20$ mark the magnification of the vectors.

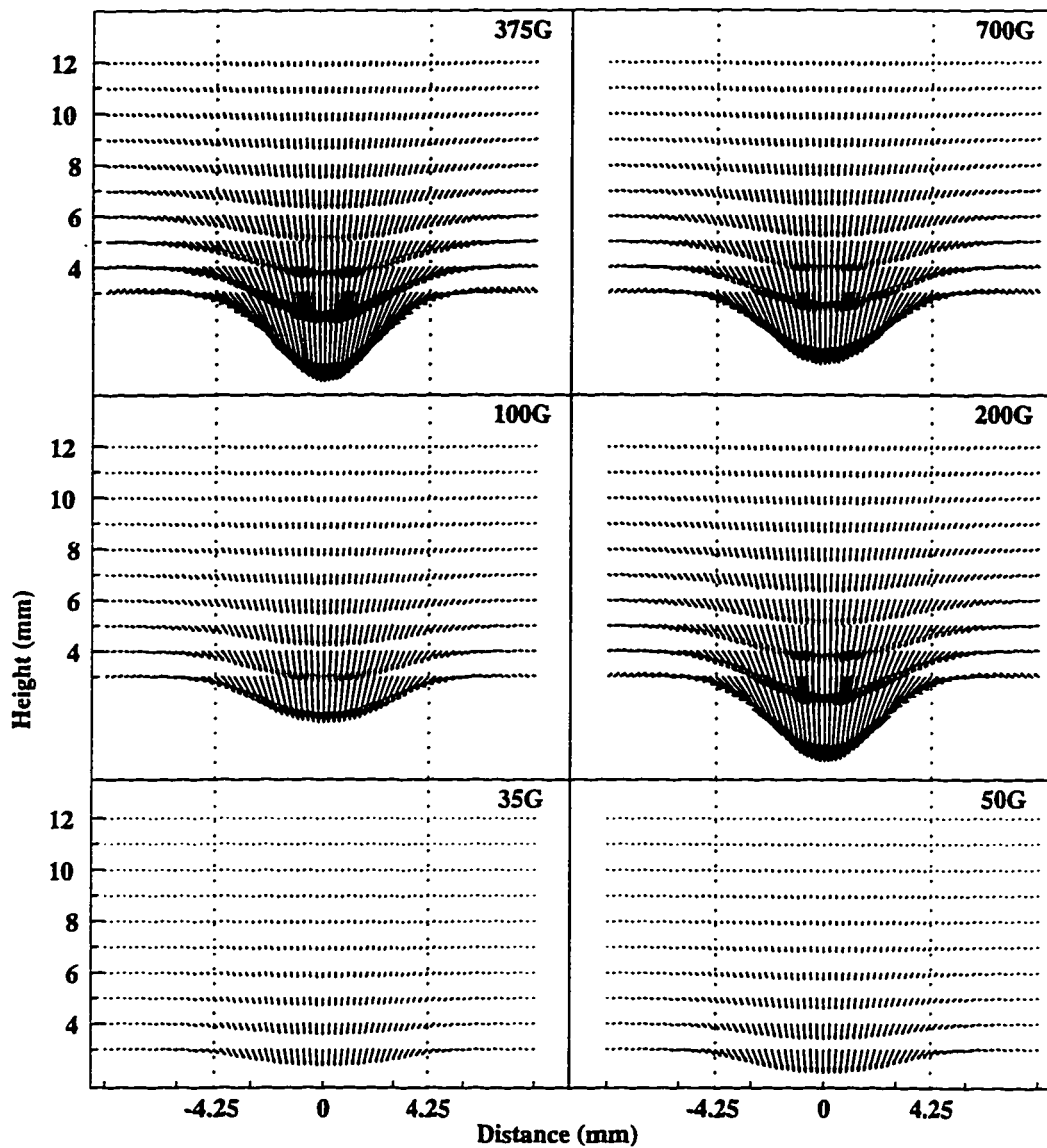


Figure 5.1.13: The vectors of the shielding field measured at distances between 3 and 12mm (every 1mm) above the surface of ring #1 at 30K and at applied magnetic fields of 35, 50, 100, 200, 375 and 700G. The magnitude of each vector is proportional to the magnitude of the total field at the same position normalized to the maximum magnitude of the shielding field in each Figure. Distances $\pm 4.25\text{mm}$ and $\pm 2.50\text{mm}$ mark the outer and inner ring's edges, respectively.

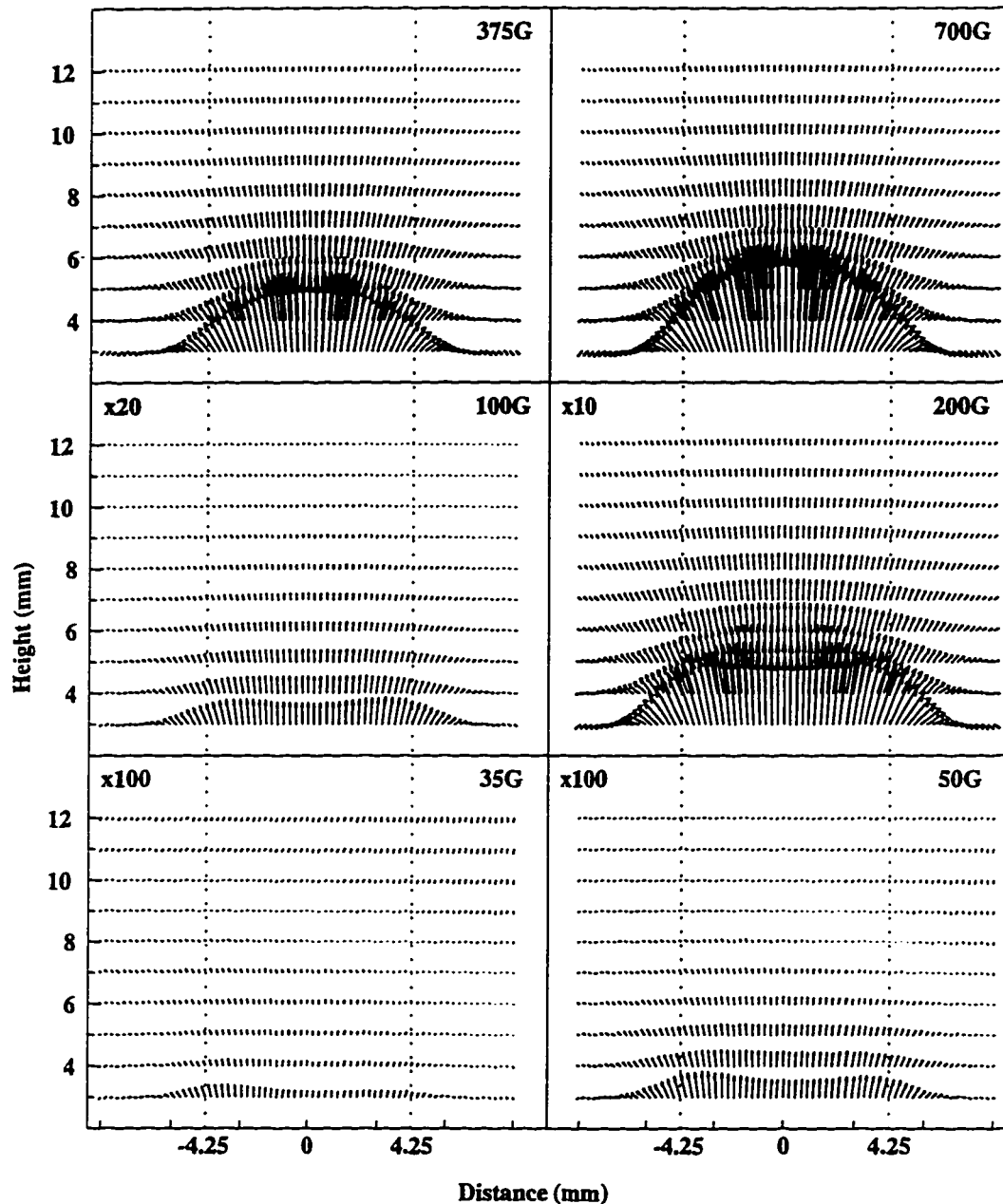


Figure 5.1.14: The vectors of the trapped field measured at distances between 3 and 12mm (every 1mm) above the surface of ring #1 at 30K and at applied magnetic fields of 35, 50, 100, 200, 375 and 700G. The magnitude of each vector is proportional to the magnitude of the total field at the same position normalized to the maximum magnitude of the trapped field in each Figure. Distances $\pm 4.25\text{mm}$ and $\pm 2.50\text{mm}$ mark the outer and inner ring's edges, respectively. $\times 10$, $\times 20$ and $\times 100$ mark the magnification of the vectors.

5.1.2 Crossover between partial and complete flux penetration regimes

The crossover was investigated in YBCO disk #1 using temperature dependence of the axial component of the magnetic field trapped in the disk. The profiles of the axial component of the magnetic field shielded by disk #1 when an external magnetic field of 200 G was applied to the zero-field-cooled (ZFC) sample are plotted in Figure (5.1.15) for various temperatures between 60 K and 86 K. These distributions do not indicate which temperature corresponds to a complete penetration of the magnetic flux into the disk. This information is provided by the profiles of the axial components of the magnetic field trapped in the disk at various temperatures when an external field of 200 G was reduced to zero [Figure (5.1.16)]. The crossover between partial and complete flux penetration can be seen even more clearly in Figure (5.1.17) where the magnetic field trapped in the disk's center is plotted versus temperature for constant applied magnetic fields of 40, 80, 123 and 200 G. The maximum in the trapped field (and the inflection point on the shielding field versus temperature curve) indicate the crossover temperature. The magnitude of the trapped field at the maximum decreases linearly with increasing crossover temperature [Figure (5.1.18)(a)]. This could also be seen in Figure (5.1.17)(d). The maximum trapped field is also proportional to the minimum magnitude of the applied field required for a complete flux penetration [Figure (5.1.18)(b)].

5.1.3 Magnetic relaxation in the partial and complete flux penetration regimes

Magnetic relaxation measurements were performed on two samples of different geometry: disk #1 and ring #1 which was etched out from disk #1. The magnetic

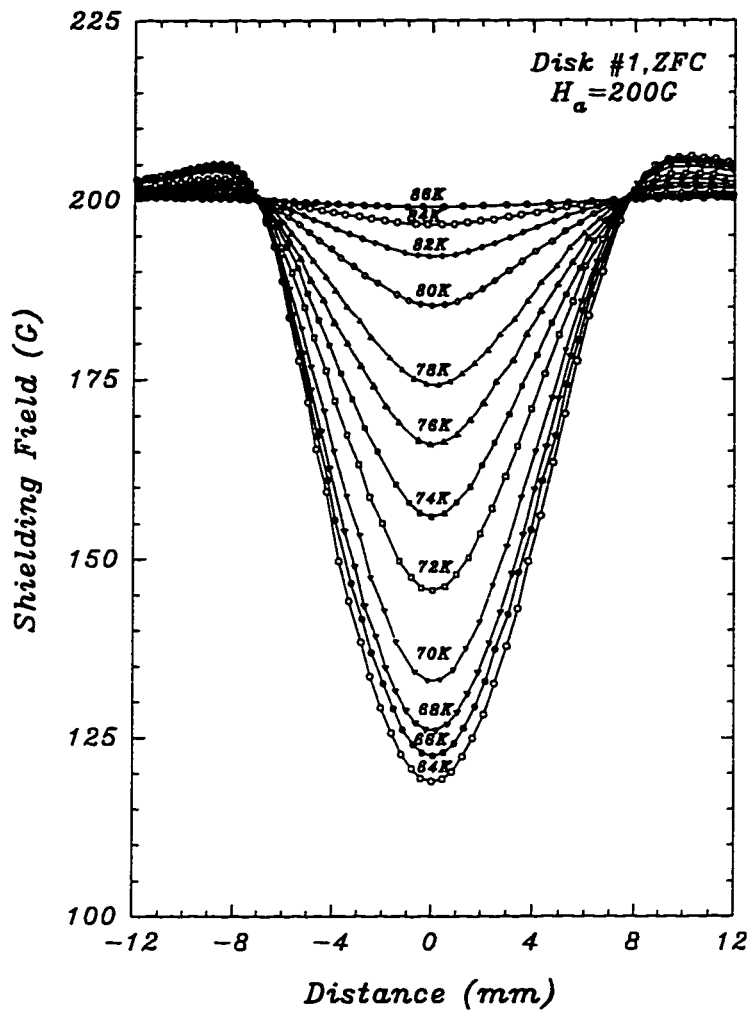


Figure 5.1.15: The profiles of the axial component of the magnetic field shielded by a zero-field-cooled disk #1 which were measured at a distance of 3mm above the disk's surface at various temperatures between 60 and 90 K in the presence of an external field of 200 G. Distances +7.5 mm and -7.5 mm mark the disk's edges.

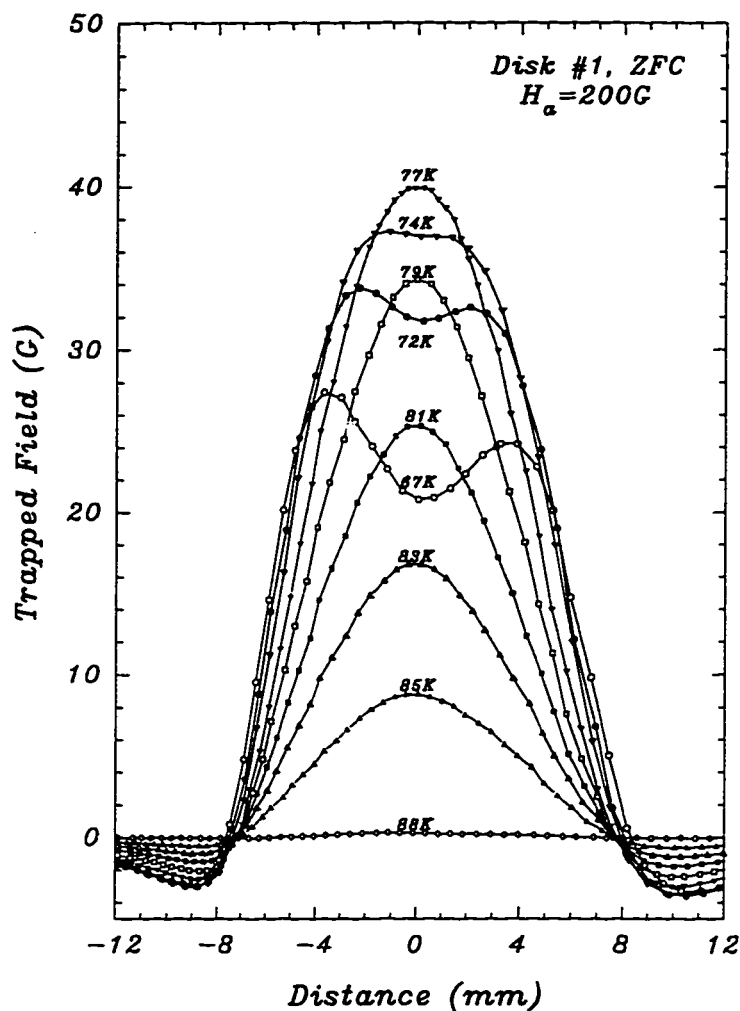


Figure 5.1.16: The profiles of the axial component of the magnetic field trapped in a zero-field cooled disk #1 which were measured at a distance of 3mm above the disk's surface at various temperatures between 60 and 90K after an external field of 200 G was removed. A complete flux-penetration-state is reached, above 77K. Distances +7.5 mm and -7.5 mm mark the disk's edges.

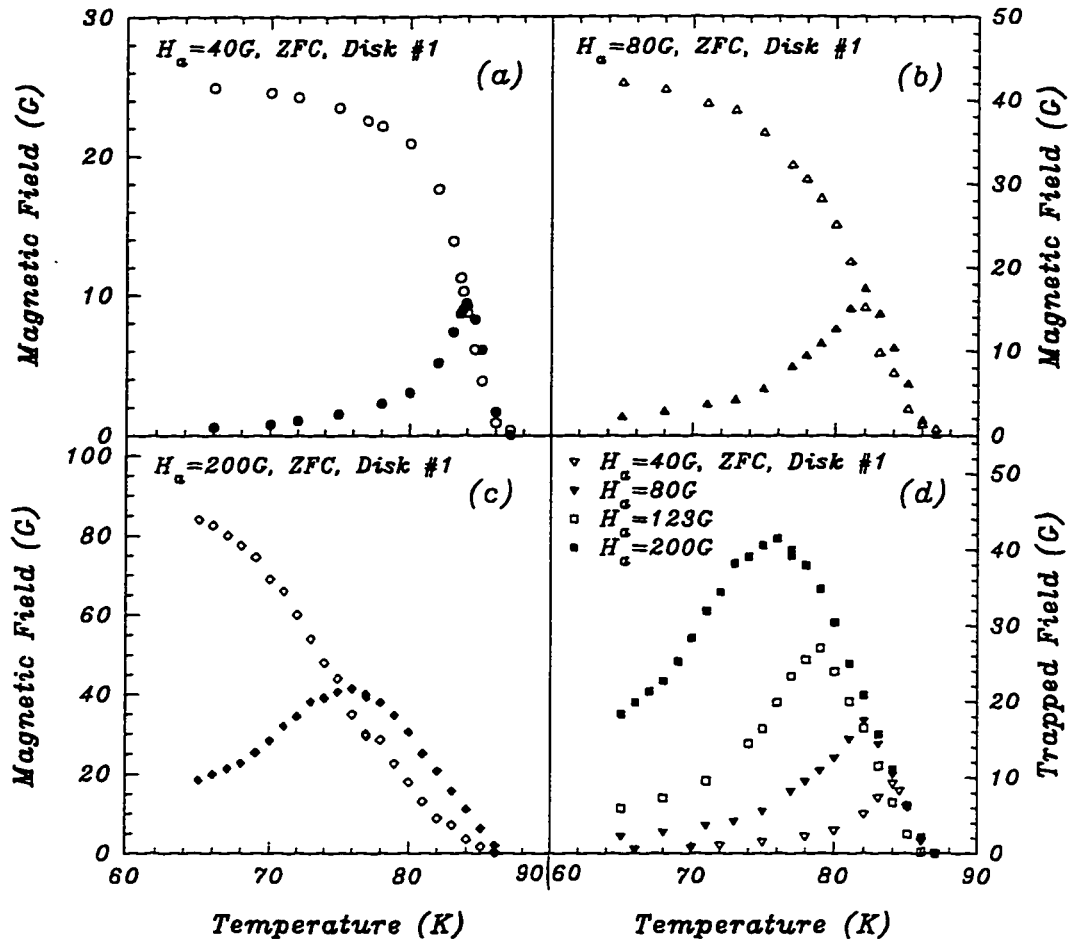


Figure 5.1.17: Open symbols mark temperature dependence of the axial component of the magnetic field shielded in the center of a zero-field-cooled disk #1 in the presence of external fields of 40 G (a), 80 G (b) and 200 G (c). Solid symbols mark temperature dependence of axial component of the the magnetic field trapped in the center of the disk after the applied field was reduced to zero. The maximum trapped field indicates the crossover between a partial and complete flux-penetration-regimes. Note that this maximum coincides with the inflection point on the shielding field versus temperature curve. (d) Temperature dependence of the field trapped in disk #1, plotted for various applied fields between 40 G and 200 G. The complete-flux-penetration regime is common for all trapped fields at temperatures higher than that corresponding to the maximum trapped field. Discrepancies observed for various applied fields are caused by the time decay of the trapped field.

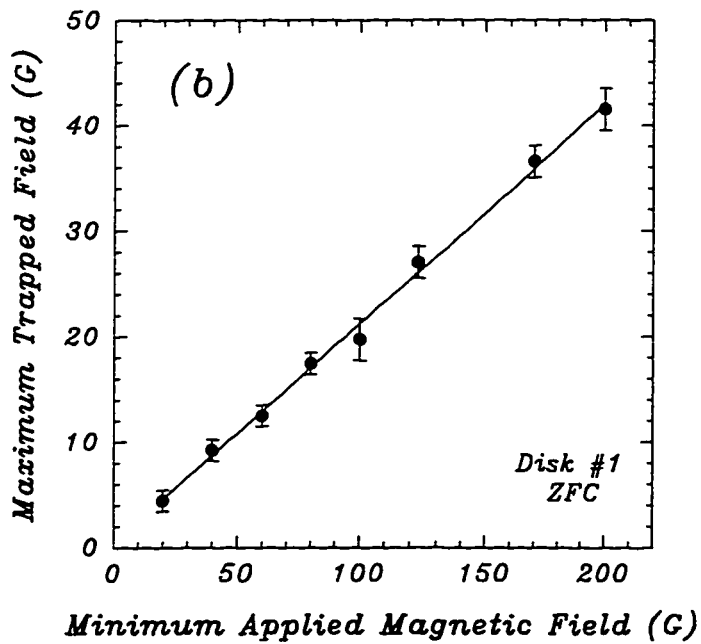
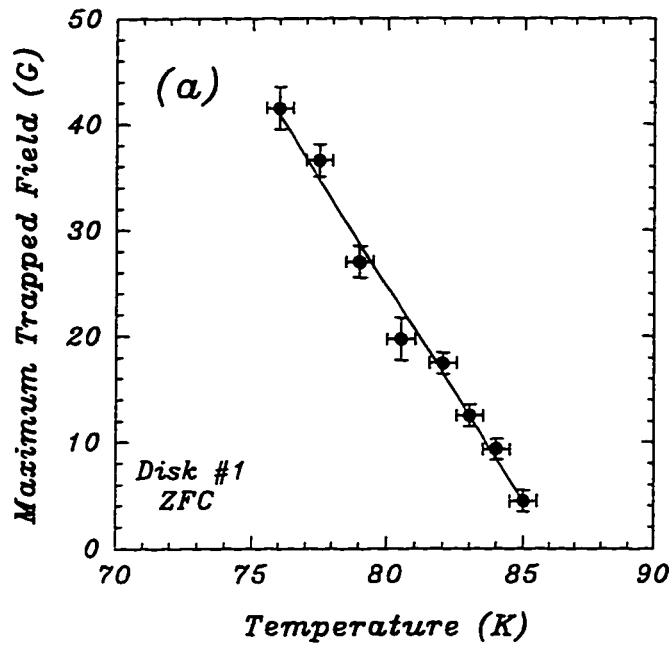


Figure 5.1.18: (a) Temperature dependence of the maximum axial magnetic field which can be trapped in the center of a zero-field-cooled disk #1. (b) Dependence of the maximum axial trapped field on the minimum magnitude of the external magnetic field required for a complete flux penetration.

properties of disk #1 and ring #1 show some similarities. For example it was found that the temperature dependence of the maximum axial field trapped in the disk and that of the axial component of the magnetic field generated by the critical persistent current circulating in the ring coincide [Figure (5.1.19)].

Figures (5.1.20) and (5.1.21) show the distributions of the axial component of the trapped magnetic flux measured across disk #1 at 79K (corresponding to a complete flux penetration state after a field of 200 G was applied to the zero-field-cooled sample and subsequently removed) and at 67K (corresponding to an incomplete flux penetration). They are plotted together with the distribution of the normalized decay rates $S = (1/B_o)dB/d \ln t$ for the motion of the trapped flux (S was measured over a time range $1 - 10^4$ sec. The decay rates are logarithmic in time up to a maximum waiting time of 10^4 sec). A complete flux penetration condition is characterized by the normalized decay rates which do not vary much ($0.012 < S < 0.015$) across the disk. For an incomplete flux penetration S has a minimum (at $S = 0.0045$) at the disk's center and a maximum (at $S = 0.012$) at the disk's edge. The magnetic field trapped in the disk's center when a field of 200 G was applied to the zero-field-cooled sample (and subsequently removed) is plotted with the corresponding normalized decay rate S versus temperature (over a range of 65 - 85K) in Figure (5.1.22). The decay rates are independent of temperature at temperatures corresponding to a complete (with an average $S = 0.015$) and an incomplete (with an average $S = 0.0055$) flux penetration regimes. The decay rates in a complete flux penetration regime are approximately two times the value observed for an incomplete flux penetration at the same temperature range.

For ring #1, the axial component of the magnetic field trapped in the center of the zero-field-cooled ring, when a field of 200 G was applied to it (and subsequently removed), is plotted together with the corresponding normalized decay rates versus

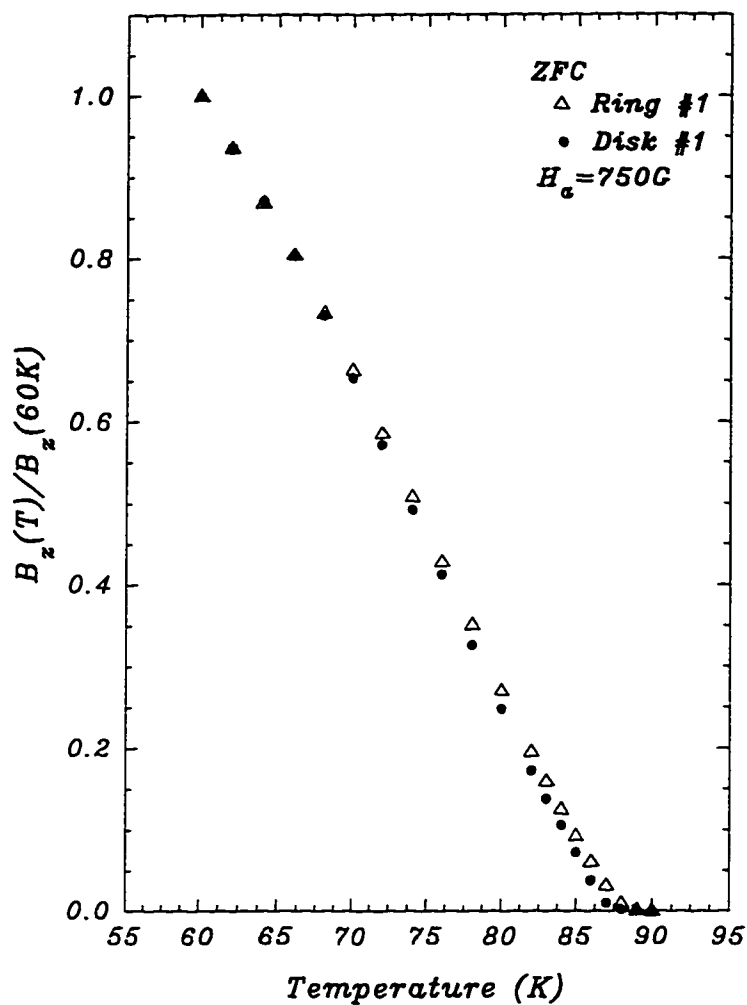


Figure 5.1.19: Temperature dependence of the maximum axial field trapped in a zero-field-cooled disk #1 (solid symbols) and that of the axial component of the magnetic field generated by the critical persistent current circulating in a zero-field-cooled ring #1 (open symbols) which was etched out from disk #1. A magnetic field of 750 G was used to saturate the trapped magnetic field and the persistent current.

temperature (over a range of 50 - 85K) in Figure (5.1.23). The decay rates are independent of temperature at temperatures above 64K, corresponding to a complete critical state (with an average $S = 0.0145$), and at temperatures below 63K, corresponding to a partial critical state (with an average $S = 0.0025$). The distributions of the axial component of the trapped magnetic field, in a complete and partial critical state, are presented in Figure (5.1.24), for temperatures between 50K and 90K.

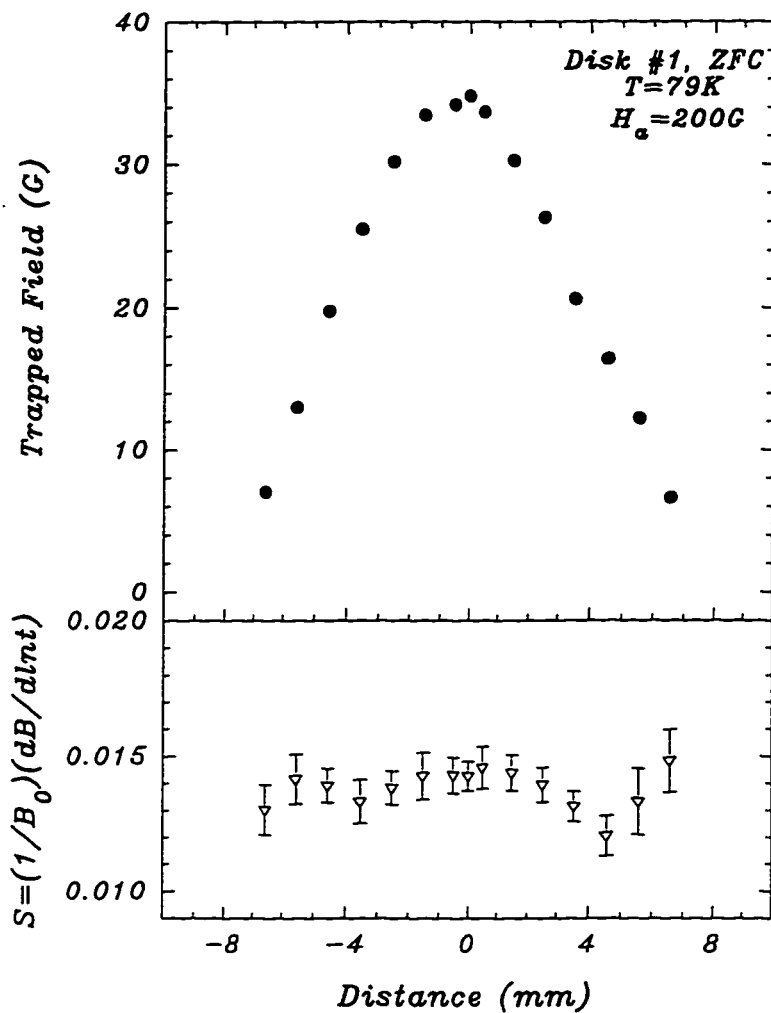


Figure 5.1.20: Upper figure: The distributions of the axial component of the trapped magnetic field measured across disk #1 at a distance of 3mm above the disk's surface at 79 K. This represents the case of a complete flux penetration after a field of 200G was applied to the zero-field-cooled sample and subsequently removed . Lower figure: The corresponding distributions of the normalized decay rate $S = (1/B_0)(dB/dlnt)$ for the motion of the trapped flux.

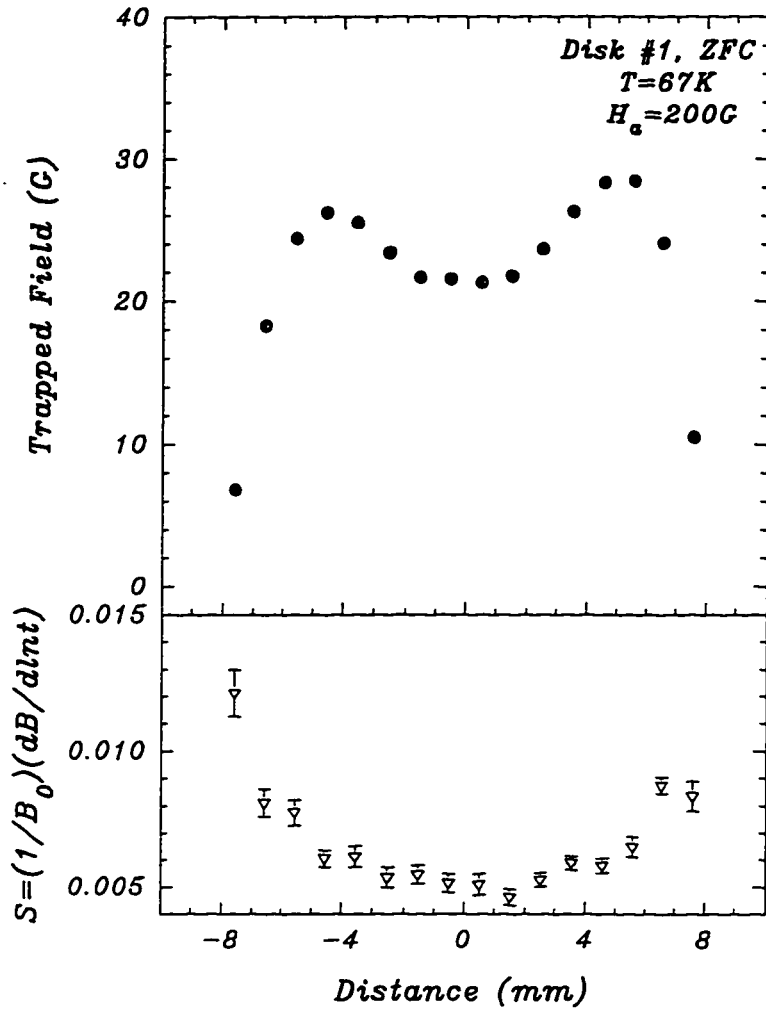


Figure 5.1.21: The distributions of the axial component of the trapped field (upper figure) and the normalized decay rate S (lower figure) measured across disk #1 at a distance of 3mm above the disk's surface at 67K. This represents the case of an incomplete flux penetration after a field of 200 G was applied to the zero-field-cooled sample and subsequently removed.

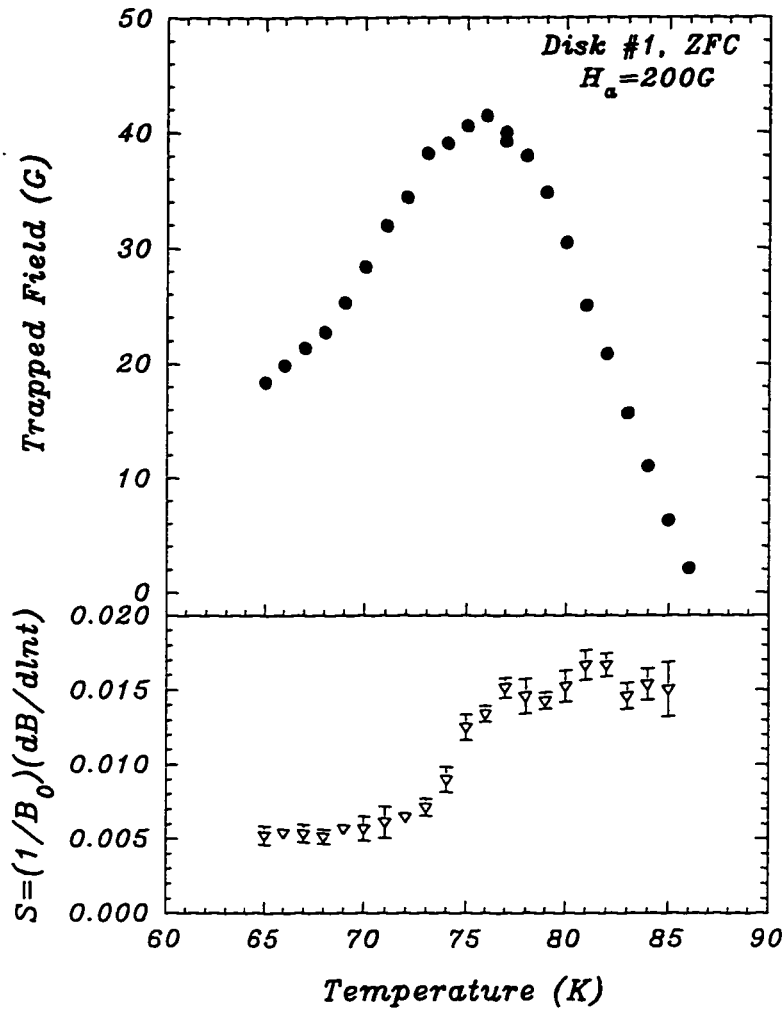


Figure 5.1.22: Temperature dependence of the axial component of the trapped field (upper figure) and the normalized decay rate S (lower figure) measured in the center of disk #1 at a distance of 3mm above the surface when a field of 200 G was applied to the zero-field-cooled sample and subsequently removed.

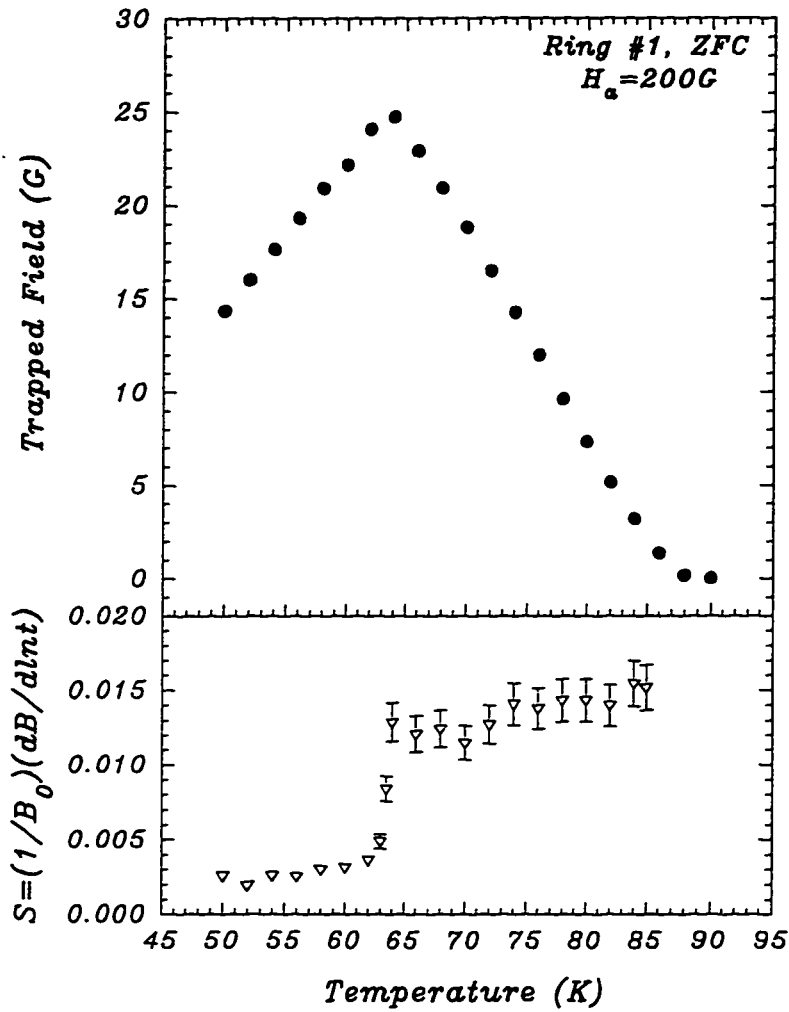


Figure 5.1.23: Temperature dependence of the axial component of the trapped field and the normalized decay rate S measured in the center of ring #1 at a distance of 3mm above the ring's surface when a field of 200 G was applied to the zero-field-cooled sample.

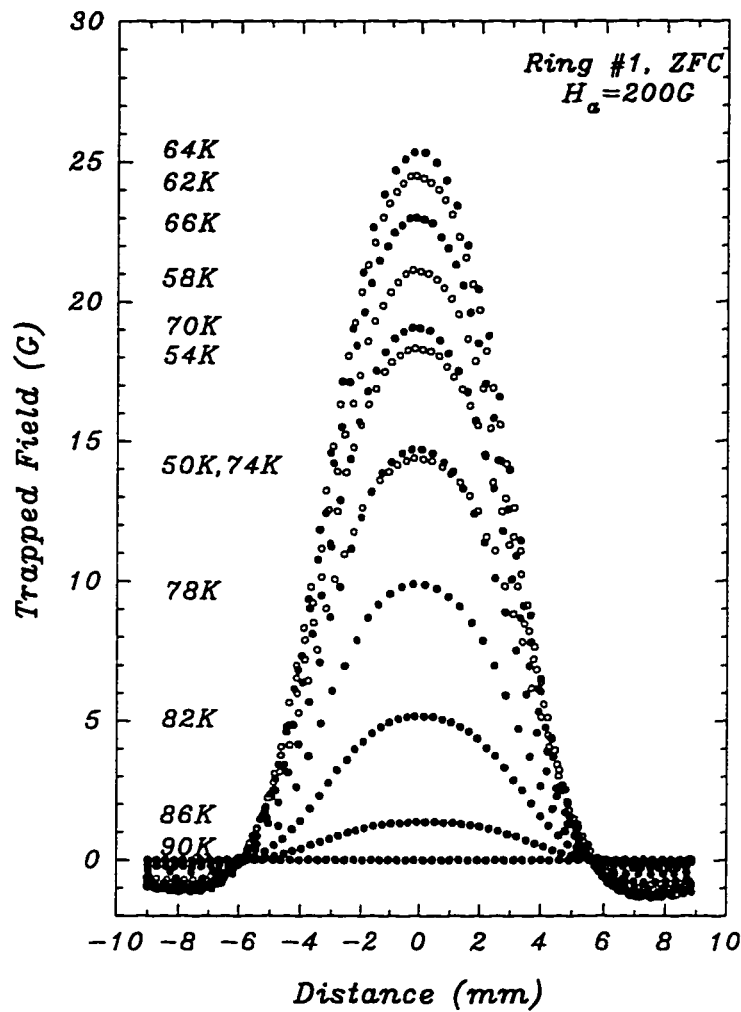


Figure 5.1.24: The distributions of the axial component of the trapped field in ring #1 at various temperatures between 50 and 8K, after an external field of 200 G was applied to the zero-field-cooled sample. Distances $\pm 4.25mm$ and $\pm 2.50mm$ mark the outer and inner ring's edges, respectively.

5.2 Discussion:

5.2.1 Calculation of the current density profiles in a disk- and ring-shaped YBCO thin films

The observed stages of flux penetration into disk-shaped YBCO thin film [Section (5.1.1)] is quantitatively described by theoretical models of Mikheenko and Kuzovlev [27] and Zhu et al [48]. These models predict that in the presence of an applied field, magnetic vortices penetrate symmetrically into disk-shaped superconducting thin film from its edge towards a circular area of a radius a smaller than the radius R of the disk. The central area of the disk (of radius a) is free of trapped vortices. Shielding currents of magnitude I_c are induced in a ring of inner radius a and outer radius R . The radius of the vortex-free region decreases with an increasing applied field. This was observed in experiments on disk #2 [Figures (5.1.7) and (5.1.11)] where at very low fields the disk is shielded within a large circular area whose radius decreases with an increasing applied field. We used a computer simulation described in Section (2.2.5) to calculate the magnetic profiles generated by theoretical current distributions predicted by the above models. Figure (5.2.1) presents the experimental results for the axial and radial shielding field profiles for disk #2 at a temperature of $30K$ and in different applied fields from $H_a = 12.5G$ up to $650G$. The solid lines are the theoretical fits with the current distributions defined by Equation (1.17). The current distributions are shown in Figure (5.2.2). Theoretical critical current value J_c used in the simulation was taken to be $J_c = 8.7 \times 10^6 A/cm^2$, which corresponds to the characteristic field $H_d \simeq 110G$ (see Section (5.1.1)). The agreement between the theoretical fits and the experimental data is clear, especially for high applied magnetic fields.

In the remnant state, Zhu *et al* found that when the external field is reduced

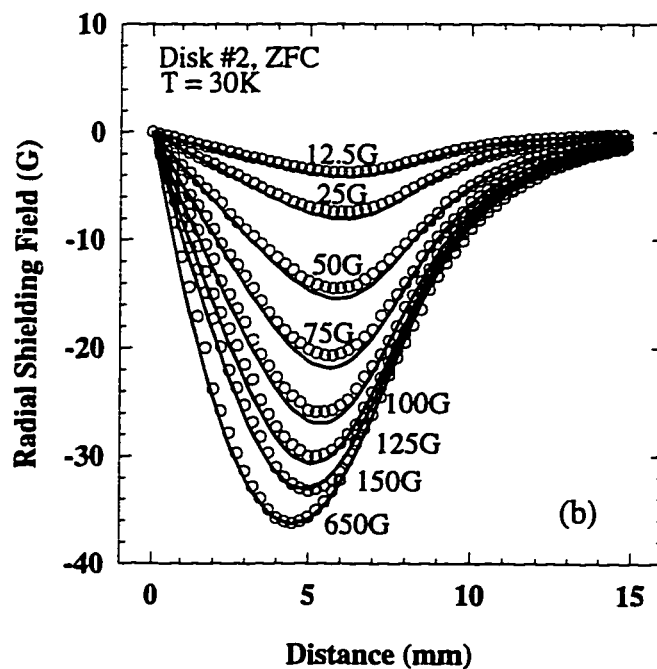
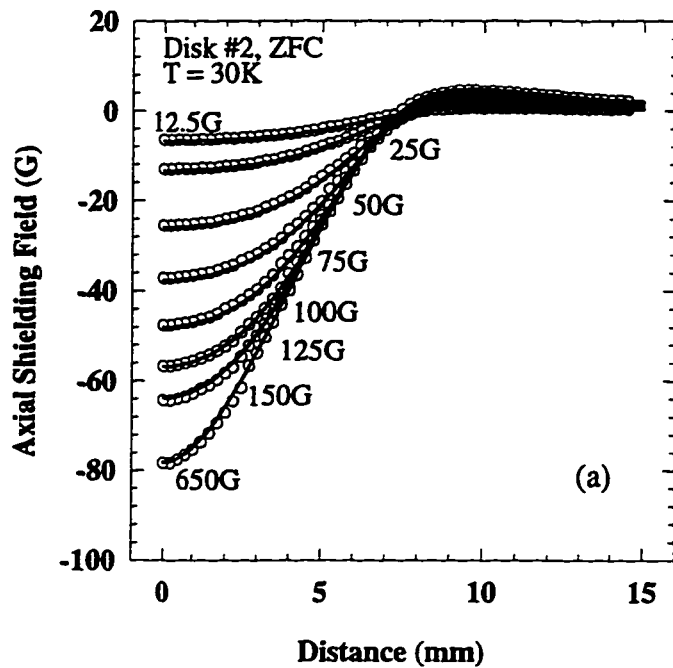


Figure 5.2.1: The profiles of the axial (a) and radial (b) magnetic fields shielded by a zero-field cooled disk #2 in various applied fields and at 30K. Open symbols represent the experimental data measured at a distance of 3mm above the sample, and the solid lines are the theoretical fits based on the current distributions shown in Figure (5.2.2).

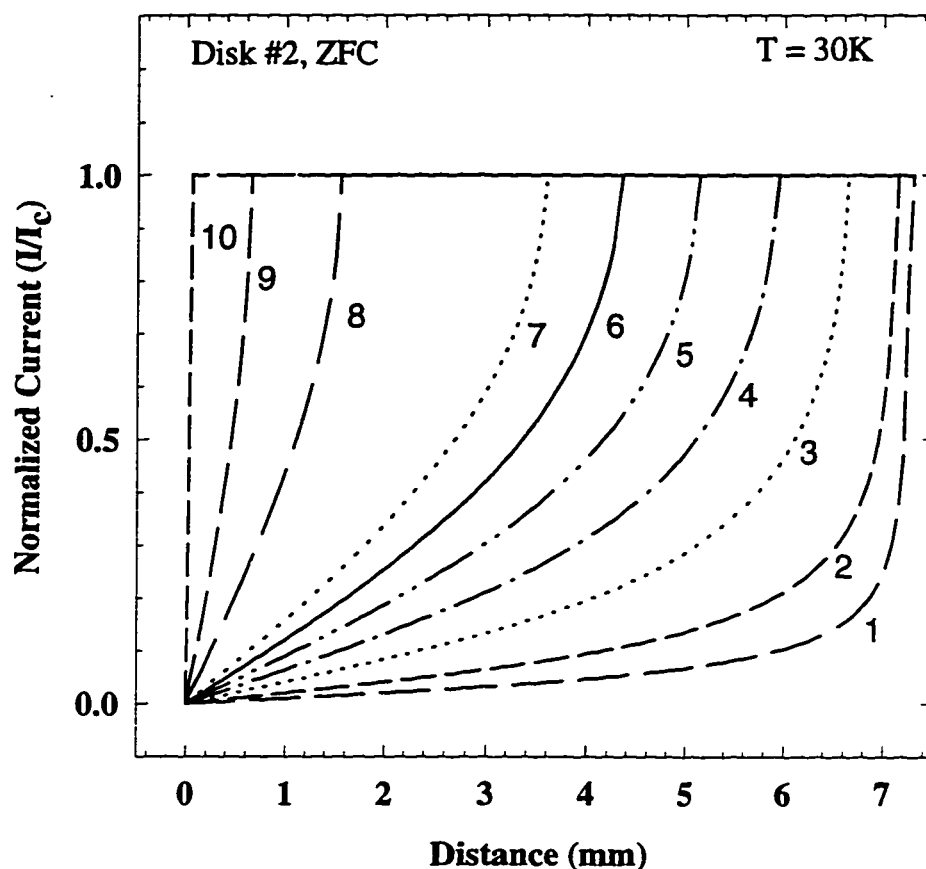


Figure 5.2.2: Normalized current density profiles across disk #2 for the shielding at 30K, calculated using Equation (1.17) for applied fields (H_a) of (1) 12.5 , (2) 25, (3) 50, (4) 75, (5) 100, (6) 125, (7) 150, (8) 350, (9) 650 and (10) 750G . The radius a of the vortex free region was calculated from the formula $a = R/\cosh(H_a/H_d)$ and it marks a distance at which the current I reaches I_c . The critical current density J_c was taken to be $8.7 \times 10^6 \text{ A/cm}^2$.

down to a field $|H| < H_a$ the resulting profile of the current-density have J equal to J_c within an annulus of inner and outer radii b and R , respectively. The reason for this is that the vortices near the outer radius R experience a Lorentz force that drives them out of the sample when the field is decreasing [49]. We performed computer simulation of the magnetic field generated by the theoretical current distribution defined by Equation (1.19), and obtained the theoretical fits to the experimental data shown in Figure (5.2.3). The theoretical current distributions, that were applied to perform the fits with $J_c = 9.9 \times 10^6 \text{ A/cm}^2$ and $H_d \simeq 125G$, are shown in Figure (5.2.4). The theoretical fits agree with most of the experimental data, but the fits are better when the trapped field reaches saturation at high applied fields. A discrepancy at smaller applied fields could be due to non-symmetrical distribution of the penetrating vortices. Density of the vortices increases with an increasing applied field and the vortex distribution is more symmetric around the center of the disk. However, different fitting values of J_c (and H_d) that were used to fit the shielding and trapped fields at the same temperature is inconsistent with the theory. In order to explain this discrepancy we refer to the dependence of the trapped and shielding fields on the applied field [Figure (5.1.5)]. The trapped fields saturate at higher fields [Figures (5.1.5)(a) and (5.1.5)(c)] while the shielding fields reach a maximum before decreasing with an increasing applied field [Figures (5.1.5)(b) and (5.1.5)(d)]. Therefore, it appears that in the trapped field regime the influence of local fields on J_c is negligible but in the presence of an external field (the shielding field regime) a local field $B(r)$ is strong enough to affect J_c . Moraitakis *et al* [103] found that taking the Kim's relationship $J_c = J_c(0)/(1 + H_a/B_0)$, where $J_c(0)$ is the critical current at zero field and B_0 is a constant, gives better theoretical fits to their experimental data of $J_c(H_a)$ at very high applied fields.

The current distribution of Mikheenko and Kuzovlev and Zhu *et al* describes well the magnetic profiles for a complete and partial flux penetration in the remnant

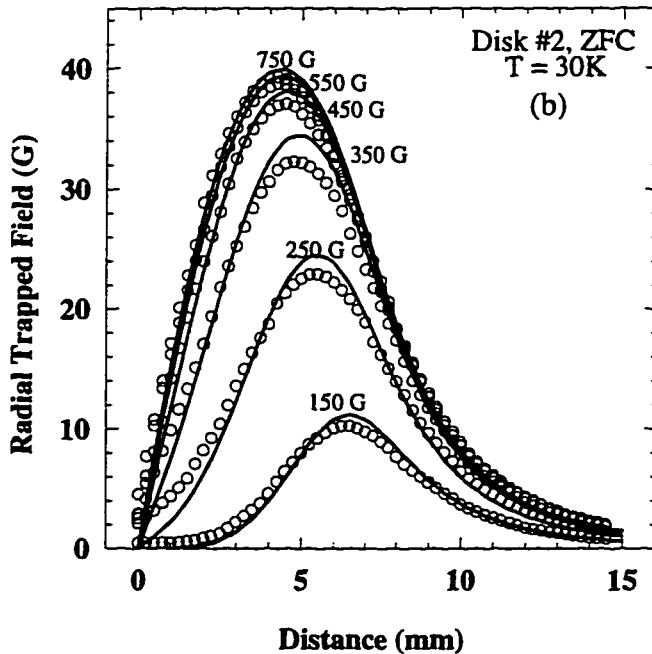
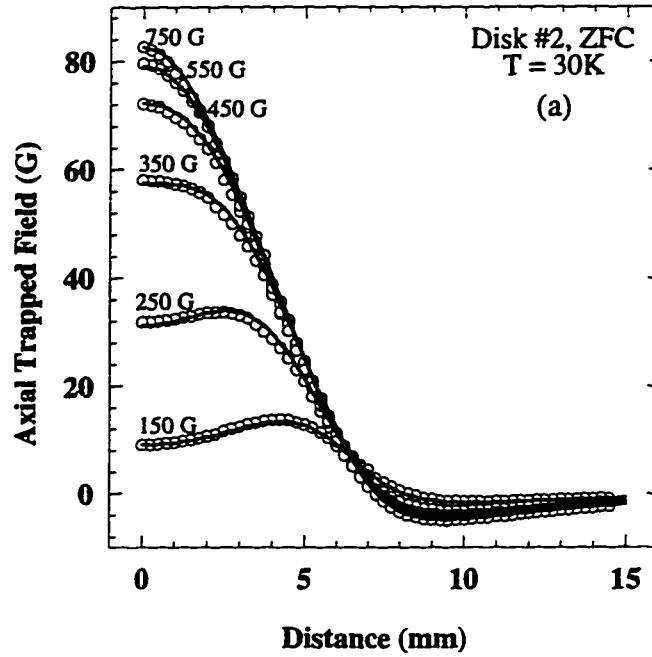


Figure 5.2.3: The profiles of the axial (a) and radial (b) magnetic fields trapped in zero-field-cooled disk #2 in various applied fields and at 30K. Open symbols represent the experimental data measured at a distance of 3mm above the sample, and the solid lines are the theoretical fits based on the current distributions shown in Figure (5.2.4).

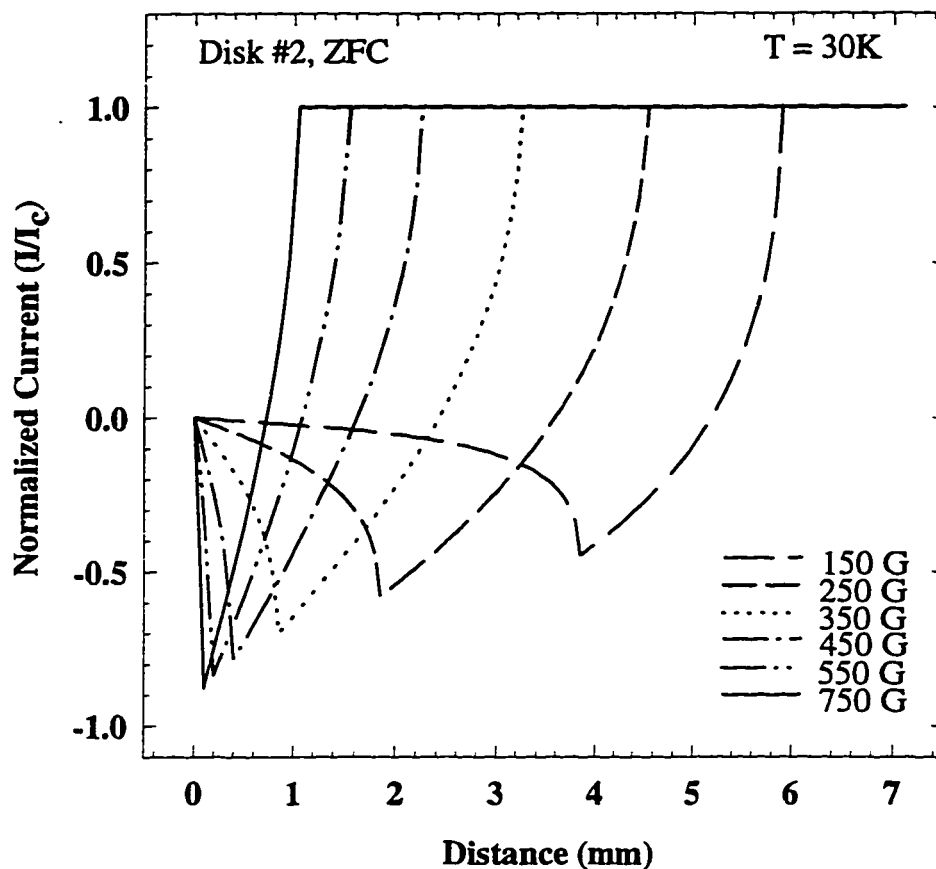


Figure 5.2.4: Normalized current density profiles across disk #2 at 30K calculated using Equation (1.19) for an applied field $H_a = 150, 250, 350, 450, 550$ and $750G$. The radius a of the vortex free shielded region was calculated from the formula $a = R/\cosh(H_a/H_d)$ and it marks a distance at which the current I (for each H_a) achieves the lowest negative value. The inner radius b of the annular ring at which the current I reaches I_c is given by $b = R/\cosh(H_a/2H_d)$. The critical current density was taken to be $9.9 \times 10^6 A/cm^2$.

state (trapped field regime) for temperatures higher than $30K$. Figures (5.2.5) and (5.2.7) show the theoretical fits to the experimental data for trapped fields using the critical state model in a disk at temperatures of $40K$ and $50K$ with the corresponding characteristic fields $H_d = 98G$ and $77G$, and the critical densities J_c of $7.8 \times 10^6 A/cm^2$ and $6.1 \times 10^6 A/cm^2$, respectively.

According to Mikheenko and Kuzovlev and Zhu *et al* model for finite fields H_a , the annular region where J_c is constant never fills the entire disk (the vortex free region has a radius $a = R / \cosh(H_a/H_d)$ which is zero only at an infinitely large applied field), implying that the critical state flux does not reach the disk's center. We calculated the radius a of this flux-free region together with the inner radius b of the annular region where J_c is constant in the remnant state ($b = R / \cosh(H_a/2H_d)$) for a maximum available field of $750G$ and a minimum applied field at which trapped fields saturate [Table 5.1]. In the presence of the external field (shielding regime), the radius a at $30K$ and a maximum applied field of $750G$ is only 0.5% of the disk radius R but it decreases down to $1 \times 10^{-8} \%$ at $70K$. This indicates that the critical state flux penetrates the disk almost to the center. In the remnant regime, the inner radius b of the annular ring with constant J_c for $750G$ is 10% of the disk radius R at $30K$, and decreases down to $1.5 \times 10^{-3} \%$ at $70K$. We observed a saturation of the trapped field profiles at $b \lesssim 0.1R$. The radius b decreases with an increasing applied field, however the magnetic field profiles do not change. This could mean that the magnetic fields generated by the currents inside the disk of radius b are too small to be detected at a distance of $3mm$ above the sample where the measurements are taken. The value of b decreases considerably for fields which are ten times higher than the full penetration field H_d . For example for $H_a \sim 10H_d$, $b \sim 0.01R$ (Table 5.1). This implies that Mikheenko and Kuzovlev and Zhu *et al* model could be replaced by the Bean model for fields $H_a \sim 10H_d$ or higher. In order to verify this approximation we calculated the magnetic field profiles at temperatures of $50K$ and $70K$ for an applied

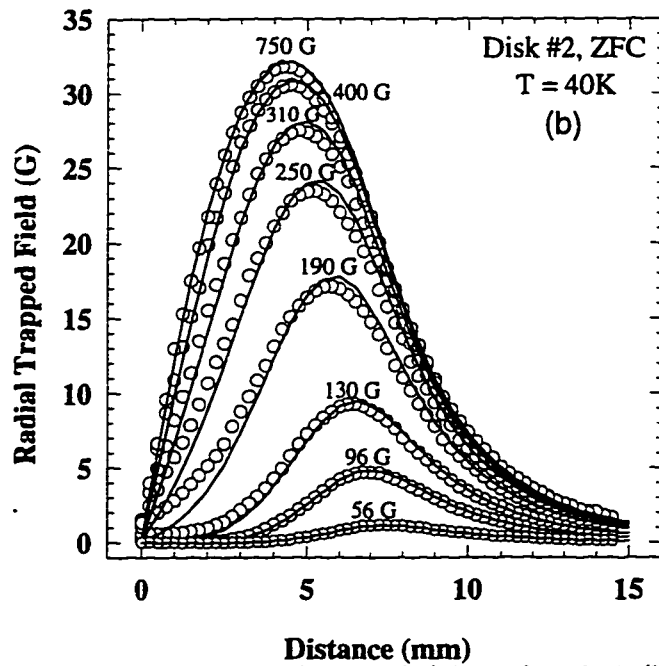
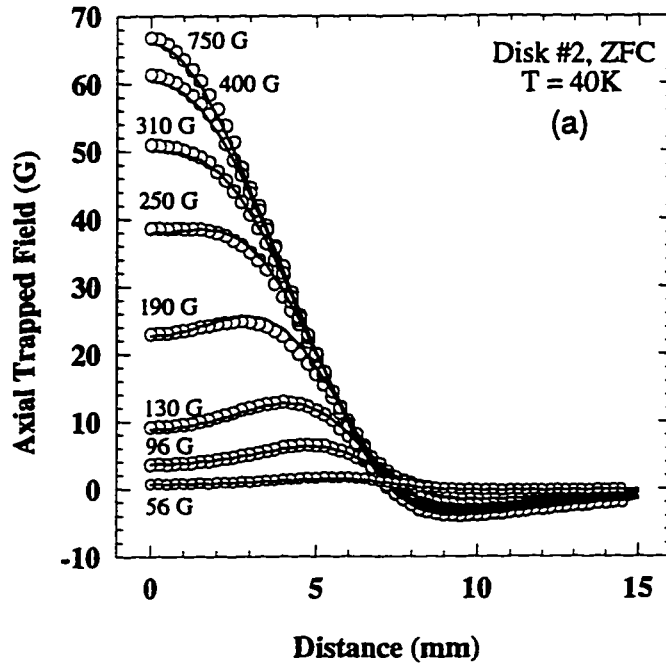


Figure 5.2.5: The profiles of the axial (a) and radial (b) magnetic fields trapped in a zero-field-cooled disk #2 in various applied fields and at 40K. Open symbols represent the experimental data measured at a distance of 3mm above the sample, and the solid lines are the theoretical fits based on the current distributions shown in Figure (5.2.6).

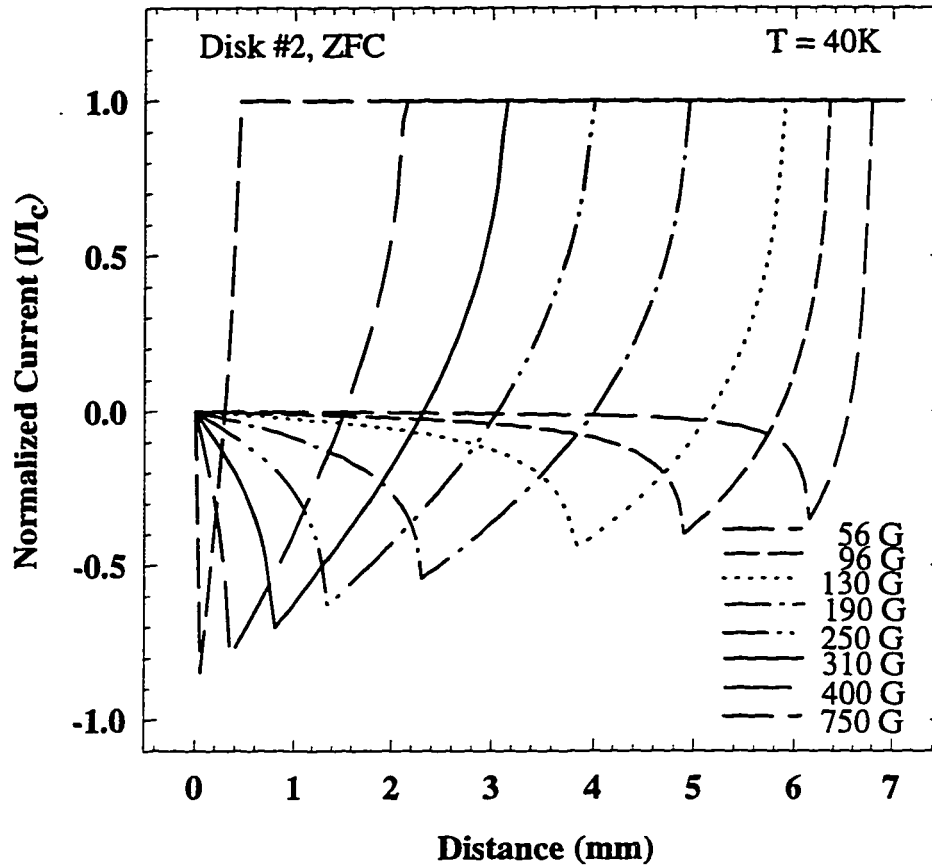


Figure 5.2.6: Normalized current density profiles across disk #2 at 40K calculated using Equation (1.19) for an applied field $H_a = 56, 96, 130, 190, 250, 310, 400$ and 750G . The radius a of the vortex free shielded region was calculated from the formula $a = R/\cosh(H_a/H_d)$ and it marks a distance at which the current I (for each H_a) achieves the lowest negative value. The inner radius b of the annular ring at which the current I reaches I_c is given by $b = R/\cosh(H_a/2H_d)$. The critical current density was taken to be $7.8 \times 10^6 \text{ A/cm}^2$.

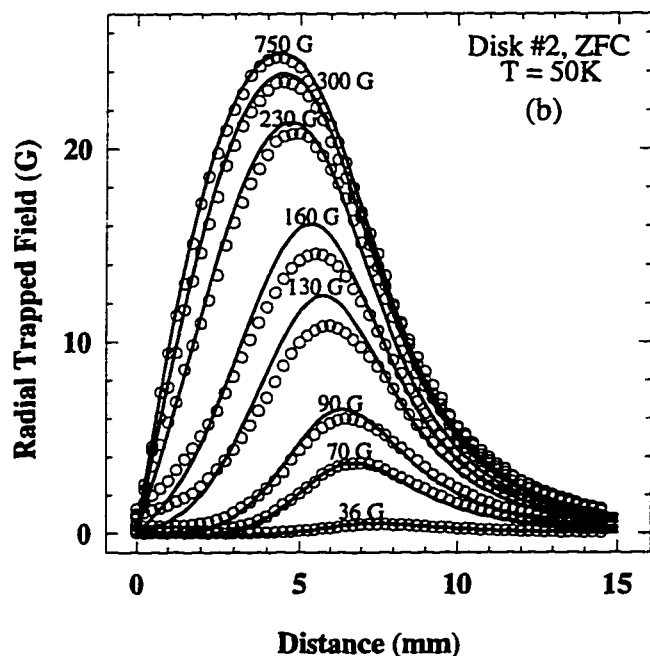
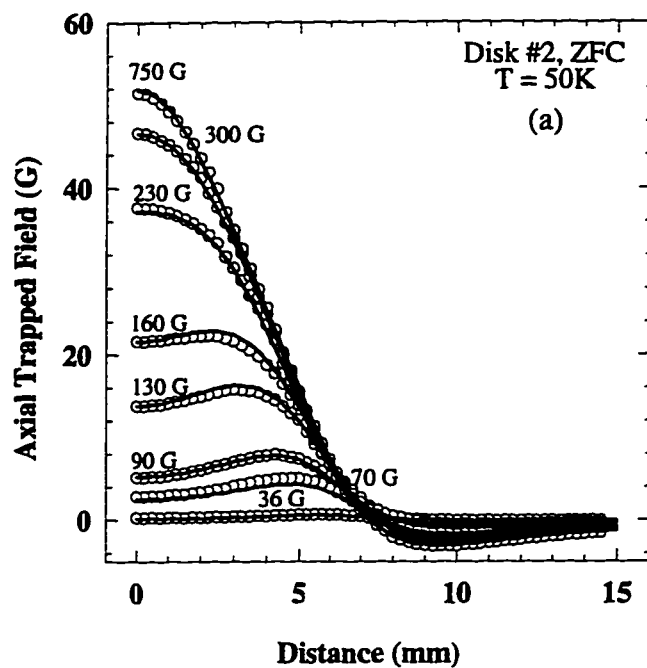


Figure 5.2.7: The profiles of the axial (a) and radial (b) magnetic fields trapped in a zero-field-cooled disk #2 in various applied fields and at 50K. Open symbols represent the experimental data measured at a distance of 3mm above the sample, and the solid lines are the theoretical fits based on the current distributions shown in Figure (5.2.8).

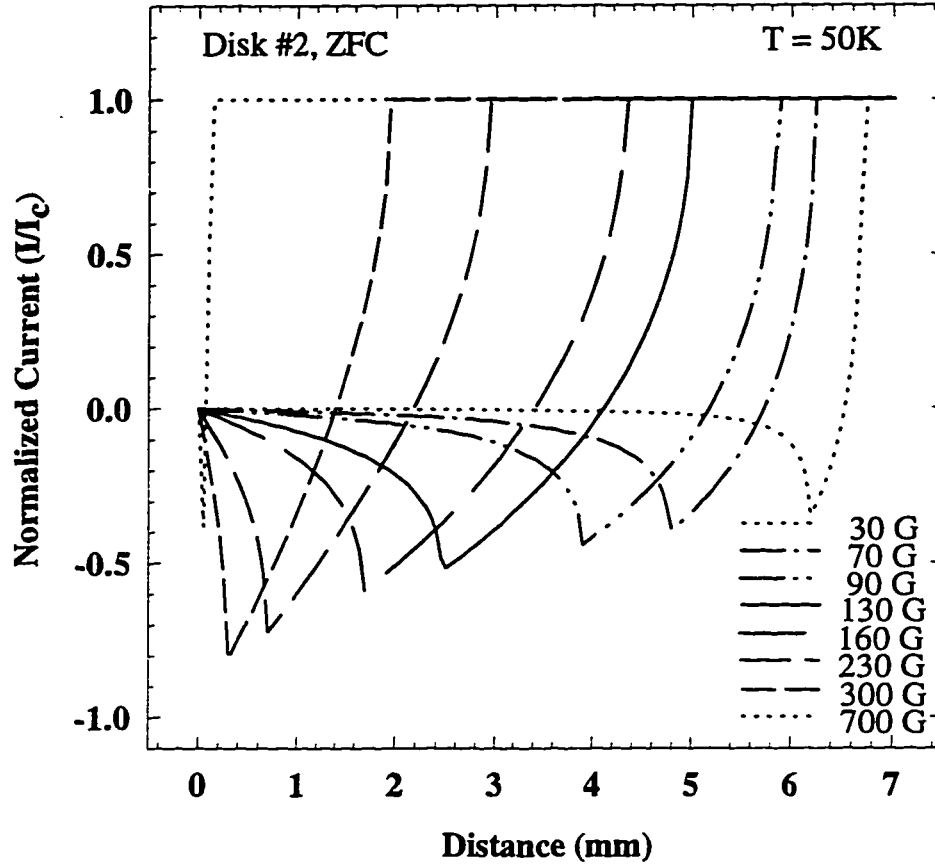


Figure 5.2.8: Normalized current density profiles across disk #2 at 50K calculated using Equation (1.19) for an applied field $H_a = 30, 70, 90, 130, 160, 230, 300$ and $700G$. The radius a of the vortex free shielded region was calculated from the formula $a = R/\cosh(H_a/H_d)$ and it marks a distance at which the current I (for each H_a) achieves the lowest negative value. The inner radius b of the annular ring at which the current I reaches I_c is given by $b = R/\cosh(H_a/2H_d)$. The critical current density was taken to be $6.11 \times 10^6 A/cm^2$.

Table 5.1: The calculated normalized radius a/R (where $a = R/\cosh(H_a/H_d)$) of the vortex free region and the normalized inner radius b/R (where $b = R/\cosh(H_a/2H_d)$) of the annular region where J_c is constant for the remnant regime. The computations were performed for different temperatures at a maximum available applied field of 750G and minimum applied field at which a saturation of the trapped field is observed.

T (K)	H_a (G)	H_d (G)	a/R	b/R	J_c (A/cm ²)
30	750	125	4.96×10^{-3}	0.099	9.9×10^6
40	600	98	4.39×10^{-3}	0.093	7.8×10^6
	750		0.95×10^{-3}	0.043	
50	475	77	4.18×10^{-3}	0.084	6.11×10^6
	750		0.12×10^{-3}	0.015	
70	250	31.6	7.33×10^{-4}	0.038	2.5×10^6
	750		9.85×10^{-11}	1.5×10^{-5}	

field of 700G and at different distances $h \geq 3mm$ above the disk [see Figures (5.2.9) and (5.2.10) for profiles at 50K, and Appendix A for profiles at 70K]. The agreement of the theoretical fits with the experimental data shows that the Bean model can be applied in the trapped field regime for H_a over a range between $10H_d$ and $1kG$, and in the shielding field regime with a field dependent critical current $J_c(H_a)$.

Bean's model was extended to simulate the magnetic field profiles above ring #1 at an applied field $H_a = 700G$ for both shielding and trapped field cases [see Figures (5.2.11) and (5.2.12) for results at a temperature of 30K, and Appendices A and B for results at temperatures of 50K and 70K]. The critical current density $J_c = 8.55 \times 10^6 A/cm^2$ in the remnant regime and $J_c = 6.30 \times 10^6 A/cm^2$ in the shielding regime was used in the calculations. Bean model describes well the magnetic field profiles above a ring for a complete flux penetration. However, the field dependence of J_c should be taken into account in the shielding field regime in order to calculate the dependence of the shielding field on the applied magnetic field [Figure (5.1.6)].

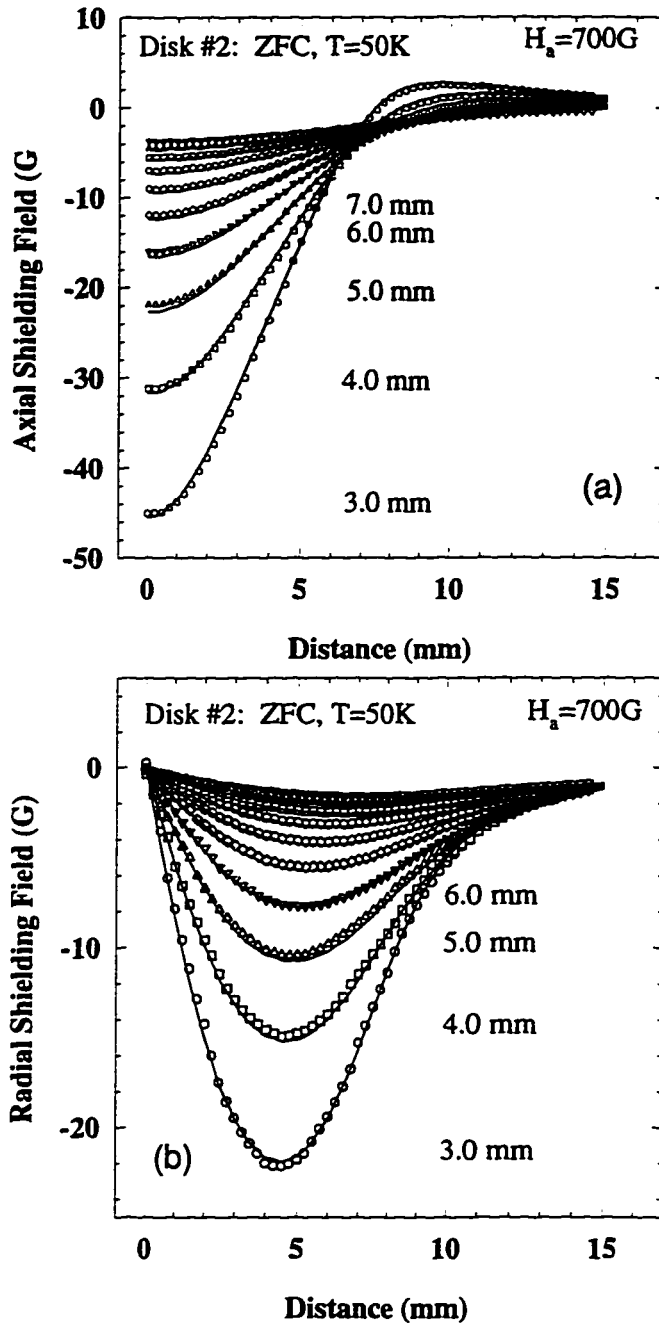


Figure 5.2.9: The profiles of the axial (a) and radial (b) magnetic shielding fields in a zero-field-cooled disk #2 at 700G, and 50K, which were measured as a function of an increasing distance above the sample from 3 up to 12mm. Open symbols represent the experimental data and the solid lines are the theoretical fits which use the Bean current distribution with $J_c = 5.2 \times 10^6 A/cm^2$ over the entire disk.

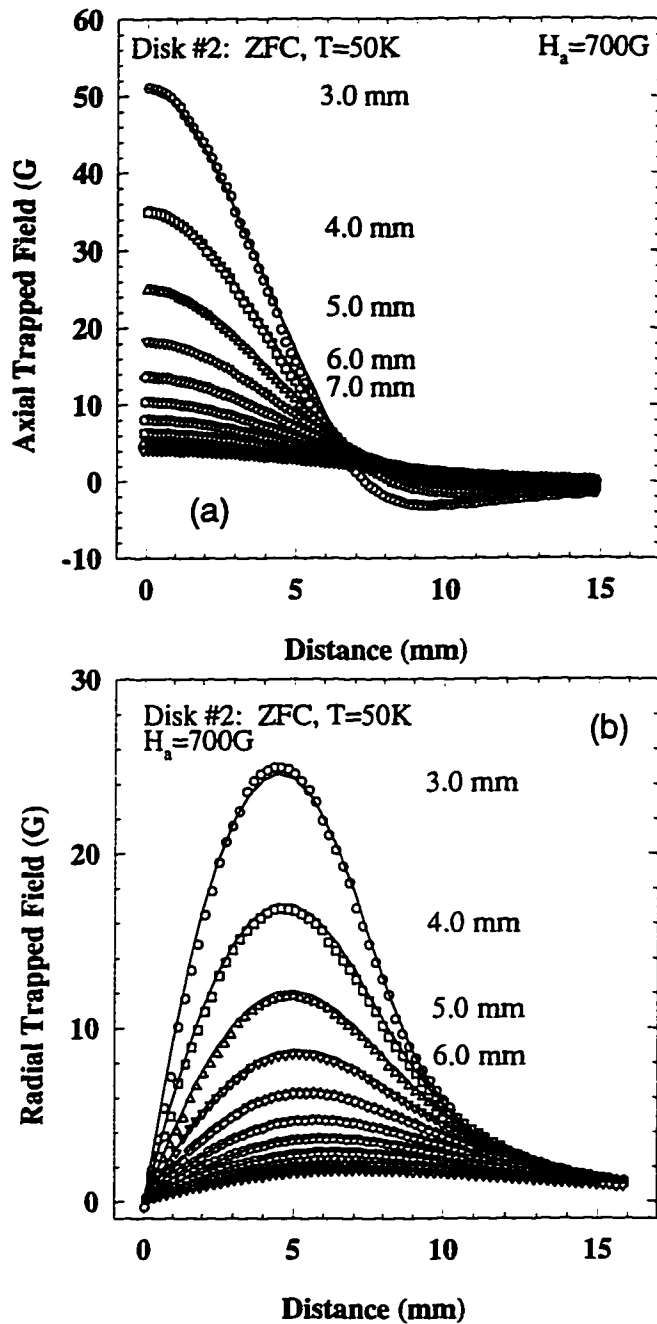


Figure 5.2.10: The profiles of the axial (a) and radial (b) magnetic trapped fields in a zero-field-cooled disk #2 at 700G, and 50K, which were measured as a function of an increasing distance above the sample from 3 up to 12mm. Open symbols represent the experimental data and the solid lines are the theoretical fits which use the Bean current distribution with $J_c = 6.11 \times 10^6 \text{ A/cm}^2$ over the entire disk.

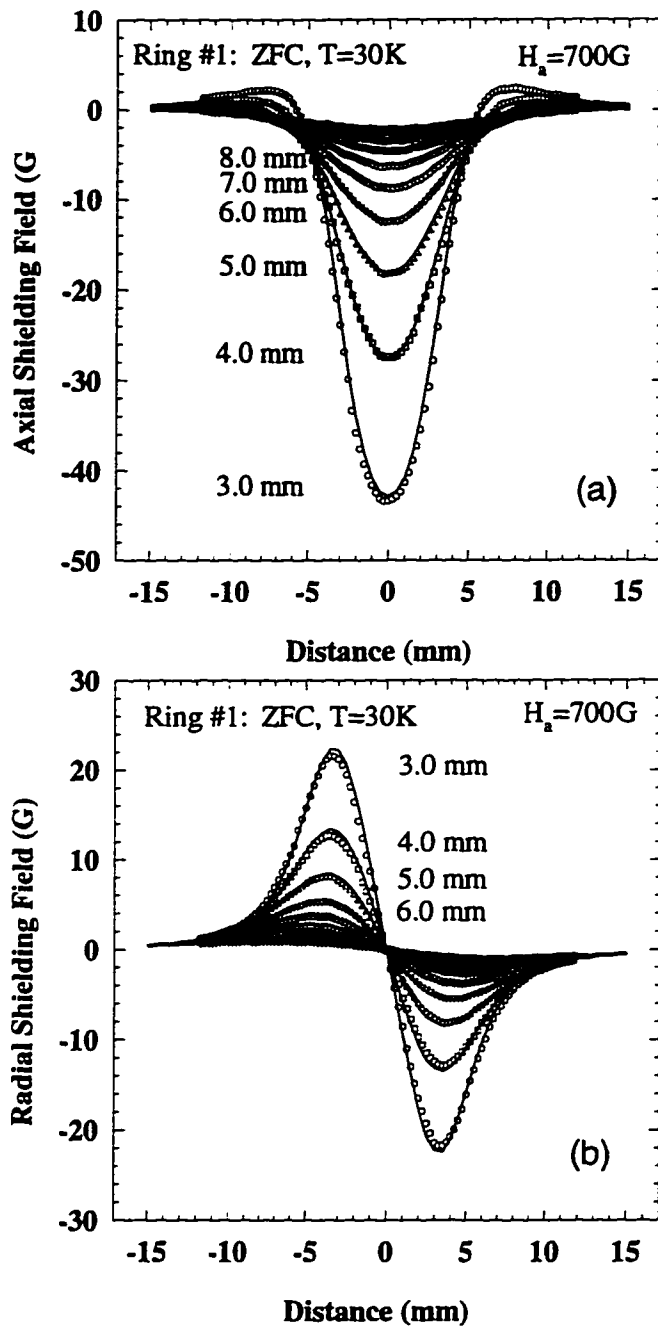


Figure 5.2.11: The profiles of the axial (a) and radial (b) magnetic shielding fields in a zero-field-cooled ring #1 at 700G, and 30K, which were measured as a function of an increasing distance above the sample from 3 up to 12mm. Open symbols represent the experimental data and the solid lines are the theoretical fits which use the Bean current distribution with $J_c = 6.3 \times 10^6 A/cm^2$ over the entire width of the ring.

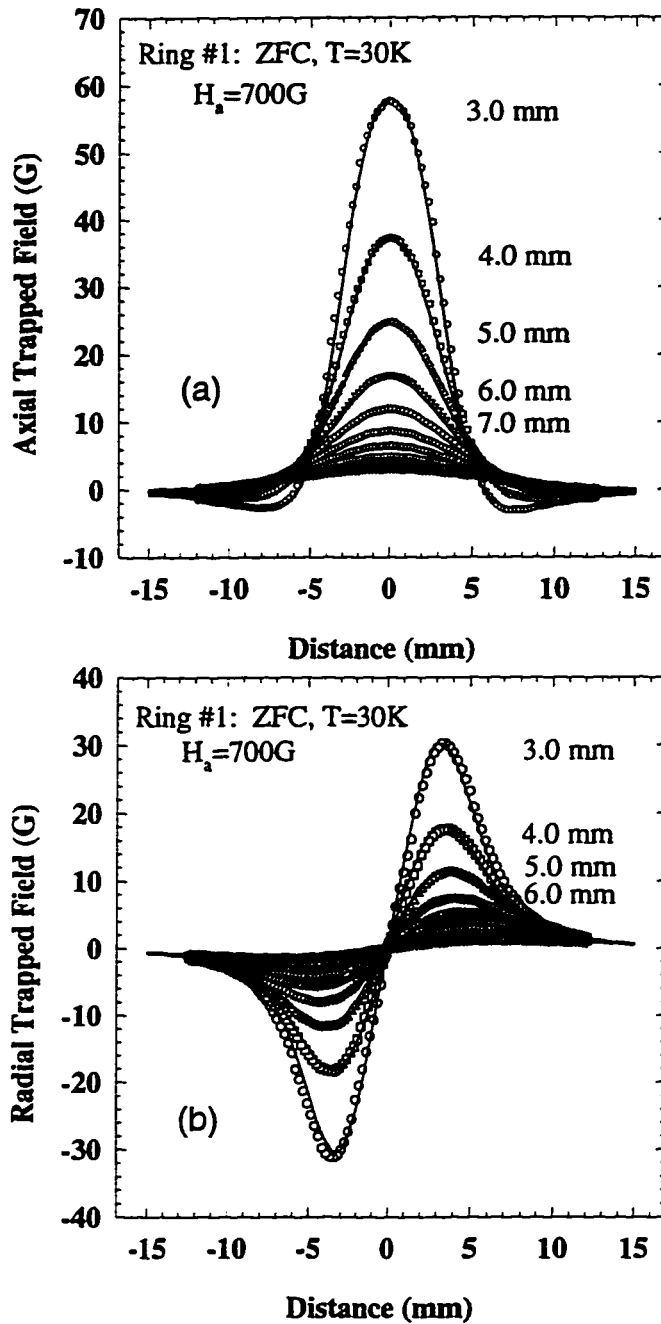


Figure 5.2.12: The profiles of the axial (a) and radial (b) magnetic trapped fields in a zero-field-cooled ring #1 at 700G, and 30K, which were measured as a function of an increasing distance above the sample from 3 up to 12mm. Open symbols represent the experimental data and the solid lines are the theoretical fits which use the Bean current distribution with $J_c = 8.55 \times 10^6 A/cm^2$ over the entire width of the ring.

5.2.2 Temperature dependence of the magnetic flux penetration in YBCO thin films

The pyramid-like shape of the induction profiles generated by thin film disks (when an external field is shielded by it) [Figure (5.1.15)] is observed at all applied temperatures (over a range of 64-84 K). These profiles do not provide any indication of a crossover between a partial and a complete flux penetration into the disk. The partial-complete flux penetration crossover can be seen in the temperature dependence of the profiles of the magnetic field trapped in the zero-field-cooled disk [Figure (5.1.16)] when a constant external field is applied to the sample. By simply plotting the magnitude of the magnetic field trapped in the disk's center (which is measured after applying and subsequently removing a constant external field) versus temperature [Figure (5.1.17)], one can determine the crossover temperatures from a partial to a complete flux penetration. This temperature is also given by the inflection point on the shielding field-temperature curve [Figures (5.1.17)(a), (b), (c)]. The crossover temperature decreases with an increasing magnitude of the applied magnetic field [Figure (5.1.17)(d)]. All crossover temperatures indicate the maximum amount of the axial field $(B_z)_{max}$ that can be trapped in the disk's center. This means that at temperatures above the crossover temperatures a complete critical state is reached across the disk. In this regime, $B_z(T)_{max}$ is proportional to temperature; $B_z(T) \propto (T_c - T)$. $B_z(T)_{max}$ is also proportional to the minimum applied magnetic field B^* required for a complete flux penetration at a given temperature. This is not surprising since B^* equals $B_z \propto I_c$, the field shielded at the surface and in the center of the disk, when it just reached the full critical state. The proportionality of $B_z(T)_{max}$ to $I_c(T)$ means that both must have the same temperature dependence. This was verified using ring #1 which was etched from disk #1. In the persistent current mode, the magnetic

induction generated in the ring's center is due entirely to the current and it is directly proportional to the magnitude of the critical current. The measurements of a saturation value of the magnetic induction at various temperatures have the same temperature dependence as that for $B_z(T)_{max}$ trapped in the disk's center [Figure (5.1.19)]. $B_z(T)_{max} \propto I_c(T)$ for the disk is also consistent with the calculation of the magnetic induction from the Biot-Savart law (see Section (5.2.1)).

5.2.3 Characterization of the complete and partial penetration regimes using magnetic relaxation measurements

Partial and complete flux penetration regimes for a disk are characterized by different flux-relaxation phenomena. In a complete flux penetration regime, the normalized decay rate $S = (1/B_o)(dB/d \ln t)$ measured at various points across the disk fluctuates between 0.012 and 0.015 (with an average value of 0.0135). In a partial flux penetration regime S changes from a minimum value of 0.0045 at the disk's center up to a maximum equilibrium value of 0.012 at the disk's edge [Figure (5.1.19)].

The magnitude of S measured in a complete flux penetration regime and that measured in the disk's center in a partial flux penetration regime are weakly temperature dependent [Figure (5.1.22)] and independent of the magnitude of the trapped magnetic flux. The weak temperature dependence of S in the disk's center for an incomplete penetration is surprising but it could mean that we record S in a complete flux penetration reduced by a constant amount of the flux creep rate towards the center of the disk. The weak temperature dependence of S is also seen for a partial critical regime in ring #1 [Figure (5.1.23)] at temperatures below 63K. S exhibits a sharp jump to higher values at a temperature of 63.5K which corresponds to a transition between a partial and a complete critical states after applying a magnetic field of 200G. In a partial critical state, S has a value approximately two times less than

the corresponding one for the disk. In a complete critical state S matches the values obtained for the disk over the same temperature range, confirming independence of S on the sample geometry in a complete critical state regime (a complete flux penetration for the disk). In a partial critical state regime (a partial flux penetration for the disk), the behavior of $S(T)$ is similar for both the disk and the ring. The weak temperature dependence of S in the full critical state close to T_c for the disk and the ring [Figures (5.1.22) and (5.1.23)] is consistent with data of Keller *et al* [104] and Isaac *et al* [67] on grain-aligned c-axis oriented melt-textured YBCO at remanence after application of saturating fields along the c-axis.

Chapter 6

Summary and Conclusions

We investigated the critical currents and the intrinsic properties of $Y_1Ba_2Cu_3O_{7-\delta}$ (YBCO) thin films. The studies included the following

- (1) The temperature dependence of the critical current;
- (2) Relaxation of the current and the corresponding flux pinning;
- (3) Magnetic flux penetration and the distribution of the currents.

The temperature dependence of the critical current $I_c(T)$ was investigated in thin film and granular YBCO over a temperature range of 10–90K and in magnetic fields up to 700G. The measurements were performed using superconducting rings in a persistent mode and a scanning Hall probe to record the profile of the magnetic field across the ring, generated by the persistent current at the critical level. The magnitude of I_c was deduced from the magnitude of the persistent current's self-field in the center of the ring. This technique eliminated the contribution of normal currents to the measured value of I_c and allowed one to distinguish between depairing and depinning critical currents. The results revealed the crossover between an Ambegaokar-Baratoff-like (AB) temperature of the critical current at low temperatures to a Ginzburg-Landau-like (GL) $(T_c - T)^{\frac{1}{2}}$ dependence at high temperatures. The crossover effects were observed for both depairing and depinning critical currents in c-axis-oriented YBCO thin films and in a granular YBCO. The AB to GL crossover effects in the temperature dependence of the critical current has been described by the Clem's model [5] for the case of strongly coupled granular superconductors. According to Clem at the

$AB \rightarrow GL$ crossover temperature in $I_c(T)$ of granular superconductors, the Ginzburg-Landau coherence length is of the order of the grain size. The observation of the $AB \rightarrow GL$ crossover effects in YBCO, in combination with the short coherence length in this compound, indicate, therefore, the presence of a nanometer-size granularity (domains). The experimental data imply that the superconducting domains have an effective size of about 30-40 Å, and are coupled by Josephson tunnel junctions in the a-b planes of YBCO thin films and in granular YBCO with $T_c \simeq 90 - 91K$. The size of these domains decreases with an increasing oxygen deficiency and with an increasing applied magnetic field leading to a Ginzburg-Landau $I_c(T)$ over a wide range of temperatures. We believe that the oxygen vacancies, the associated Cu^{2+} magnetic moments, and the external magnetic field (as a secondary effect) could break up YBCO into smaller domains through pair-breaking interaction.

The presence of a Ginzburg-Landau regime in $I_c(T)$ could suggest spatial homogeneity, since in this case the supercurrent does not “see” the intrinsic Josephson junctions and other intrinsic defects. This is especially important for research on YBCO single crystals. The measurement of $I_c(T)$ in YBCO single crystals of $T_c \simeq 91 - 92K$ by either the transport or magnetization methods [29, 30, 31] shows a Ginzburg-Landau-like behavior of $I_c(T)$ with $I_c(T) = 0$ between 70 - 77 K. This confirms that these single crystals could be well oxygenated on their surface and poorly oxygenated in the bulk, and $I_c(T) = 0$ above 70 - 77 K is not necessarily caused by the magnetic flux lattice melting.

In granular YBCO the temperature dependence of the intergrain critical current illustrates that the intergrain connections in granular YBCO have a form of clean microbridges (or thin wire-like bridges) with a nanometer-size domain structure, the same as that of the grain. These microbridges can be easily penetrated by an external magnetic field, therefore, the $AB \rightarrow GL$ crossover in the intergrain $I_c(T)$ can be

induced by weak magnetic fields. For the zero-field cooling case, the low temperature part of the $I_c(T)$ in pure granular YBCO and YBCO thin films is governed by an Ambegaokar-Baratoff regime, characteristic of SIS tunnel junctions. SNS normal metallic junctions appear only in an YBCO/Ag composite. Therefore, this implies that superconducting domains are coupled by tunnel junctions and not by proximity (normal) junctions.

The experimental observations discussed above, of the presence of nanometer size domains coupled by Josephson junctions in the a-b planes of $Y_1Ba_2Cu_3O_{7-\delta}$ support theoretical models developed by Stroud, Emery and Kivelson for the analysis of various physical properties of high temperature superconductors such as; specific heat in a magnetic field [105], flux-flow resistivity [106], flux pinning and phase transitions in a superconductor with columnar defects [107], and the effect of phase fluctuations on the low temperature penetration depth [108, 109]. A discrete representation was used in each case, in which the superconducting layers are described as an array of very small “grains” each comparable in size to the coherence length and coupled together by resistively shunted Josephson junctions.

Our results which imply the presence of Josephson nanostructures in YBCO, are also in agreement with recent high resolution electron microscopy investigations of $Y_1Ba_2Cu_3O_{7-\delta}$ ($\delta < 0.1$) at $T = 300K$ by Etheridge [43]. This study revealed the presence of electron diffraction patterns due to cells of the size approximately 10-20 Å in the a-b planes, in addition to those due to twin boundaries with spacing about 500 Å- 1000 Å.

In the second part of this thesis we investigated how the presence of the a-b plane Josephson nanostructures influences magnetic flux pinning and consequently the dissipation of the transport current. We investigated this problem in c-axis oriented YBCO thin films of various thickness and T_c , that were grown on different substrates

using various deposition methods. We measured the time decay of the persistent current's self-field from the critical level using a scanning Hall probe over a time scale up to 30000s, at temperatures over a range of 10-90 K. We calculated the effective barrier $U_{eff}(J)$ for vortex motion on the current density using Maley's method [45]. We found the correlation between the temperature dependence of the critical current $I_c(T)$ and the $U_{eff}(J)$. An empirical formula for $U_{eff}(J)$ was found to depend on a particular regime of $J_c(T)$, which is represented by either an AB-like or a GL-like behavior

$$U_{eff}(J) = J_c(T)[F(J) - F(J_c)] \quad (6.1)$$

where $F(J)$ is given by

$$F(J) = a \exp\left(-\frac{3\pi}{2} \frac{J}{J_{c0}}\right) \quad (6.2)$$

for a GL-like regime of $I_c(T)$, and by

$$F(J) = a_1 \exp\left(-\frac{3\pi}{2} \frac{J}{J_{c0}}\right) + a_2 \exp\left(-\frac{9\pi}{2} \frac{J}{J_{c0}}\right) \quad (6.3)$$

for an AB-like regime. The exponential factors represent the tilted washboard potentials for an overdamped Josephson junction, locked at phases of $\frac{3\pi}{2}$ and $\frac{9\pi}{2}$. For a GL-like regime of $I_c(T)$ at low temperatures, $U_{eff}(J)$ is governed by the Josephson potential with a phase of $\frac{3\pi}{2}$. For an AB-like behavior of $I_c(T)$, $U_{eff}(J)$ is described by a double exponential function with the Josephson potentials locked at phases of $\frac{3\pi}{2}$ and $\frac{9\pi}{2}$.

From the point of view of vortex motion, YBCO thin film behaves like a single resistively-shunted Josephson junction or an extremely coherent array of resistively-shunted Josephson junctions. This behavior is independent of the growth conditions of the YBCO films, film thickness, substrates, and the magnitude of J_c and T_c . We interpret the dissipation of the persistent current as due to the collective motion of vortices through the nanometer-scale array of overdamped Josephson junctions. The array is associated with the presence of superconducting cells, each of the size of the

order of the coherence length, in the a-b planes of YBCO [43, 44]. These cells are coupled by Josephson tunnel junctions in the a-b planes and between the adjacent planes in the c-direction. The pinning of vortices arises from the modulation of the Josephson coupling energy in these junctions. The motion of Josephson vortices is responsible for spatially coherent voltage oscillations in the array, with phases of $\frac{3\pi}{2}$ and $\frac{9\pi}{2}$ which could represent the first and the third harmonics.

The coherent oscillations of the Josephson junction array suggest an intrinsic mechanism of dissipation. The experimental results imply that the dissipation of the persistent current due to the motion of vortices through Josephson nanostructures, is a universal phenomenon, which describes behavior of the relaxation of magnetization in YBCO thin films.

Our investigations have generated the following open questions about the origin of both the exponential form of the energy barrier (Equations 6.2 and 6.3) and the Josephson nanostructures in the a-b planes of YBCO:

- (1) Does the exponential form of the energy barrier, with the phase locking and the missing factor of $k_B T$ in the exponents, imply quantum resonant tunnelling of vortices through a coherent array of Josephson junctions?
- (2) Is the phase separation responsible for the formation of the nanoscale cell structure in the a-b planes of YBCO and consequently for the Josephson nanostructures?

Regarding the exponential energy barrier, it is similar in form to the effective Euclidean action $S_E^{(eff)}$, which determines the tunnelling rate of vortices through a barrier during quantum tunnelling process [110]. If the pinning in the Josephson nanostructures is determined by the variation of the Josephson coupling energy over

distances comparable to the cell size, one could expect very narrow barriers with a large curvature of the potential at the top of the barrier. This would raise the barrier frequency and decrease the tunnelling time, leading to an increase of the crossover temperature from the quantum to the classical regime [111]. Another question is how the spatial coherence of the Josephson junction array could enhance the quantum resonant tunnelling of Josephson vortices.

Regarding the origin of the nanoscale cell structure in the a-b planes of YBCO, Etheridge [43] has suggested that the cells are formed in struggle to relieve intralayer internal stresses. However, it may be important to investigate a relationship between these cells and the phase separation which forms superconducting islands separated by antiferromagnetic regions [112]. Such relationship would mean that the Josephson nanostructures are formed by antiferromagnetic insulating layers which couple superconducting cells.

In the last part of this thesis, we investigated the penetration of the magnetic flux into zero-field-cooled disk- and ring-shaped YBCO thin films (both the trapped and shielding field regimes). The magnetic flux penetrates the disk symmetrically from the edge. Critical currents are induced in the annular ring penetrated by the flux. The inner radius of the flux-penetrated ring increases with increasing applied field. A Complete and partial penetration of flux into disk-shaped YBCO thin film is well described by the critical state model of Mikheenko and Kuzovlev [27] and Zhu et al [48] at weak fields. However, the field dependence of J_c should be taken into account in the shielding field regime. When the applied field is $H_a \simeq 10H_d$, the ring that is filled with constant critical current spans the entire area of the disk and the simple Bean model with constant J_c could be applied to describe the full penetration state in disk-shaped and also ring-shaped YBCO superconductors in weak fields.

We also investigated the temperature dependence of the penetration process of the magnetic flux into disk-shaped YBCO thin films, especially the transition between partial and complete flux penetration regimes. A complete flux penetration regime is characterized by the normalized logarithmic decay rates constant across the disk ($0.012 < S < 0.015$). S in a partial flux penetration regime has a minimum in the disk's center ($S \simeq 0.005$) and a maximum ($S \simeq 0.012$) at the disk's edges. The temperature dependence of the magnetic induction at the transition between partial and complete flux penetration regimes for different applied magnetic fields is governed by the temperature dependence of the critical current. The maximum field trapped in the disk's center and the self-field of the critical current flowing in the ring (which was etched out from the disk) have the same temperature dependence. This confirms that the trapped- or shielding-field profiles above the thin film disk can be simulated by summing up self-fields of a large number of concentric current loops.

Bibliography

- [1] M. Murakami, M. Morita, and N. Koyama, *Jpn. J. Appl. Phys.* **28**, L1125 (1989);
M. Murakami, *Modern Phys. Lett. B* **4**, 163 (1990)
- [2] M. Tinkham, *Introduction to Superconductivity* (McGraw-Hill, New York, 1996)
2nd edition.
- [3] J. Mannhart in *Earlier and Recent Aspects of Superconductivity*, edited by J.
G. Bednorz and K. A. Müller, Springer Series in Solid-State Sciences, Vol. 90
(Springer-Verlag Berlin, 1990)
- [4] R. Kleiner and P. Müller, *Phys. Rev. B* **49**, 1327 (1993).
- [5] J. R. Clem, B. Bumble, S. I. Raider, W. J. Gallagher and Y. C. Shih, *Phys. Rev.*
B **35**, 6637 (1987).
- [6] J. R. Clem, *Physica C* **153-155**, 50 (1988)
- [7] D. C. Ling, G. Young, J. T. Chen and L. E. Wenger, *Phys. Rev. Lett.* **75**, 2011
(1995).
- [8] M. Daeumling, J. M. Seuntjens and D. C. Larbalestier, *Nature* **346**, 332 (1990).
- [9] M. S. Osofsky, J. L. Cohn, E. F. Skelton, M. M. Miller, R. J. Soulen, S. A. Wolf
and T. A. Vanderah, *Phys. Rev. B* **45**, 4916 (1992).
- [10] B. H. Moeckly, D. K. Lathrop and R. A. Buhrman, *Phys. Rev. B* **47**, 400 (1993).
- [11] S. Horiuchi, *Jap. J. Appl. Phys.* **31**, L1335 (1992).
- [12] P. G. DeGennes, *Rev. Mod. Phys.* **36**, 225 (1964).

- [13] B. D. Josephson, *Phys. Lett.* **1**, 251 (1962); *Adv. Phys.* **14**, 419 (1965)
- [14] V. Ambegaokar and A. Baratoff, *Phys. Rev. Lett.* **10**, 486 (1963); **11**, 104(E) (1963).
- [15] R. T. Kampwirth and K. E. Gray, *IEEE Trans. Magn.* **MAG-17**, 565 (1981)
- [16] M. Tinkham, *Helv. Phys. Acta* **61**, 443 (1988).
- [17] V. L. Ginzburg, *Zh. Eksp. Teor. Fiz.* **23**, 236 (1952).
- [18] K. K. Likharev, *Rev. Mod. Phys.* **51**, 115 (1979).
- [19] J. Mannhart, P. Chaudhari, D. Dimos, C. C. Tsuei and T. R. McGuire, *Phys. Rev. Lett.* **61**, 2476 (1988).
- [20] V. Strbik, R. Adam, S. Benacka and S. Chromik, in *Progress in High Temperature Superconductivity*, Vol. 30; Eds. M. Baran, W. Gorzkowski and H. Szymczak (World Scientific, Singapore, 1992), p.366.
- [21] S. Tahara, S. M. Anlage, J. Halbritter, C.-B. Eom, D. K. Fork, T. H. Geballe and M. R. Beasley, *Phys. Rev. B* **41**, 11203 (1990).
- [22] M. A. M. Gijs and R. J. E. Jansen, *Appl. Phys. Lett.* **56**, 1484 (1990).
- [23] E. C. Jones, D. K. Christen, J. R. Thompson, R. Feenstra, S. Zhu, D. H. Lowndes, J. M. Phillips, M. P. Siegal and J. D. Budai, *Phys. Rev. B* **47**, 8986 (1993).
- [24] D. K. Christen, C. E. Klabunde, J. R. Thompson, H. R. Kerchner, S. T. Sekula, R. Feenstra and J. D. Budai, *Physica C* **162-164**, 653 (1989).
- [25] G. Tome-Rosa, G. Jakob, A. Walkenhorst, M. Maul, M. Schmitt, M. Paulson and H. Adrian, *Z. Phys. B* **83**, 221 (1991).

- [26] E. C. Jones, D. K. Christen, C. E. Klabunde, J. R. Thompson, D. P. Norton, R. Feenstra, D. H. Lowndes and J. D. Budai, *Appl. Phys. Lett.* **59**, 3183 (1991).
- [27] P. H. Mikheenko and Y. E. Kuzovlev, *Physica C* **204**, 229 (1993).
- [28] L. Antognazza, S. J. Berkowitz, T. H. Geballe and K. Char, *Phys. Rev. B* **51**, 8560 (1995).
- [29] C. E. Gough, A. Gencer, G. Yang, M. Z. Shoustari, A. I. M. Rae and J. S. Abell, *Cryogenics* **33**, 339 (1993).
- [30] J. R. Thompson, Y. R. Sun, L. Civale, A. P. Malozemoff, M. W. McElfresh, A. D. Marwick and F. Holtzberg, *Phys. Rev. B* **47**, 14440 (1993).
- [31] Y. Abulafia, A. Shaulov, Y. Wolfus, R. Prozorov, L. Burlachkov, Y. Yeshurun, D. Majer, E. Zeldov, V. M. Vinokur, *Phys. Rev. Lett.* **75**, 2404 (1995).
- [32] P. W. Anderson, *Phys. Rev. Lett.* **9**, 309 (1962) ; P. W. Anderson and Y. B. Kim *Rev. Mod. Phys.* **36**, 39, (1964)
- [33] E. Zeldov, N. M. Amer, G. Koren, A. Gupta, M. W. McElfresh, and R. J. Gambino, *Appl. Phys. Lett.* **56**, 680 (1990)
- [34] C.J. van der Beek, G. J. Nieuwenkuys, P.H. Kes, H.G. Schnack and R. Griessen , *Physica C* **197**, 320 (1992).
- [35] V.M. Vinokur, M.V. Feigelman and V.B. Geshkenbein *Phys. Rev. Lett.* **67**, 915 (1991).
- [36] M. P. A. Fisher, *Phys. Rev. Lett.* **62** (1989) 1415 ; D. S. Fisher, M. P. A. Fisher and D.A Huse, *Phys. Rev. B* **43**, 130 (1991).
- [37] M.V. Feigelman, V.B. Geshkenbein, A.I. Larkin, and V.M. Vinokur, *Phys. Rev. Lett.* **63**, 2303 (1989).

- [38] G. Blatter, M.V. Feigelman, V.B. Geshkenbein, A.I. Larkin and V.M. Vinokur, *Rev. Mod. Phys.* **66**, 1125 (1994).
- [39] R. Griessen, Wen Hai-hu, A.J.J. van Dalen, B. Dam, Y. Rector and H.G. Schnack, *Phys. Rev. Lett.* **72**, 1910 (1994).
- [40] A.J.J. van Dalen, R. Griessen, S. Libbrecht, Y. Bruynseraede, and E. Osquiguil, *Phys. Rev. B* **54**, 1366 (1996).
- [41] P. Berghuis, R. Herzog, R.E. Somekh, J.E. Evetts, R.A. Doyle, F. Baudenbacher, and A.M. Campbell, *Physica C* **256**, 13 (1996).
- [42] T.L. Hylton and M.R. Beasley, *Phys. Rev. B* **41**, 11669 (1990).
- [43] J. Etheridge, *Phil. Mag. A* **73**, 643 (1996).
- [44] H. Darhmaoui and J. Jung, *Phys. Rev. B* **53**, 14621 (1996).
- [45] M.P. Maley, J.O. Willis, H. Lessure, and M.E. McHenry, *Phys. Rev. B* **42**, 2639 (1990).
- [46] C. P. Bean, *Phys. Rev. Lett.* **8**, 250 (1962); *Rev. Mod. Phys.* **36**, 31 (1994)
- [47] A. M. Campbell and J. E. Evetts, *Adv. Phys.* **21**, 199 (1972)
- [48] J. Zhu, John Mester, James Lockhart and John Turneaure *Physica C* **212**, 216 (1993)
- [49] J. R. Clem and A. Sanchez, *Phys. Rev. B* **50**, 9355 (1994)
- [50] Y. Yokoyama, Y. Hasumi, H. Obara, Y. Suzuki, T. Katayama, S. Gotoh, N. Koshizuka, *Jap. J. Appl. Phys.* **30**, L714 (1991).
- [51] A. Forkl, *Physica Scripta* **T49**, 148 (1993).
- [52] H. Theuss, A. Forkl and H. Kronmüller, *Physica C* **190**, 345 (1992).

- [53] M. Däumling and D. C. Larbalestier, Phys. Rev. B **40**, 9350 (1989).
- [54] L. W. Conner and A. P. Malozemoff, Phys. Rev. B **43**, 402 (1991).
- [55] E. H. Brandt, Physica C **235-240**, 2939 (1994).
- [56] E.H. Brandt, M. V. Indenbom and A. Forkl, Europhys. Lett. **22** 735 (1993)
- [57] E. H. Brandt, Phys. Rev. B **54**, 4246 (1996)
- [58] M. Darwin, J. Deak, L. Hou, M. McElfresh, E. Zeldov, J. R. Clem, and M. Indenbom Phys. Rev. B **48**, 13192 (1993)
- [59] D. J. Frankel, J. Appl. Phys. **50**, 5402 (1979).
- [60] M. Däumling and D.C. Larbalestier, Phys. Rev. B **40**, 9350 (1989).
- [61] Y.B. Kim, C. F. Hempstead and A. R. Strnad, Rev. Mod. Phys. **36**, 43 (1964).
- [62] W. Xing, B. Heinrich, H. Zhou, A. A. Fife and A. R. Cragg, J. Appl. Phys. **76**, 4244 (1994).
- [63] Rinke J. Wijngaarden, H. J. W. Spoelder, R. Surdeanu, and R. Griessen, Phys. Rev. B. **54**, 6742 (1996) J. C. Irwin, B. Heinrich, H. Zhou, A. A. Fife and A. R. Cragg, Physica C **229**, 289 (1994).
- [64] U. Jeschke, R. Schneider, G. Ulmer and G. Linker, Physica C **243**, 243 (1995).
- [65] J. Talvacchio, M. G. Forrester, J. R. Gavaler and T. T. Braggins, in *Science and Technology of Thin Film Superconductors II*, edited by R. McConnell and S. A. Wolf (Plenum, New York, 1990).
- [66] H. Darhmaoui, J. Jung, J. Talvacchio, M. A-K. Mohamed and L. Friedrich, Phys. Rev. B **53**, 12330 (1996).

- [67] I. Isaac, J. Jung, M. Murakami, S. Tanaka, M. A-K. Mohamed and L. Friedrich, Phys. Rev. B **51**, 11806 (1995).
- [68] M. R. Beasley, R. Labusch, and W. W. Webb, Phys. Rev. **181**, 682 (1969)
- [69] P.J. Kung, M.P. Maley, M.E. McHenry, J.O. Willis, J.Y. Coulter, M. Murakami, and S. Tanaka, Phys. Rev. B **46**, 6427 (1992).
- [70] P.J. Kung, M.P. Maley, M.E. McHenry, J.O. Willis, M. Murakami, and S. Tanaka, Phys. Rev. B **48**, 13922 (1993).
- [71] H.G. Schnack, R. Griessen, J.G. Lensink, C.J. van der Beek, and P.H. Kes, Physica C **197**, 337 (1992).
- [72] W.R. Smythe, Static and Dynamic Electricity (McGraw-Hill, New York, 1950).
- [73] J. Jung, I. Isaac and M. A-K. Mohamed, Phys. Rev. B **48**, 7526 (1993).
- [74] J. -Y. Lin, M. Gurvitch, S. K. Topygo, A. Bourdillon, S. Y. Hou and Julia M. Phillips, Phys. Rev. B **54**, R12717 (1996).
- [75] J. D. Jorgensen, B. W. Veal, A. P. Paulikas, L. J. Nowicki, G. W. Crabtree, H. Claus and W. K. Kwok, Phys. Rev. B **41**, 1863 (1990).
- [76] J. D. Goettee, Y. B. Kudasov, W. D. Zerwekh, A. I. Bykov, M. I. Dolotenko, C. M. Fowler, B. L. Freeman, J. C. King, N. P. Kolokolchikov, W. Lewis, B. R. Marshall, B. J. Papatheofanis, V. V. Platonov, P. J. Rodriguez, M. G. Sheppard, O. M. Tatsenko and L. R. Veaser, Physica C **235-240**, 2090 (1995).
- [77] N. E. Phillips, R. A. Fisher, J. E. Gordon, S. Kim, A. M. Stacy, M. K. Crawford and E. M. McCarron III, Phys. Rev. Lett. **65**, 357 (1990).
- [78] A. Junod in *Physical Properties of High Temperature Superconductors*, Vol. 2; Ed. D. M. Ginsberg (World Scientific, Singapore, 1990).

- [79] D. C. Larbalestier, S. E. Babcock, X. Cai, L. Cooley, M. Daeumling and D. P. Hampshire in *Progress in High Temperature Superconductivity*, Vol. 18; Ed. S. Nakajima (World Scientific, New Jersey, 1989).
- [80] J. Halbritter in *Superconductivity and Applications*; Eds. H. S. Kwok, Y. H. Kao and D. T. Shaw (Plenum Press, New York, 1990).
- [81] R. Beyers, B. T. Ahn, G. Gorman, V. Y. Lee, S. S. P. Parkin, M. L. Ramirez, K. P. Roche, J. E. Vazquez, T. M. Gür and R. A. Huggins, *Nature* **340**, 619 (1989).
- [82] D. J. Werder, C. H. Chen, R. J. Cava and B. Batlogg, *Phys. Rev. B* **38**, 5130 (1988).
- [83] T. Zeiske, R. Sonntag, D. Hohlwein, N. H. Andersen and T. Wolf, *Nature* **353**, 542 (1991).
- [84] H. L. Edwards, D. J. Derro, A. L. Barr, J. T. Markert and A. L. de Lozanne, *Phys. Rev. Lett.* **75**, 1387 (1995).
- [85] T. Imai, T. Shimizu, T. Tsuda, H. Yasuoka, T. Takabatake, Y. Nakazawa and M. Ishikawa, *J. Phys. Soc. Jpn.* **57**, 1771 (1988).
- [86] O. N. Bakharev, A. G. Volodin, A. V. Duglav, A. V. Egorov, O. B. Marvin, V. V. Naletov, M. A. Teplov and D. Wagner, *JETP Lett.* **58**, 608 (1993).
- [87] K. Maki in *Superconductivity*, Ed. R. Parks (Marcel Dekker, New York, 1969).
- [88] S. Skalski, O. Betbeder-Matibet and P. R. Weiss, *Phys. Rev.* **136**, A1500 (1964).
- [89] V. Z. Kresin and S. A. Wolf, *Phys. Rev. B* **51**, 1229 (1995) and references therein.
- [90] J. C. Phillips, *Physica C* **228**, 171 (1994).
- [91] D. Guban and O. Stoppard, *Physica C* **213**, 109-125 (1993).

- [92] A. Gurevich and H. K pfer, Phys. Rev. B **48**, 6477 (1993).
- [93] H.G. Schnack, R. Griessen, J.G. Lensink and H.H. Wen, Phys. Rev. B **48**, 13178 (1993).
- [94] I.O. Kulik and I.K. Yanson, The Josephson Effect in Superconductive Tunnelling Structures (Israel Program for Scientific Translations, Jerusalem, 1972).
- [95] S.G. Lachenmann, T. Doderer, R.P. Huebener, T.J. Hagenaars, J.E. van Himbergen, P.H.E. Tiesinga, and J.V. Jose, Phys. Rev. B (1997) in press.
- [96] J.R. Clem and M.W. Coffey, Phys. Rev. B **42**, 6209 (1990).
- [97] A. Erb, E. Walker, and R. Flukiger, Physica C **258**, 9 (1996).
- [98] Z.Zhai, H. Srikanth, S. Sridhar, A. Erb, E. Walker, and R.lukiger, Proc. of M2S-HTSCV, Physica C, 1997, in press.
- [99] Y. Zhu, M. Suenaga, Y. Xu, R.L. Sabatini, and A.R. Moodenbaugh, Appl. Phys. Lett. **54**, 374 (1989).
- [100] Y. Zhu, M. Suenaga, J. Tafto, and D.O. Welch, Phys. Rev. B **44**, 2871 (1991).
- [101] J. Halbritter, Phys. Rev. B **46**, 14861 (1992).
- [102] W. Mexner, J. Hoffmann, S. Heede, K. Heinemann, H.C. Freyhardt, F. Lademberger, and E. Schwarzmann, Z. Phys. B **101**, 181 (1996).
- [103] E. Moraitakis, M. Pissas and D. Niarchos, Supercond. Sci. Technol. **8** 647 (1995).
- [104] C. Keller, H. K pfer, R. Meier-Hirmer, U. Welch, V. Selvamanickam and K. Salama, Cryogenics **30**, 410 (1990).
- [105] C. Ebner and D. Stroud, Phys. Rev. B **39**, 789 (1989).

- [106] K.H. Lee and D. Stroud, *Phys. Rev. B* **46**, 5699 (1992).
- [107] K.H. Lee, D. Stroud and S.M. Girvin, *Phys. Rev. B* **48**, 1233 (1993).
- [108] E. Roddick and D. Stroud, *Phys. Rev. Lett.* **74**, 1430 (1995).
- [109] V.J. Emery and S.A. Kivelson, *Phys. Rev. Lett.* **74**, 3253 (1995).
- [110] G. Blatter and V. Geshkenbein, *Phys. Rev. B* **47**, 2725 (1993).
- [111] E. Šimánek, private communication.
- [112] R.S. Markiewicz, *J. Phys. Chem. Solids* 1997, in press.

Appendix A

Magnetic flux penetration at temperatures of $50K$ and $70K$ into disk #2.

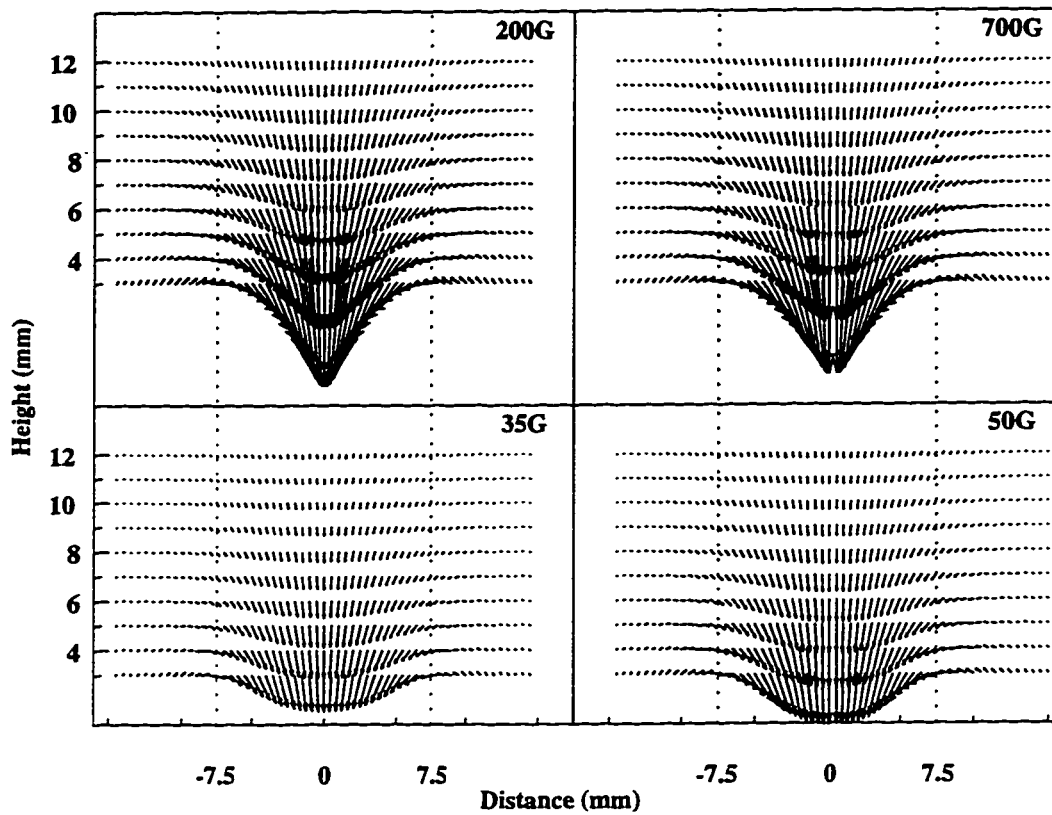


Figure 1.0.1: The vectors of the shielding field measured at distances between 3 and 12mm (every 1mm) above the surface of disk #2 at 50K and at applied magnetic fields of 35, 50, 100, 200, 375 and 700G. The magnitude of each vector is proportional to the magnitude of the total field at the same position normalized to the maximum magnitude of the shielding field in each Figure. Distances -7.5mm and 7.5mm mark the disk's edges.

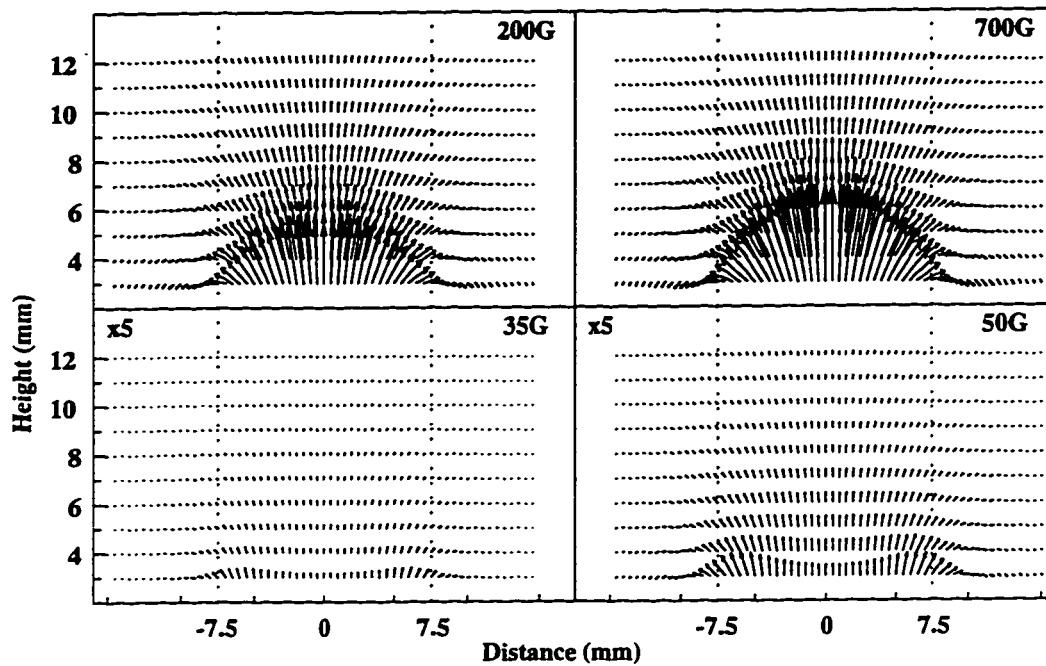


Figure 1.0.2: The vectors of the trapped field measured at distances between 3 and 12mm (every 1mm) above the surface of disk #2 at 50K and at applied magnetic fields of 35, 50, 100, 200, 375 and 700G. The magnitude of each vector is proportional to the magnitude of the total field at the same position normalized to the maximum magnitude of the trapped field in each Figure. Distances -7.5mm and 7.5mm mark the disk's edges. $\times 5$ marks the magnification of the vectors.

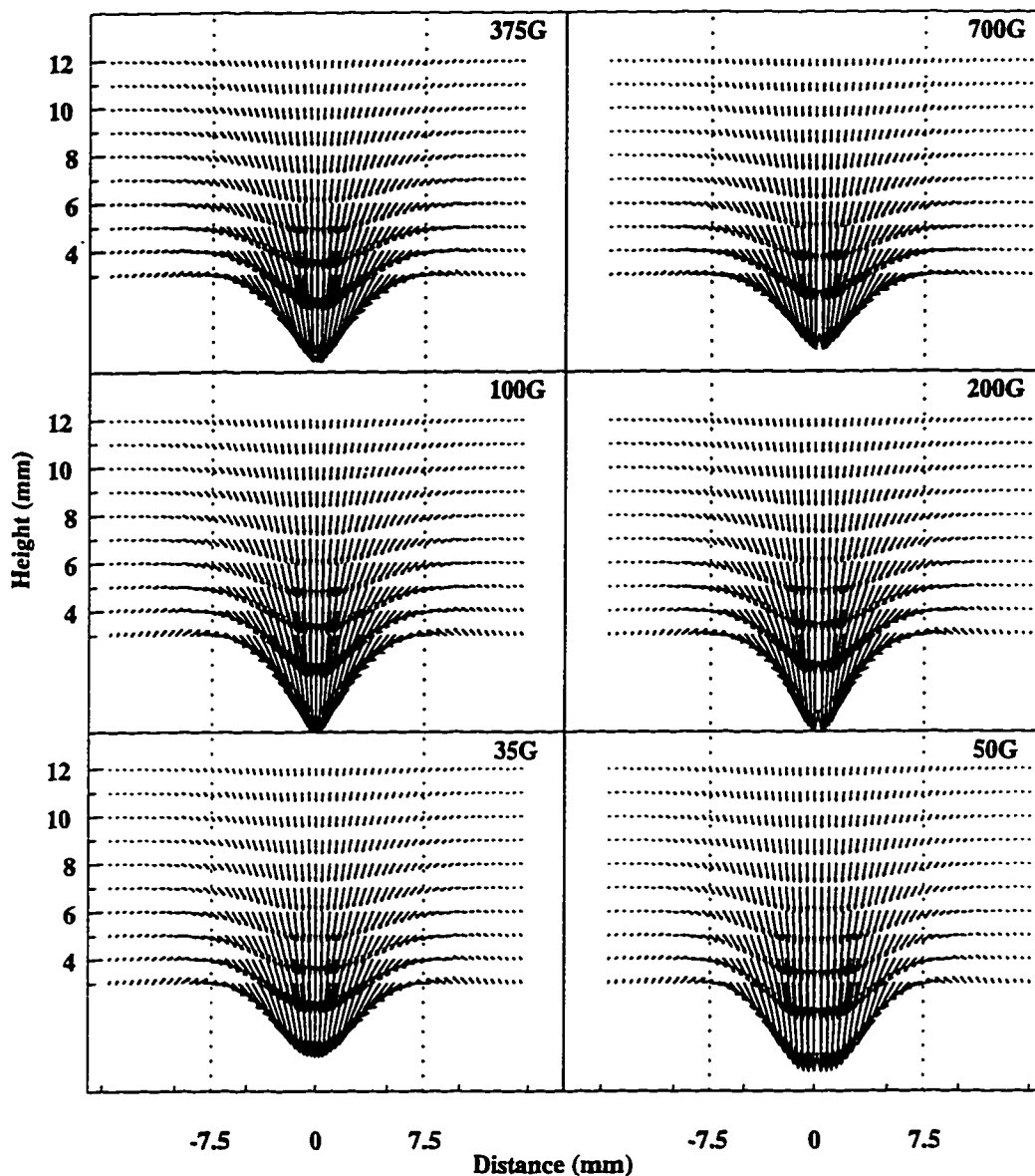


Figure 1.0.3: The vectors of the shielding field measured at distances between 3 and 12mm (every 1mm) above the surface of disk #2 at 70K and at applied magnetic fields of 35, 50, 100, 200, 375 and 700G. The magnitude of each vector is proportional to the magnitude of the total field at the same position normalized to the maximum magnitude of the shielding field in each Figure. Distances -7.5mm and 7.5mm mark the disk's edges.

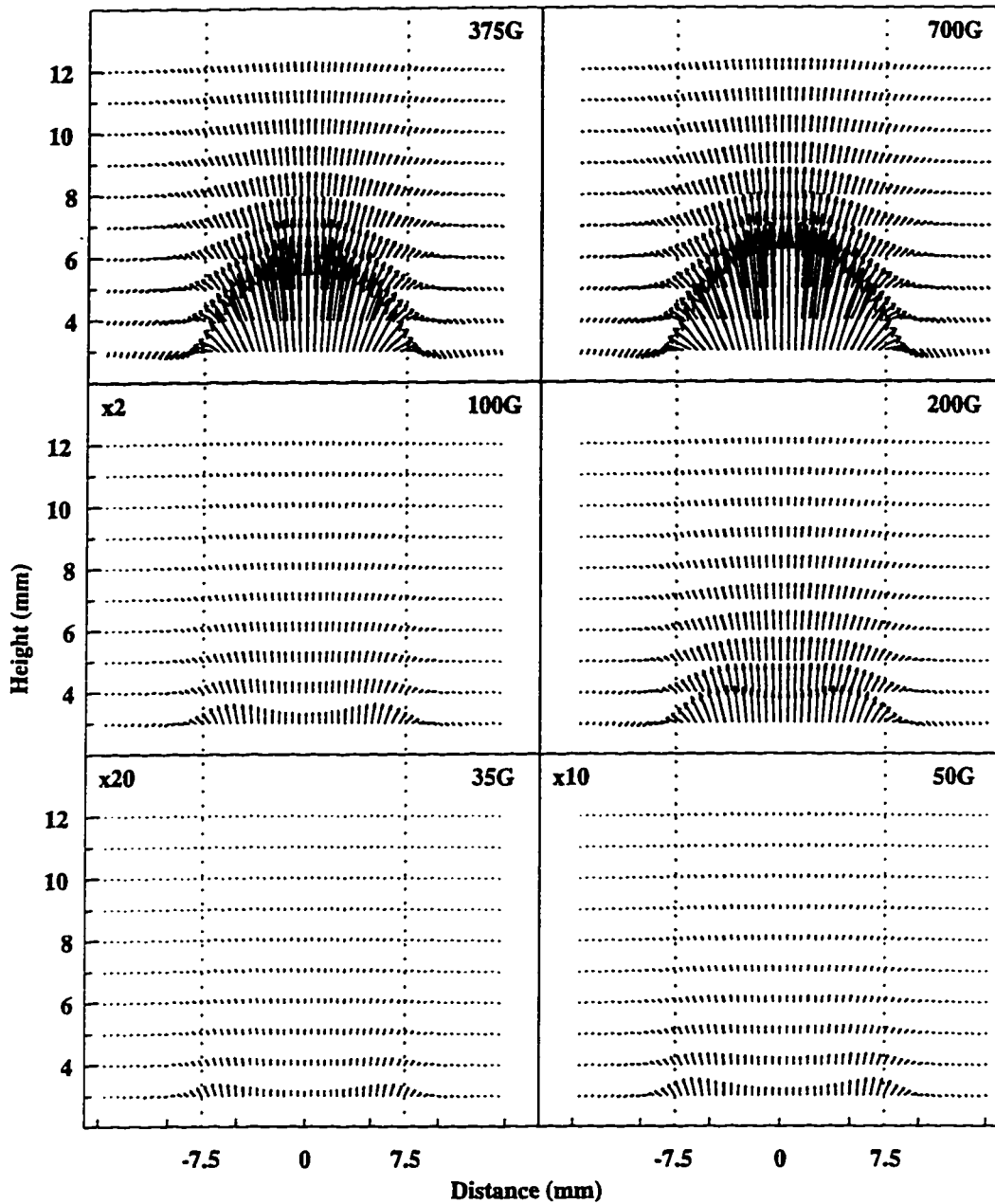


Figure 1.0.4: The vectors of the trapped field measured at distances between 3 and 12mm (every 1mm) above the surface of disk #2 at 70K and at applied magnetic fields of 35, 50, 100, 200, 375 and 700G. The magnitude of each vector is proportional to the magnitude of the total field at the same position normalized to the maximum magnitude of the trapped field in each Figure. Distances -7.5mm and 7.5mm mark the disk's edges. $\times 2$, $\times 10$, and $\times 20$ mark the magnification of the vectors.

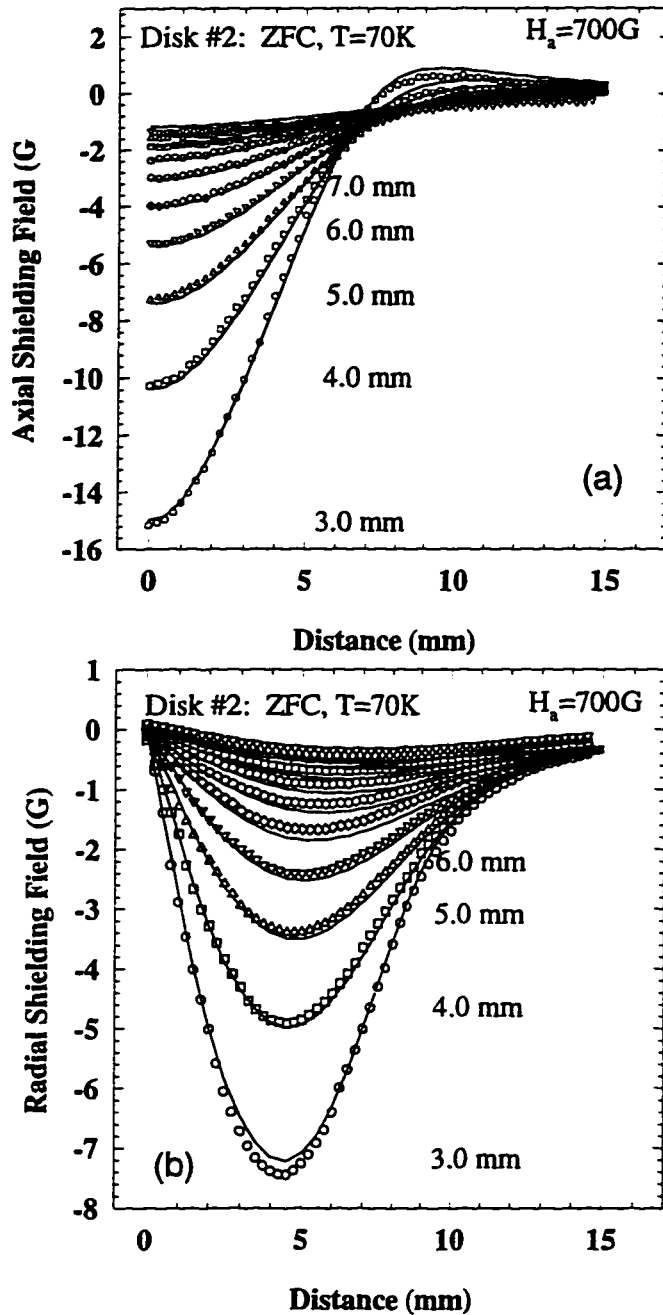


Figure 1.0.5: The profiles of the axial (a) and radial (b) magnetic shielding fields in a zero-field-cooled disk #2 at 700G, and 70K, which were measured as a function of an increasing distance above the sample from 3 up to 12mm. Open symbols represent the experimental data and the solid lines are the theoretical fits which use the Bean current distribution with $J_c = 1.75 \times 10^6 A/cm^2$ over the entire disk.

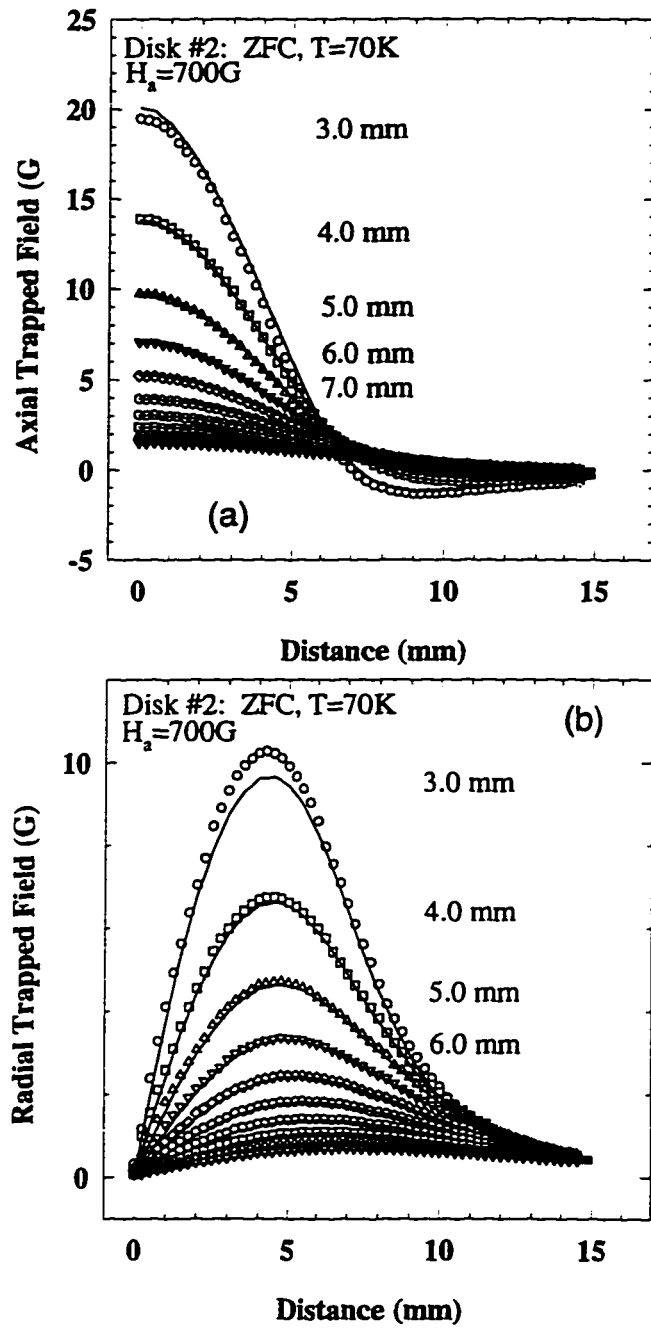


Figure 1.0.6: The profiles of the axial (a) and radial (b) magnetic trapped fields in a zero-field-cooled disk #2 at 700G, and 70K, which were measured as a function of an increasing distance above the sample from 3 up to 12mm. Open symbols represent the experimental data and the solid lines are the theoretical fits which use the Bean current distribution with $J_c = 2.5 \times 10^6 \text{ A/cm}^2$ over the entire disk.

Appendix B

Magnetic flux penetration at temperatures of $50K$ and $70K$ into ring #1.

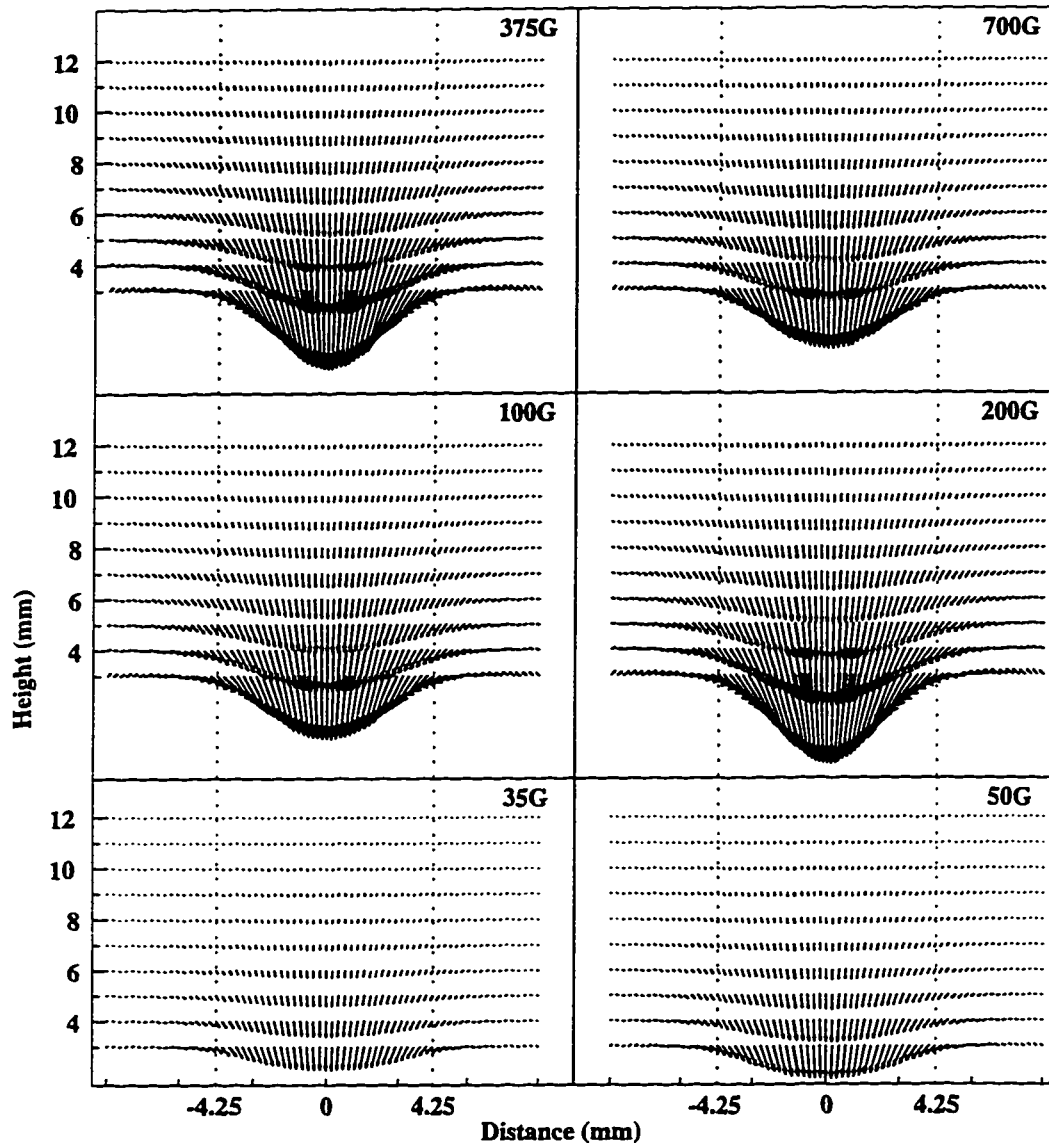


Figure 2.0.1: The vectors of the shielding field measured at distances between 3 and 12mm (every 1mm) above the surface of ring #1 at 50K and at applied magnetic fields of 35, 50, 100, 200, 375 and 700G. The magnitude of each vector is proportional to the magnitude of the total field at the same position normalized to the maximum magnitude of the shielding field in each Figure. Distances $\pm 4.25\text{mm}$ and $\pm 2.50\text{mm}$ mark the outer and inner ring's edges, respectively.

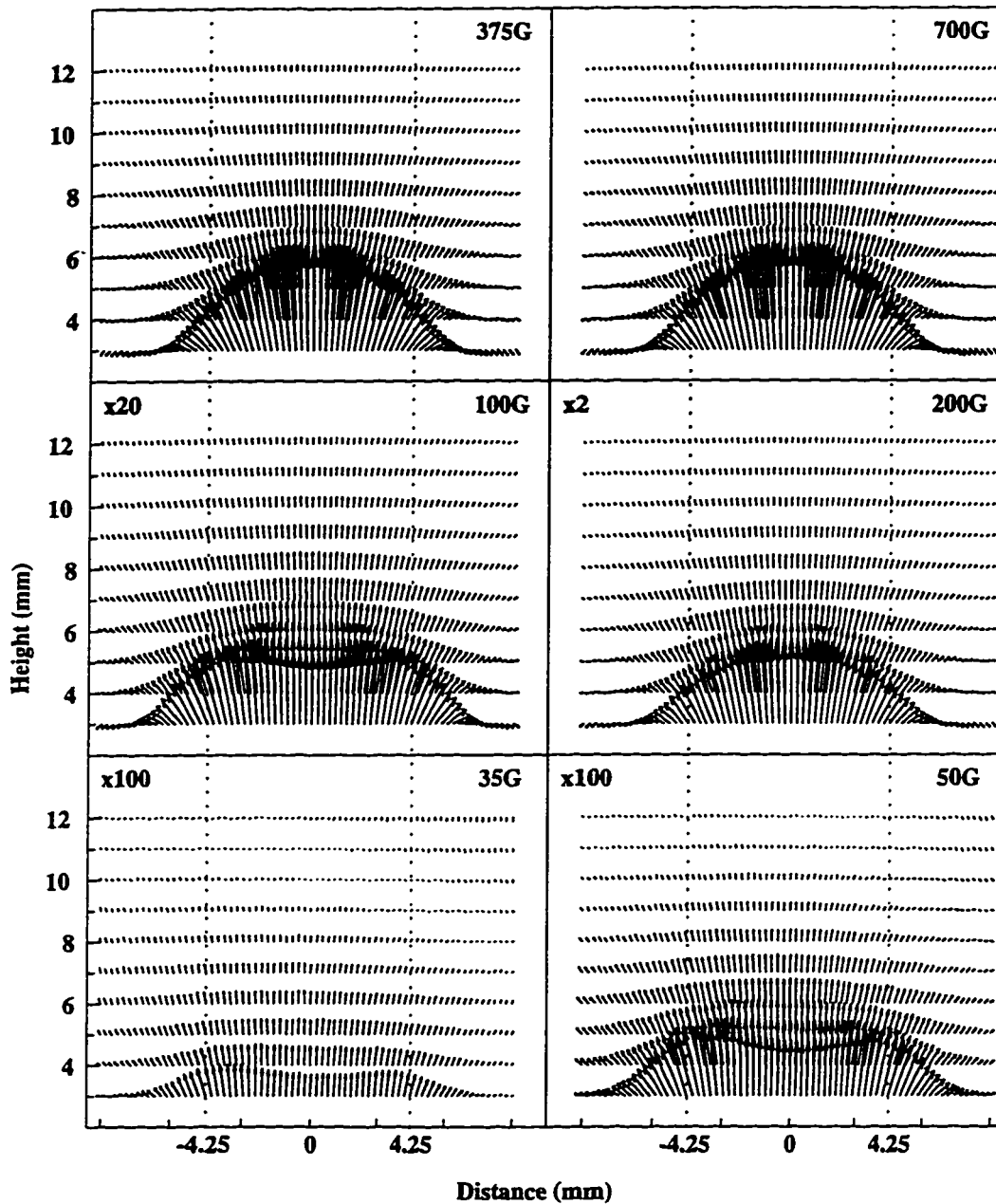


Figure 2.0.2: The vectors of the trapped field measured at distances between 3 and 12mm (every 1mm) above the surface of ring #1 at 50K and at applied magnetic fields of 35, 50, 100, 200, 375 and 700G. The magnitude of each vector is proportional to the magnitude of the total field at the same position normalized to the maximum magnitude of the trapped field in each Figure. Distances ± 4.25 mm and ± 2.50 mm mark the outer and inner ring's edges, respectively. $\times 2$, $\times 20$ and $\times 100$ mark the magnification of the vectors.

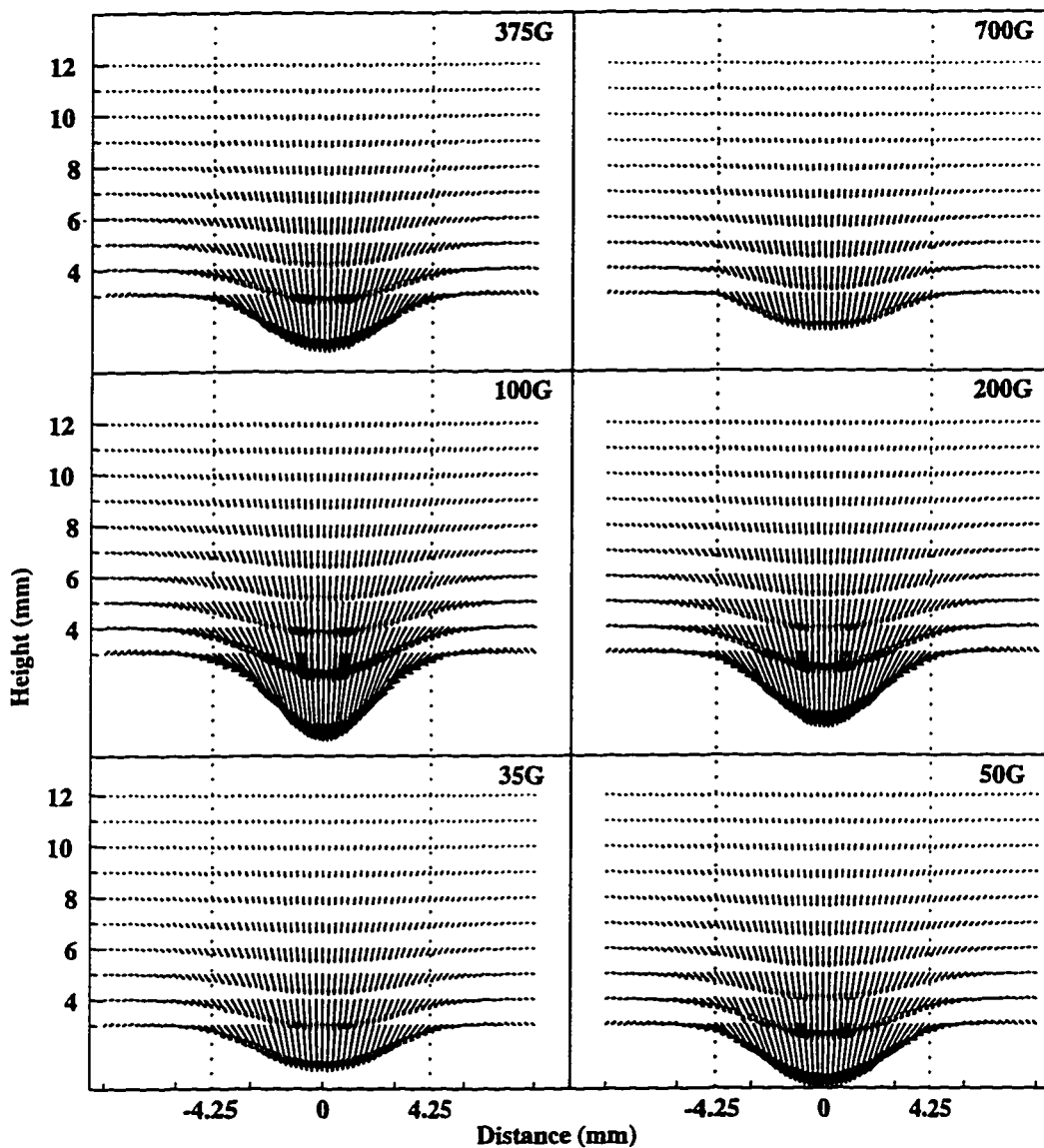


Figure 2.0.3: The vectors of the shielding field measured at distances between 3 and 12mm (every 1mm) above the surface of ring #1 at 70K and at applied magnetic fields of 35, 50, 100, 200, 375 and 700G. The magnitude of each vector is proportional to the magnitude of the total field at the same position normalized to the maximum magnitude of the shielding field in each Figure. Distances $\pm 4.25\text{mm}$ and $\pm 2.50\text{mm}$ mark the outer and inner ring's edges, respectively.

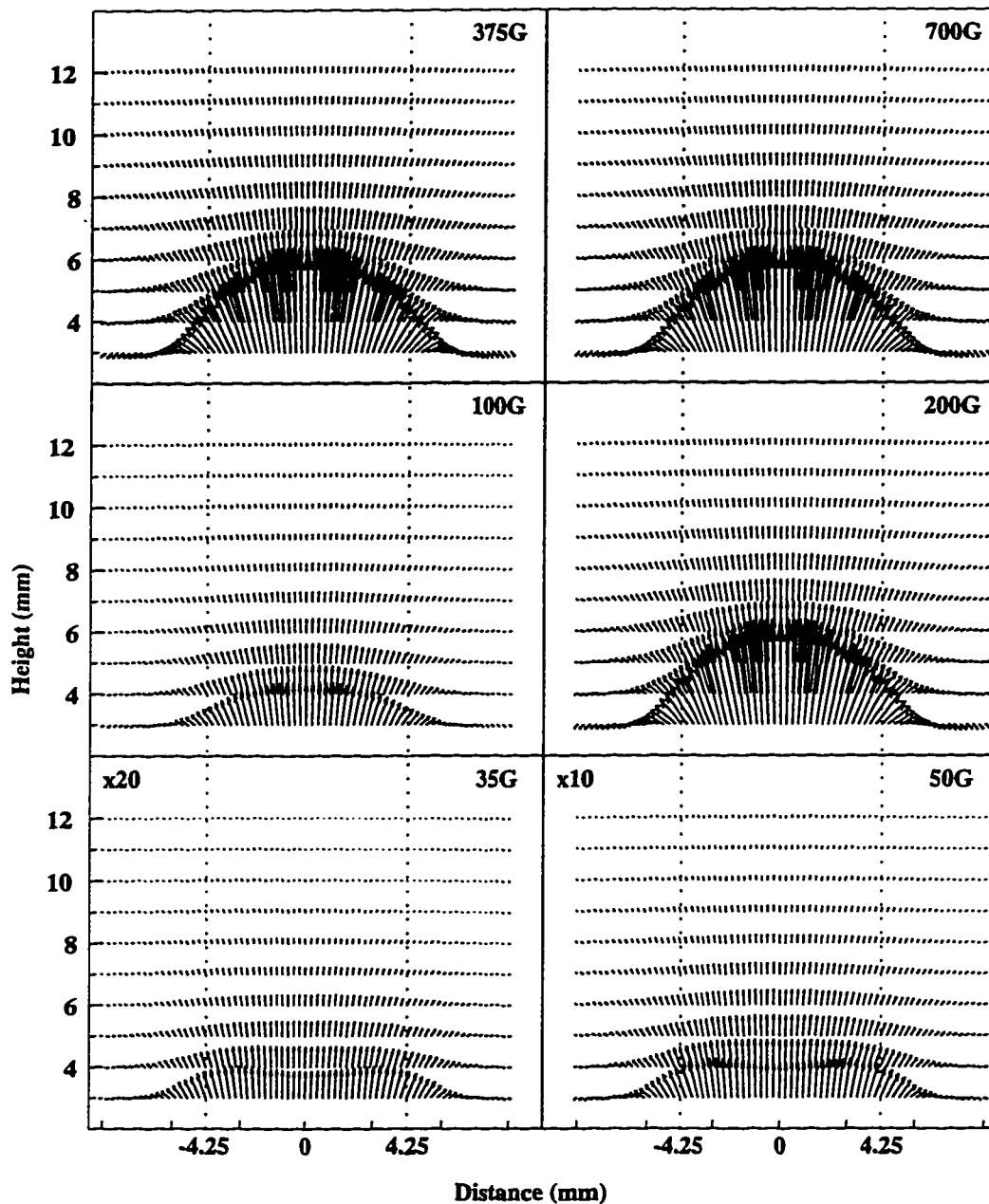


Figure 2.0.4: The vectors of the trapped field measured at distances between 3 and 12mm (every 1mm) above the surface of ring #1 at 70K and at applied magnetic fields of 35, 50, 100, 200, 375 and 700G. The magnitude of each vector is proportional to the magnitude of the total field at the same position normalized to the maximum magnitude of the trapped field in each Figure. Distances $\pm 4.25\text{mm}$ and $\pm 2.50\text{mm}$ mark the outer and inner ring's edges, respectively.

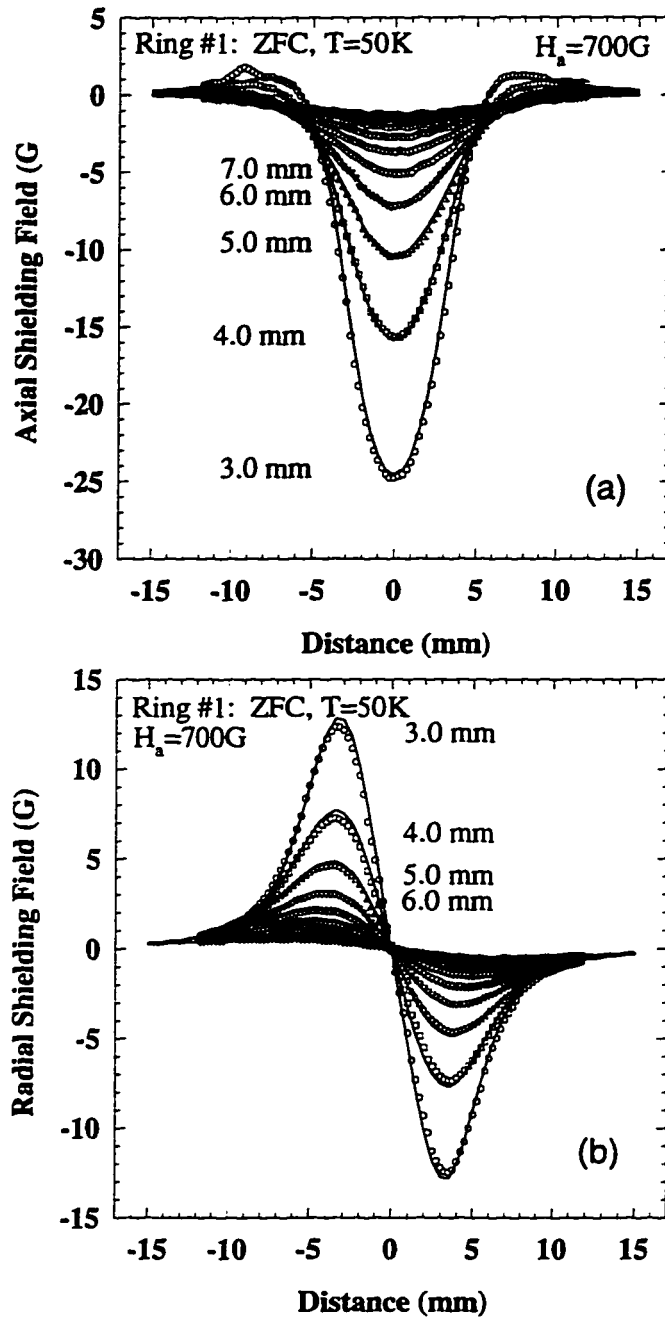


Figure 2.0.5: The profiles of the axial (a) and radial (b) magnetic shielding fields in a zero-field-cooled ring #1 at 700G, and 50K, which were measured as a function of an increasing distance above the sample from 3 up to 12mm. Open symbols represent the experimental data and the solid lines are the theoretical fits which use the Bean current distribution with $J_c = 3.61 \times 10^6 A/cm^2$ over the entire width of the ring.

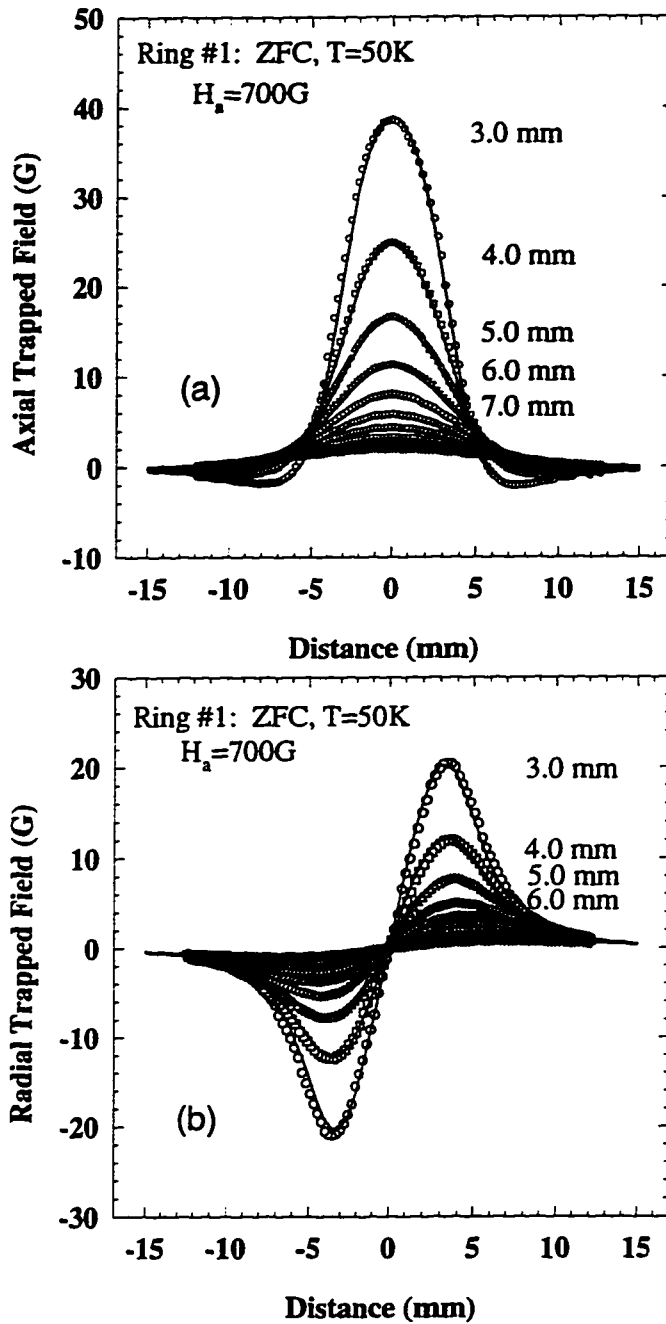


Figure 2.0.6: The profiles of the axial (a) and radial (b) magnetic trapped fields in a zero-field-cooled ring #1 at 700G, and 50K, which were measured as a function of an increasing distance above the sample from 3 up to 12mm. Open symbols represent the experimental data and the solid lines are the theoretical fits which use the Bean current distribution with $J_c = 5.73 \times 10^6 \text{ A/cm}^2$ over the entire width of the ring.

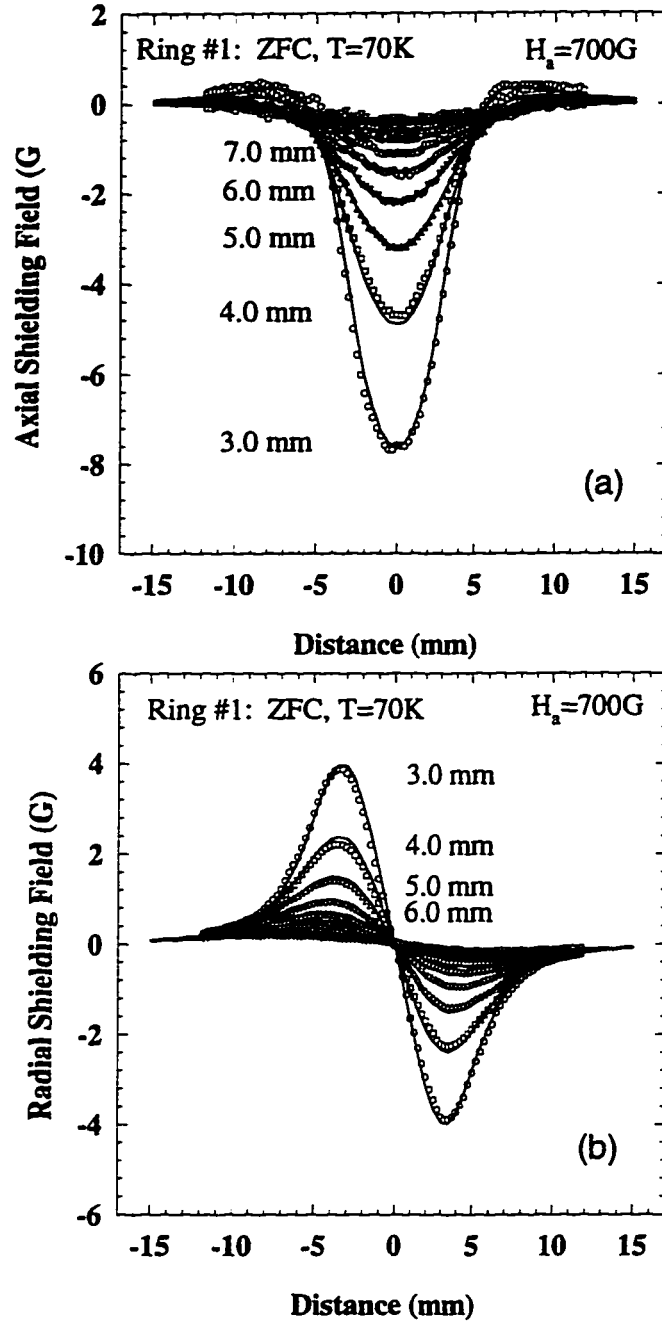


Figure 2.0.7: The profiles of the axial (a) and radial (b) magnetic shielding fields in a zero-field-cooled ring #1 at 700G, and 70K, which were measured as a function of an increasing distance above the sample from 3 up to 12mm. Open symbols represent the experimental data and the solid lines are the theoretical fits which use the Bean current distribution with $J_c = 1.12 \times 10^6 \text{ A/cm}^2$ over the entire width of the ring.

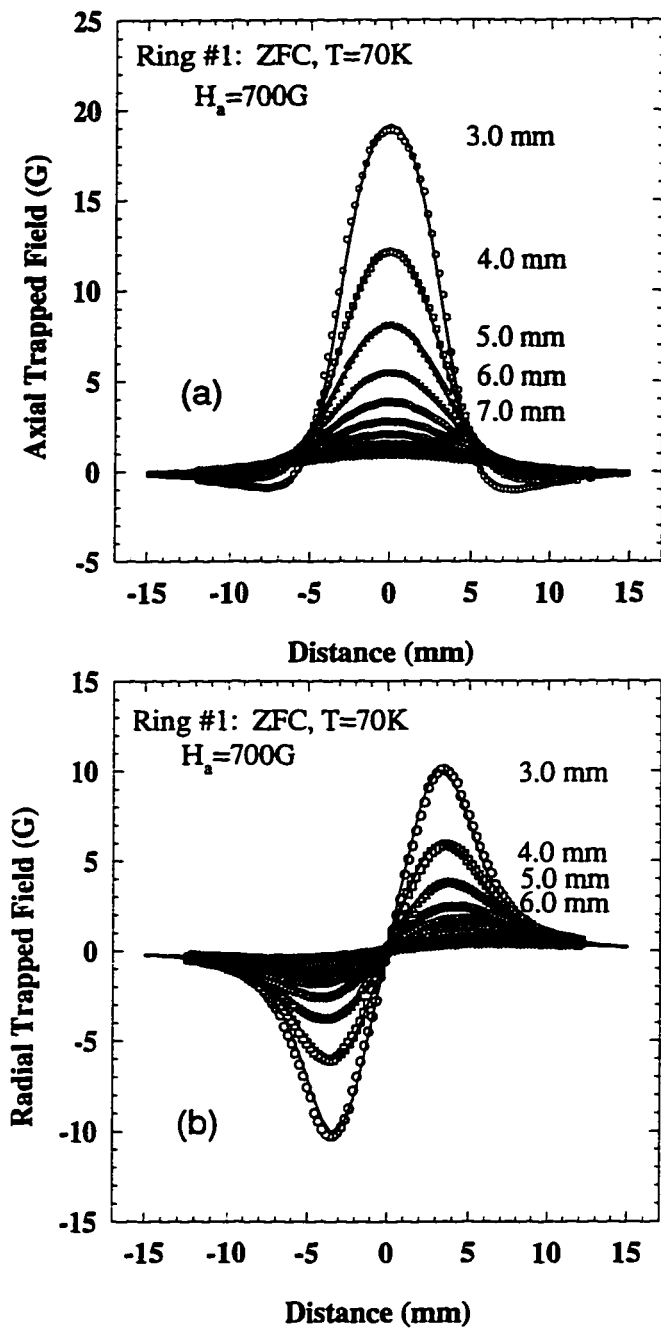


Figure 2.0.8: The profiles of the axial (a) and radial (b) magnetic trapped fields in a zero-field-cooled ring #1 at 700G, and 70K, which were measured as a function of an increasing distance above the sample from 3 up to 12mm. Open symbols represent the experimental data and the solid lines are the theoretical fits which use the Bean current distribution with $J_c = 2.82 \times 10^6 A/cm^2$ over the entire width of the ring.